

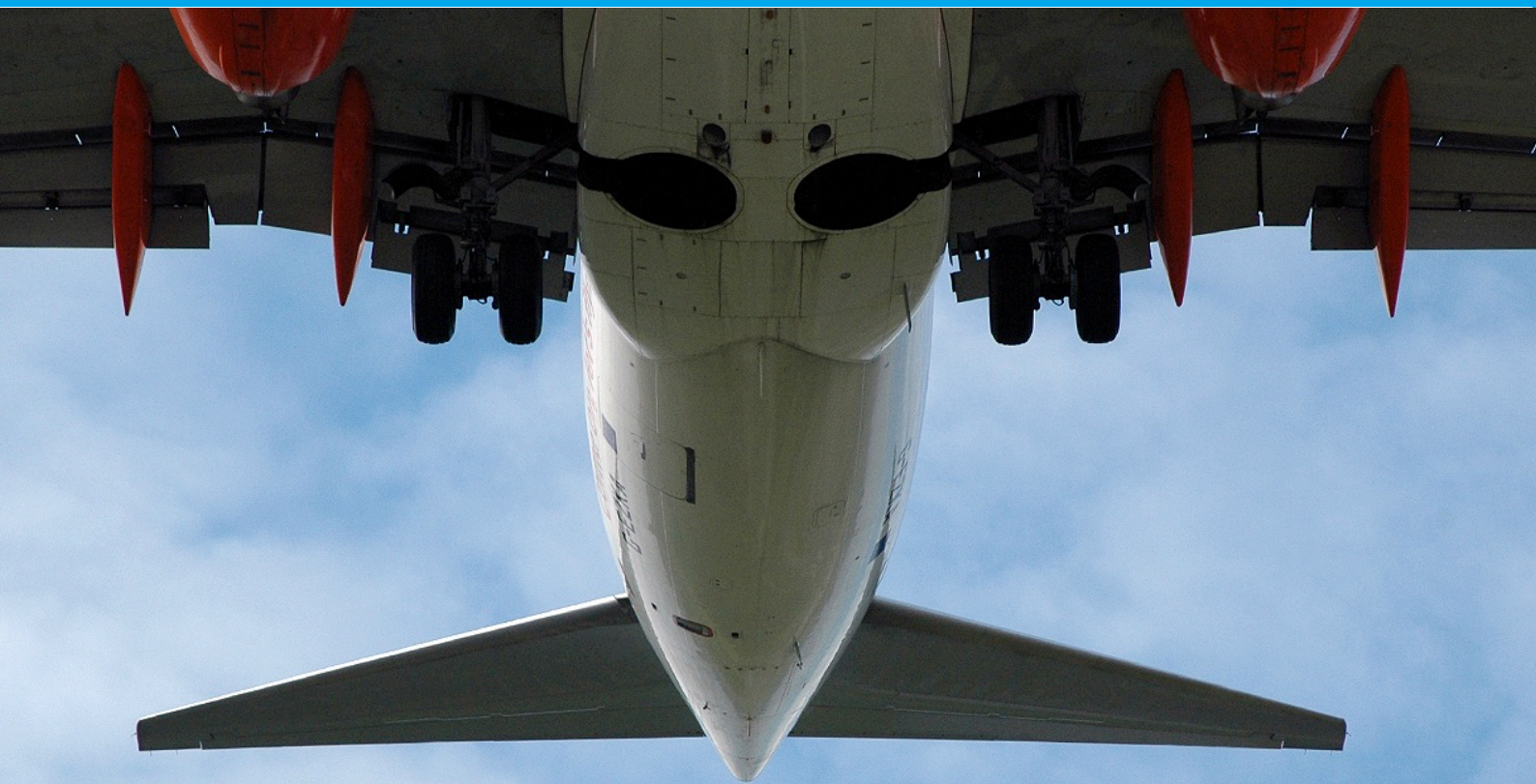


Aircraft noise calculation and synthesis in a non-standard atmosphere

Customer

National Aerospace Laboratory NLR

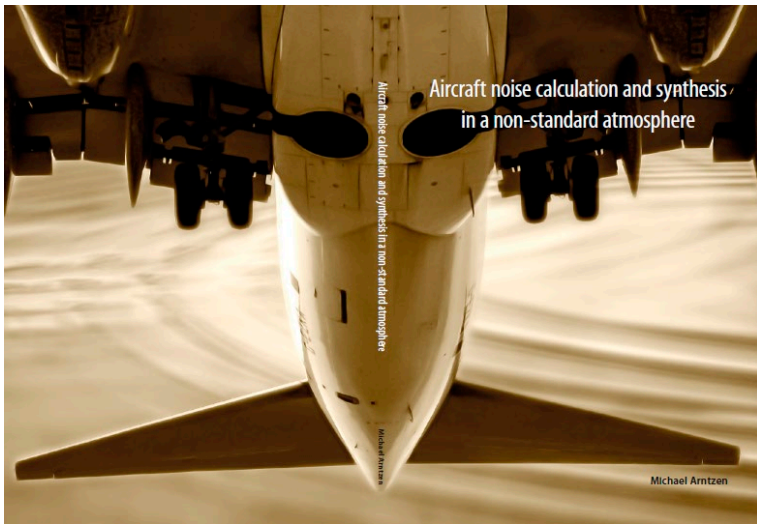
NLR-TP-2015-290 - July 2015



National Aerospace Laboratory NLR
Anthony Fokkerweg 2
1059 CM Amsterdam
The Netherlands
Tel +31 (0)88 511 3113
www.nlr.nl

EXECUTIVE SUMMARY

Aircraft noise calculation and synthesis in a non-standard atmosphere



Problem area

Aircraft noise auralization, or synthesis, is a technique to transform an aircraft noise prediction into an audible result. Such result can be used in NLR's Virtual Community Noise Simulator (VCNS). The current report is a copy of the dissertation of M. Arntzen that describes improvements of many aspects of this auralization capability at the NLR. Furthermore, insight was generated in the impact of non-standard atmosphere on aircraft noise contours.

Description of work

Aircraft noise synthesis comprises many aspects ranging from source noise prediction, atmospheric propagation to final delivery of the aircraft noise using the VCNS. This dissertation describes and improves the current state-of-the-art techniques that can be used in both source noise prediction and atmospheric

Report no.

NLR-TP-2015-290

Author(s)

M. Arntzen

Report classification

UNCLASSIFIED

Date

July 2015

Knowledge area(s)

Aircraft Noise

Aeroacoustic and Experimental Aerodynamics Research

Descriptor(s)

Virtual community noise simulator

Auralization

Atmospheric induced acoustic propagation loss

Ray tracing

propagation. Furthermore, comparisons to real-life measurements are included.

Results and conclusions

The research provides new insight in the atmospheric effect on noise contours. For instance, multi-event noise contours, such as often used in aircraft noise policies, are more affected by atmospheric absorption than by refraction effects. Auralization results for the VCNS have been brought more in line with measurements by including advanced atmospheric propagation effects. Both a curved ray propagation technique and a method to include turbulence induced coherence were developed to that end.

Applicability

The results from this dissertation advance the knowledge on aircraft noise auralization and can be directly applied in the VCNS. For instance, some of the developed digital signal processing technique was applied to create auralizations of future air traffic near Lelystad airport.

National Aerospace Laboratory NLR

Anthony Fokkerweg 2, 1059 CM Amsterdam,
P.O. Box 90502, 1006 BM Amsterdam, The Netherlands
Telephone +31 (0)88 511 31 13, Fax +31 (0)88 511 32 10, www.nlr.nl



Aircraft noise calculation and synthesis in a non-standard atmosphere

M. Arntzen

Customer
National Aerospace Laboratory NLR
July 2015

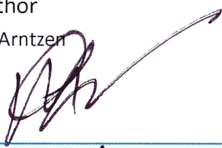
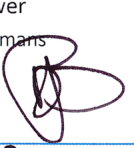
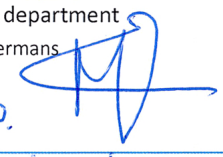
Aircraft noise calculation and synthesis in a non-standard atmosphere

This report is based on a dissertation defended, successfully, by the author at the Technical University Delft on the 4th of December 2014.

The contents of this report may be cited on condition that full credit is given to NLR and the author.

Customer	National Aerospace Laboratory NLR
Contract number	5003103
Owner	NLR + partner(s)
Division NLR	Air Transport
Distribution	Unlimited
Classification of title	Unclassified
Date	July 2015

Approved by:

Author  M. Arntzen	Reviewer  D. Bergmans	Managing department  F.J.M.M. Hermans i.o.
Date 31/07/15.	Date 31/07/15	Date 03/08/15

Aircraft noise calculation and synthesis in a non-standard atmosphere

PROEFSCHRIFT

ter verkrijging van de graad van doctor
aan de Technische Universiteit Delft,
op gezag van de Rector Magnificus Prof. Ir. K.C.A.M. Luyben,
voorzitter van het College voor Promoties,
in het openbaar te verdedigen
op donderdag 04 december 2014 om 15.00 uur
door

Michael ARNTZEN

ingenieur Luchtvaart en Ruimtevaart
geboren te Amersfoort.

Dit proefschrift is goedgekeurd door de promotor:

Prof. Dr. D.G. Simons

Copromotor: Dr. Ir. H.G. Visser

Samenstelling promotiecommissie:

Rector Magnificus

Prof. Dr. D.G. Simons

Dr. Ir. H.G. Visser

Prof. Dr.-Ing. E. Stumpf

Dr. S.A. Rizzi

Prof. Dr. Ir. C.P.A. Wapenaar

Prof. Dr. Ir. M. Mulder

Prof. Dr. Ir. L.L.M. Veldhuis

voorzitter

Technische Universiteit Delft, promotor

Technische Universiteit Delft, copromotor

RWTH Aachen

NASA Langley

Technische Universiteit Delft

Technische Universiteit Delft

Technische Universiteit Delft



This research was funded by the National Aerospace Laboratory (NLR).

Copyright © 2014 by M. Arntzen

All rights reserved. No part of the material protected by this copyright notice may be reproduced or utilized in any form or by any means, electronic or mechanical, including photocopying, recording or by any information storage and retrieval system, without written permission of the copyright owner.

An electronic version of this dissertation (including audio samples) is available at
<http://repository.tudelft.nl/>

Printed in the Netherlands by Ipsonkamp Drukkers

ISBN-978-94-6259-464-7

Contents

Summary	vii
Samenvatting	ix
Nomenclature	xi
1 Introduction	1
1.1 Historic perspective	1
1.2 Community impact	4
1.3 Virtual Community Noise Simulator	6
1.4 Research objectives	8
1.5 Thesis outline	8
2 Aircraft source noise prediction	11
2.1 Acoustic wave equation	11
2.2 Aerodynamic sound sources	16
2.3 Elementary sources	19
2.4 Moving source effects	22
2.5 A toolchain for aircraft source noise prediction	25
2.6 Acoustic source models	28
2.7 Overall aircraft noise	38
3 Atmospheric propagation of sound	41
3.1 Atmospheric absorption	41
3.2 Ground reflection	46
3.3 Spreading losses	53
3.4 Combined propagation model	67
4 Noise contours in non-standard atmospheres	71
4.1 Noise contour algorithms	71
4.2 Ray tracing based EA implementation for Doc.29	72
4.3 Multi-event calculation setup	75

4.4	Results	79
4.5	Discussion	82
4.6	Conclusions	87
5	Signal processing for aircraft noise synthesis	89
5.1	Source noise synthesis	89
5.2	Signal processing steps for propagation	93
5.3	Combining source synthesis and propagation	100
6	Atmospheric propagation effects in aircraft noise synthesis	105
6.1	Review of the prior approaches	105
6.2	New simulation framework	106
6.3	Results	111
6.4	Conclusions	122
7	Synthesis of aircraft departures	125
7.1	Objective	125
7.2	Study setup	126
7.3	Results and Discussion	129
7.4	Conclusion	136
8	Turbulence-induced coherence loss and ray tracing parallelization	137
8.1	Turbulence-induced coherence loss in ground reflection	137
8.2	Ray tracing parallelization	146
9	Conclusions	153
9.1	Conclusions	153
9.2	Future topics	157
	Bibliography	168
	Appendix	169
	A Coherent addition of sound waves	169
	B Spectral analysis and noise metrics	173
	C Propagation effects	177
	D Toolchain variables, gasturbine and flight mechanics	189
	E Supplementary audio files	195
	Acknowledgements	197
	Publications	199
	About the author	201

Summary

Aircraft noise has to propagate over long distances through the atmosphere before reaching an observer. The atmosphere modifies the sound waves during propagation and is therefore important in the calculation of aircraft noise contours or synthesis. Noise contours present the resulting noise levels on the ground and are, as such, often applied for regulatory purposes. Aircraft noise synthesis is a technique that allows to transform a calculated prediction into audible sound that can be experienced in a virtual reality environment such as the Virtual Community Noise Simulator (VCNS). Noise synthesis techniques allow people to be subjected to aircraft, routes or procedures that are still being designed and aids in communication with an affected population. This dissertation describes recent research to improve the modeling of atmospheric propagation effects in aircraft noise contours as well as aircraft noise synthesis.

Aircraft noise contours or synthesis requires modeling of both the source noise and the propagation losses. An algorithm was created, based on multiple source noise prediction methods, to generate the source noise level. The employed (empirical) source noise models predicted jet mixing noise, fan noise, combustor noise and airframe noise in 1/3rd octave-bands. The applied propagation algorithm is based on ray tracing described by Snell's law. The use of such a method allows to calculate the deviation of straight line propagation between the source and receiver due to temperature and wind gradients in the atmosphere. The resulting algorithm combines atmospheric absorption, ground interference and geometrical spreading to calculate the transmission loss. A correction mechanism is included for diffraction in shadow zones as ray tracing is limited in such a condition.

Multi-event noise contours are usually calculated with standardized models that take non-standard propagation into account in an empirical fashion. The developed propagation algorithm was used to augment such a model. This dissertation shows that the effects of refraction are minimal on a yearly noise contour for the Dutch atmosphere. Atmospheric absorption proved to be a larger factor than refraction, especially the accumulated absorption over the ray path. The accumulated absorption is not included in standardized noise contour algorithms and leads to a varying contour size on a monthly basis. Single event noise contours are even more different in both the enclosed area and form.

Signal processing steps can be applied to transform a source noise prediction into an audible result. Furthermore, such steps can be utilized to apply propagation effects to a source noise signal. The role of a non-standard atmosphere is described by a simulation framework developed in this dissertation. The framework is applied to a flyover to demonstrate the effects associated with multiple ray paths and shadow zones. These effects are prominent only at shallow elevation angles of the aircraft source with respect to the observer. In case of an aircraft passing overhead, the effect of refraction on sound metrics is negligible. A real-time inclusion of the non-standard propagation algorithm in the VCNS is feasible if use is made of Graphical Processing Units of a computer.

Besides demonstrating non-standard atmospheric effects, the framework was used to create synthesized results of actual flyovers near an airport. Subsequently, a comparison between measured results and synthesized results was executed. Noise metrics were approximated relatively well by the synthesized results, although audible differences remain. Such differences can also be expected to be caused by empirical source noise modeling that are necessarily hampered by approximations. The application of the signal processing techniques led to the distinctive presence of ground interference, especially at high frequencies, in the synthesized results. This characteristic interference is usually absent in the measured results for high frequencies. A method was designed to include the effect of turbulence-induced coherence loss of the direct and ground reflected ray in noise synthesis. As a result, the distinctive presence of the ground interference was reduced and brought more in line with the actual measured results.

Samenvatting

Vliegtuiggeluid legt een lange weg af door de atmosfeer voordat het bij een ontvanger aankomt. De atmosfeer modificeert de geluidsgolven gedurende dat proces en is, vandaar, van groot belang bij het berekenen van vliegtuiggeluidcontouren en vliegtuiggeluidssynthese. Een geluidscontour representeert de geluidsdosage die wordt waargenomen op de grond en wordt veelal gebruikt voor handhaving. Vliegtuiggeluidssynthese maakt het mogelijk om berekend geluid daadwerkelijk te ervaren door middel van een virtuele omgeving zoals de Virtual Community Noise Simulator (VCNS). Dit is interessant aangezien vliegtuigen, routes en procedures, die de ontwerpfasen nog niet ontgroeid zijn, nu al kunnen worden ervaren. Vandaar levert vliegtuiggeluidssynthese een positieve bijdrage aan de communicatie met omwonenden van vliegroutes. Dit proefschrift beschrijft onderzoek ten behoeve van een verbeterde modellering van atmosferische voortplanting voor zowel geluidscontouren als geluidssynthese.

Om een vliegtuiggeluidcontour of synthese mogelijk te maken, moeten zowel bron als voortplanting expliciet gemodelleerd worden. Voor geluidssynthese wordt gebruik gemaakt van empirische modellen die het vliegtuiggeluid voorspelen in $1/3^{\text{e}}$ oktaaf banden. Hierdoor zijn modellen voor 'jet', 'fan', 'combustor' en 'airframe' lawaai, in een algoritme opgenomen om tot een voorspelling van het bronniveau te komen. De atmosferische voortplanting van het geluid is gebaseerd op straalakoestiek zoals beschreven door de wet van Snellius. Hiermee kan de afwijking van een rechte lijn tussen de bron en ontvanger, door de atmosferische invloed van temperatuur- en windgradiënten, worden berekend. Er is een algoritme ontwikkeld waarin de effecten van atmosferische absorptie, grond reflectie en geometrische spreiding worden gecombineerd. Bovendien is er een correctie voor schaduwzones opgesteld, een beperking van straalakoestiek.

Geluidscontouren worden normaliter berekend met standaardmodellen waarin de rol van atmosferische voorplanting empirisch gemodelleerd is. Deze empirische relatie zou representatief moeten zijn voor een geheel jaar. In dit proefschrift is aangetoond dat de gevolgen van het afbuigen van geluid, voor een geluidscontour gebaseerd op een jaar lang verkeer, minimaal zijn voor de gegeven Nederlandse atmosferische condities. Atmosferische absorptie bleek van grotere invloed en leidde tot veranderende afmetingen van de geluidscontouren op maandbasis. Daarentegen kan voor een enkele vlucht, ten gevolge van de atmosfeer, een groot verschil optreden in de geluidscontour.

Met behulp van signaalverwerking kunnen voorspellingen van het brongeluid hoorbaar worden gemaakt. Daarnaast kan men, middels signaalverwerking, de voortplanting van geluid in het signaal opnemen. Atmosferische effecten hebben een grote impact op algoritmes die daarvoor ontwikkeld zijn. Daarom is een nieuw algoritme voorgesteld waardoor effecten van meerdere geluidspaden en schaduwzones kunnen worden meegenomen. Deze effecten zijn voornamelijk relevant onder kleine hoeken van het vliegtuig ten opzichte van de luisteraar. Indien het vliegtuig echter recht over een ontvanger heen vliegt, zullen de effecten op gebruikelijke geluidsmetrieken niet groot zijn. Om deze effecten real-time in een virtuele omgeving te simuleren, met het huidige algoritme, zal gebruik gemaakt moeten worden van de kracht van de grafische kaarten in computers.

Eveneens is onderzocht of de resultaten van de vliegtuiggeluidssynthese, overeen kwamen met gemeten resultaten nabij vliegvelden. Geluidsmaten zoals het 'Sound Exposure Level' en de ' $L_{A,max}$ ' werden relatief goed benaderd. Desalniettemin bleven er hoorbare verschillen bestaan, mede veroorzaakt door de empirische bronmodellering en de aannames die zulke modellen (moeten) maken. Ook onstond er een hoorbaar verschil tussen een meting en geluidssynthese in het door de grond veroorzaakte interferentie patroon. In de praktijk wordt dit beïnvloed door turbulentie wat resulteert in een coherentieverlies van de directe en grond-gereflecteerde akoestische straal, in het bijzonder bij hoge frequenties. In dit proefschrift is een methode ontwikkeld die het mogelijk maakt om deze effecten mee te nemen in de synthese van vliegtuiggeluid. Het resultaat daarvan is dat de invloed van grondreflectie nu beter correspondeert met de praktijk.

Nomenclature

Roman symbols

A	Plane wave amplitude	Pa
A_A	Overall transmission loss due to atmospheric absorption	dB
A_d	Spreading loss component due to diffraction	dB
A_G	Ground interference effect on transmission loss	dB
A_r	Spreading loss component due to geometric spreading	dB
A_S	Spreading loss effect on overall transmission loss	dB
b_d	FIR Filter coefficients	—
c	Speed of sound	m/s
C_p	Coefficient of heat capacity at constant pressure	$J/(kgK)$
C_v	Coefficient of heat capacity at constant volume	$J/(kgK)$
D	Empirical directivity function	dB
d_j	Jet diameter	m
F	Empirical spectral shape function	dB
F	Spherical wave reflection coefficient correction factor	—
$F_{1,2,3}$	External force in Cartesian directions	N
f	Frequency in Hertz	Hz

G	Green's function	—
g	Gain	—
$g_{1,2}$	Arbitrary function	—
H	Fraction of water molecules in the air	%
h	Impulse response (time domain)	
h_d	Path traverse distance	m
h_m	Microphone height	m
\mathbf{I}	Identity tensor	—
I	Acoustic intensity	W/m^2
k	Wave number	$1/m$
$k_{1,2,3}$	Constants for Fink model	—
l	Turbulent eddy length	m
$L_{1,2}$	Components of diffractive spreading loss	—
L_0	Outer scale of turbulence	m
M	Mach number	—
m	Mass	kg
P	Empirical acoustic loading function	dB
p	Pressure	Pa
p_i	Acoustic tonal (harmonic) signal	Pa
Q	Ground reflection coefficient	—
R	Specific (ideal) gas constant, 287 for air	$J/(kgK)$
r	Distance from source \vec{y} to observer \vec{x} , i.e. $r = \vec{y} - \vec{x} $	m
R_c	Reciprocal filter function	—
RH	Relative Humidity	%
R_p	Plane wave reflection coefficient	—
s	Ray path arc length	m

St	Strouhal number	—
\mathbf{T}	Lighthill stress tensor	—
T	Temperature	K
T_c	Coherence function	—
t	Time	s
t_c	Convection time for turbulent eddy	s
t_p	Period of a harmonic wave	s
u	Velocity	m/s
u_c	Convection velocity for turbulent eddy	m/s
u_s	Jet outflow velocity	m/s
V	Source volume	m^3
w	Ray position	m
x	Input signal	—
y	Output signal	—
Z_n	Normalized ground impedance	—

Greek symbols

α	Atmospheric absorption coefficient	dB/m
δ	Dirac delta function or the Kronecker delta	—
η	Refractive index	—
γ	Specific heat ratio	—
Γ	The day-evening-night multiplier, i.e. 1, 5 or 10	—
λ	Wavelength	m
μ	Viscosity	$kg/(sm)$
$\langle \mu^2 \rangle$	Fluctuating index of refraction	—
ω	Angular frequency	rad/s

ϕ	Ground reflection phase change angle	<i>rad</i>
ψ	Sideline angle	<i>rad</i>
π	Ratio of circle circumference to diameter	—
ρ	Density	<i>kg/m³</i>
ρ_c	Phase covariance	—
σ_e	Effective flow resistivity	<i>kPa/m² · s</i>
σ_t	Phase fluctuation variance	—
τ	Viscous stress tensor	—
τ	Eikonal	—
τ	Emission time	<i>s</i>
τ_v	Molecular relaxation time	<i>s</i>
Θ	Phase argument of a harmonic wave	<i>rad</i>
θ	Polar angle	<i>rad</i>
θ_i	Incident ray angle	<i>rad</i>
θ_t	Transmitted ray angle	<i>rad</i>

Sub- and Superscripts

'	Acoustic variable
e	Effective
∞	Ambient conditions
ISA	International Standard Atmosphere
j	Jet
0	Origin
<i>cl</i>	Classical (absorption)
<i>v</i>	Atmospheric molecular component

Mathematical notations

\hat{u}	Frequency domain notation of variable u
\mathbf{u}	A bold font indicates a tensor (second order or dyad); $\mathbf{u} = \begin{pmatrix} u_{11} & u_{12} & u_{13} \\ u_{21} & u_{22} & u_{23} \\ u_{31} & u_{32} & u_{33} \end{pmatrix},$ where $u_{12} = u_1 u_2 \vec{e}_1 \vec{e}_2.$
$[u]$	Discrete time notation of continuous signal u
$\vec{e}_{1,2,3}$	Unit vector in Cartesian (x, y, z) direction
\vec{u}	Vector notation of u using Cartesian components; $u_1 = \vec{u} \cdot \vec{e}_1$
$\vec{u} \cdot \vec{u}$	Dot product of u ; $\vec{u} \cdot \vec{u} = \sum_i u_i u_i$
$\vec{u}\vec{u}$	Dyadic vector product of u ; $\vec{u}\vec{u} = u_i u_j = \mathbf{u}$
$ \vec{u} $	Vector norm of u ; $\sqrt{\vec{u} \cdot \vec{u}}$
$\frac{\partial u}{\partial t}$	Partial time derivative of u
$\frac{Du}{Dt}$	Material derivative of u ; $\frac{\partial u}{\partial t} + \vec{v} \cdot \nabla u$ and \vec{v} is a convective velocity
∇u	Gradient of a scalar; $\frac{\partial u}{\partial x} \vec{e}_1 + \frac{\partial u}{\partial y} \vec{e}_2 + \frac{\partial u}{\partial z} \vec{e}_3$
$\nabla \cdot \vec{u}$	Divergence of a vector; $\frac{\partial u_x}{\partial x} + \frac{\partial u_y}{\partial y} + \frac{\partial u_z}{\partial z}$
$\nabla \cdot \mathbf{u}$	Divergence of a tensor; $\nabla \cdot \mathbf{u} = \nabla \cdot \vec{u}\vec{u} = (\nabla \cdot \vec{u}) \vec{u} + (\vec{u} \cdot \nabla) \vec{u}$

Acronyms

AAS	Amsterdam Airport Schiphol
ANOPP	Aircraft Noise Prediction Program
BPF	Blade Passage Frequency
CFD	Computational Fluid Dynamics
CNOTE	Community Noise Test Environment
CPU	Central Processing Unit
DSP	Digital Signal Processing

EA	Excess Attenuation
ECAC	European Civil Aviation Conference
ESDU	Engineering Sciences Data Unit
FAA	Federal Aviation Authority
FIR	Finite Impulse Response (filter)
GE	General Electric
GPU	Graphics Processing Unit
HRTF	Head Related Transfer Function
IDFT	Inverse Discrete Fourier Transform
INM	Integrated Noise Model
LA	Lateral Attenuation
NASA	National Aeronautics and Space Agency
NLR	Dutch National Aerospace Laboratory
NPD	Noise-Power-Distance relation (usually tabulated)
OASPL	Overall A-weighted Sound Pressure Level
OLA	Overlap-Add (method)
OSPL	Overall Sound Pressure Level
PE	Parabolic Equation
RPM	Revolutions Per Minute
SPL	Sound Pressure Level
TL	Transmission Loss
UOSPL	Unrefracted Sound Pressure Level
VCNS	Virtual Community Noise Simulator
VDL	Variable Delay Line

Chapter 1

Introduction

This introduction sets the stage for the reported research in aircraft noise and its synthesis. Before defining the research goals, the historical background of atmospheric propagation and aircraft noise is briefly described. After this review, the introduction continues by looking forward to the research goals and dissertation outline.

1.1 Historic perspective

1.1.1 Acoustical propagation

Sound is a pressure disturbance, in a medium such as air, around a mean barometric pressure level. The pressure disturbance at a source spreads through the medium as energy is transferred between air particles until it hits the ear drum. As the ear drum starts to vibrate due to the alternating acoustic pressure, a signal is sent to the brain that interprets the disturbance as sound.

Sound, plus the influence of absorption on propagation, has been studied long before research in aviation was started. In the 19th century, researchers started to discover the intriguing propagation phenomenon of refraction. Refraction is the bending of sound rays, a deviation of the normal straight line assumption. It appears that George Stokes⁽¹⁾ was the first to correctly describe the refraction phenomena. Research into sound propagation was important for shipping. Ships were easily shipwrecked near the coast, in fog conditions they would hit the rocks, if they were not warned in advance. Since traditional light-houses would not suffice in foggy conditions, acoustic signals were believed to provide an alternative solution. However, researchers observed large differences between sound levels in different atmospheric conditions. At first it was believed that sound rays, in an analogy to light rays, were obstructed by fog explaining reduced sound levels. This was an appealing explanation since both light and sound were known to be wave phenomena. Although some observers denied the

observation that fog decreased the sound level, the common opinion became that optical transparency was a measure of acoustic transparency. However, experimental campaigns by John Tyndall showed⁽²⁾ that even in non-opaque conditions the sound level varied:

I refer to the rapid fall of intensity on both sides of the signal-station. We had halted between the station at a distance of 2.5 miles. The trumpets and whistles were sounded, but they were quite unheard. We moved nearer; but even at a mile distance, with the instruments plainly in view, their sound failed to reach us. A light wind, however, was here opposed to the sound.

The experimental campaign by Tyndall was designed to find a good (acoustic) fog signaling mechanism, which were believed to be either a steam pressure horn or a gun. The wind, however, played a major role as noted and the experiment offered contradictory results:

The acoustic transparency of the air was still further augmented on the 26th: at a distance of 9.25 miles from the station the whistles and horns were plainly heard against a wind with a force of 4;... ...Plainly, therefore, something else than the wind must be influential in determining the range of the sound.

The extensive report by Tyndall showed that propagation of acoustic waves was not trivial and influenced by more than optical transparency. The effect of wind was suspected but not yet exactly coined by his measurements. His campaign was executed in the summer of 1873 whereas in his report, dated February 1874, he referred to a lecture by Professor Osborne Reynolds who had a theoretical explanation for the effect of wind on acoustic propagation.

Reynolds was aware that he was preceded by Stokes, apparently Stokes's paper was not well known within the acoustics community, but independently came to the same conclusions regarding refraction. His experiment to prove refraction was particularly clever. He posed that acoustic waves would follow the same physical laws as those of waves in water. Consequently, he dropped small drops of water in a streaming river near a wall. The resulting wave pattern was sketched by him and shown in his article⁽³⁾ and is copied here in figure 1.1. Figure 1.1 shows that the waves do not form perfect circles. This is due to the river flowing in the direction of the arrow. As such, the waves going downstream approached the wall whereas in the upstream direction the waves died out. Reynolds accentuated this in his figure by using thicker lines in the downstream direction to show a greater intensity. Notice that he also denoted an interference pattern in the upstream direction.

Hereby the effect of refraction, i.e. the change in direction of waves due to a moving medium, was experimentally proven to exist by Reynolds. This effect will form a major role in aspects of this dissertation since it plays a role in propagating aircraft noise to the ground.

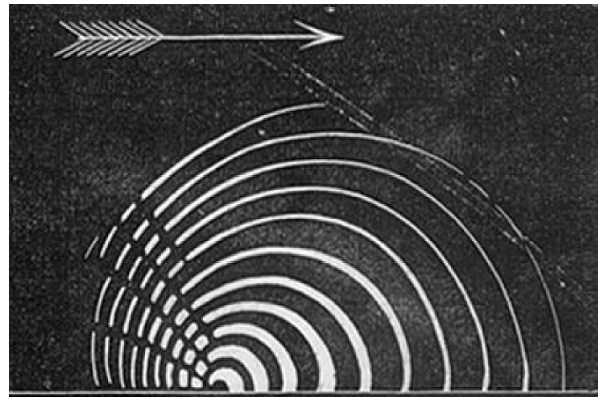


Figure 1.1: A sketch created by Reynolds⁽³⁾ reflecting his experimental observations thereby confirming refraction already in 1874.

1.1.2 Aircraft noise

Aircraft are one of the greatest inventions of the last centuries. As people only dreamed of flying as free as a bird, engineers like Lilienthal made it happen. The Wright brothers went a step further and extended the airplane by the addition of a steering mechanism and a power source. As such, the age of aviation was born. The few aircraft that habited the earth were an attraction and amazed people.

After the first world war, transportation of passengers and cargo by means of air transport was explored. Soon thereafter mail could be delivered considerably faster than before and voyages towards the far outskirts of the world came within reach. The need for air transportation gradually increased and research into faster and more advanced aircraft flourished. The outbreak of the second world war meant another boost for (aircraft) research. Research was not directed into the acoustics of aircraft but rather in the aerodynamic performance and propulsion. Aircraft were designed to go faster, higher and further. It was, however, the roar of a jet engine that stirred the first research in the field of aviation noise.

Jet engines were developed in the United Kingdom and Germany around the same time. The roar that these engines made was quite different from the usual propeller sound. Jet engines provide thrust by increasing the momentum of the air flowing through the engines. To achieve this, heat energy is added to the flow leading to an increased velocity of the air by expansion in the turbine and engine nozzle. This high velocity stream is referred to as a jet. In 1949, a few years after the war, the British government was trying to interest scientists to study the noise that these jets made. Although experimental work was underway to find empirical relations, a solid theoretical framework was lacking.

A young mathematician named Lighthill became interested in the problem and studied it in the subsequent years. He realized that the task ahead was challenging from both

a physical and mathematical stand point. The set of equations that would have to be studied were the Navier-Stokes equations, a set of partial differential equations describing the dynamics of air. He rearranged these equations to obtain the density (or pressure) disturbances. Additionally, he posed that the non-linear contribution would be of importance near the source but not further downstream. As such, he rearranged the Navier-Stokes equations in a linear part (classical wave equation) and a non-linear part (source terms). His paper⁽⁴⁾ was published in 1952 and he, single handedly, started the field of Aeroacoustics.

One of the stunning discoveries of Lighthill's analysis^(4;5), is the fact that the acoustic pressure of jet noise is typified by a quadrapole that scales with the eight power of the jet velocity. The first jet engines were designed to maximize the air momentum by accelerating a small mass of air to great velocities leading to much noise. Modern (civil) gasturbines work different by accelerating a larger mass of air to reduced velocities, leading to the same momentum, but a reduced acoustic pressure. Besides the beneficial fuel savings it is a direct application of Lighthill's theoretical work. The Lighthill analogy, i.e. rearrangement of governing equations, is still applied in various forms today to study and reduce aircraft noise.

1.2 Community impact

Modern aircraft are still able to amaze people and capture their imagination. They have become a regular occurrence compared to the early days of aviation. As such, downsides of aircraft like noise and pollution need to be evaluated carefully to ensure a 'habitable' environment for communities. Airports are, especially in the Netherlands, surrounded by residential areas. To evaluate the noise impact on residents, noise contours are calculated, an example is provided in figure 1.2.

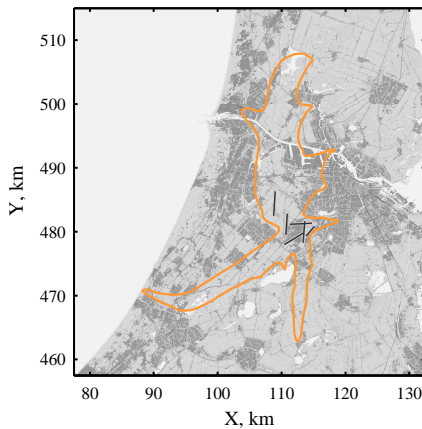


Figure 1.2: An example of a 50 L_{DEN} noise contour near Schiphol airport.

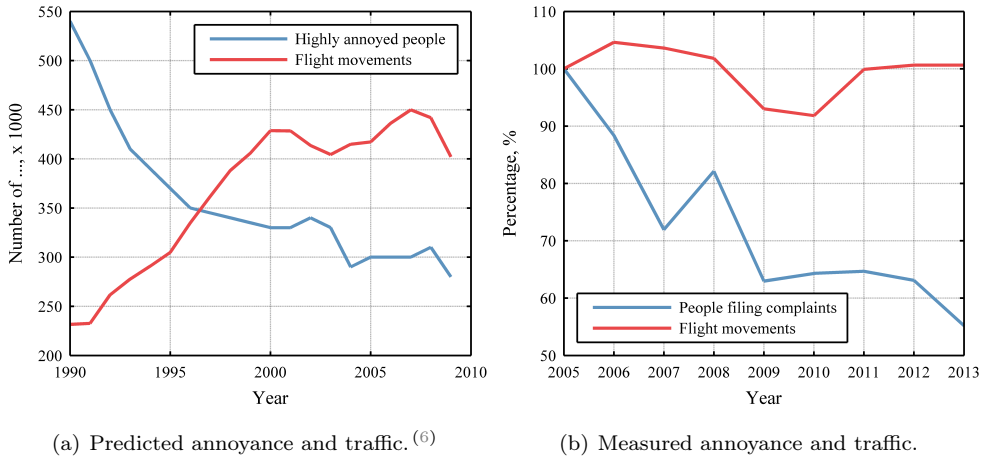


Figure 1.3: Modeling and measuring the number of annoyed people around Schiphol over time.

Figure 1.2 shows a noise contour plotted on top of a map of the vicinity of Amsterdam. This is a fictitious case but illustrates the way in which aircraft noise, from an entire year of operations, is regularly presented. Regulations are usually based on such noise contour calculation algorithms to balance both aircraft operations and noise annoyance. Thereby, governments have been more or less successful in controlling the predicted annoyance.

An example of such a study is provided in figure 1.3(a). This figure, adopted from⁽⁶⁾, shows the amount of operations at Schiphol airport in the Netherlands and the corresponding predicted annoyance based on a dose-response relationship. Furthermore, figure 1.3(a) illustrates that despite the increase in air traffic the amount of predicted annoyance has decreased. Looking closely to the period from 2005 onwards shows that the calculated annoyance is relatively constant until 2007.

Figure 1.3(b) shows the amount of people who actually complained versus the traffic at Amsterdam Airport Schiphol (AAS). This figure was created by combining public data from AAS and the organization that files the complaints near Schiphol due to aircraft noise annoyance.* If we look at the same period as was just illustrated for figure 1.3(a), from 2005 till 2007, figure 1.3(b) shows that despite the higher traffic, the amount of people complaining reduced. Whereas from 2007 to 2008, the amount of traffic declined but there were more people complaining. This illustrates the complexity of the matter and shows that more variables need to be taken into account for an accurate prediction.

The impact of aircraft on experienced annoyance is not solely due to aircraft noise. It is well known^(6;7) that many non-acoustic factors can contribute to aircraft (noise)

*Data originates from yearly reports of AAS and Bewoners Aanspreekpunt Schiphol (BAS).

annoyance. Managing expectations regarding aircraft noise and clear communication remains of vital importance in aircraft noise. For instance, residents of areas that are not directly neighboring a noise contour, as depicted in figure 1.2, may expect that they are not exposed (or to a small extent) to aircraft noise. As such, if unexpected noise occurs, this unexpected noise can be highly annoying.⁽⁸⁾ As already introduced in the previous section, wind is known to affect acoustic propagation. How much it influences noise contours is, however, not thoroughly researched.

Noise contours only provide partial information regarding the actual noise and annoyance. Difficulties in selecting noise metrics, dose-response curves and differences between single-event vs. multi-event, all contribute to uncertainty in analyzing contour plots or predicting the number of annoyed people. The complexity of such noise contours, and using contours thus as a means of communication, is very challenging. To evaluate noise mitigations measures on a subjective level requires new modeling steps and tests.

Subjective evaluations of aircraft flyover noise are not common in the design phase, but can give valuable information regarding the impact of design changes, e.g. alternative configurations or operations. One of the lucid examples is the synthesis of a flying wing configuration (Hybrid Wing Body) by the National Aeronautics and Space Agency (NASA).⁽⁹⁾ Simulation of aircraft flyover noise is also an effective tool to communicate noise impact to stakeholders. Neighboring communities often struggle to understand the impact of new aircraft, procedures or atmospheric conditions on their sound exposure. They would benefit from audible (and visual) demonstrations of future situations in addition to noise exposure maps. To do such subjective evaluations, a system was envisaged where people are exposed to flyover noise in a virtual reality environment. In this environment, the new measures can be evaluated on different locations by different people.

1.3 Virtual Community Noise Simulator

The National Aerospace Laboratory (NLR) in the Netherlands acquired such a virtual reality system in 2007. The NASA designed system included custom developed software and commercial off-the-shelf hardware, including the AuSIM Gold-Server⁽¹⁰⁾ to execute the real-time rendering of sound, i.e. applying positional audio and propagation effects. Working with AuSIM, NASA integrated a system for the NLR including their Community Noise Test Environment (CNoTE) software. This started the co-operative effort between the NASA and the NLR to work in this area and has, since then, included many (software) upgrades.

At the NLR, the system was renamed as the Virtual Community Noise Simulator (VCNS) and used to replay recorded flyover noise. An impression of the system can be obtained from figure 1.4(a). In figure 1.4(b), a person wearing a Helmet Mounted Display (HMD) through which the visuals are provided, experiences a recorded flyover. The HMD visuals are augmented by audio as is supplied via headphones. A small gyroscope, attached to the headphones, tracks the head movement and allows to



(a) The VCNS system.



(b) The Dutch King in the VCNS.

Figure 1.4: *The VCNS system and a demonstration session depicting the use of the VCNS.*

update the visuals and audible cues. The visuals are created using OpenSceneGraph* and supplied to the HMD. NLR recently integrated the Oculus-Rift visualization glasses to enhance visual immersion.[†]

Using the VCNS allows people to judge aircraft noise mitigation measures on both the visual and audible aspects. The VCNS can also serve as an educational tool to evaluate the actual situation that people are exposed to. For instance, policy makers can experience the impact of their own policies or explain the consequences to a bigger audience. A good example is the recent work (2014) for Lelystad Airport, where the VCNS was employed to create an experience of expected noise due to aircraft in communities near the route.[‡]

The VCNS adds perceived experience to evaluate noise annoyance and is therefore an attractive psychoacoustic analysis tool. However, there is a need to not only replay (rescaled) recorded sounds but to predict the actual sound at the listener position for an arbitrary aircraft, trajectory, atmosphere and/or a combination thereof. A toolchain/framework is required that can actually treat these simulations with real-time implementation possibilities. The work done at the NLR until the start of the current research was insufficient, given these requirements. More precisely, there was a lack off fan and airframe source noise, curved rays, soft ground reflection, limited Doppler shift simulation, only 1/3rd octave band signal processing, real-time possibility and an assessment of the results.

*OSG is an open-source visualization toolkit, see <http://www.openscenegraph.org/>

[†]Take a look at the Oculus website for an impression, <http://www.oculusvr.com/>

[‡]For more information please consult the created movies, with help of the VCNS, as available through: <http://www.alderstafel.nl/routes-en-geluid.html>

1.4 Research objectives

Noise contours will remain the most important tool in the nearby future to establish operational limitations and noise mitigation measures. Within standardized noise contour algorithms, the effects of wind on sound propagation are modeled poorly for single-event results. Such models correct the single-event results based on a year-long average trend due to weather after which a summation is executed to obtain the year-long average. This correction method is based on measurements and averaging, but has never been explicitly modeled using propagation tools. One of the objectives is thus to assess the ability of the current general methodology in comparison to explicit modeling of atmospheric propagation effects. This enhances the capabilities of the scientific community to include these effects and, eventually, to study weather based adaptive noise abatement procedures.

The primary objective of this dissertation is to direct research to provide new means of generating and propagating synthesized aircraft noise for the VCNS. Aircraft noise synthesis, a translation of calculations into audible pseudo-recordings, should be applied to give a first impression of a flyover without the need of a recording. This is due to the reason that a resynthesis of a recording has limited potential to be extrapolated to other situations regarding aircraft trajectory, source spectrum, atmospheric conditions and/or ground constitution. As such, an integrated toolchain/framework for aircraft noise synthesis and atmospheric propagation effects is studied for (potential) real-time implementation. In particular, the integration of wind effects in aircraft noise synthesis needs to be addressed. Furthermore, a qualification of the results of such a toolchain should be provided as well.

1.5 Thesis outline

Figure 1.5 presents the general outline of the dissertation and the related chapters ordered by the two research objectives, i.e. related to the VCNS toolchain or noise contours. Both the VCNS toolchain and noise contours need an understanding of aircraft source noise and atmospheric propagation. Therefore, after this introductory chapter, chapter 2 will explain the basics in aircraft source noise modeling. The physical background, modeling options and results are described. Chapter 3 will describe the atmospheric propagation and models. Chapter 2 and 3 form the background for the remainder of the dissertation, readers familiar with one or both subjects may skip to the other chapters.

In chapter 4, an expansion to a commonly used noise contour modeling algorithm is made to include atmospheric propagation effects at a high level of detail. This allows the assessment of the overall effect of atmospheric variation over an entire year thereby estimating this effect from a theoretical perspective.

Chapter 5 will highlight the elementary steps involved in synthesizing aircraft noise. These fundamental signal processing steps are necessary to generate audible sound

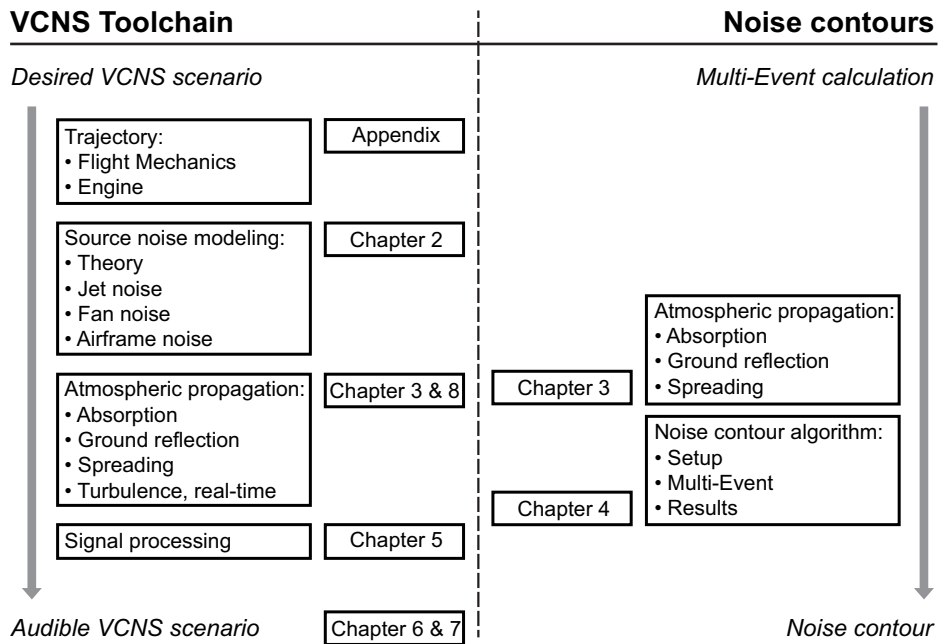


Figure 1.5: *The dissertation outline and corresponding chapters related to noise synthesis (left hand side) and noise contours (right hand side).*

and propagate it towards a receiver. The author hopes that future researchers in aircraft noise synthesis may use this chapter as a first starting point.

Chapter 6 outlines a framework that allows the inclusion of advanced atmospheric propagation effects in (aircraft) noise synthesis. Non-uniform atmosphere propagation effects are included and auralized. Chapter 7 will demonstrate the integrated approach of a toolchain (consisting out of source noise prediction, propagation and synthesis) by synthesizing results of a Boeing 747-400 in take-off and comparing them to measured results.

Chapter 8 contains further developments regarding propagation modeling, including an approach to speed up ray tracing and turbulence in ground reflection, in light of aircraft noise synthesis. Chapter 9 will conclude this dissertation by capturing the most important findings and provide an outlook regarding future research.

Chapters 4, 6, 7 and 8 are based on journal articles and rewritten slightly to eliminate repeated theory, observations, statements and/or results. A complete list of publications, as a result of this research, is added at the end of the dissertation.

Accompanying this dissertation, are synthesized flyover results that can be downloaded as audible (wave) files from the digital repository of the TU Delft. Appendix E provides an overview of the available files.

Chapter 2

Aircraft source noise prediction

An aircraft is comprised of multiple acoustic sources of different nature. There are a variety of methods available to assess such sources, for example based on first-order principles or empirical solutions. To obtain a background in the underlying (aero)acoustic principles, a condensed overview of the physics related to acoustics is given in sections 2.1-2.4. An overview of the mathematical notation is provided in the nomenclature. Theoretical sections 2.1-2.4 are by no means originally derived by the author but merely a reflection on the current publicly known principles of (aero)acoustics as found in literature.⁽¹¹⁻¹⁷⁾ In parts where other sources are used, the references are explicitly included.

The overall noise of an aircraft can only be evaluated if the operating condition of the aircraft engine and airframe configuration are known. A toolchain was made and described in section 2.5 that provides the input required for source noise prediction for empirical source noise models. The latter models, described in section 2.6, are preferred over rigorous physical models since they are able to deal with various configurations, operating conditions and are computationally efficient. Section 2.7 combines the previous sections into an overall source noise prediction of a Boeing 747-400. At the end of this chapter the reader should have a concise introduction in aircraft source noise.

2.1 Acoustic wave equation

Sound is a small pressure deviation around the barometric mean pressure of the medium in which the (longitudinal) wave propagates. In air, the atmospheric pressure is on the order of 10^5 Pascal whereas an acoustic wave of (only) 200 Pascal, at a frequency of 1000 Hz, would lead to considerable pain. In other words, the acoustic pressure is small compared to the barometric pressure. The other end of the scale, the hearing threshold, is generally defined at 20 micro Pascal. Note that the difference

in acoustic amplitudes encompasses 7 orders of magnitude, hence the Sound Pressure Level (SPL) is expressed in a logarithmic scale, called decibel (dB), as:

$$\text{SPL} = 10 \log_{10} \left(\frac{p_e^2}{p_{\text{ref}}^2} \right), \quad (2.1)$$

where, p_e is the effective acoustic pressure* and p_{ref} is a reference pressure of 20 micro Pascal. The dB scale thus effectively quantifies the sound amplitude in reference to an (ideal) hearing threshold.

To describe the generation and propagation of acoustic waves in a medium, the governing equations for the fluid have to be examined. Therefore a start is made by the fluid equations for mass and momentum:

$$\frac{\partial \rho}{\partial t} + \nabla \cdot \rho \vec{u} = m \quad (2.2)$$

$$\frac{\partial}{\partial t} \rho \vec{u} + \nabla \cdot (\rho \vec{u} \vec{u}) + \nabla \cdot \mathbf{P} = \vec{F}_n + m \vec{u}, \quad (2.3)$$

where, ρ , \vec{u} and p are the fluid density, velocity and pressure. Variables m , t and \vec{F}_n denote the mass injection, time and force. The factor $\vec{u} \vec{u}$ denotes a dyadic product, i.e. $u_i u_j$ as is also explained in the mathematical notation section of the nomenclature. $\mathbf{P} = p \mathbf{I} - \boldsymbol{\tau}$ is the fluid stress tensor including the unit tensor \mathbf{I} ($\mathbf{I} = \delta_{ij}$, where δ_{ij} is the Kronecker delta†) and the viscous tensor $\boldsymbol{\tau}$. Viscous effects are, especially when considering acoustics, small compared to inertial forces. Therefore viscous effects are neglected and, using equation 2.2, equation 2.3 is rewritten as,

$$\rho \left(\frac{\partial \vec{u}}{\partial t} + (\vec{u} \cdot \nabla) \vec{u} \right) + \nabla p = \vec{F}. \quad (2.4)$$

Given the small scale of the acoustic pressure, a linearization (denoted by a prime '), of the relevant variables around the mean ambient condition at the origin 0 is executed ($\rho = \rho_0 + \rho'$, $p = p_0 + p'$ and $\vec{u} = \vec{u}_0 + \vec{u}'$). For the homogeneous (conservation) solution, thus ignoring mass and force source terms, this leads to a linearized version of equation 2.2 and 2.4 as:

$$\frac{\partial \rho'}{\partial t} + \vec{u}_0 \cdot \nabla \rho' + \rho_0 \nabla \cdot \vec{u}' = 0 \quad (2.5)$$

$$\rho_0 \left(\frac{\partial \vec{u}'}{\partial t} + (\vec{u}_0 \cdot \nabla) \vec{u}' \right) + \nabla p' = 0. \quad (2.6)$$

*This is the root-mean-square value of an acoustic wave in a single period, see appendix A.

† $\delta_{ij} = 1$ for $i = j$ and $\delta_{ij} = 0$ if $i \neq j$.

An additional relation is required to close the set of equations for the unknown variables. Since viscosity is neglected, heat transfer can be ignored. Therefore the fluid can be considered to behave isentropically and, as a consequence, the following relation can be used,⁽¹²⁾

$$p' = c^2 \rho', \quad (2.7)$$

where,

$$c^2 = \left(\frac{\partial p}{\partial \rho} \right)_s. \quad (2.8)$$

The variable c is a medium constant that is defined at constant entropy s (isentropic flow) and can be calculated with help of the ideal gas law by,

$$c^2 = \gamma RT, \quad (2.9)$$

where, $\gamma = C_p/C_v$ is the ratio of specific heat capacity at constant pressure C_p and volume C_v , R is the specific ideal gas constant and T the temperature. Hence, the acoustic perturbation can be expressed using either pressure or density if equation 2.7 is employed.

By taking the material derivative* of equation 2.5 and divergence of equation 2.6 leads, assuming a constant medium density, to the convective wave equation,⁽¹⁸⁾

$$\frac{\partial^2 \rho'}{\partial t^2} + \frac{\partial}{\partial t} (2 (\vec{u}_0 \cdot \nabla) \rho') + (\vec{u}_0 \cdot \nabla) (\vec{u}_0 \cdot \nabla \rho') - \nabla^2 p' = 0. \quad (2.10)$$

By applying equation 2.7, assuming that the speed of sound is constant within a wavelength, allows to rewrite the equation for acoustic pressure as,

$$\frac{\partial^2 p'}{\partial t^2} + \frac{\partial}{\partial t} (2 (\vec{u}_0 \cdot \nabla) p') + (\vec{u}_0 \cdot \nabla)^2 p' - c^2 \nabla^2 p' = 0. \quad (2.11)$$

In case of zero mean flow, $\vec{u}_0 = 0$, this equation reduces to the classical wave equation:

$$\frac{1}{c^2} \frac{\partial^2 p'}{\partial t^2} - \nabla^2 p' = 0. \quad (2.12)$$

This equation is derived for homogeneous conditions. Therefore it describes the propagation of a small pressure disturbance (acoustic wave) but not the generation of

* A material derivative denotes the derivative including convective effects, i.e. $\frac{D}{Dt} = \frac{\partial}{\partial t} + \vec{v} \cdot \nabla$ where \vec{v} is the convective velocity.

such a wave. It is convenient to apply the wave equation to a harmonic wave. Such waves can be denoted using complex notation:

$$p'(t, \vec{x}) = \hat{p}(\vec{x}) e^{i\omega t}, \quad (2.13)$$

where, $\omega = 2\pi f$ is the angular frequency, $\hat{p}(\vec{x})$ denotes the amplitude of the acoustic wave independent of time and $k = \omega/c$ is the wave number. The derivatives necessary for the wave equation can be calculated,

$$\frac{\partial^2 p'}{\partial t^2} = -\omega^2 \hat{p}(\vec{x}) e^{i\omega t} \quad (2.14)$$

$$\nabla^2 p' = \nabla^2 \hat{p}(\vec{x}) e^{i\omega t}, \quad (2.15)$$

which can be substituted in the wave equation to yield the so-called Helmholtz equation:

$$\nabla^2 \hat{p} + k^2 \hat{p} = 0. \quad (2.16)$$

The Helmholtz equation is attractive since $\hat{p}(\vec{x})$ is used instead of $p'(t, \vec{x})$. Hence, the equation only depends on spatial coordinates instead of both spatial and temporal.

The fundamental solution to the wave equation is due to d'Alembert who discovered a solution for a vibrating string in 1747. The acoustic implications were made by Euler by assuming plane wave propagation, i.e. the wavefront is plane and thus typified by a single Cartesian coordinate, e.g. x . Under these assumptions the wave equation reduces to a one-dimensional form:

$$\left(\frac{\partial}{\partial x} - \frac{1}{c} \frac{\partial}{\partial t} \right) \left(\frac{\partial}{\partial x} + \frac{1}{c} \frac{\partial}{\partial t} \right) p' = 0, \quad (2.17)$$

which has a fundamental solution,

$$p'(t, x) = g_1(t - x/c) + g_2(t + x/c), \quad (2.18)$$

where g_1, g_2 are arbitrary functions. Consequently, there are two wave terms in which the covered distance x is related to c , the aforementioned (equation 2.9) medium constant. Therefore the constant c is known as the speed of sound. The solution contains two wave fronts, one moving in positive x direction and the other in negative x direction. It is also clear that the wave type remains the same since factors g_1 and

g_2 are not modified during propagation. Hence, a harmonic acoustic wave will have a single fundamental frequency f and a wavelength,

$$f = \frac{1}{t_p} \quad \text{and} \quad \lambda = \frac{c}{f}, \quad (2.19)$$

where t_p is the duration of one (harmonic) wave and λ is the wavelength, i.e. the distance in which this harmonic repetition occurs. Substituting the solution of equation 2.18 for an outgoing plane wave in equation 2.6, without mean-flow, leads to the following relation for perturbation velocity u' ,

$$u' = \frac{p'}{\rho_0 c}. \quad (2.20)$$

Equation 2.20 shows the perturbation velocity for a plane wave and is a function of the acoustic pressure, density and speed of sound. This perturbation velocity is commonly referred to as particle velocity. Notice that for this plane wave, particle velocity is in phase with pressure. To give an indication on the magnitude of the particle velocity, a plane wave having an acoustic pressure (at a pain causing level) of 200 Pa in air has a particle velocity of 0.5 m/s. The particle velocity is thus much smaller than the speed of sound. The fraction in the denominator of equation 2.20 ($\rho_0 c$) is the acoustic impedance and has units ($\text{Pa} \cdot \text{s/m}$).^{*} The acoustic intensity is defined as $I = p' u'$, similar to the use in electromagnetism, with units Watts per square meter.

If the acoustic wave front is not plane but spherical, i.e. as visualized by an expanding sphere, the wave equation can be transformed to spherical coordinates and becomes:

$$\frac{\partial^2 (rp')}{\partial r^2} - \frac{1}{c^2} \frac{\partial^2 (rp')}{\partial t^2} = 0, \quad (2.21)$$

where r is the covered distance by the wave. The result is very similar to equation 2.12 since the only difference is that the variable p' has changed to rp' . This also implies that the fundamental solution differs only by this additional factor r and becomes,

$$p'(t, r) = \frac{g_1(t - r/c)}{r} + \frac{g_2(t + r/c)}{r}. \quad (2.22)$$

In acoustics it is customary to retain only the solution in positive direction (the term containing the factor g_1 in equation 2.22) since incoming spherical waves are

*The unit of impedance is also denoted as 'Rayls' (MKS) in honor of Lord Rayleigh who was of fundamental influence in acoustics.

physically impossible.* The denominator shows the factor r , the traveled distance of the wave. It implies that the pressure decreases as $1/r$, which is an important result for propagation of spherical waves. For a spherical wave the perturbation velocity is in phase with the pressure a few wavelengths away from the source.

A solution to the non-homogeneous wave equation can be found using the Green's function. A Green's function is the impulse response of the non-homogeneous differential equation. For the wave equation the Green's function should thus satisfy,

$$\frac{1}{c^2} \frac{\partial^2 G}{\partial t^2} - \nabla^2 G = \delta(\vec{x} - \vec{y}) \delta(t - \tau) \quad (2.23)$$

where $G = G(\vec{x}, \vec{y}, t - \tau)$ is the causal Green's function ($G = 0$ for $t < \tau$), \vec{x} denotes the receiver and \vec{y} the source position, t is the receiver time and τ is the emission time. The Green's function for the acoustic wave equation under free-space conditions is,^(12;16;17)

$$G = \frac{1}{4\pi r} \delta\left(t - \tau - \frac{r}{c}\right), \quad (2.24)$$

where $r = |\vec{x} - \vec{y}|$ is the distance between the source and receiver. By convolving the Green's function with an arbitrary acoustic source signal, the acoustic signal at the receiver is found.

2.2 Aerodynamic sound sources

The wave equation and its solution by d'Alembert were well known in the 19th century, but aerodynamic sources of sound remained theoretically undescribed until the 20th century. It was Lighthill who provided insight in this matter by examining the sound produced by the aerodynamic flow.^(4;5)

Lighthill draws an analogy between a non-homogeneous version of the fluid equations and the classical wave equation including an acoustic source term. Within the non-homogeneous fluid there is only a finite source region where unsteady flow appears, the remainder of the fluid is at rest apart from small motions induced by the passage of acoustic waves. More specifically, in the remainder of the fluid the classical wave equation governs the propagation of acoustic waves. Therefore Lighthill compared the density fluctuations in the non-homogeneous flow with those in a uniform acoustic medium at rest. The resulting difference is captured as a fluctuating stress field that can be applied to the classical wave equation as an acoustic source term.

Lighthill applied a time derivative to a homogeneous version of equation 2.2 and the divergence to a homogeneous version of equation 2.3,

*This is also known as the Sommerfield radiation condition.

$$\frac{\partial^2 \rho}{\partial t^2} + \frac{\partial}{\partial t} (\nabla \cdot (\rho \vec{u})) = 0 \quad (2.25)$$

$$\nabla \cdot \left(\frac{\partial}{\partial t} (\rho \vec{u}) \right) + \nabla \cdot \nabla \cdot (\rho \vec{u} \vec{u} + \mathbf{P}) = 0, \quad (2.26)$$

where \mathbf{P} represents $p\mathbf{I} - \boldsymbol{\tau}$. The factor $\vec{u}\vec{u}$ denotes a dyadic product, i.e. $u_i u_j$ as is also explained in the mathematical notation section of the nomenclature. By subtracting both equations, the following relation is found,

$$\frac{\partial^2 \rho}{\partial t^2} - \nabla \cdot \nabla \cdot (\rho \vec{u} \vec{u} + p\mathbf{I} - \boldsymbol{\tau}) = 0, \quad (2.27)$$

and subtracting $c^2 \nabla^2 \rho$ (c defined at the receiver) from both sides, results in,

$$\frac{\partial^2 \rho}{\partial t^2} - c^2 \nabla^2 \rho = \nabla \cdot \nabla \cdot (\rho \vec{u} \vec{u} + (p - c^2 \rho) \mathbf{I} - \boldsymbol{\tau}). \quad (2.28)$$

Equation 2.28 is known as Lighthill's equation and is an exact rearrangement of the governing equations. The right hand side is the 'Lighthill stress tensor' \mathbf{T} ,

$$\mathbf{T} = \rho \vec{u} \vec{u} + (p - c^2 \rho) \mathbf{I} - \boldsymbol{\tau}. \quad (2.29)$$

The Lighthill stress tensor contains variations in flow velocity $\rho \vec{u} \vec{u}$ (turbulence as induced by, for instance, a jet), a deviation from the isentropic behavior and a change in viscous stresses $\boldsymbol{\tau}$. Lighthill's analogy uses the stress tensor \mathbf{T} as a source term of a jet for an equivalent acoustic medium at rest. The latter is recognized as the classical wave equation on the left hand side of equation 2.28.

Up until now, no assumptions have been made and therefore the form of equation 2.28 and 2.29 is an exact rearrangement of the governing equations. Within the source region where \mathbf{T} is non-zero, the Reynolds number is usually high and therefore viscous stresses are small. Furthermore, if the jet flow has an equivalent temperature as the medium at rest then isentropic relations hold. For these conditions, the only significant contribution to the stress tensor is due to the fluctuating velocity. Outside the flow, i.e. the source region, the only variations in density are those related to acoustic disturbances. Hence, the following relation holds,

$$\frac{\partial^2 \rho'}{\partial t^2} - c^2 \nabla^2 \rho' = \nabla \cdot \nabla \cdot (\rho \vec{u} \vec{u}) \quad (2.30)$$

where c refers to the sound speed at the listener position, i.e. that region where the classical wave equation governs propagation. Assuming low Mach number flow allows to replace the jet flow density ρ by the mean density ρ_0 of the jet, resulting in,

$$\frac{\partial^2 \rho'}{\partial t^2} - c^2 \nabla^2 \rho' = \nabla \cdot \nabla \cdot (\rho_0 \vec{u} \vec{u}). \quad (2.31)$$

Since isentropic relations are assumed, equation 2.31 can be converted using pressure as acoustic variable by application of equation 2.7.

The application of dimensional analysis to Lighthill's stress tensor, using equation 2.24 where $\tau = 0$, leads to an estimate of jet mixing noise for a source volume V ,⁽¹⁴⁾

$$p'(t, \vec{x}) = \int_V \frac{\nabla \cdot \nabla \cdot \mathbf{T}(\vec{y}, t - r/c)}{4\pi r} dV. \quad (2.32)$$

An estimate of the source strength can be given based on estimating the individual components of \mathbf{T} . Assuming isentropic flow, constant density and the notion that velocity \vec{u} scales with jet speed u_s , allows a simplification where $\mathbf{T} \propto \rho u_s^2$.

The characteristic frequency of the turbulence is estimated to be $1/t_c$ where t_c is the time to convect a turbulent eddy of length l with speed u_c . The frequency is inversely proportional to the characteristic dimension and directly proportional to the convective velocity, i.e. $1/t_c \propto u_c/l$.

The double divergence is proportional, in the far field at the observer, to the temporal derivative following $\frac{\partial^2}{\partial x^2} \propto \frac{1}{c^2} \frac{\partial^2}{\partial t_c^2}$.^(4;12;14) This is non-trivial and holds only for acoustic disturbances observed in the far field.

Furthermore, the convective velocity of the turbulent eddy u_c is proportional to the jet speed u_s and a characteristic dimension. For a circular jet, the jet diameter (d_j) is a logical choice, i.e. $l = d_j$. Consequently, the temporal derivative $\frac{\partial}{\partial t_c}$ is proportional to the characteristic frequency and thereby the jet operating condition $\frac{u_s}{d_j}$.⁽¹⁴⁾ Therefore, $\nabla \cdot \nabla \propto (u_s/d_j c)^2$.

A volume integral over a source region is proportional to the characteristic length raised to the third power, i.e. d_j^3 . Combining all these proportionalities leads to Lighthill's grand observation that:

$$p' \propto \frac{\rho u_s^4 d_j}{r c^2}, \quad (2.33)$$

which leads, together with the observation that the acoustic intensity is $I = p' u' = p'^2/\rho c$, to:

$$I \propto \frac{\rho d_j^2 u_s^8}{r^2 c^5}. \quad (2.34)$$

Equation 2.34 is the acoustic power law of Lighthill describing that a turbulent jet generates a sound intensity proportional to the eight power of the jet speed.

Similar results have been calculated for turbulence in the vicinity of boundaries by Ffowcs-Williams & Hall⁽¹⁹⁾ and by Curle⁽²⁰⁾. They found that the sound intensity depends on the 5th or 6th power of the convection velocity instead of the 8th power as found by Lighthill for free turbulence. This is, for instance, used in the estimation of aircraft wing trailing edge noise. A different approach is to calculate the sound of moving bodies in a flow as demonstrated by Ffowcs-Williams & Hawkings.⁽²¹⁾ Such results are applicable to the prediction of helicopter noise, propeller noise or gasturbine fan noise.

Estimating the actual behavior of the Lighthill stress tensor, thus the precise acoustic waves emanating from a source region, remains difficult. Advanced Computational Fluid Dynamics (CFD) calculations are required to obtain a solution to the aerodynamics problem before the acoustic problem can be evaluated. Such results in general closely coincide with reality for steady flows since not many approximations need to be made and the problem is solved by first-order principles. This is generally however not the case for unsteady turbulent flows. Simulating an entire aircraft with CFD remains computationally expensive, especially if the fine time scales associated with acoustics need to be retained. An overview of some pertinent issues regarding the use of CFD in aeroacoustics is described in the literature.⁽²²⁾

Full CFD calculations on aircraft are usually calculated by aerodynamicists. The field of aerodynamics and aeroacoustics is thus very closely related since the same set of equations is used, although their objective is different. In aerodynamics, scientists usually search for the pressure loading on a surface whereas aeroacousticians are interested in the pressure fluctuations in the fluid. A worthwhile reference containing lucid examples on different viewpoints and differences between the underlying equations is provided by Morino.⁽²³⁾

2.3 Elementary sources

A deviation from the homogeneous condition in the wave equation can be interpreted as an acoustic source, as was demonstrated by Lighthill. Acoustic sources are typically classified according to three elementary source types; the monopole, dipole and quadrupole. The dipole and quadrupole can be constructed by placing multiple monopole sources at a distance from each other, using an opposite phase.⁽¹¹⁾ Each elementary source can be related to a flow phenomenon and radiates acoustic energy in a different radiation pattern. An example of the three different radiation profiles is shown in figure 2.1, this behaviour is derived for each source type in the following sections.

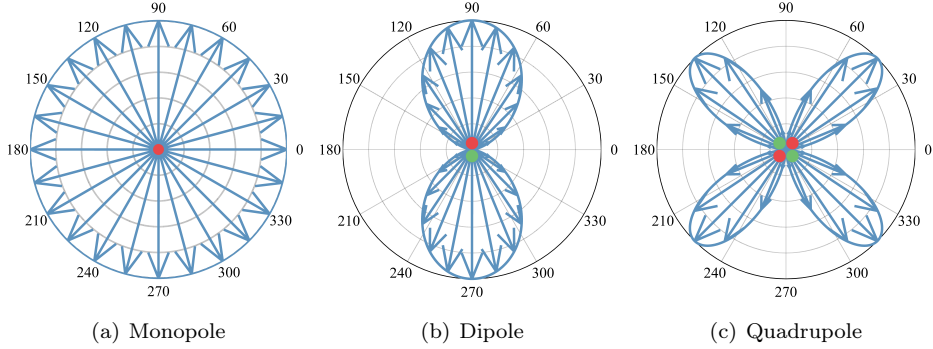


Figure 2.1: Radiation patterns of the three elementary sources. The dots indicate the arrangement of (multiple) monopoles of an opposite (color) phase.

2.3.1 Monopole

Acoustic source terms can be analyzed by retaining the mass and force terms in the linearized mass and momentum equations, equation 2.5 and 2.6. Upon executing a similar analysis, i.e. applying a time derivative and divergence and a subtraction, in a stationary medium, the following equation is obtained,

$$\frac{\partial^2 \rho'}{\partial t^2} - c^2 \nabla^2 \rho' = \frac{\partial m}{\partial t} - \nabla \cdot \vec{F}. \quad (2.35)$$

For isentropic disturbances such as sound, see equation 2.7, a familiar wave equation for pressure is obtained,

$$\frac{1}{c^2} \frac{\partial^2 p'}{\partial t^2} - \nabla^2 p' = \frac{\partial m}{\partial t} - \nabla \cdot \vec{F}. \quad (2.36)$$

A fluctuating mass thus leads to acoustic waves, as well as a spatially varying force field. If the mass source is defined as $q = \partial m / \partial t$ and is combined with the Green's function solution of equation 2.24, the solution of the acoustic pressure at the receiver \vec{x} is,

$$p'(\vec{x}, t) = \frac{q}{4\pi r} \delta(t - \tau - r/c), \quad (2.37)$$

where δ is the Dirac delta function, i.e. 1 at emission time ($\tau = 0$) and 0 otherwise. As a result the acoustic pressure for the mass source at position \vec{y} is,

$$p'(\vec{x}, t) = \frac{1}{4\pi} \frac{q(\vec{y}, t - r/c)}{r}. \quad (2.38)$$

Equation 2.38 shows that the acoustic pressure is a function of the radial distance. This implies that the radiation pattern is thus equal in all directions, i.e. similar to a point source. Consequently, fluctuations in mass lead to a monopole behavior with a uniform radiation pattern.

2.3.2 Dipole

The force term of equation 2.36 leads to a different radiation pattern. If a force in x-direction is considered then the following equation results,

$$p'(\vec{x}, t) = \frac{-1}{4\pi} \frac{\partial}{\partial x} \left(\frac{F_x(\vec{y}, t - r/c)}{r} \right) \quad (2.39)$$

$$p'(\vec{x}, t) \approx \frac{-1}{4\pi r} \frac{\partial}{\partial x} (F_x(\vec{y}, t - r/c)), \quad r \rightarrow \infty \quad (2.40)$$

where the latter equation results by application of the product rule of differentiation and using a far-field approximation to eliminate the second term, i.e. $r \rightarrow \infty$. By replacing the spatial derivative with a time derivative,

$$\frac{\partial F_x(t - r/c)}{\partial x} = \frac{\partial F_x(\vec{y}, t - r/c)}{\partial t} \frac{\partial(t - r/c)}{\partial x} \quad (2.41)$$

$$= -\frac{\partial F_x(\vec{y}, t - r/c)}{\partial t} \frac{x}{cr}, \quad (2.42)$$

this will lead to,

$$p'(\vec{x}, t) = \frac{1}{4\pi r c} \frac{x}{r} \left(\frac{\partial F_x(t - r/c)}{\partial t} \right). \quad (2.43)$$

The x-coordinate follows as $x = r \cos(\theta)$ for a 2-dimensional case (polar coordinate system), where θ represents the polar angle. If this relation is substituted the following equation follows,

$$p'(\vec{x}, t) = \frac{\cos(\theta)}{4\pi r c} \left(\frac{\partial}{\partial t} F_x(t - r/c) \right), \quad (2.44)$$

which shows a radiation profile that depends on θ and is therefore not uniform as the monopole. The corresponding (cosine) radiation profile is known to correspond to the profile resulting from two monopole of opposite phase. Therefore, this elementary source is known as a dipole and reflects the radiation profile of fluctuating forces. Note that there is an additional variable (sound speed) in the denominator, compared to the monopole, and therefore the acoustic efficiency of a dipole is less than that of a monopole.

2.3.3 Quadrupole

If a contribution from shear stress is involved, in the case of equation 2.32, the radiation pattern is again different. Consider a similar approach to equation 2.32 where the stress tensor \mathbf{T} is assumed to contain only a stress tensor in cartesian xy-direction, i.e. T_{xy} . Hence, the following equation is established in the far field,

$$p'(\vec{x}, t) = \frac{1}{4\pi r} \frac{\partial^2}{\partial x \partial y} (T_{xy}(\vec{y}, t - r/c)) \quad (2.45)$$

and upon a similar replacement of the spatial derivative for a time derivative,

$$p'(\vec{x}, t) = \frac{1}{4\pi r c^2} \frac{x}{r} \frac{y}{r} \left(\frac{\partial^2}{\partial t^2} T_{xy}(\vec{y}, t - r/c) \right) \quad (2.46)$$

where a similar substitution for the Cartesian directions, i.e. $x = r \cos(\theta)$ and $y = r \sin(\theta)$, leads to,

$$p'(\vec{x}, t) = \frac{\sin(2\theta)}{8\pi r c^2} \left(\frac{\partial^2}{\partial t^2} T_{xy}(\vec{y}, t - r/c) \right). \quad (2.47)$$

Equation 2.47 shows that the radiation profile is characterized by a $\sin(2\theta)$ term, leading to four preferred radiation directions. Such a radiation behavior may also be obtained when combining two dipoles and therefore this source is also known as a quadrupole. Note that the source is modified, by a term $2c$ in the denominator, compared to the dipole behavior of equation 2.44. Hence, a dipole source is a less efficient radiator than a monopole source. On the other hand, a quadrupole is an even less efficient source of noise.

2.4 Moving source effects

During a flyover the noise source is moving, which affects the radiated sound. In the analysis of a moving source, the velocity potential function is utilized. In the case of a non-viscous, incompressible and irrotational fluid, both fluid pressure and velocity are related to one variable known as the velocity potential. The same potential can be used for acoustic variables since they are shown to behave according to the aforementioned limitations.^(14;24) As a result, the acoustic pressure is related to the potential function ψ by,^(12–14)

$$p' = -\rho_0 \frac{\partial \psi}{\partial t}. \quad (2.48)$$

Furthermore, the acoustic potential satisfies the same wave equation as acoustic pressure 2.12. For a moving source, such as aircraft, the situation compared to equation

2.38 is slightly different since the source is not fixed at one position. Figure 2.2 illustrates the situation.

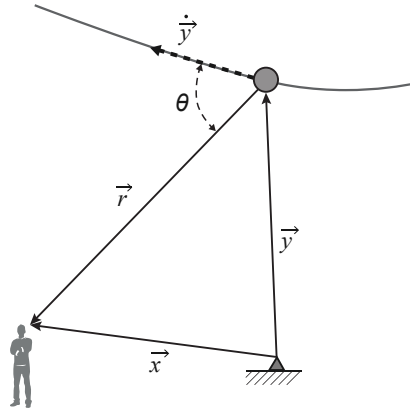


Figure 2.2: A moving source along a trajectory.

The source is allowed to move with respect to the origin and therefore \vec{y} is a function of time. The listener is fixed, in time and space, at position \vec{x} . The source is, in this case, defined as a monopole (or fluctuating mass injection) as in equation 2.36. For a monopole this leads to the following solution for the acoustic potential based on the Green's function approach,

$$\psi(\vec{x}, t) = \frac{-1}{4\pi\rho_0} \int_{-\infty}^{\infty} \frac{m(\tau)}{r} \delta\left(t - \tau - \frac{r}{c}\right) d\tau \quad (2.49)$$

where m denotes the monopole mass at emission time τ . Note that the use of the potential function allows us to use $m(\tau)$ instead of the derivative to receiver time. The vector \vec{r} is defined as $\vec{r} = \vec{x} - \vec{y}(\tau)$, i.e. the path between the source and observer at emission time. The radial distance r is defined as the vector norm of \vec{r} , i.e. $r = |\vec{r}|$. A useful property of the delta function is,^(12;14)

$$\int_{-\infty}^{\infty} m(\tau) \delta(g(\tau)) d\tau = \sum_{i=1}^n \frac{m(\tau_i)}{\left| \frac{dg_i}{d\tau} \right|}, \quad (2.50)$$

where the summation is over the roots of g_i , i.e. $g_i(\tau) = 0$. In the case of a subsonic source, there is only one root.⁽¹⁶⁾ This particular factor is identified as,^(12;14)

$$g_1(\tau) = t - \tau - r/c \quad (2.51)$$

$$\frac{dg_1}{d\tau} = -1 + \frac{\vec{r}}{r} \cdot \frac{d\vec{y}}{d\tau} \frac{1}{c}. \quad (2.52)$$

The first fraction in the second term of equation 2.52 results due to the derivative w.r.t. source position whereas the second is with respect to (retarded) time. The former is a change in orientation and the second term leads to velocity term,

$$\frac{dg_1}{d\tau} = -1 + M \cos(\theta) \quad \text{or,} \quad \left| \frac{dg_1}{d\tau} \right| = 1 - M \cos(\theta), \quad (2.53)$$

where θ is the polar observation angle between source and observer at emission time and M is the Mach number of the source. Upon substituting this result in equation 2.49 yields,

$$\psi(\vec{x}, t) = \frac{-1}{4\pi r \rho_0} \left(\frac{m(\tau)}{1 - M \cos(\theta)} \right). \quad (2.54)$$

Note that the source term is still expressed at emission time. By applying the chain rule, i.e. $\partial m / \partial t = (\partial m / \partial \tau)(\partial \tau / \partial t)$, the source can be expressed at receiver time t . Therefore the partial derivative of emission time to receiver time must be calculated, i.e. a time derivative of equation 2.51 where $g = 0$,

$$0 = 1 - \frac{\partial \tau}{\partial t} + M \cos(\theta) \frac{\partial \tau}{\partial t} \quad (2.55)$$

$$\frac{\partial \tau}{\partial t} = \frac{1}{1 - M \cos(\theta)}. \quad (2.56)$$

The latter equation can be used, together with equation 2.48, to express equation 2.54 in the far field using acoustic pressure as variable. This results in the following relation,

$$p'(\vec{x}, t) = \frac{1}{4\pi r} \frac{\frac{\partial m}{\partial t}}{(1 - M \cos(\theta))^2}, \quad (2.57)$$

Please note that the acoustic pressure amplitude at the receiver position, in equation 2.57, is modified by a factor $(1 - M \cos(\theta))^2$. Due to this factor, an increased acoustic pressure occurs, with respect to equation 2.38, if the aircraft is approaching. If the aircraft is receding, a decreased acoustic pressure occurs. This effect is called convective amplification. Further analysis⁽²⁵⁾ shows that this effect differs per elementary source type and a brief overview is found in literature.⁽²⁶⁾

Not only is the amplitude of the signal changed, the frequency of the sound is modified as well. For instance, if we assume a simple mass source ($\sigma = \frac{\partial m}{\partial t}$) propagating to a receiver, the signal at the receiver is,

$$p'(t, \vec{x}) = \frac{\sigma(\omega_g \tau)}{4\pi r (1 - M \cos(\theta))^2}, \quad (2.58)$$

where, $\omega_{\vec{y}}$ is the frequency at the source. The phase* of the field is given by $\Theta = \omega_{\vec{y}}\tau$. In general, the time derivative of the phase yields the frequency of the wave and allows to evaluate the wave at the observer as,

$$\omega_{\vec{x}} = \frac{\partial \Theta}{\partial t} = \omega_{\vec{y}} \frac{\partial \tau}{\partial t}, \quad (2.59)$$

and by substituting equation 2.56 this will lead to,

$$\omega_{\vec{x}} = \frac{\omega_{\vec{y}}}{1 - M \cos(\theta)}. \quad (2.60)$$

Equation 2.60 describes a variation in frequency at the receiver due to a moving source, which is also known as the 'Doppler' shift. The factor in the denominator, similar to the one in equation 2.57, is therefore known as the Doppler shift factor. Similar equations can also be derived in the case of an inhomogeneous medium, thus including wind effects.⁽²⁷⁾

2.5 A toolchain for aircraft source noise prediction

An aircraft is comprised of several noise generating mechanisms. To predict all these sources with physics based models requires a vast amount of analysis and detailed input data. To provide design engineers with tools that can be used in a design processs, where limited information is available, empirical tools were developed that provide results within ample time. As such, modeling assumptions were made to simplify the physical relations resulting in empirical relations and models. The physics are retained, to some extent, by including parts of the fundamental analysis where possible. For instance, empirical jet noise models use power-law trends such as the one developed by Lighthill. Due to the differences in aircraft noise source mechanisms, individual empirical methods are constructed to approximate the underlying physics. Figure 2.3 shows typical aircraft noise sources that need to be addressed in aircraft noise prediction.

There are two prominent aircraft system noise prediction tools that combine all the noise sources of figure 2.3. These tools are NASA's ANOPP⁽²⁸⁾ and DLR's PANAM^(29;30). The core of ANOPP is a set of empirical predictions codes developed by researchers in the 1970's. These codes have been updated a few times as aircraft evolved. DLR's PANAM code is, especially for engine noise sources, based on the same set of empirical prediction codes. The airframe noise models involved in both tools is, in some parts, slightly different since different dedicated experiments were carried out to that extent.

*The phase denotes the angle of a harmonic wave during its cycle.

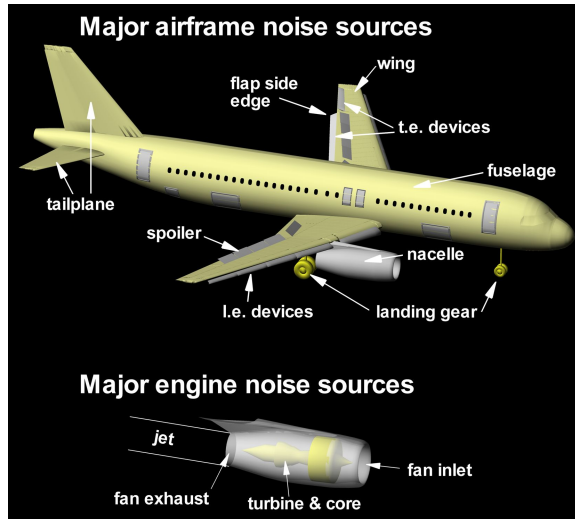


Figure 2.3: *Different sources of aircraft noise.**

The advantage of both methods is that they are generic and provide a prediction for various aircraft types, as long as they concern conventional configurations. Advanced configurations, for instance blended-wing-bodies, need to be addressed carefully as the prediction might become erroneous. Currently a revised version of ANOPP, i.e. ANOPP2, is being finished by NASA.⁽³¹⁾ The new version retains all the old functionalities and includes advanced shielding effects and atmospheric propagation. Moreover, user specific codes and modules can be added to tailor the system noise prediction and retain more of the underlying physics. As a result, ANOPP2 will allow the evaluation of unconventional configurations.

Noise synthesis of a flyover requires a source noise prediction of all the aircraft noise components suggested in figure 2.3. Besides covering all noise components, the prediction should be able to assess a variety of configurations and provide results in a short computational time. Consequently, the choice was made to create a toolchain for aircraft source noise prediction based on the published empirical codes of ANOPP. The toolchain of figure 2.4 illustrates all the models and input data needed for a source noise prediction.

Figure 2.4 has 4 main elements at the top of the figure; Input data, Trajectory, Gasturbine and Source noise. The information in this chart flows from left to right, i.e. to obtain a source noise prediction the gasturbine, trajectory and input data should be known and/or calculated. The required input data to start a calculation exists out of aircraft and atmospheric data. Aircraft geometry data is, for instance, required for the airframe noise calculation. Furthermore, aerodynamic data and aircraft weight is required to calculate an aircraft's trajectory. Atmospheric data is required in all aircraft source noise models, the gasturbine and the trajectory.

*Source: <http://www.qice.dlr.de/images/Fig1.jpg>, accessed on 14-08-2013

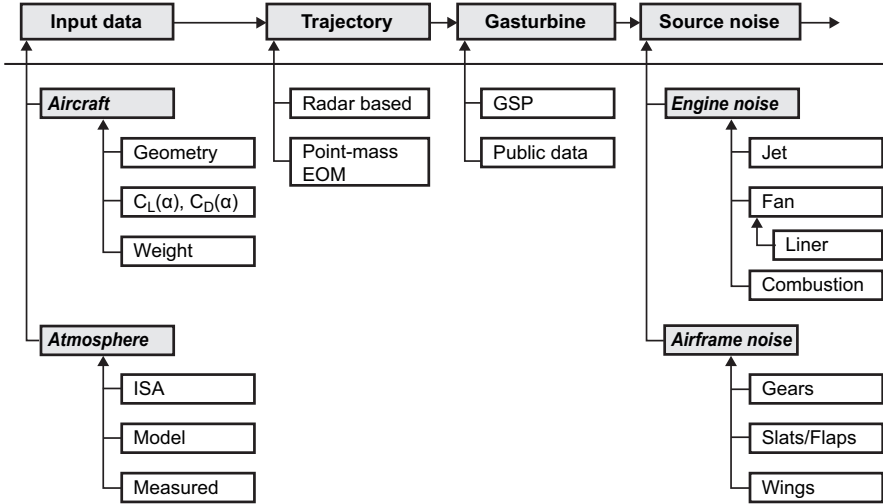


Figure 2.4: An overview of the toolchain and modeling steps necessary for a complete aircraft source noise prediction.

The second step is to assess the aircraft trajectory. There are two options, a full simulation of a trajectory based on the Equations of Motion (EOM) or using an actual trajectory measured by radar. Computations are required here to assess the aircraft airspeed, angle of attack and required thrust. Especially the latter is of vital importance since this drives the gasturbine modeling and therefore engine source noise. Appendix D illustrates some of the concepts and equations that allow to calculate the required thrust.

Engine source noise prediction models need the operational variables (operational states) of the engine. A gasturbine simulation is therefore required for every (discrete) point along a trajectory during the flyover. The engine operational state can be obtained if the desired thrust level of the aircraft, as obtained through the trajectory analysis, is known. A gasturbine is controlled by supplying a specific amount of fuel, thrust is not controlled directly in a gasturbine. Hence, an iterative procedure is used, by adjusting the fuel flow, to set the required thrust level equal to the simulated level. If this iteration converged, the engine operational state corresponding to that point along the aircraft trajectory is found. NLR's Gasturbine Simulation Program (GSP) is used to this end, details are included in appendix D.

All previous steps culminate in the aircraft source noise prediction. The aircraft source noise prediction is separated in engine and airframe noise sources. The engine noise models used in this toolchain comprise jet mixing noise, fan noise and combustion noise. The fan noise model is complemented by a liner model since acoustic lining in the nacelle attenuates a portion of the sound. Airframe noise is predicted by a single model in which several elements, such as gears, flaps, slats and wings, are described. The empirical acoustic source models are explained in the next section, whereas an overview of the input data for each source noise model is found in appendix D.

2.6 Acoustic source models

Empirical models predict the source level and are, given a short calculation time, very attractive for noise synthesis. An overview of the used models is provided in the next subsections. The implementations for fan, combustion and airframe noise have been verified with the help of implementations from the Engineering Sciences Data Unit (ESDU).⁽³²⁻³⁴⁾ The jet noise and liner models, not available through the ESDU, were verified by visual inspection of example calculations in literature.

The empirical models do not predict the waveform, i.e. the actual acoustic pressure-time signal, at the source position. They predict the spectral content of the signal at the source. By grouping particular frequencies together, in so-called bands, the analysis of a wide-range of frequencies can be characterized by a limited set of bands. All empirical model used in the current work predict the spectral content on a 1/3rd octave band basis. Details regarding spectral analysis, Fourier transforms, 1/3rd octave-bands and A-weighting can be found in appendix B.

2.6.1 Jet noise - Stone

Jet noise is one of the primary noise sources of aircraft. This has lead to the theory of Lighthill as described in section 2.2. Lighthill has shown, in equation 2.34, that variations in acoustic intensity due to jet noise are proportional to the eight power of the jet outflow velocity. For hot streams (featuring a rise in entropy) this result does not hold and the velocity power coefficient is, in general, lowered to a value of 5-6.⁽³⁵⁾

The empirical model created by Stone⁽³⁶⁾ relies on the theoretical trend of Lighthill's power law. The model starts by predicting the Overall Sound Pressure Level (OSPL) normal to the engine symmetry axis, i.e. at a directivity angle of 90°, using jet velocity and other relevant variables. As a final step, frequency dependent directivity patterns, specified in 1/3rd octave-bands, are applied to the results. Stone further improved his methods over the years, adding the effect forward flight and noise reducing chevrons.⁽³⁷⁻³⁹⁾ An overview of the complete model is available that includes all the aforementioned improvements.⁽⁴⁰⁾ The prediction toolchain developed in this study is thus based on the model reported in that document. The core calculation process, effectively producing the sound emanating from jet mixing noise, is repeated for multiple source regions in the jet, see figure 2.5.

Figure 2.5 illustrates the three jet mixing noise sources defined in the model of Stone. There are two shear layers, due to differences in outflow and ambient fluid velocity, that give rise to sound waves. The outer shear layer is due to the bypass air of the engine mixing with the ambient air, whereas the inner shear layer is due to the same bypass air mixing with the core air. The outer shear layer is said to generate 'transitional scale' mixing noise, the inner shear layer produces 'small scale' mixing noise. A third source is the merged region behind the engine where 'large scale' mixing occurs with the ambient fluid. In this merged flow region, large turbulent

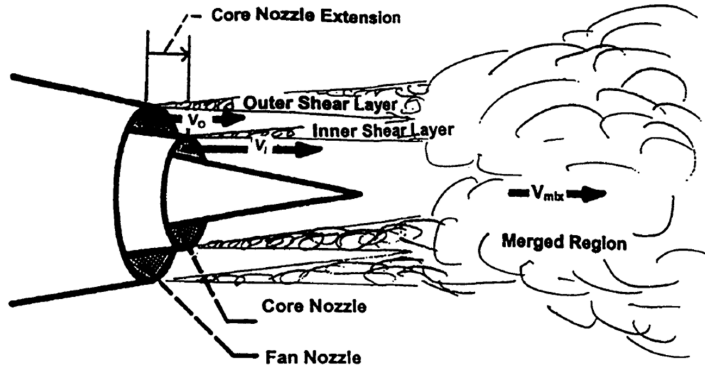


Figure 2.5: Simplified jet noise model as used by Stone.⁽⁴⁰⁾

structures are present that are the primary cause of low frequency sound from a jet engine. These three sources depend on the gasturbine outflow jet velocity. As such, the outflow velocity, which is also a measure of engine thrust, is an important parameter that is obtained after gasturbine analysis.

A jet is, in general, not a single source but comprises many acoustic sources along the jet plume. In flyover situations, where the distance to a listener is large, assuming a point where sound originates is allowed if the directivity is taken into account (see section 2.3). Stone evaluated the different sources to originate at different downstream locations. This is not further discussed here, but the interested reader can find details in the literature.⁽⁴⁰⁾ The equation describing the sound level for each jet mixing source of figure 2.5 follows as,

$$\begin{aligned} \text{UOSPL} = & C + 10 \log_{10} \left(\left(\frac{\rho_\infty}{\rho_{\text{ISA}}} \right)^2 \left(\frac{c_\infty}{c_{\text{ISA}}} \right)^4 \right) + 10 \log_{10} \left(\frac{A_n}{r^2} \right) + 10\xi \log_{10} \left(\frac{\rho_e}{\rho_\infty} \right) \\ & + 10 \log_{10} \left(\frac{\left(\frac{V_e}{c_\infty} \right)^N}{1 + b \left(\frac{V_e}{c_\infty} \right)^{N-3}} \right) - 5\epsilon \log_{10} \left((1 + M_c \cos(\theta))^2 + (\zeta M_c)^2 \right), \end{aligned} \quad (2.61)$$

where, $\rho_\infty, c_\infty, c_{\text{ISA}}$ are the density and sound speed at ambient condition and the sound speed at standard conditions. Other variables are the nozzle area A_n , the convective amplification coefficient ϵ and an empirical scaling coefficient ζ . UOSPL is the jet unrefracted overall sound pressure level, C is a source region dependent scaling coefficient, ξ is a non-dimensional value that depends on outflow velocity, M_c is the convective Mach number of the jet flow and N is a velocity power coefficient.

The value of N is 8 for the large scale mixing noise and 7.5 for the other source regions. Please note the similarity between N in the equation by Stone (equation 2.61) and Lighthill (equation 2.34). In equation 2.61 the power coefficient operates on the effective velocity V_e defined by,

$$V_e = V_{\text{mix}} \sqrt{1 - M \left(\frac{c_\infty}{V_{\text{mix}}} \right)} \quad (2.62)$$

where V_{mix} is the outflow velocity used for a specific region and depends on the engine operating state. To get the Sound Pressure Level (SPL) at a distant point, the frequency behavior and directivity needs to be taken into account. Stone provided look-up tables for values of SPL-UOSPL as a function of the Strouhal number (St),

$$St = \frac{fd_j}{V_e} \left(\frac{T_j}{T_\infty} \right)^{0.4(1+\cos(\tilde{\theta}))}, \quad (2.63)$$

where f is the frequency, d_j is the characteristic diameter of the jet plume and T_j is the stagnation temperature of the jet whereas T_∞ refers to the ambient temperature. The used observer angle $\tilde{\theta}$ is different from the polar observation angle, i.e. based on a straight path between the engine inlet symmetry axis and the receiver, due to refraction in the jet caused by temperature differences. An explanation of the refraction effect is postponed until chapter 3; at this point it suffices to note that this effect is included in the directivity. The tables differ for each of the source regions and provide a way to find the resulting SPL as a function of frequency and polar angle. A typical result from such a calculation for a bypass engine (as shown in figure 2.5), is illustrated in figure 2.6.

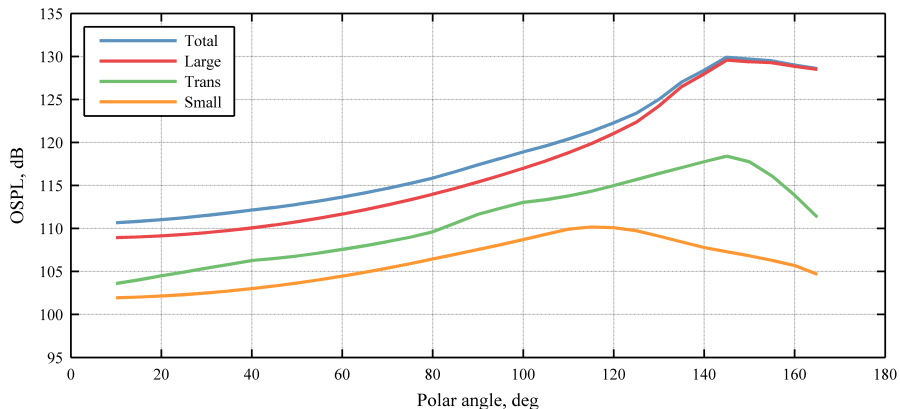


Figure 2.6: The OSPL calculated by the current implementation of Stone's model, after figure 23 in his report.⁽⁴⁰⁾

The different contributions in figure 2.6 are from the different source mechanisms typified in the model, i.e. large-, transitional- and small-scale mixing noise. The highest amplitudes are emitted at an angle of roughly 140-150 degrees from the inlet, i.e. the exhaust. This directivity can be linked to the intrinsic quadrupole behavior of jet noise. Furthermore, the large scale mixing area proves to be the dominant noise contribution. Frequency spectra at 150 degrees can be found in figure 2.7.

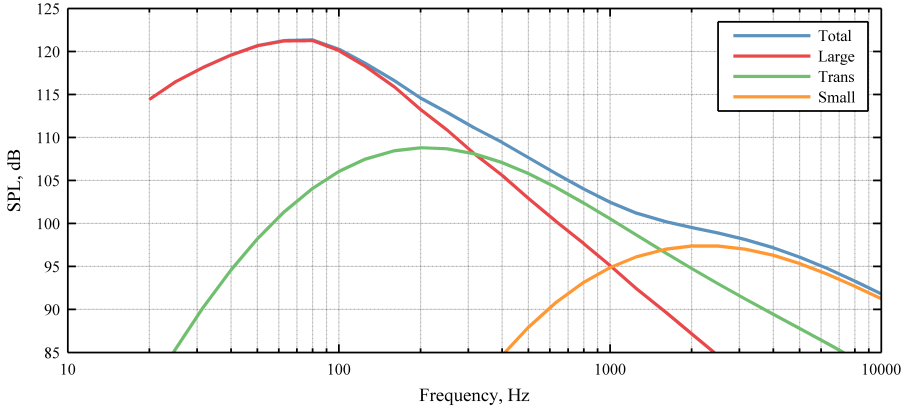


Figure 2.7: The result at a polar angle of 150 degrees.

In figure 2.7 it is observed that large scale mixing noise involves low frequencies, transitional scale mixing noise is of a higher frequency whereas small scale mixing noise is, again, higher in frequency.

2.6.2 Fan noise - Heidmann

The objective of a gasturbine is to generate propulsive force by increasing the momentum of the airflow. To that end, different gasturbine stages increase (or decrease) the momentum of the flow. Each stage is, more or less, a cylindrical disk of blades. The first stage in the engine is generally referred to as the engine fan. Figure 2.8 shows the inlet of an aircraft engine and the fan.

Simulating the air flow through different engine stages comprises unsteady air inflow, different fan rotational speeds, complex blade geometry, rotating blades (exerting force on the airflow) and static blades (transferring load to the structure or reducing swirl), both high and low temperatures and other complicating matters. Such a prediction is extremely complex and the aeroacoustic field is hard to ascertain.

System noise predictions requires that fan noise predictions are executed in a short computational time. The model developed by Heidmann⁽⁴¹⁾ was developed based on this requirement. Heidmann's model forms the fan noise prediction basis in the most aircraft noise prediction tools and has not yet been surpassed by other empirical methods. Over the years, updates have improved the equations as modern engines



Figure 2.8: *Airbus A-380 engine nacelle equipped with a Rolls Royce Trent 900 gasturbine.**

became available, thereby increasing the empirical database of the method. The most relevant updates^(32;42) are the basis of the implemented version for the current study. Furthermore, effects of acoustic lining are added as well.⁽⁴³⁾ Acoustic lining is a treatment of the engine inner nacelle with perforated materials that attenuate sound within the engine duct. Lining material is visible in front of the fan in figure 2.8 as the black wall portion. The perforations act as small Helmholtz resonators that attenuate portions of the sound at specific frequencies.

In the model by Heidmann, there are three fundamental source mechanisms. Two radiate efficiently to both the front and back of the engine, whereas one only radiates to the front. Consequently, there are five sources explicitly modeled;

1. Discrete tones from the inlet
2. Broadband sound from the inlet
3. Multiple pure tones from the inlet
4. Discrete tones from the exhaust
5. Broadband sound from the exhaust

Discrete tones are caused by rotor-stator interaction. Unsteady forces are generated by the wake of the rotor blades that hit the stator blades. This interaction creates an acoustic pressure signature that repeats itself with every blade passage. As a consequence, this particular pressure is repetitive and proportional to the fan rotational speed and the number of blades. The fundamental frequency at which this repeats is therefore known as the Blade Passage Frequency (BPF),

$$\text{BPF} = \frac{B \cdot \text{RPM}}{60} \quad (2.64)$$

*Source: www.airbus.com/galleries/photo-gallery/, accessed on 12-09-2013.

where B represents the number of fan blades and RPM denotes the engine rotational speed measured in Revolutions Per Minute. Although the BPF is a single frequency, higher harmonics are present at integer multiples of the BPF. Broadband noise is generated by turbulence in the blade wakes, boundary layers and unsteady inflow of the engine. These phenomena involve different length and time scales thereby leading to a broad range of acoustic frequencies.

Multiple pure tones are generated by shocks on the blades when the local fan tip Mach number becomes supersonic. Each blade contains such a shock that generates an acoustic wave that radiates upstream of the blade. The waves coalesce (grow together) in the inlet duct due to blade imperfections and slightly different aeroelastic loading conditions. As such, these tones do not repeat themselves at every blade passage, but at every engine rotation or shaft order. This makes a very typical sound, popularly referred to as 'Buzz-Saw' noise.

Heidmann's model predicts the spectrum shape, level and directivity for each of these components. The main equation, per source mechanism, is constructed as,

$$SPL = L_b + F1(M_t) + F2(RSS) + F3(\theta) + F4(f) \quad (2.65)$$

$$L_b = 20 \log_{10} \left(\frac{\Delta T}{\Delta T_{ref}} \right) + 10 \log_{10} \left(\frac{\dot{m}}{\dot{m}_{ref}} \right), \quad (2.66)$$

where L_b is a base level of the fan depending on the temperature rise ΔT and the massflow \dot{m} relative to empirical reference values ΔT_{ref} and \dot{m}_{ref} . $F1$ is a function accounting for the fan tip Mach number M_t , $F2$ takes the Rotor-Stator Spacing (RSS) into account, $F3$ applies a directivity correction and $F4$ represents the spectrum shape. Every fan noise component is calculated using equation 2.65. The spectrum shape for each component is constant, but varies from component to component. Heidmann assumed different, but constant, directivity patterns for each component. Several corrections are applied for engine specific conditions such as rotor-stator spacing and inlet flow distortion. The most important correction is due to 'tone cut-off'. Depending on the operating conditions and rotor-stator layout, specific tones can not propagate efficiently in the duct⁽⁴⁴⁾ and are attenuated, i.e. they are cut-off.

Figure 2.9 shows the fan noise results for a simulated General Electric (GE) CF6-80C2 of a Boeing 747-400. The engine is providing take-off thrust and flying at a velocity of Mach 0.2. Due to the 1/3rd octave band representation, discrete tones are included in some bands leading to a spike in the spectrum. More specifically, the 1st BPF in figure 2.9 is at 2000 Hz while the 2nd BPF harmonic is present at 4000 Hz. The Buzz-Saw tones are also included, for instance noticeable at 500 Hz at an angle of 60 degrees. The Buzz-Saw tones are predicted to radiate only in the forward arc of the engine at high thrust settings. Also note that the model predicts the fan broadband noise to peak around the 2nd BPF harmonic frequency of 4000 Hz.

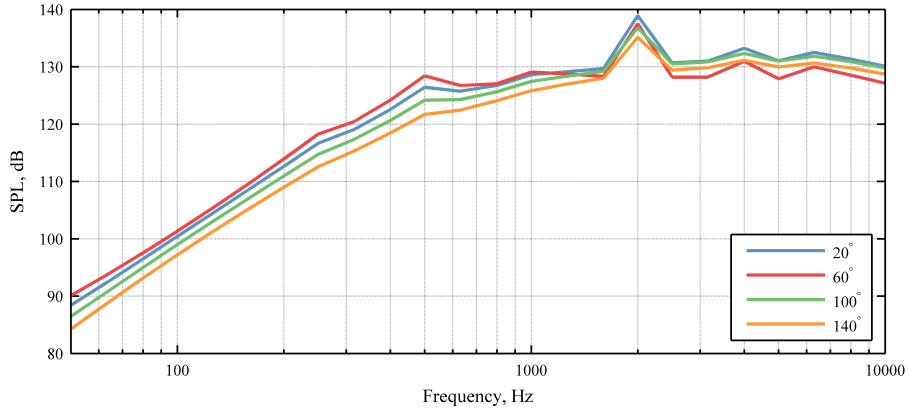


Figure 2.9: Fan noise spectra at different polar angles.

Engine nacelles are usually treated with acoustic lining material to suppress noise in the inlet as well as the (bypass) exhaust. To calculate the exact behavior of acoustic liners is a challenging task involving many parameters that are usually company proprietary. ANOPP uses an empirical correction⁽⁴³⁾ to evaluate the effects of liners on fan noise. Simple parameters as the duct diameter and length of the applied lining area provide input to polynomials fitted through measured results of GE engines. The method is therefore, at least, applicable to GE engines such as the aforementioned CF6-80C2. Consequently, the method was implemented and figure 2.10 shows the results for the inlet and exhaust suppression.

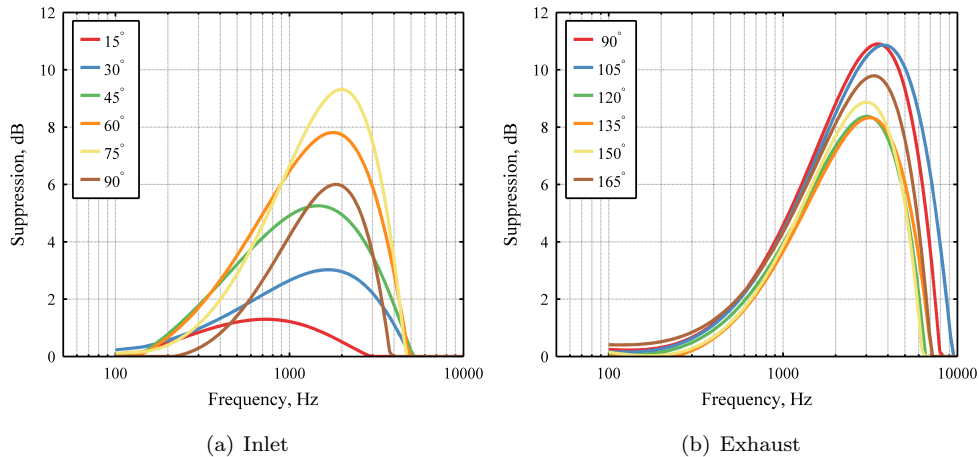


Figure 2.10: Suppression of inlet and exhaust noise due to acoustic liners.

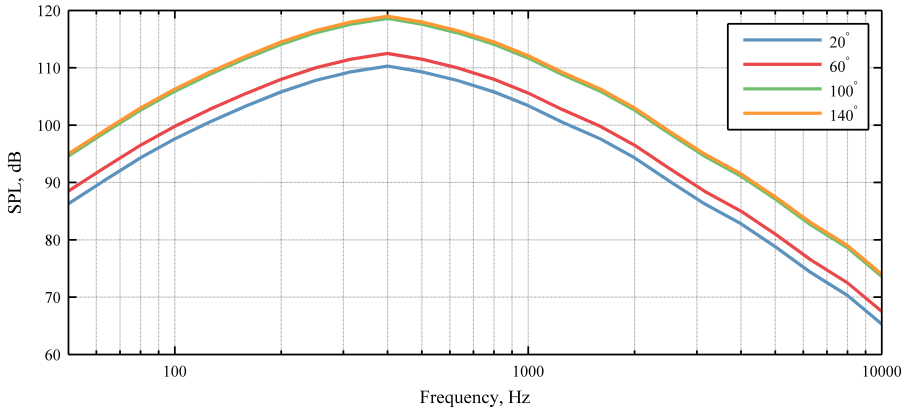


Figure 2.11: Combustion noise spectra at different polar angles.

2.6.3 Combustion noise

In the gasturbine combustion chamber, heat energy is added to the flow by burning fuel. The noise generated by this process is twofold and usually categorized as direct or indirect combustion noise. Direct combustion noise is associated with the expansion of the gas mixture in the combustion chamber. As such, the expanding gas exerts work on its surroundings which produces sound waves in the surrounding gas.⁽⁴⁴⁾ Indirect combustion noise, also known as entropy noise, is due to the convection of non-uniformities through the pressure gradients in the turbine. This generates fluctuations in entropy and thereby gives rise to acoustic waves. The relative importance of direct and indirect combustion noise is still an unresolved issue since it is hard to discriminate the combustion noise from other sources in an experiment.⁽⁴⁵⁾

The current method involved in ANOPP is also found in^(33;46) and is based on literature^(47;48). The general formulation of the empirical combustion models is,

$$p_e^2 = \frac{PDF}{4\pi r^2}, \quad (2.67)$$

where, P is the acoustic loading, D is the directivity function and F is the spectral shape. Each of these three functions differ per component whereas the denominator remains the same. To calculate the sound levels at the source, r should be set to one. For combustion noise, the acoustic loading P depends on the temperature rise, mass flow and pressure in the combustion chamber. Figure 2.11 shows a result of the current implementation of the empirical method. Typical for combustion noise is the spectral peak around 400-500 Hz^(44;47-49), radiating towards the aft of the engine. The interest in fan noise and jet noise has led to a decreased noise level from these particular components. Therefore, it is believed that combustion noise will become a more important aircraft engine source in the coming decades.⁽⁴⁹⁾

2.6.4 Airframe noise - Fink

Airframe noise is unrelated to the engine, in that sense that it is defined as in-flight noise that is nonpropulsive in nature.⁽⁴⁴⁾ As such, it is generated by aerodynamic flow around the airframe such as, for instance, boundary layers, turbulent wakes and cavities. The engine has traditionally been the most prominent source. Nowadays, at low engine power settings, which occur during approaches, the airframe makes a clear contribution to the overall sound from the aircraft that cannot be ignored. During an approach phase, the slats, flaps and gears (see figure 2.3) are extended, which lead to a higher noise level.* An overview of airframe noise issues through the last decades is found in literature.⁽⁵⁰⁾

The model of Fink⁽⁵¹⁾ is the baseline model used for airframe noise prediction in AN-OPP. The model relates the aircraft general geometry to specific source components such as wings, slats, flaps, gears and tailplane sections. Its intention is to determine overall noise trends for full aircraft studies rather than the individual source generating mechanisms.

Although the method of Fink has been around since the late 1970's, it is still used by many researchers. Measurements of aircraft flyover noise, with idle thrust settings, were executed and lay at the basis of the empirical functions. More importantly, the Boeing 747 was used as one of the aircraft in the measurement campaign. Predictions for that type of airframe, as demonstrated later in for instance chapter 7, should thus be matched relatively well. The individual airframe noise component levels are formed by a nondimensional acoustic power loading P , a directivity function D and a spectral shape function F . Consequently, a similar parametric equation as in the case of combustion noise, repeated here for convenience, appears,

$$p^2 = \frac{PDF}{4\pi r^2}. \quad (2.68)$$

Variables P, D, F are altered per airframe noise component. In general, directivity D depends on the observation angles and spectrum F depends on Strouhal number (similar to equation 2.63). Airframe noise is generated by the presence of a turbulent airflow (boundary layer) near an aerodynamic surface such as a wing. A rigorous analysis, similar to the theory of Lighthill for jet noise (see section 2.2), was executed by Curle.⁽²⁰⁾ Curle found a theoretical power law dependency (6th power) on the airflow Mach number and predicted a dipole radiation profile. If a sharp surface edge is present, the dependency on Mach number increased to a 5th power.⁽¹⁹⁾ Consequently, the power loading P in Fink's model follows as,

$$P = k_1 M^{k_2} k_3 \quad (2.69)$$

*This is, for instance, clearly experienced within an aircraft cabin during a landing.

where k_1 and k_2 are constant per component. Constant k_1 is an empirical efficiency constant and k_2 denotes the power-law coefficient. Coefficient k_3 depends on the airframe variables like wing span, flap deflection angle and surface area. For wing-type surfaces, the acoustic power is proportional to the trailing edge boundary-layer thickness, determined by a turbulent flat-plate model, and scales with the fifth power of the Mach number ($k_2 = 5$).

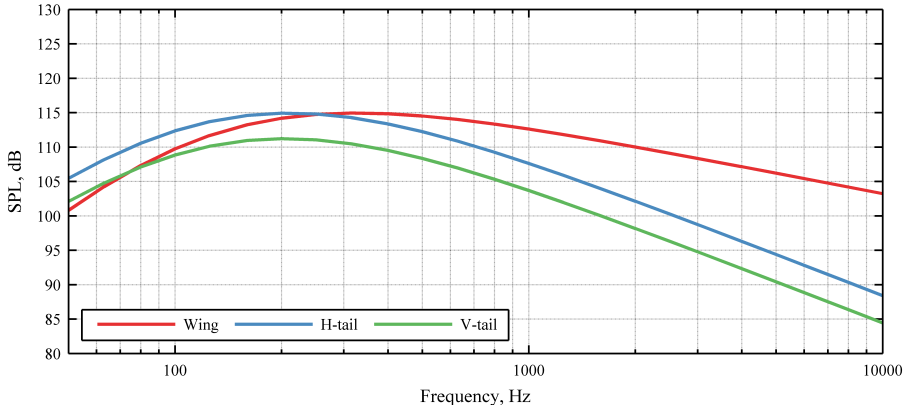
Similar scaling laws are devised for the flaps and slats, although the acoustic loading scales with the sixth power of the Mach number ($k_2 = 6$). This was found to give a better fit to the measured flyover data available to construct the model. Landing gear noise in the model by Fink follows different power loading functions for wheels and gear struts. They follow the same sixth Mach power ($k_2 = 6$) dependency as flaps and slats.

Unlike jet or fan noise, airframe noise is not axis-symmetric. Therefore, directivity variable D depends, besides different for each airframe component, on both the polar angle θ as well as sideline angle ψ . The sideline angle ψ is defined as the angle, in the plane normal to the ground track, between aircraft height and observer. For a typical component, such as the leading edge slats on a wing, the directivity variable D_s is calculated by,

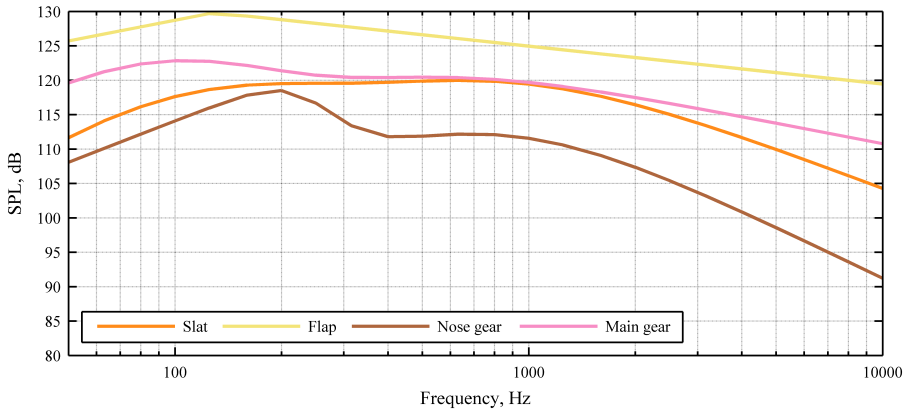
$$D_s = 4 \cos^2(\psi) \cos^2(\theta/2) \quad (2.70)$$

where the cosine forms a dipole directivity pattern, see equation 2.44. If flaps are considered, the directivity is modified by the flap deflection angle as well. All directivity functions of airframe noise components, as modeled by Fink, follow a dipole radiation pattern. To illustrate typical results from the model, figure 2.12 shows the different component for a fictitious aircraft found in literature⁽³⁴⁾ at polar and sideline angle of 45 degrees.

Figure 2.12 shows that there is a clear difference between a 'clean' and 'dirty' airframe, where dirty implies slats, flaps and gears extended. Consequently, airframe noise forms an important contribution to the overall noise from the aircraft during the landing phase. In PANAM⁽³⁰⁾ there are other airframe noise components reported, such as Flap-Side-Edge noise and spoiler noise. These components are not yet included. There are also other 'parasitic' noise sources on the airframe, such as cavities from fuel vents, that are not included in any current empirical noise methodology.^(50;52)



(a) Clean airframe



(b) Dirty airframe

Figure 2.12: Airframe noise components at 45 degrees sideline and polar angle.

2.7 Overall aircraft noise

By combining the individual source noise modules, an overall estimation of aircraft noise can be ascertained. The overall source level, referenced at a unit sphere with a radius of 1 meter, is,

$$SPL_1 = 10 \log_{10} \left(\sum_{id} 10^{(SPL_{id}/10)} \right), \quad (2.71)$$

where id refers to the individual components, i.e. jet mixing noise, fan noise, combustion noise and airframe noise. The individual components are demonstrated by

calculating the source noise of a Boeing 747-400 equipped with 4 GE CF6-80C2 engines. For such a calculation, the engine operating conditions need to be predicted as well. Such an engine prediction is not explicitly included here and based on NLR's Gasturbine Simulation Program (GSP).⁽⁵³⁾ Some details regarding the modeling of a gasturbine are included in appendix D.

The individual engines are added incoherently, on a 1/3rd octave band basis for the entire aircraft, i.e. effectively adding 6 dB since there are 4 engines. The maximum noise output of an aircraft engine is in a take-off condition as maximum power is necessary to accelerate. The corresponding source noise, at a reference sphere with 1 meter radius, is shown in figure 2.13.

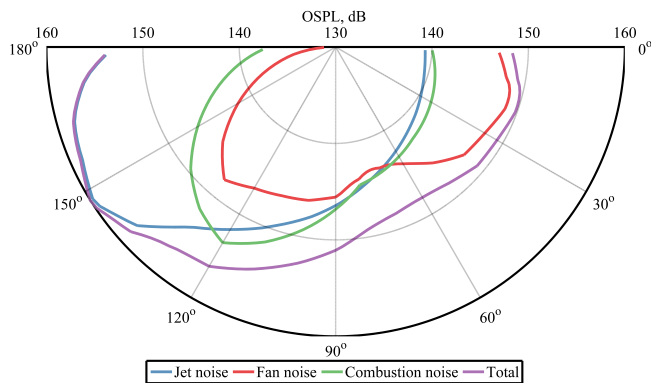


Figure 2.13: Predicted aircraft noise using take-off power (100%N1) for different polar angles. The aircraft is not moving and therefore there is no airframe noise.

Note that the maximum OSPL level is due to jet noise and radiates to the back of the engine. This particular condition can cause annoyance during take-off.^(54;55)

If the aircraft is moving, the jet mixing noise will reduce since the velocity difference between the outflow and ambient airspeed is reduced. Figure 2.14 shows this effect but notice that the A-weighting is applied (see appendix B) to represent the listeners ear sensitivity.

The difference in airframe noise between figure 2.13 and 2.14 is caused by the airflow over the airframe at Mach 0.25. In case of an approach, less power is required by the aircraft as it glides towards the runway. To have a low speed and retain good visibility for the pilots on the final approach, the slats and flaps are fully extended (at 30 degrees). This results in a significant airframe noise contribution and is illustrated in figure 2.15. This figure confirms that airframe noise, in an approach configuration, is roughly of the same level as engine noise.

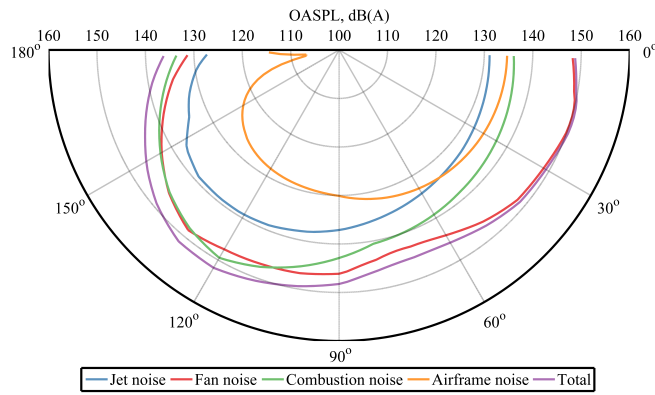


Figure 2.14: Predicted aircraft noise at different polar angles. The aircraft at take-off power (100%N1) is moving at Mach 0.25 with gear up, slats extended and flaps at 10 degrees.

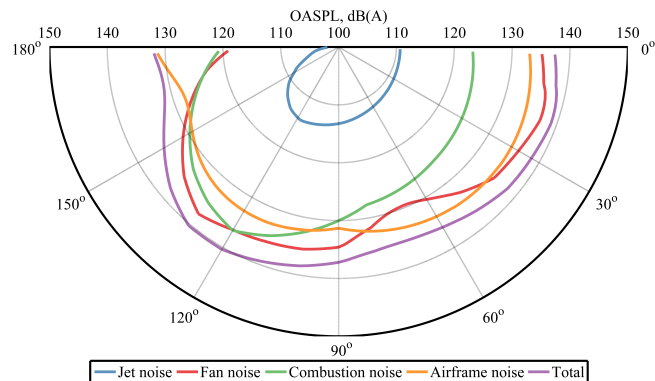


Figure 2.15: Predicted aircraft noise using approach power (60%N1) for different polar angles. The aircraft is moving at Mach 0.22 in final approach configuration, i.e. gear and slats deployed and flaps at 30 degrees.

Chapter 3

Atmospheric propagation of sound

The previous chapter described, primarily, the generation of source noise. This chapter treats the propagation of sound from the source towards a receiver on the ground. As the sound travels through the atmosphere, three distinctive effects play a role that affect sound before it reaches the listener.

Sound is absorbed by the atmosphere during propagation due to viscous and molecular relaxation effects. Section 3.1 describes the background and results of this phenomenon. Acoustic waves, or rays, are bounced off the ground. Therefore, a ray pair of a direct and ground reflected ray reaches a listener. During reflection of the ground, the ground reflected ray may lose some of its acoustic energy and undergo a phase change. Section 3.2 describes the resulting ground interference effect. Ray paths are curved due to a non-homogeneous atmosphere, specifically gradients in wind and temperature. This effect is known as refraction and is calculated using ray tracing based on Snell's law. With help of ray tracing, the geometric spreading loss is established in section 3.3 together with the limitations of ray tracing.

By combining atmospheric absorption, ground reflection and spreading losses, an overall transmission loss during propagation is established. The final section (3.4) of this chapter combines the aforementioned results and presents the overall effects. From hereon in this dissertation, the use of the prime to denote an acoustic variable is dropped, i.e. p' becomes p .

3.1 Atmospheric absorption

Absorption of acoustic waves during propagation is due to two different effects. The first is due to viscous effects that are not taken into account when deriving the wave equation, see equation 2.4. These effects are much smaller than the inertial effects when describing source noise. Over long distances, or high frequencies, such as en-

countered in atmospheric propagation, these effects become important and cannot be ignored. The second effect is due to the molecular composition of the atmosphere. These effects occur due to molecules that, upon collision during a passing acoustic wave, exchange energy from translational to rotational and vibrational modes. This energy exchange is proportional to the relaxation time⁽⁵⁶⁾, i.e. the time required for the molecule to reach equilibrium after excitation. Due to this process the specific heat of the gas is time dependent, which is a deviation from the ideal gas law, and causes absorption. The absorption is proportional to the distance the wave has traveled and is conveniently integrated using a complex (plane wave) notation in,

$$p(t, r) = p_0 e^{i(\omega t - kr)} \quad (3.1)$$

where, p is the acoustic pressure, at a distance r , of an acoustic plane wave with an initial amplitude p_0 and wave number $k = \omega/c$. By substituting a complex wave number $k = \beta - i\alpha$ the equation becomes,

$$p(t, r) = p_0 e^{-\alpha r} e^{i\omega(t-\beta r)}, \quad (3.2)$$

where, α is the (frequency dependent) attenuation coefficient in Nepers per meter, β is related to the phase speed and equals here ω/c . To transform coefficient α to decibels per meter, a multiplication factor of $20/\ln(10) = 8.6859$ should be used. A good overview on the individual equations used in the modeling of atmospheric absorption is found in literature.⁽¹⁵⁾ That analysis is repeated here briefly and starts with the dissipative formulation of the classical wave equation (equation 3.218 in⁽¹⁵⁾),

$$\nabla^2 p - \frac{1}{c^2} \frac{\partial^2}{\partial t^2} \left(p - \frac{2\delta_{cl}}{c^2} \frac{\partial p}{\partial t} - 2 \sum_v \frac{(\Delta c)_v}{c} \tau_v \frac{\partial p_v}{\partial t} \right) = 0, \quad (3.3)$$

where, p_v is the partial pressure of an individual component v of the atmosphere.* The terms outside the parentheses are identified as the wave equation, i.e. equation 2.12. The second term and third term in the parentheses represent a deviation of the wave equation caused by viscous and relaxation effects. The second term is the classical (viscous) contribution whereas the third term is due to relaxation. The deviation from the reference sound speed of the atmosphere is denoted, for a particular component, as $(\Delta c)_v$ and τ_v is the corresponding relaxation time. The variable δ_{cl} representing the viscous absorption is,

$$\delta_{cl} = \frac{1}{2\rho} \left[\frac{4}{3} \mu + \mu_b + \frac{\kappa(\gamma - 1)}{C_p} \right], \quad (3.4)$$

*The four main atmospheric components are Nitrogen (78%), Oxygen (21%), Argon (0.9%) and Carbon-Dioxide ($\leq 0.1\%$). The percentages indicate, roughly, the volume fraction of the components at sea level, other even smaller contributions from other components are present.

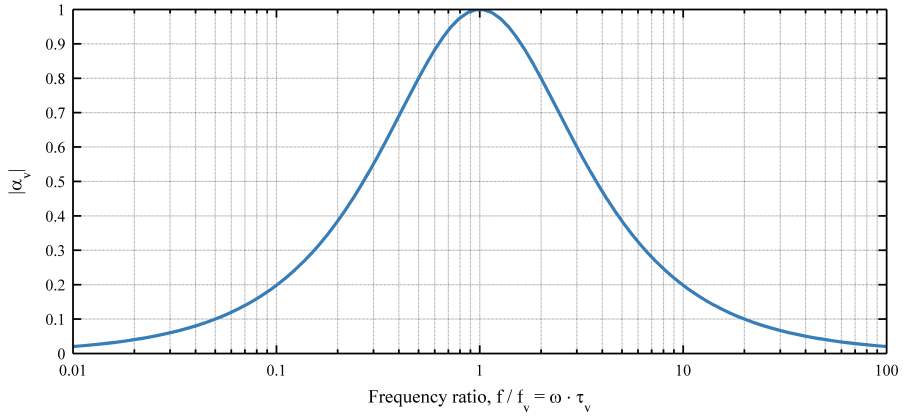


Figure 3.1: The normalized absorption as a function of relaxation frequency ratio.

where, ρ is the density, C_p is the heat capacity at constant pressure, μ is the viscosity, μ_b is the bulk viscosity ($\mu_b \approx 0.6\mu^{(57)}$) and κ is the thermal conductivity. All of these terms depend on temperature. The pressure of the individual molecular components follows from,⁽¹⁵⁾

$$p_v = \frac{1}{1 - i\omega\tau_v} p. \quad (3.5)$$

By substituting this relation in equation 3.3 the imaginary wave number is calculated to first order by,⁽¹⁵⁾

$$k = \frac{\omega}{c} \left(1 + \frac{i\omega\delta_{cl}}{c^2} + \sum_v \frac{(\Delta c)_v}{c} \frac{i\omega\tau_v}{1 + (\omega\tau_v)^2} \right). \quad (3.6)$$

By following the initial definition of α in equation 3.2, the imaginary (dispersive*) part of the wave number will form the absorption. As such, the total absorption coefficient is established as,

$$\alpha = \alpha_{cl} + \sum_v \alpha_v, \quad \alpha_{cl} = \frac{\omega^2\delta_{cl}}{c^3}, \quad \alpha_v = \frac{(\Delta c)_v}{c^2} \frac{\omega^2\tau_v}{1 + (\omega\tau_v)^2}, \quad (3.7)$$

where α_v is the absorption due to vibrational relaxation of molecules in the atmosphere. The typical form of α_v is sketched in figure 3.1 by setting the fraction $(\Delta c)_v/c$ to unity. From this figure it is inferred that a relaxation process will cause an attenuation maximum at the relaxation frequency. In general, only vibrational relaxation

*Dispersion means that the speed of sound depends on frequency.

of Oxygen (O_2) and Nitrogen (N_2) are taken into account in most atmospheric absorption models. When sound travels at very high altitudes, like for instance in the case of infrasound propagation, other molecular compositions need to be studied.^(58;59)

Notice that, in general, the absorption scales with frequency squared. This means that high frequency sound is more effectively absorbed by the atmosphere. A derivation of the factor $(\Delta c)_v/c$ is given by Pierce,⁽⁵⁷⁾

$$\frac{(\Delta c)_v}{c} = \frac{(\gamma - 1)^2}{2\gamma} \frac{n_v}{n} \left(\frac{T_v}{T} \right)^2 e^{-\frac{T_v}{T}}, \quad (3.8)$$

where, n_v/n is the volumetric ratio of a component in air (0.78 for N_2 and 0.21 for O_2 at sea level), T_v is a characteristic temperature commonly referred to as relaxation temperature, which is 2239 K for O_2 and 3352 K for N_2 . This relaxation temperature is a measure for the energy exchange, between molecular modes, involved in the relaxation process. The relaxation times of the oxygen and nitrogen molecules are influenced by water vapor. This effect, together with the relaxation times, has been measured and results in the following empirical expressions,

$$\frac{1}{2\pi\tau_{O_2}} = \frac{p}{p_{\text{ref}}} \left[24 + H \cdot 4.04 \cdot 10^6 \cdot \left(\frac{0.02 + 100H}{0.391 + 100H} \right) \right] \quad (3.9)$$

$$\frac{1}{2\pi\tau_{N_2}} = \frac{p}{p_{\text{ref}}} \left[\sqrt{\frac{T_{\text{ref}}}{T}} (9 + H \cdot 2.8 \cdot 10^4 \cdot e^{-F_H}) \right], \quad (3.10)$$

where τ_{O_2} and τ_{N_2} are the relaxation times and p, T denote the ambient values for pressure (kPa) and temperature (K). The value for T_{ref} is 293.16 K, whereas p_{ref} is a standard pressure of 100 kPa. The factors F_H and H are the effect of humidity on relaxation times,

$$F_H = 4.17 \left[\left(\frac{T_{\text{ref}}}{T} \right)^{1/3} - 1 \right], \quad H = 10^{-2} (RH) \frac{p_{vp}}{p}, \quad (3.11)$$

where, RH is the relative humidity (defined as a percentage relative to the waver-vapor pressure) and p_{vp} is the water-vapor pressure at the local ambient temperature. Equations 3.7-3.11 are the basis of the current absorption standard.⁽⁶⁰⁾ The individual components are calculated, using the standard, and plotted in figure 3.2. Figure 3.2 illustrates that the vibrational relaxation of Oxygen and Nitrogen form the largest contribution to the overall absorption coefficient. The absorption peak (see figure 3.1) of Nitrogen occurs at 525 Hz, for Oxygen this is 62 kHz. Classical absorption is not dominant for this particular atmospheric condition. The variation of these components as a function of temperature and humidity is provided in figure 3.3 for a wave of 1000 Hz.

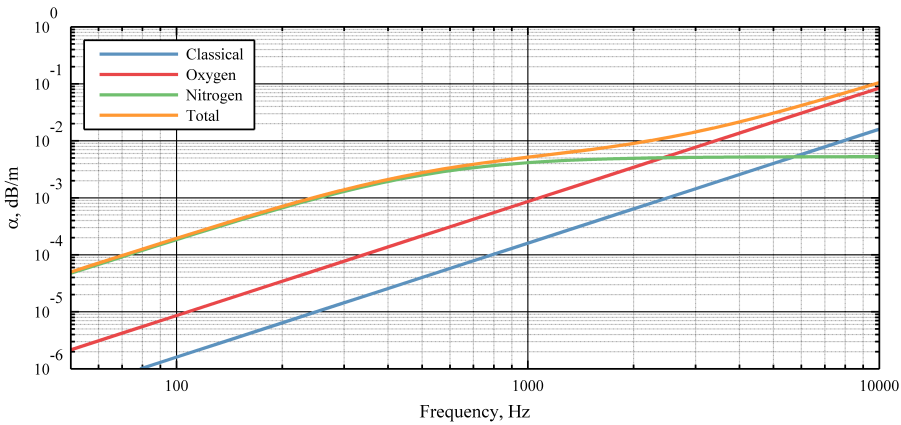


Figure 3.2: The individual absorption components, at $RH = 80\%$, $T = 20^\circ C$ and $p = 101.325 \text{ kPa}$.

In figure 3.3 it is observed that the absorption peak of Oxygen formed by the relaxation process shifts due to a change in humidity and temperature. This also holds for Nitrogen. Note that the maximum absorption of Oxygen is reached in dry conditions, whereas for Nitrogen this is in humid conditions. Classical absorption, i.e. viscous effects, are not influenced by humidity in this model and are only a function of viscosity (and hence temperature). Adding these individual contributions to obtain the total absorption, see figure 3.3(d), reveals a trough near standard day conditions of $T = 15^\circ C$ and $RH = 80\%$. Any deviation in temperature near this point will thus lead to higher absorption.

The current derivation stems from literature of 2007⁽¹⁵⁾, but the absorption effects were originally described and published in 1972.⁽⁶¹⁾ A theoretical foundation for the relaxation effects was published by Pierce.⁽⁵⁷⁾ Consequently, the coefficients used in the models were updated and clarified.^(62;63) Given these studies, the method was adopted for standardization in the ANSI norm⁽⁶⁰⁾ and ISO⁽⁶⁴⁾. In 2004 the method was extended to higher altitudes for infra-sound propagation studies.^(58;59)

The overall effect of absorption on propagation is applied a posteriori to the propagation results obtained by the wave equation without dissipative and relaxation effects. This overall factor is taken into account as,

$$A_A = -\alpha r, \quad (3.12)$$

where α is the attenuation coefficient in dB/m, r the propagation path length and A_A the total transmission loss due to absorption for this acoustic ray path.

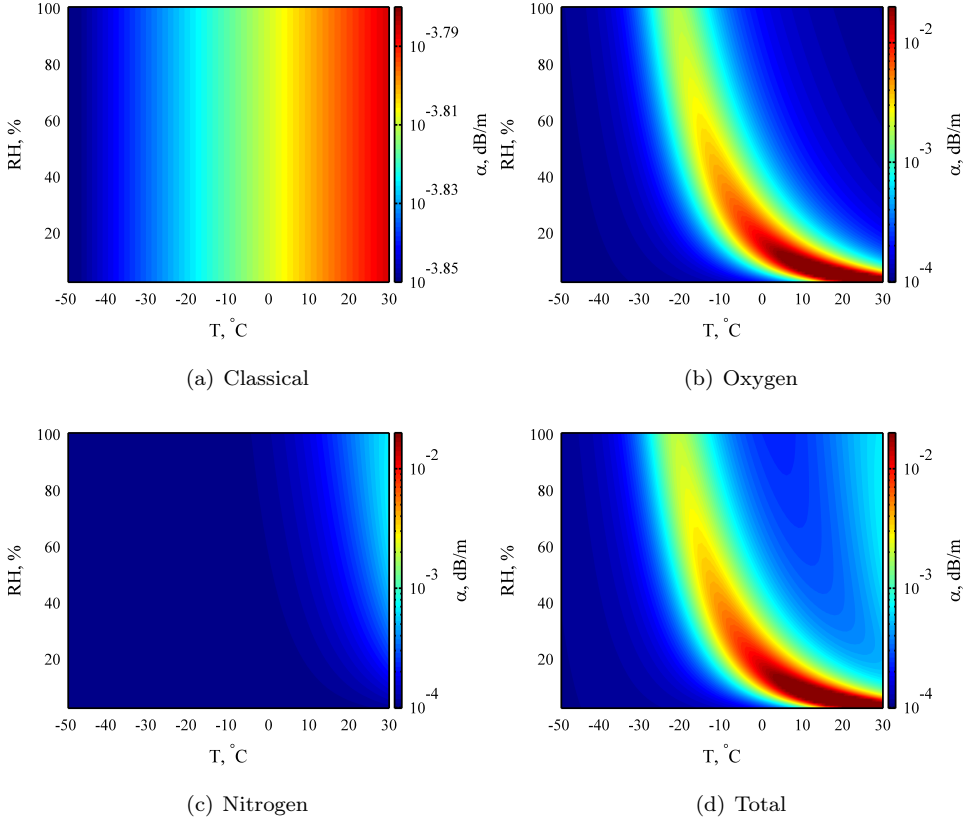


Figure 3.3: Absorption components, at 1000 Hz, for varying temperature and humidity. Please notice the difference in color scale axis of figure 3.3(a).

3.2 Ground reflection

If an acoustic wave hits the ground, or another surface, it is reflected and/or absorbed. In case of a rough surface the reflected wave may be scattered in different directions, in which case the reflection is diffuse. A convenient assumption is to assume that the wave is specularly reflected, i.e. the sound is fully reflected in the direction normal to the incident field, as is illustrated in figure 3.4.

The consequence is that a microphone, or observer, situated above the ground receives a direct (r_1) and ground reflected (r_2) wave as shown in figure 3.4. These two ray path lengths are calculated by,

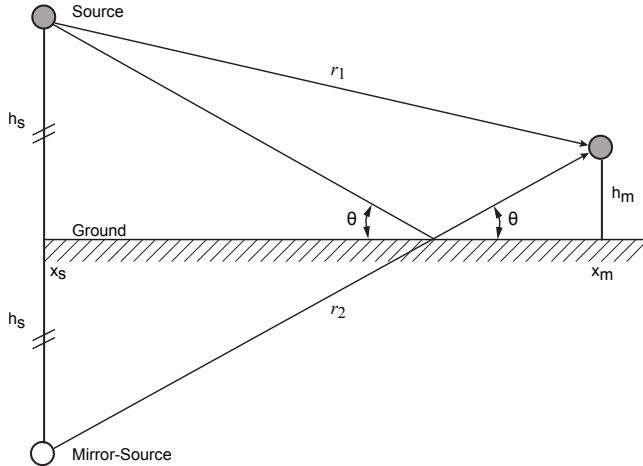


Figure 3.4: Reflection of a sound ray by the ground

$$r_1 = \sqrt{(x_s - x_m)^2 + (h_s - h_m)^2} \quad (3.13)$$

$$r_2 = \sqrt{(x_s - x_m)^2 + (h_s + h_m)^2}, \quad (3.14)$$

where x denotes the x-position and h is the height, subscripts denote the source or microphone position. Many textbooks describe the general outline on how to include this effect in the wave equation.^(65;66) The derivation defines a Helmholtz equation in both the propagation medium and the ground including an impedance jump on that boundary. On the boundary, the particle velocity and acoustic pressure should be continuous. This results, after considerable mathematical manipulation, in,

$$p = \frac{e^{ikr_1}}{r_1} + Q \frac{e^{ikr_2}}{r_2} \quad (3.15)$$

$$Q = R_p + (1 - R_p) F \quad (3.16)$$

$$R_p = \frac{Z_n \sin(\theta) - 1}{Z_n \sin(\theta) + 1}, \quad (3.17)$$

where equation 3.15 shows that the acoustic pressure is the summation of the direct and ground reflected wave, Q is the ground reflection coefficient and Z_n is the normalized (normalized to air by ρc) surface impedance. To calculate the ground reflection coefficient, two factors are necessary; the plane wave reflection coefficient R_p and the spherical wave correction factor F . If F is zero, the plane wave reflection coefficient is retained as the resulting difference between the plane-wave and spherical-wave reflection coefficient is negligible. This holds if the speed of sound and density (impedance)

of the ground is much higher than air. Such a condition is referred to as an acoustically hard surface as all energy is reflected without a phase change of the wave. If F is zero, the traditional mirror-source approach is obtained, where the interpretation of 3.15 is the sum of a direct wave and a reflected wave from the ground. However, if the ground reflection surface is not hard an additional contribution can exist. This is due to ground and surface waves, respectively the second and third term in equation 3.16. A ground wave arises due to a curved wave front hitting the ground at different angles of incidence, in contrast to a plane wave having a constant angle of incidence along the wavefront. Surface waves exist if the ground is so porous that it influences the particle velocity, thereby reducing the wave phase velocity near the surface.⁽⁶⁷⁾ This traps some of the sound energy near the surface. The spherical wave correction factor F is calculated by,

$$F = 1 + iw\sqrt{\pi}e^{-w^2} \operatorname{erfc}(-iw) \quad (3.18)$$

$$w^2 = ik \frac{r_2}{2} \frac{(\sin(\theta) + 1/Z_n)^2}{1 + \sin(\theta)/Z_n}, \quad (3.19)$$

where, w is the integration variable (frequently referred to as numerical distance) for the complex complementary mathematical error function erfc .⁽⁶⁷⁻⁶⁹⁾ It is slightly different than commonly used versions^(15;65), which are found using an incidence angle (defined with respect to the normal of the ground) instead of a grazing angle (angle with respect to the ground surface). Furthermore, it is often assumed that the term $\sin(\theta)$ in the denominator of equation 3.19 is 0. This is reasonable since surface waves only occur for very shallow grazing angles. However, such a simplification is not really necessary since the complexity or computational expense is not much affected by including this contribution. Other small differences stem from the sign convention between different researchers, i.e. $e^{-i\omega t}$ or $e^{i\omega t}$.⁽⁷⁰⁾ The complex error function can be calculated using the standardized (tabulated) form⁽⁷¹⁾ or with approximations⁽⁶⁵⁾. Differences between the different formulations in the calculation of F and w are small.^(65;68)

In the derivation of equations 3.17-3.19, it was assumed that the ground is locally reacting. This means that the traverse component of the wave is ignored. This is usually a reasonable approximation since from Snell's law, which will be explained in the next section, a higher speed of sound in the ground (relative to air) means that the wave is refracted towards the normal.

Furthermore, the exponential relationship in F decays proportionally to $\sqrt{r_2}$ which, for a fixed source position and receiver range, is solely a function of receiver altitude above the ground. As such, surface and ground waves decay exponentially with height above the surface. Note that the $1/r_2$ relation in equation 3.15 is modified due to the factor r_2 in w of equations 3.18 and 3.19. Consequently, such terms decay by $1/\sqrt{r_2}$ instead of $1/r_2$, i.e. cylindrical instead of spherical spreading. Therefore, surface waves cannot be ignored for long range propagation under shallow elevation angles.

The ground impedance is different for different ground constitutions, i.e. snow absorbs more sound energy than concrete upon reflection. Different models exist, each trying to model the ground impedance using more physical parameters relating to the properties of the ground. In general, these models are made by fitting a relationship to impedance tube measurements of different porous materials. One of the easiest models to implement is that by Delany and Bazley, who suggested a power-law for the surface impedance.⁽⁷²⁾ The normalized surface impedance follows as,

$$Z_n = 1 + 0.0511 \left(\frac{f}{\sigma_e} \right)^{-0.75} + i0.0768 \left(\frac{f}{\sigma_e} \right)^{-0.73}, \quad (3.20)$$

where, f is the frequency and σ_e is the effective flow resistivity representing the ratio of applied pressure gradient to the induced volume flow rate per unit thickness of material, i.e. the difficulty of air to flow through a surface.⁽¹⁵⁾ This model is one of the most used and reported to give reasonable results⁽⁶⁸⁾, especially for grassy surfaces. The benefit of this model is that surface impedance is modeled with one parameter. Typical values for the σ_e ⁽⁷³⁾ are presented in table 3.1.

Table 3.1: *Typical range of effective flow resistivity.*⁽⁷³⁾

Soil	Range of $\sigma_e, kPa/m^2 \cdot s$
Concrete	30,000-100,000
New asphalt	5,000-15,000
Dirt, wet	4,000-8,000
Dirt, roadside	300-800
Grass lawn	125-300
Forest floor	20-80
Snow	1.3-50

In this dissertation a value of $\sigma_e = 250kPa/m^2 \cdot s$ is used for grass. However, this only holds for grass that is slightly moist. If the grass becomes fairly wet by rain the impedance is different and hard to be captured by such a power-law.⁽⁷⁴⁾

Figures 3.5 and 3.6 show a calculation of both the magnitude and phase of the reflection coefficient for different effective flow resistivities ($\sigma_e = 25, 250, 2500 kPa/m^2 \cdot s$, roughly denoting snow, grass and a dirt (hard) reflection). The source height is 100 meters and the magnitude $|Q|$ and phase angle ϕ follow from $Q = |Q| e^{i\phi}$. Notice that in figures 3.5 and 3.6 the distance to the receiver (x) is solely a function of source height h_s , a fixed microphone height of $h_m=1.2$ m and grazing angle θ ; i.e. $x_m = (h_s + h_m) / \tan \theta$.

Figure 3.5 illustrates that the plane and spherical wave reflection coefficient magnitude is different due to the ground and surface waves. This difference becomes larger for shallow grazing angles, low frequencies and low effective flow resistivities. The differences in phase (figure 3.6) are smaller and barely noticeable. A spherical wave is approximately plane at large distances. A difference in reflection coefficient is thus

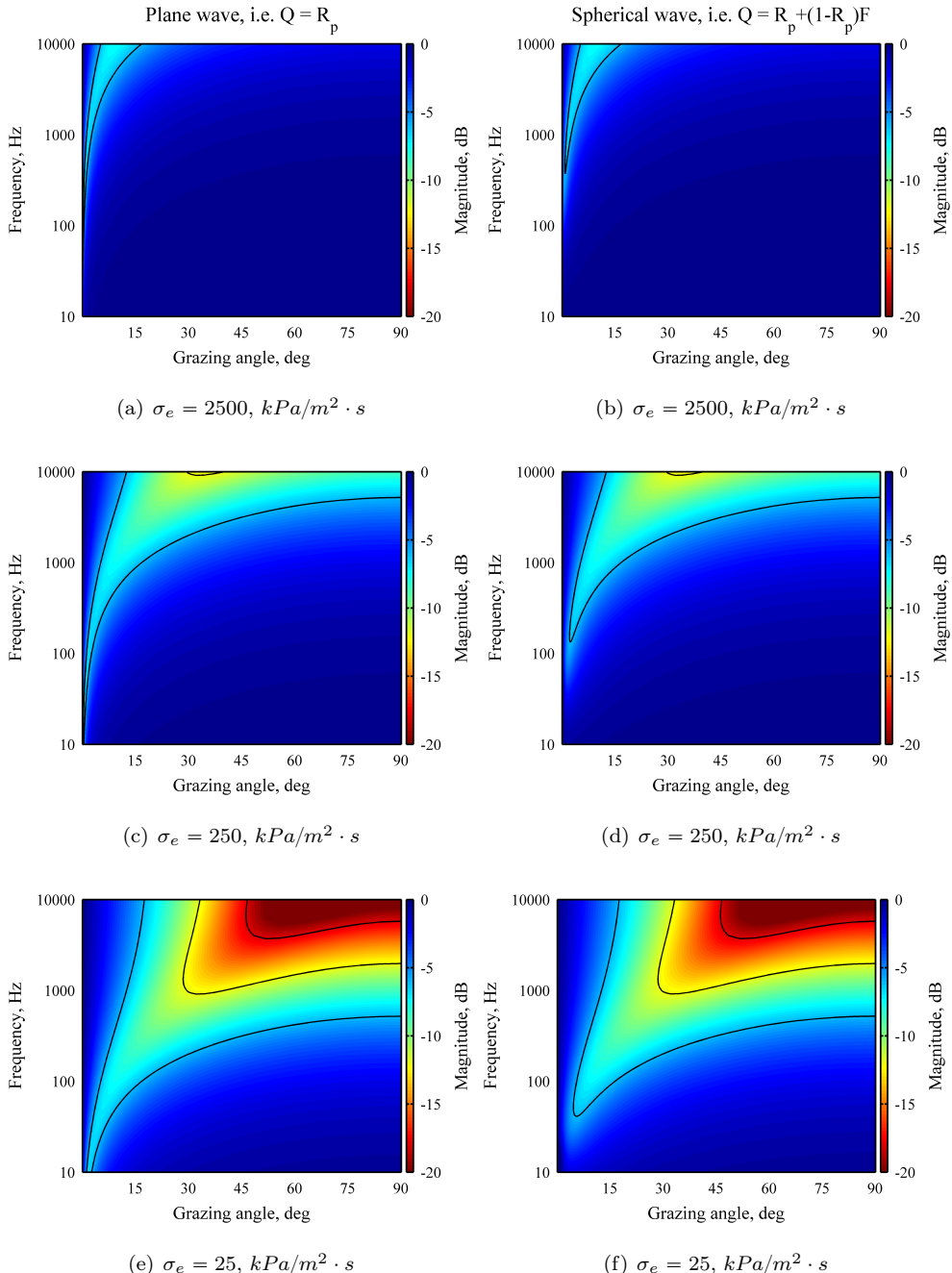


Figure 3.5: Magnitude of reflection coefficient, $20 \log_{10}(|Q|)$, for a plane (left column) or spherical (right column) wave approximation. The contour lines depict intervals of 6 dB.

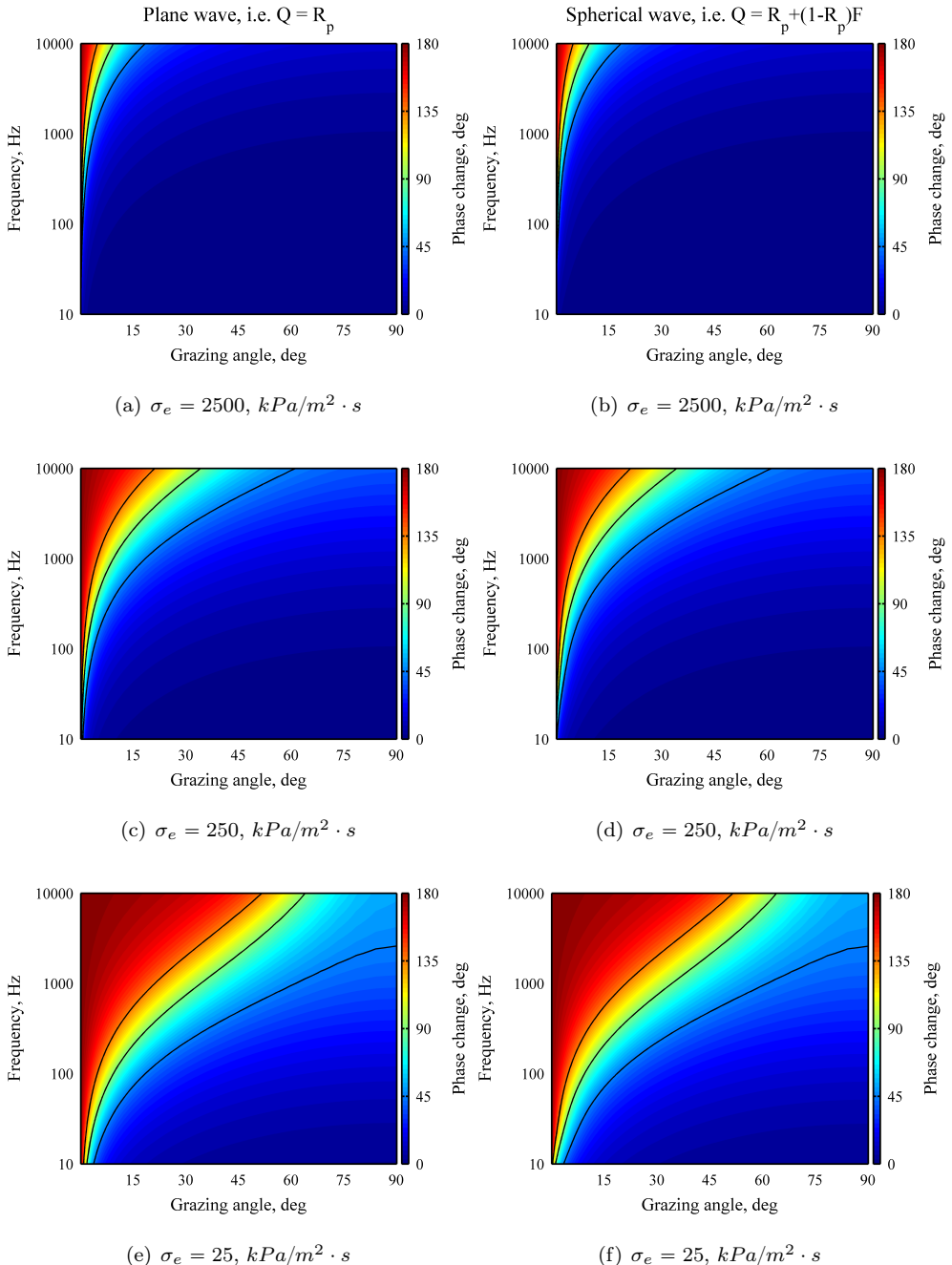


Figure 3.6: Phase of reflection coefficient Q for a plane (left column) or spherical (right column) wave approximation. The contour lines depict intervals of 45 degrees.

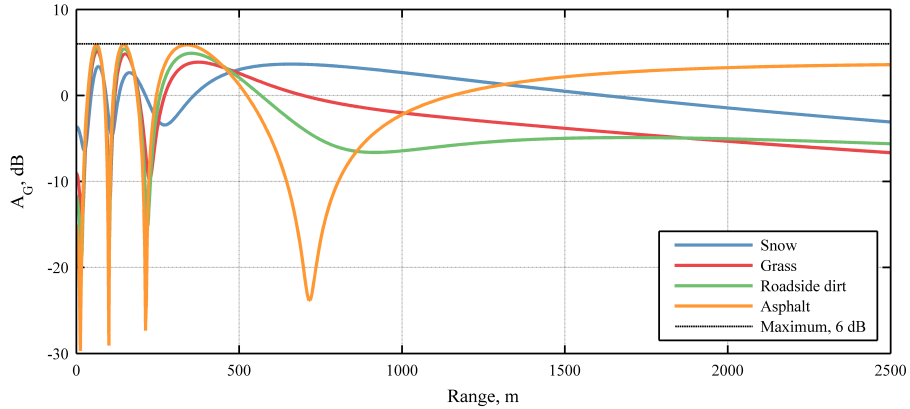


Figure 3.7: The effect of ground interference for different ground constitutions from table 3.1 at 500 Herz.

noticeable in cases where this approximation is limited, i.e. short range and small grazing angles. In case of aircraft flying overhead, the plane wave approximation is valid. This approximation is not applicable in case of ground-to-ground propagation, i.e. for aircraft flying near the ground. In appendix C, the differences between the two approximations are included for different source heights. The differences of figure 3.5 and 3.6 are found in figure C.13.

The overall effect of ground interference is calculated by subtracting the results of equation 3.15, in dB, from a solution without a ground surface. More details of adding both wave contributions, using the effective pressure, is provided in appendix A as equation A.21. The result of this calculation is repeated here as,

$$A_G = 10 \log_{10} \left(1 + \left(\frac{r_1}{r_2} |Q| \right)^2 + 2 \frac{r_1}{r_2} |Q| \cos(k(r_2 - r_1) + \phi) \right), \quad (3.21)$$

where A_G is the overall ground interference effect in dB and $r_2 - r_1$ is the path length difference that contributes, besides the ground induced contribution ϕ , to the phase difference. If both waves arrive in phase, a maximum (coherent) amplification of 6 dB can occur. Figure 3.7 shows a ground interference pattern, calculated by equation 3.21 for a source at 100 meters height and a microphone height of 1.2 meters.

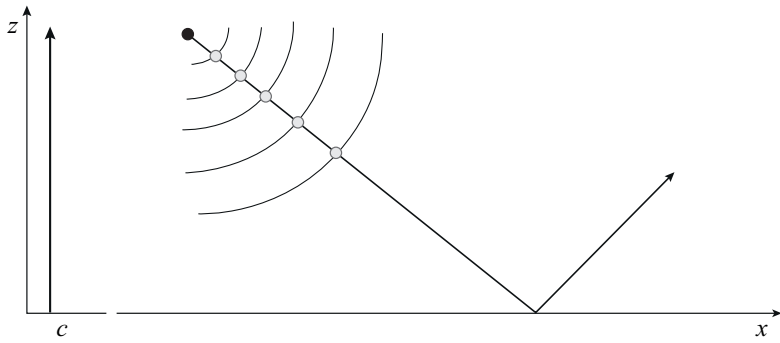


Figure 3.8: A ray path is formed by a straight line, connecting the same initial point of an acoustic wave-front, if the speed of sound is uniform.

3.3 Spreading losses

3.3.1 Theory

In chapter 2, the spherical spreading of an acoustic wave in equation 2.22, lead to an inverse proportionality of the amplitude inverse with respect to r . This is used to establish the spreading losses, relative to 1 meter from a source, by the spherical spreading law as,

$$A_S = 20 \log_{10} (r) . \quad (3.22)$$

In essence, the sound is assumed to travel along a straight-line path between the source and observer. Such a path connects the points on the acoustic wave front and is known as an acoustic ray, see figure 3.8.

In deriving the spherical spreading law, moving medium and non-uniform temperature effects on sound speed, have been neglected. It is well-known that temperature and velocity gradients will lead to a curved path rather than a straight path.^(13;15;65;66) This leads to a difference in spreading loss, absorption and ground reflection effects. Two distinctive propagation effects, refraction and diffraction, cause curvature of the ray path. The curvature due to atmospheric inhomogeneities is known as refraction whereas diffraction is the curvature of rays around an object.

There are many methods available to model these propagation effects.^(66;75) Well-known methods within this area are the Fast Field Program (FFP), Parabolic Equation (PE) method and Ray Tracing (RT).^(65;66;76) The FFP model uses a one-way Helmholtz equation whereas the PE method employs an angular limitation to the same equation. The one-way notion limits both methods to forward propagation and thus excludes the backscatter at objects. Both methods are frequency dependent

and require multiple evaluations if a broad-band sound source is considered. The RT model solves only the refraction part of the wave-equation and is frequency independent. Therefore it is a very popular model and allows quick calculations, over a broad range of frequencies, in a single run. For that purpose, it was selected as the backbone of the propagation modeling in this research and is described in more detail following literature.^(15;76)

Ray tracing models have been around for quite some time and come in many forms. The least amount of computational operations, i.e. a relative computational inexpensive algorithm, can be obtained by using Snell's law. Hence, such an algorithm was used in the current work since a real-time functionality is desired for auralization purposes. Snell's law complies with the more computational demanding ray tracing equations, which is shown in the following analysis. The analysis uses the convective wave equation (equation 2.11) as a start, which is repeated here for convenience,

$$\frac{\partial^2 p}{\partial t^2} + \frac{\partial}{\partial t} (2(\vec{u}_0 \cdot \nabla) p) + (\vec{u}_0 \cdot \nabla)^2 p - c^2 \nabla^2 p = 0. \quad (3.23)$$

Note that in equation 3.23 the acoustic variable is denoted as p instead of p' . By assuming a plane wave of a single frequency,

$$p = A e^{i\omega\Phi}, \quad \Phi = t - \tau(x, y, z), \quad A = A(x, y, z), \quad (3.24)$$

where, the phase factor Φ contains the 'Eikonal' τ , which is a representation of the wavefront phase as a function of space. The derivatives in equation 3.23 are calculated by substituting a plane wave, such a substitution yields,

$$e^{i\omega\Phi} \left[-\omega^2 A + 2i\omega (\vec{u}_0 \cdot \nabla) A - 2\omega^2 A (\vec{u}_0 \cdot \nabla) \Phi + (\vec{u}_0^2 - c^2) \cdot (-\omega^2 A (\nabla\Phi)^2 + i\omega A (\nabla^2\Phi) + 2i\omega (\nabla\Phi \cdot \nabla A) + \nabla^2 A) \right] = 0, \quad (3.25)$$

which features a real and imaginary part:

$$\mathbb{R} : \quad \omega^2 + 2\omega^2 (\vec{u}_0 \cdot \nabla) \Phi + (\vec{u}_0^2 - c^2) \cdot \left(\omega^2 (\nabla\Phi)^2 - \frac{\nabla^2 A}{A} \right) = 0, \quad (3.26)$$

$$\mathbb{I} : \quad 2\omega (\vec{u}_0 \cdot \nabla) A + (\vec{u}_0^2 - c^2) \cdot (\omega A (\nabla^2\Phi) + 2\omega (\nabla\Phi \cdot \nabla A)) = 0. \quad (3.27)$$

Inspection of equation 3.26 shows that one term ($\nabla^2 A/A$) does not depend on ω^2 . This term is independent of frequency and is often neglected since the other terms

dominate the solution, due to the square, at high frequencies. This assumption implies, because this equation turns out to establish the ray path, that the ray path (or wave front position) is independent of the amplitude. Therefore, diffraction effects, such as bending around objects, are ignored. Hence, ray tracing is a plane-wave, high frequency approximation that only accounts for refraction.^(12;15;77) Using these assumptions allows to obtain the common 'Eikonal' equation of ray tracing,

$$(\nabla \Phi)^2 = \frac{1 + 2(\vec{u}_0 \cdot \nabla) \Phi + (\vec{u}_0 \cdot \nabla)^2 \Phi}{c^2} = \left(\frac{1 + (\vec{u}_0 \cdot \nabla) \Phi}{c} \right)^2. \quad (3.28)$$

This Eikonal equation describes the propagation of the wave-front in space, irrespective of frequency and amplitude. A different approach is to expand the factor $A(x)$ in inverse powers of frequency ($A_0 + \frac{A_1}{\omega} + \frac{A_2}{\omega^2} \dots$). Such an approach leads to the same Eikonal equation. In that case, equation 3.27 becomes a recurrence relation that equals, to first order, the result of equation 3.27. A substitution of Φ , see equation 3.24, into the Eikonal equation results in,

$$|\nabla \tau| = \frac{(1 - \vec{u}_0 \cdot \nabla \tau)}{c}. \quad (3.29)$$

By tracking the ray direction $\vec{w} = \nabla \tau$, a vector normal to the wavefront, we are able to trace the sound rays emanating from the source through the atmosphere. This system of equations is solved by the method of characteristics and follows as,^(12;15;18;78)

$$\frac{d\vec{r}}{dt} = \frac{\vec{w}}{|\vec{w}|} c + \vec{u}_0 \quad (3.30)$$

$$\frac{d\vec{w}}{dt} = -|\vec{w}| \nabla c + \nabla \cdot \vec{u}_0, \quad (3.31)$$

these six ordinary differential equations need to be solved to trace the ray position. The sound rays change direction proportional to the gradient of the sound speed, wind and orientation of the ray. A popular assumption is to add the wind velocity to the sound speed, which leads to an effective sound speed c_e ,^(12;13)

$$c_e = c + \vec{n} \cdot \vec{u}_0, \quad (3.32)$$

where \vec{n} denotes the ray direction and \vec{u}_0 the wind vector. This assumption thus only takes the effect of wind in the direction of propagation into account. The impact of the effective sound speed approximation is estimated in literature⁽⁷⁹⁾ and shows that, to first order, the results from the more comprehensive approach are matched. The benefit of the effective sound speed is that the differential equations collapse to

(even) simpler versions that only take the speed of sound into account. In that case, equation 3.29 becomes,

$$|\nabla\tau| = \eta, \quad (3.33)$$

where, η is defined by $1/c_e$. The arc length s of the ray path is defined normal to a wavefront ($\nabla\tau$) and its direction \vec{s} is defined as,

$$\vec{s} \equiv \frac{\nabla\tau}{|\nabla\tau|}, \quad \vec{s} = \frac{dx}{ds}\vec{e}_1 + \frac{dy}{ds}\vec{e}_2 + \frac{dz}{ds}\vec{e}_3, \quad (3.34)$$

where \vec{s} is a unit vector pointing in the direction of propagation and $\vec{e}_1, \vec{e}_2, \vec{e}_3$ are unit vectors in the corresponding directions. Consequently,

$$\nabla\tau = \eta\vec{s}. \quad (3.35)$$

The change in direction of a ray path (d/ds) is evaluated using the gradient,⁽⁷⁶⁾

$$\frac{d}{ds} = \vec{s} \cdot \nabla \quad \Rightarrow \quad \frac{d}{ds}(\nabla\tau) = \nabla(\vec{s} \cdot \nabla\tau) = \nabla\eta. \quad (3.36)$$

From equation 3.36 it is observed that the change in ray path direction is thus, as expected, proportional to the gradient of the refractive index. If a stratified atmosphere is assumed, where temperature and wind velocity (or c_e) are only a function of height, the gradient of η in x and y direction is zero. Therefore the ray follows a two dimensional trajectory in the (x,z)-plane, as shown in figure 3.9(a).

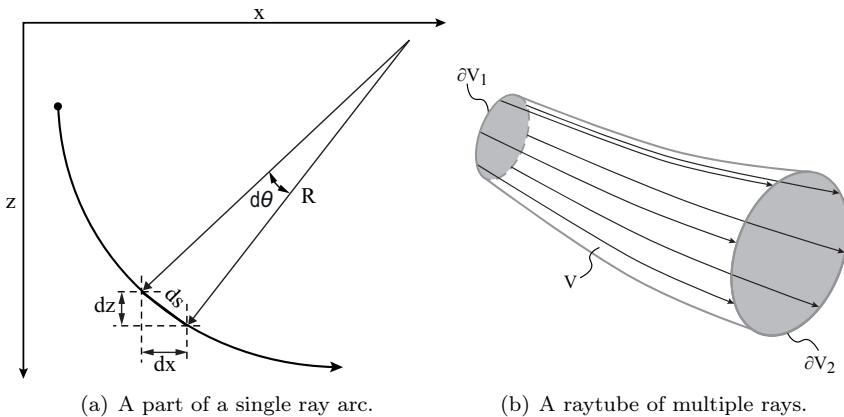


Figure 3.9: A single ray and a raytube.

Consequently, a ray path segment ds follows as,

$$ds = R d\theta, \quad dx = \cos(\theta) ds, \quad dz = \sin(\theta) ds \quad (3.37)$$

where R is the radius of the circular segment. Upon evaluation of dx in equation 3.36, it follows that,

$$\frac{d}{ds} (\eta \cos(\theta)) = 0. \quad (3.38)$$

Equation 3.38 shows that the product of refractive index and ray direction is conserved along the path. Hence, if η (also known as the refractive index) changes, the ray incidence angle should change as well, i.e.,

$$\sin(\theta_1) \eta_1 = \sin(\theta_2) \eta_2, \quad \text{or,} \quad \frac{\sin(\theta_1)}{\sin(\theta_2)} = \frac{\eta_2}{\eta_1}. \quad (3.39)$$

Equation 3.39 is known as Snell's law. By evaluating the incidence angle through different layers of the atmosphere, i.e. a discrete approximation where c is constant within a layer, the ray path can be traced. The travel time (or phase) of the wave follows by the summation of the travel time in each layer.

If the gradient of the effective sound speed is positive, i.e. the sound speed increases with an increase in height, a ray will bend downwards compared to its straight ray equivalent. The opposite holds for a negative gradient. The ray tracing process, for a layered atmosphere with changing sound speed, is sketched in figure 3.10. Notice that upward and downward bending occurs based on the sound speed profile.

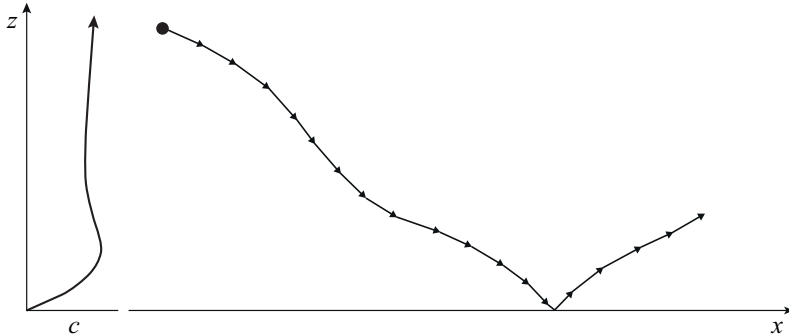


Figure 3.10: A ray path is, due to a non-uniform effective sound speed, curved instead of straight.

Although the ray path can be traced, no amplitude information is yet known. Therefore an assessment of equation 3.27 is necessary. This equation is commonly known as the 'Transport' equation as it describes the evolution of the amplitude over the

ray path. Since an effective sound speed is adopted, thus factor u_0 of equation 3.27 is zero, the amplitude A follows as,^(12;15;18;76)

$$2(\nabla A) \cdot (\nabla \Phi) + (\nabla^2 \Phi) \cdot A = 0, \quad \text{or,} \quad \nabla \cdot (A^2 \nabla \tau) = 0. \quad (3.40)$$

Neighboring rays form a ray tube, as illustrated in figure 3.9(b), that enclose a volume (V). By applying the divergence theorem* to the factor $A^2 \nabla \tau$ of equation 3.40,^(76;78)

$$\int_V \nabla \cdot (A^2 \nabla \tau) dV = \int_{\partial V} (A^2 \nabla \tau \cdot \vec{n}) dS, \quad (3.41)$$

where, \vec{n} is the unit normal on the raytube surface. The only contribution to this integral is by the bounding surface, at equal τ , on either side of the ray tube, i.e. $\partial V_{1,2}$ in figure 3.9(b). This is due to the fact that these surfaces point in the same direction as the normal of the ray, per definition, and thus contribute to the dot product. Consequently, the amplitude is related on different surface slices of the raytube volume by,

$$\int_{\partial V_1} \frac{A_1^2}{c_1} ds = \int_{\partial V_2} \frac{A_2^2}{c_2} ds, \quad (3.42)$$

where $c_{1,2}$ is the sound speed and $A_{1,2}$ the amplitude at the respective surfaces $\partial V_{1,2}$ of figure 3.9(b). Consequently, the plane wave amplitude follows from,

$$A_r = A_s \sqrt{\frac{c_{e_r} S_s}{c_{e_s} S_r}}, \quad (3.43)$$

where, S denotes the area of the raytube surface area and subscripts s, r denote source and receiver. If no effective sound speed would be applied the 'Blokhintzev' invariant, named after the researcher⁽¹⁸⁾, would be obtained. This is basically the same statement, stating that the amplitude along a raytube is proportional to the square root of the raytube area. For a uniform atmosphere, this equation retains the spherical spreading law results.

3.3.2 Implementation

Although ray tracing is a fast method, due to its simplifying assumptions, the computation time varies per software implementation.^(77;80–82) In case of large grid calculations (noise contours) and auralization (aircraft noise synthesis), the ray tracing calculation has to be run many times. Therefore it was chosen to base the algorithm

*The flux of a variable (amplitude) through the volume surfaces (raytube surfaces) equals the divergence of the enclosed volume (raytube).

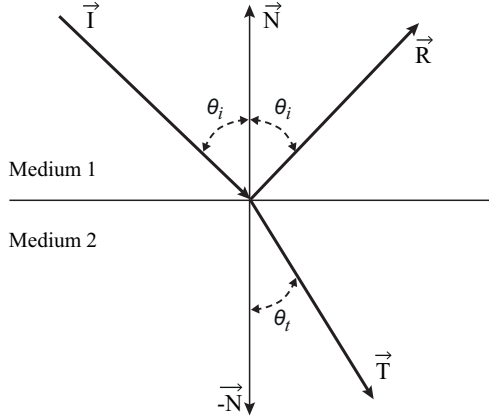


Figure 3.11: The boundary at two different media.

on Snell's law (equation 3.39) rather than solving the set of differential equations (equations 3.30, 3.31). This allows a quick algebraic implementation to calculate the actual ray path. Within the world of optics, ray tracing is used to render computer images for artist impressions, games and virtual environments. In that field, research has led to calculate Snell's law with a minimum of algebraic operations for a single refractive steps. To benefit from this developments, an implementation from literature⁽⁸³⁾ was chosen following figure 3.11 where incident ray (I) is refracted and becomes the transmitted ray (T).

The reflected ray (R) usually contains no significant portion of acoustic energy unless the medium boundary is a ground plane or if internal reflection occurs. Internal reflection is the case when the ray strikes the medium boundary at such a shallow grazing angle that no transmitted ray occurs. The vector \vec{N} is the unit normal in the upward direction and all rays have unit length $|\vec{I}, \vec{T}, \vec{R}| = 1$. As such,

$$\vec{T} = \eta_{it} \vec{I} + \left(\eta_{it} \cos(\theta_i) - \sqrt{1 + \eta_{it}^2 (\cos(\theta_i)^2 - 1)} \right) \vec{N}, \quad (3.44)$$

where η_{it} is the refractive index ratio moving from the incident medium i to the transmitted medium t defined in figure 3.11. Equation 3.44 is derived in Appendix C. For every (discrete) change of the refractive index, the ray changes direction. Since equation 3.44 provides directional unit vectors, a multiplication with the segment length provides the ray segment. The segment length equates the time step multiplied with the local sound speed, which is integrated to obtain the total ray path. By launching rays in different directions from a point source, rays are traced to illustrate the refractive effects due to a gradient in effective sound speed. Figure 3.12 shows a source at 500 meters height and a theoretical (linear), downward refracting, sound speed profile.

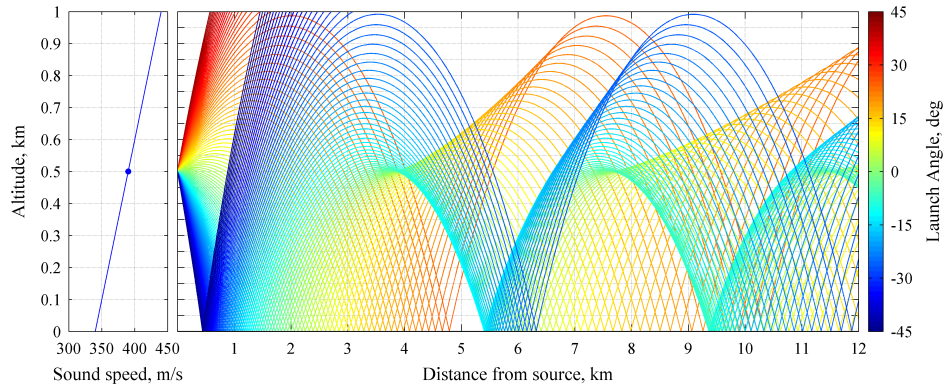


Figure 3.12: *Rays from a source at 500 m in an atmosphere with a linearly increasing (positive gradient) sound speed with altitude.*

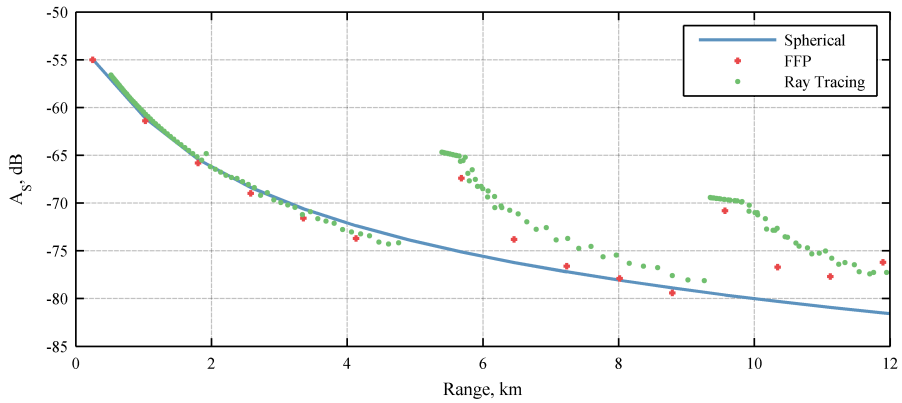


Figure 3.13: *The spreading loss at 500 Hz, calculated by three methods, associated with figure 3.12.*

In figure 3.12, rays bend downward due to the increasing sound speed with altitude. Rays launched upward from the source hit the ground at 2 km. From 2 km onwards, sound is thus not only coming from the downward radiated direction of the source. Furthermore, there are areas where rays are very close together whereas there are also regions where they are further separated. At 5.4 km there is a high density of rays. This implies that the sound is focused at this specific spot and therefore more intense. The opposite occurs if the sound speed decreases with altitude and no rays will hit the ground as we will see further on in this section.*

*This is also observed in figure 3.12 around 5 km, but this is an implementation anomaly since rays above 1 km are cut off.

If rays focus, it is possible that consecutive rays cross and form a so-called caustic. Due to the crossing of the rays the raytube area vanishes and, as implied by equation 3.43, the pressure at the receiver becomes infinite. This is physically unrealistic and is a limitation of ray tracing. In practice, higher sound levels are present in that area but they are not unbounded.⁽⁶⁶⁾ Propagation models based on the wave equation do not have this limitation since they retain the full wave character, including diffraction, rather than just the wavefront characteristics.

In figure 3.12, a caustic near the ground is present around 5.4 km and 9.4 km. In case of a caustic, caustic diffractive fields can be calculated⁽¹¹⁾ through a complex computational procedure. It was chosen, based on observations by Chessel⁽⁶⁸⁾, to bound the focused pressure due to a caustic. The increase in sound level implied by Chessel, due to a caustic, is 10 dB with respect to spherical spreading. This neglects the phase properties in and due to a caustic. To check the applicability of this assumption, caustic pressure was bound accordingly in the ray tracing code and the outcome compared to a calculation by a Fast Field Program (FFP). The used FFP was obtained from an external source.⁽⁸⁴⁾

To give a comparison between the FFP and RT for the spreading losses without the ground reflection, the microphone height was set to zero and the theoretical 6 dB amplification was subtracted. Subsequently, the spreading loss (A_S) of the rays in figure 3.12 was calculated by the spherical spreading law (equation 3.22), FFP and ray tracing (equation 3.43) and is illustrated in figure 3.13.

In figure 3.13 it is observed that the ray tracing results follow the trend predicted by the FFP. Noticeable is, for instance, that both the FFP and RT solutions start to predict a slightly higher spreading loss from 2.5 to roughly 5 km compared to the spherical spreading law. This is due to defocusing of the rays that have been launched upwards instead of downwards. Around 5.4 km, the first area of increased sound level is predicted due to the focusing of rays. The peak of the ray tracing level is slightly above that of the FFP, i.e. the ray tracing thus slightly overpredicts the sound level at this grid point. Moving away from the caustic, the FFP predicts that the sound level nears the spherical spreading law result. The RT slightly overpredicts the losses in this area. The same observation is made for the second caustic encounter near 9.5 km. To evaluate the differences for other source heights and frequencies, similar calculations were made and figures 3.14-3.17 show the results. The 500 Hz frequency was picked to represent a low to mid range frequency that is not fully diminished by A-weighting (see Appendix B) and for a comparison to figure 3.12, the 1000 Hz was selected since it is the first 0 dB level in A-weighting and the 2000 Hz frequency was selected to be representative of a BPF tone.

Figure 3.14 roughly shows the same structure as figure 3.12 although the source height has clearly changed to 100 m. The first caustic hits the ground just before 2.5 km instead of 5.4 km. Refraction effects thus play a role near shallow incidence angles. The reader is attended to the fact that figures showing sound rays, such as figures 3.12 and 3.14 as typically found in literature, imply dramatic atmospheric effects. This is due to the different scale of the horizontal and vertical axes of these figures. If the same horizontal and vertical range would be selected for the axes, the rays would

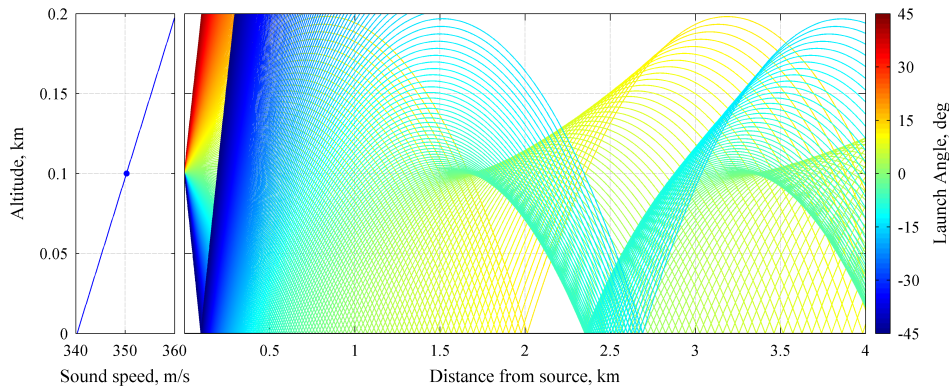


Figure 3.14: Rays from a source at 100 m in an atmosphere with an increasing (positive gradient) sound speed with altitude.

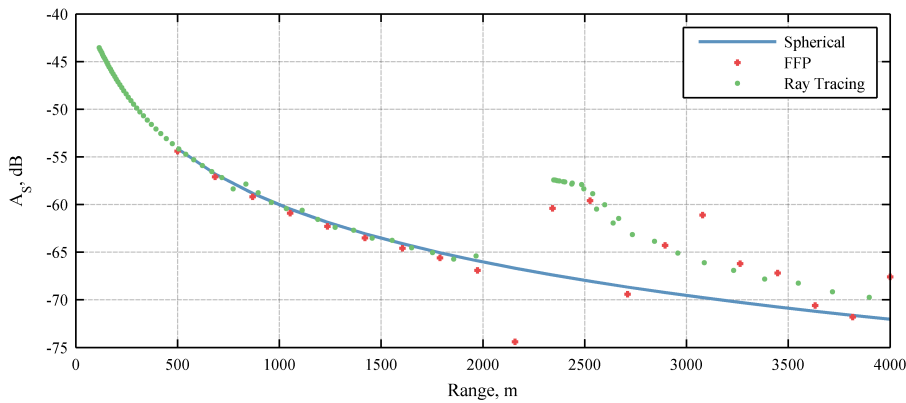


Figure 3.15: The spreading loss at 500 Hz, calculated by three methods, associated with figure 3.14.

appear straight. Refractive effects from an airborne source through such a atmosphere are thus small and become important relatively far, i.e. say at grazing angles less than 10 degrees, away from the source. For aircraft, refraction is thus relevant during take-off and landing. Other applications are low flying military jets or unmanned aerial vehicles. In case of ground-to-ground propagation like railroad, traffic or windturbine noise, i.e. at a very shallow angle compared to the listener, refractive effects may play a major role in the transmission loss at shorter distances.

Due to the fact that the rays do not suffer much from refractive effects up to 2 km, figures 3.15-3.17 show that the FFP and RT technique predict similar results as the spherical spreading law. Near the first caustic, i.e. near 2.5 km, deviations occur for the three frequencies. Within the caustic area the spreading losses seem more or less equal for the three frequencies. This complies with theoretical observations.⁽¹¹⁾

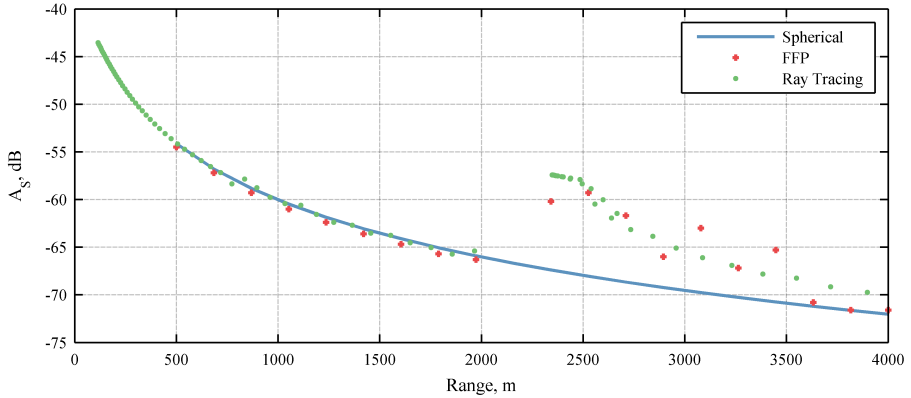


Figure 3.16: The spreading loss at 1000 Hz, calculated by three methods, associated with figure 3.14.

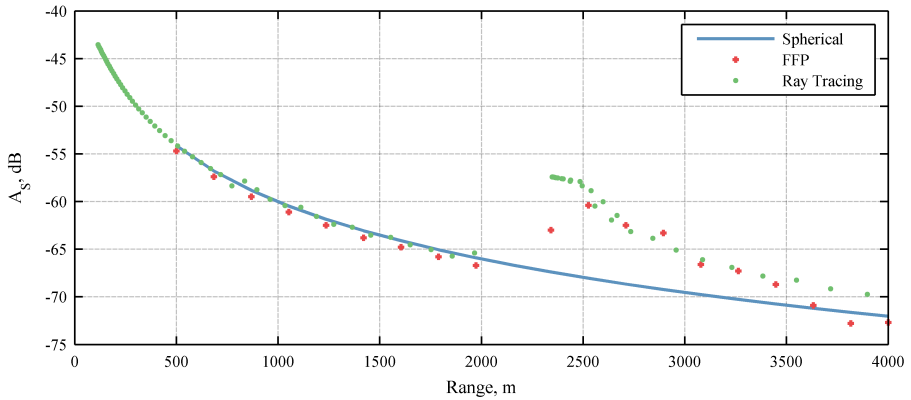


Figure 3.17: The spreading loss at 2000 Hz, calculated by three methods, associated with figure 3.14.

Further away from the caustic, the FFP and RT results tend to move towards the spherical spreading law results but are in general higher. Overall, the agreement between the FFP and RT results is judged as satisfactory. The RT results predict a slightly lower spreading loss than the FFP, also with respect to caustics. Therefore, the RT model gives conservative predictions of the sound levels in that area.

The opposite behavior is found in case of a decreasing sound speed with altitude, in this case rays are bend upwards instead of downwards. This behavior is illustrated in figure 3.18. In figure 3.18, there is a downrange area where no sound rays hit the ground. Such an area is referred to as an acoustic shadow zone since, solely based on refraction, no sound would be present. This is a limitation of ray tracing since diffraction is not taken into account. A single ray forms the boundary between the

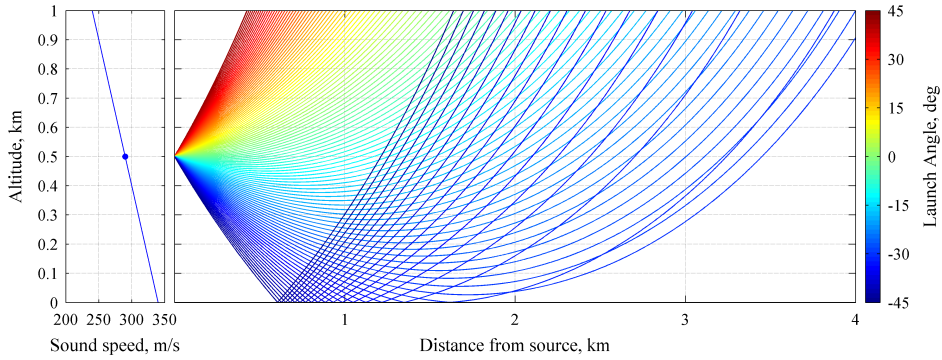


Figure 3.18: *Rays from a source at 500 m in an atmosphere with a decreasing (negative gradient) sound speed ($\frac{dc}{dz} = -0.1 \text{ s}^{-1}$) with altitude.*

shadow zone and the illuminated zone, i.e. the zone where sound rays are present, that ray is referred to as the limiting ray.

Wave equation based propagation methods, such as the FFP are not limited by ‘total silence’ in the shadow zone since they inherently take diffraction into account. Simulations with the FFP show that the transition into the shadow zone result in a smooth increase of spreading loss. A clear difference, with respect to the spherical spreading law, is that the loss becomes frequency dependent, a property of diffraction. A correction mechanism was devised, based on FFP results, to augment the ray tracing solution. The FFP was used to calculate the transmission loss in shadow zones. It appears, from the calculations and literature, that the increased transmission loss in the shadow zone follows a more or less linear pattern from the limiting ray onwards.⁽⁸⁵⁾ As such, an empirical parameterization of the spreading loss in the shadow zone is constructed where the overall spreading loss is constructed out of two terms,

$$A_S = -(A_r + A_d), \quad (3.45)$$

where A_r is the loss due to geometric spreading as calculated by equation 3.43 and A_d is the loss into the shadow zone due to diffraction. Both terms are expressed in decibel and are a function of range. The term A_d gives the additional loss within the shadow zone with respect to the spreading loss at the limiting ray position, calculated by,

$$A_d = L_1 L_2 (x_{sz} - x_{lim}), \quad (3.46)$$

where, $x_{sz} > x_{lim}$ due to the fact that the shadow zone position x_{sz} can only be further downrange than the limiting ray position x_{lim} . For $x_{sz} \leq x_{lim}$, A_d is zero.

Factor L_1 takes the frequency dependency into account whereas L_2 accounts for the dependency on the sound speed gradient according to,

$$L_1 = 0.0032 + 3.5 \cdot 10^{-5} f \quad (3.47)$$

$$L_2 = 6.7 \left(\left| \frac{dc}{dz} \right| \right) + 0.31. \quad (3.48)$$

Notice that this combination does not include the source height. From the FFP simulations, there was no indication that this factor played a role in the calculation of the additional loss into the shadow zone. This simple procedure allows the inclusion of shadow zone results in a ray tracing calculation without the computational complexity of running an FFP. To check the validity, figures 3.19-3.22 show some of the results.

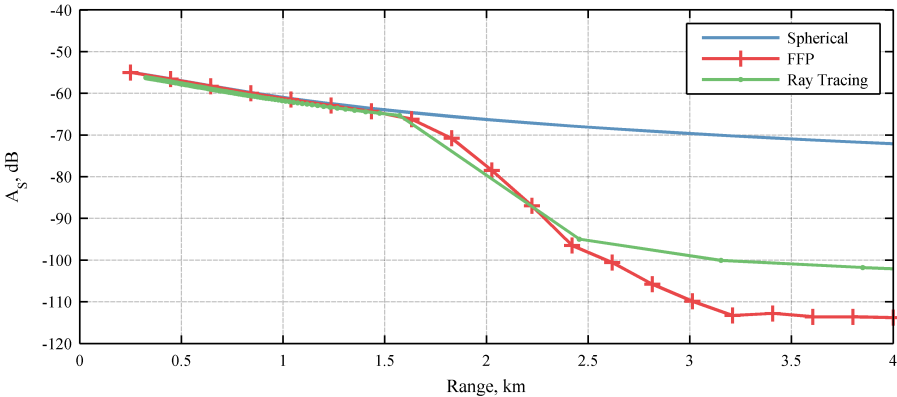


Figure 3.19: Transmission loss at 250 Hz for the situation as in figure 3.18. Notice that the difference between the ray tracing and FFP, for range ≥ 3 km, is limited to 30 dB.

Figure 3.19 shows the shadow zone transition near 1.6 km, where the FFP result illustrates the aforementioned smooth (linear) increase in transmission loss. The correction to augment the ray tracing solution in this particular area follows the same behavior as the FFP. This correction procedure is, in principal, unbounded and will increase as the distance from the limiting ray grows larger. Literature indicates that this behavior is limited due to scattering of rays into the shadow zone due to turbulence.^(66;67;86;87) The overall level, with respect to the spherical spreading results, in the shadow zone may vary from -12 dB to -30 dB.^(67;88) As a consequence, the transmission loss is limited to reach maximally a level of 30 dB below spherical spreading law results. As such, from 2.5 km onwards in figure 3.19 a lower boundary in the transmission loss is formed.

Figure 3.20 shows the transmission loss at the same frequency as figure 3.19 but with a source at a height of 100 m.

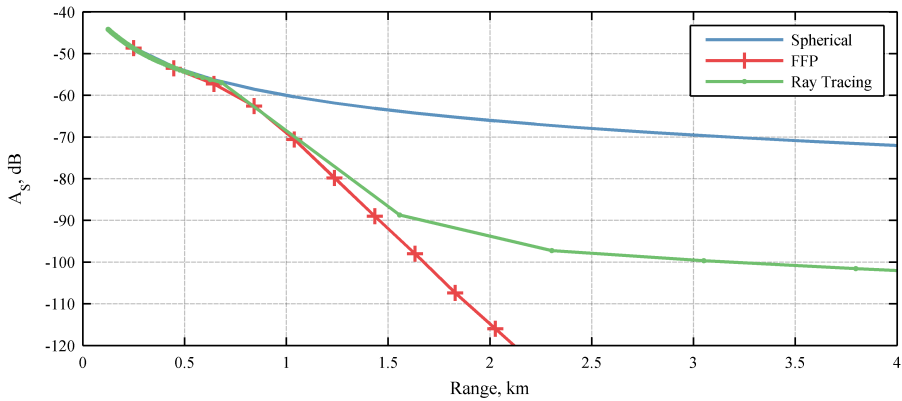


Figure 3.20: Transmission loss at 250 Hz for $(\frac{dc}{dz}) = -0.1 \text{ s}^{-1}$ and a source at 100 m height.

Figure 3.20 shows that the increased transmission loss into the shadow zone is captured despite the difference in source height, which is not a factor in equation 3.48. To check the difference with sound speed profile, the gradient was adjusted and the resulting spreading loss is shown in figure 3.21.

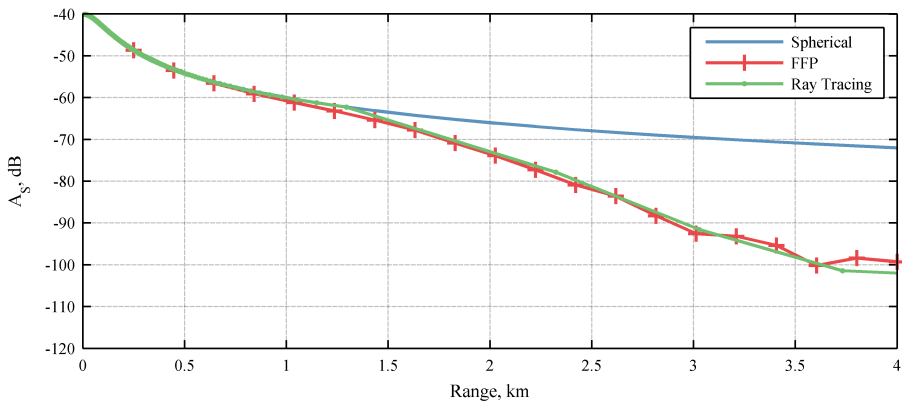


Figure 3.21: Transmission loss at 250 Hz for $(\frac{dc}{dz}) = -0.025 \text{ s}^{-1}$ and a source at 100 m height.

Figure 3.21 shows that a change in sound speed profile gradient, i.e. shadow zone further downrange, has a more gradual increase of the transmission loss compared to the results of figure 3.20. The same condition was checked at 1000 Hz, as shown in figure

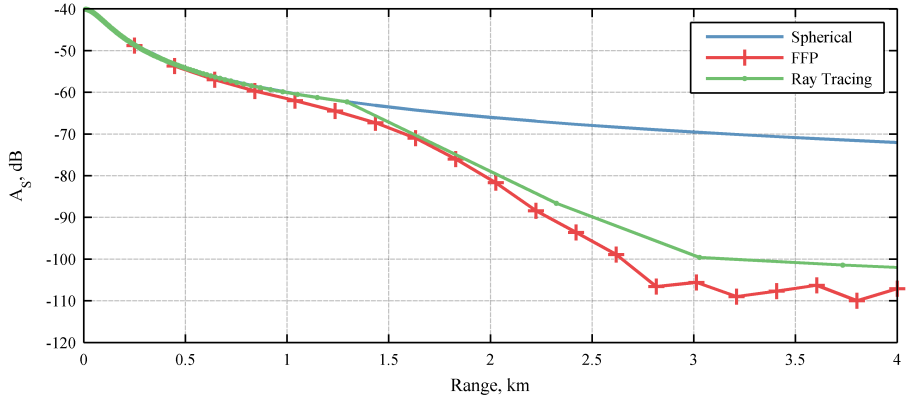


Figure 3.22: Transmission loss at 1000 Hz for $(\frac{dc}{dz}) = -0.025 \text{ s}^{-1}$ and a source at 100 m height.

3.22. Figure 3.22 shows that the transmission loss at a higher frequency, when transitioning into a shadow zone, increases more rapidly compared to a lower frequency, i.e. a diffraction effect. Plots at different frequencies are included in Appendix C that show that the method performs better for lower frequencies than for high frequencies. In general, the effects are reasonable given the simplicity of the method. The advantage of this method is the low computational cost compared to running a wave equation based model or other diffraction inclusion techniques.^(89;90)

3.4 Combined propagation model

By combining atmospheric absorption, ground reflection and spreading losses, a model for predicting the total Transmission Loss (TL) during propagation of (linear) acoustic waves through the atmosphere is constructed,

$$SPL_r = SPL_1 + TL \quad (3.49)$$

$$TL = A_A + A_G + A_S. \quad (3.50)$$

The factors that form the TL are the attenuation by absorption (A_A), ground (A_G) and spreading (A_S) and are given by equations 3.12, 3.21 and 3.45, all in dB. By adding the transmission losses to the source level referenced at a unit sphere SPL_1 , similar to the results from the empirical source noise prediction of chapter 2, the SPL at a receiver position is calculated. The TL is a function of cylindrical coordinates instead of the Cartesian coordinates. This is due to the fact that the ray tracing, as used here based on Snell's law, is a 2D (range-height) implementation. As such,

the rays are confined to travel in the 2D plane for which the effective sound speed is calculated based on the azimuthal angle ψ . The angle ψ forms the difference between the propagation and wind direction. The azimuthal dependency of the observer relative to the source and wind direction is thus encapsulated in the effective sound speed. This is a common approximation and sometimes referred to as a '2.5D' approximation. Figures 3.23(a)-3.23(f) give an impression of the combined results.

In figures 3.23(a) & 3.23(b) the geometrical (spherical) spreading is equal for both plots. Therefore the shown difference is due to ground reflection (for asphalt, see figure 3.7) at 100 Hz and 1000 Hz. The grazing angle is equal, due to the straight ray path, at a specific radial distance. As a result, the cancellation due to interference manifests itself as the (blue-ish) circle in figure 3.23(b). Such clear patterns in figure 3.23 imply an increased loss due to the out of phase arrival of the direct and ground reflected ray at microphone height. Comparing 3.23(a) to 3.23(c) shows that the atmospheric absorption does affect the results at 100 Hz, but this is much less compared to the difference at 1000 Hz depicted in figures 3.23(b) and 3.23(d). If the effect of wind is integrated as well the geometrical spreading (A_S) becomes asymmetric. Comparing 3.23(c) to 3.23(e) shows this effect clearly. There is a shadow zone to the left of the amber line whereas to the right there are areas where the transmission loss is diminished. Upon comparing 3.23(e) to 3.23(f) it becomes clear that waves at 100 Hz are able to reach further out in the shadow zone whereas those at 1000 Hz are attenuated. Comparing 3.23(b) to 3.23(f) shows that the ground interference pattern is changed as well since the grazing angle is different due to refraction.

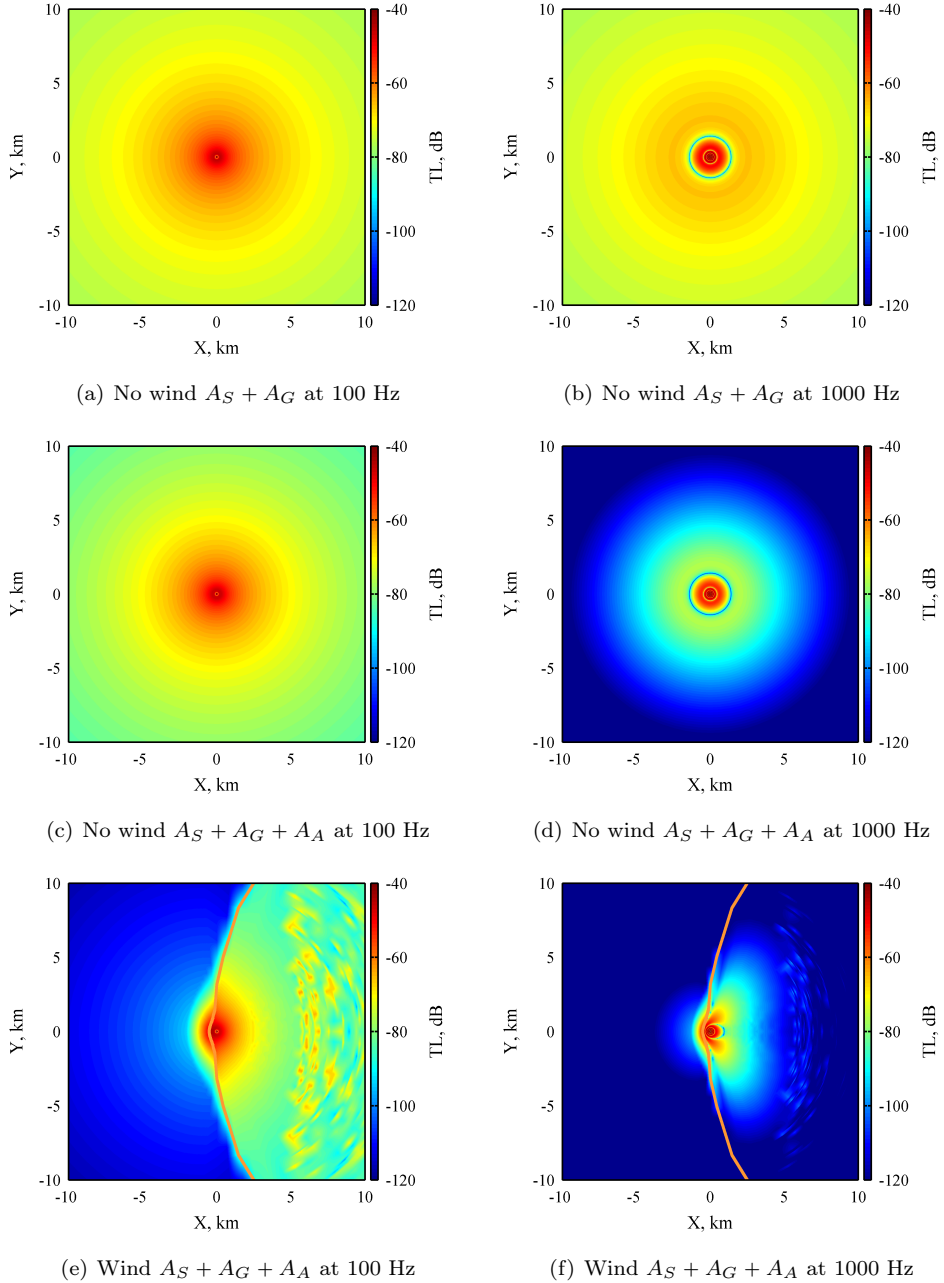


Figure 3.23: The transmission loss for a source at 100 m and a microphone at 1.2 m; figures e and f consider wind (left to right) where the amber line depicts the shadow zone boundary.

Chapter 4

Noise contours in non-standard atmospheres

Airports are continuously confronted with the need to deal with the impact of aircraft noise on the quality of life in surrounding communities. Accordingly, policies are made to deal with the growing number of aircraft and airport operations. Predictions of aircraft noise play a large role in the policy making process and resulting regulations. Such regulations are usually based on noise contour algorithms and expressed in yearly averaged metrics, like the L_{DEN} (Europe) or L_{DN} (USA), see appendix B. The effects of wind on propagation are typically included in a limited fashion. To assess the impact of propagation effects, a noise contour model is updated by the inclusion of ray tracing. The results for a simulation are included in this chapter and based on the Dutch atmosphere of 2010.

4.1 Noise contour algorithms

Current predictive noise models, like INM⁽⁹¹⁾ and the procedure prescribed by Document 29⁽⁹²⁾ (Doc 29 in short), can be improved.^(93;94) INM is the FAA's official method to calculate the noise impact. The European Civil Aviation Conference (ECAC) proposes a similar method (using identical equations) in their Doc 29. These noise models use Noise-Power-Distance (NPD) information as the back-bone of the modeling effort. An NPD relation, usually tabulated, gives the resulting aircraft sound level at a distance, at a microphone height of 1.2 meter, as a function of the aircraft thrust level. NPD data includes, for multiple engine settings, propagation effects due to spherical wave spreading, ground reflection for the microphone height and standard-day atmospheric absorption. Consequently, the physical modeling, as described in chapter 2, is partially abandoned. Such a gross simplification allows fast calculation. Therefore, NPD methods are suited for contour calculations since such

calculations involve many grid points and/or flights operations. The same holds for optimization studies were the number of noise model evaluations is high.

NPD data is typically obtained from flyover measurement, at certification conditions, and averaging of the noise results. In order to account for other propagation effects such as refraction and absorption by the ground surface, a Lateral Attenuation (LA) correction⁽⁹⁵⁾ is applied. The LA correction provides an estimate of the attenuation to the side of the aircraft in excess of the standard NPD attenuation. This is based on measurements through which an empirical standard function has been fitted. This function is used, as a default, in most NPD based models to correct for these factors.

As was shown in chapter 3, or literature^(80;82), atmospheric propagation effects may have a significant impact on the noise levels on the ground. When single-events are considered, averaging of NPD data, atmospheric absorption and utilization of the standardized LA correction method might lead to large differences due to the actual weather conditions. Neglecting the actual weather may lead to a mismatch between the prediction and the real life perception.

In case of noise maps calculated for an entire year, the cumulative effect of these differences have not yet been studied. The underlying LA correction function is based on a trend found by averaging measured Excess Attenuation (EA) throughout a long period.⁽⁹⁵⁾ The correction function thus implicitly assumes that the actual average EA is adequately modeled when using the empirical LA correction in the calculation of a yearly contour. As a result, the influence of the varying atmosphere on a daily basis on annual aircraft noise contours is not definitely answered.

Consequently, the ray tracing method developed in chapter 3 was used to augment the Doc.29 methodology. This allows to study the effect of a daily varying atmosphere on annual noise contours and answers the question how well the empirical modeling approach performs. The algorithm, and a typical result for a single-event, is briefly described in the next section before addressing multiple-events.

4.2 Ray tracing based EA implementation for Doc.29

In the current augmented implementation of Doc.29, the ray tracing algorithm effectively computes the actual EA based on atmospheric data, specified by the user, rather than using a default empirical relation. Figure 4.1 shows the relation between the EA generator (ray tracing algorithm) and the noise model.

By using the approach depicted in figure 4.1, it is possible to separate the more computational demanding EA generation from the actual contour calculation algorithm. Once the EA database is generated for a particular (stratified) atmosphere, the results can be reused for the calculation of different airport layouts or tracks. As a result, the computational efficiency of the original NPD based noise model is retained. The computational expense is only slightly increased due to input-output operations associated by including the EA database. But on an overall level, the Doc.29 runtime

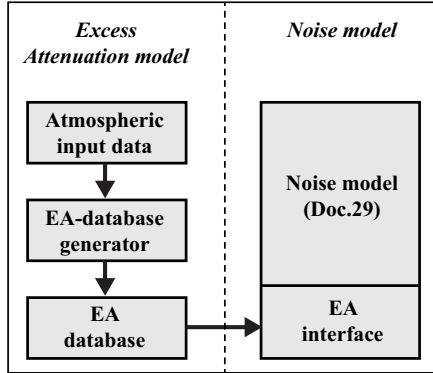


Figure 4.1: The methodology used to correct the noise model.

is similar to that of the default empirical LA function. The EA interface reads in the EA database and adds the other effects, i.e. shielding, that make up the total LA loss that is applied in the Doc.29 model.

It is stressed that only the atmospheric effects on acoustic propagation are taken into account. Although there is an effect on flight dynamics as well, it was chosen to retain the original Doc.29 methodology with regard to modeling of the flight path. As such, the current results reflect purely on the acoustical propagation effects.

The noise model should be supplied with the attenuation in excess of the attenuation that is already included in the NPD data. This calculation procedure of the EA database is illustrated in figure 4.2.

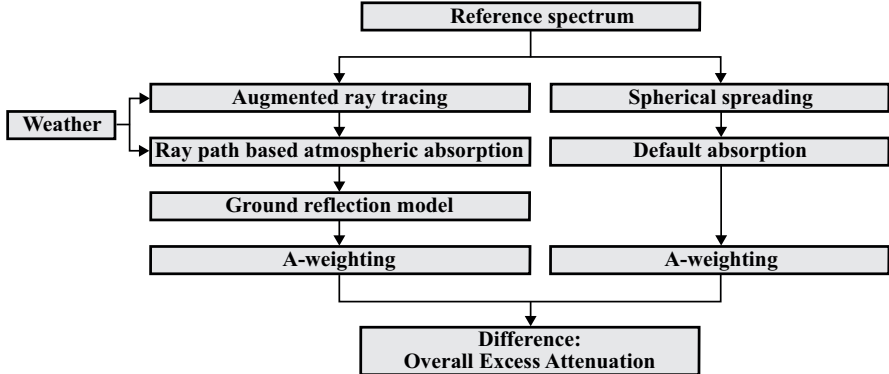


Figure 4.2: The procedure to calculate the Excess Attenuation database.

The difference in EA, resulting from the process depicted in figure 4.2, is thus based on the overall difference caused by the three attenuation mechanisms; spreadin loss, atmospheric absorption and ground attenuation.

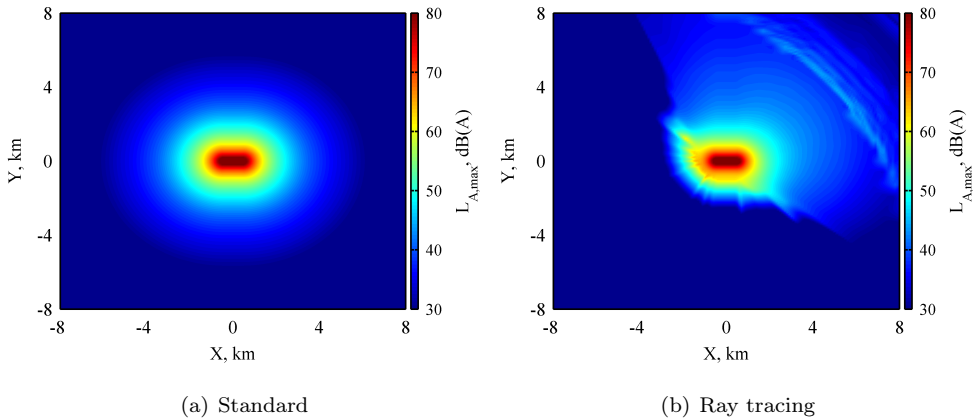


Figure 4.3: Standard (uniform atmosphere) and ray tracing (including South-West wind) footprint for a single flight segment.

NPD tables include ground reflection, as is inherited by measuring aircraft noise in the overhead position with a microphone at 1.2 m on a grass ground surface. To correct for the inherited ground reflection, the result at the overhead position (90 degrees) is subtracted in the correction. Consequently, there is no contribution to the overall attenuation by the ground model when the aircraft is exactly overhead. Only at other angles the ground model adds to the attenuation of the sound level.

The ground reflection effect is taken into account in an incoherent fashion, i.e. ignoring the third term in equation 3.21. Ignoring the phase difference is judged to be a reasonable approach since during a flyover the interference pattern is constantly changing, i.e. the reinforcement and cancellation alternate. Furthermore, the grid size typical for such calculations does not allow to accurately capture the interference pattern and would therefore lead to an inadequate representation of this effect.

NPD tables, and therefore the default Doc.29 algorithm, includes atmospheric absorption for a standard condition.⁽⁹⁶⁾ For varying atmospheric conditions a modification of the absorption effect can be used. This correction, based on a standardized method⁽⁹⁷⁾, uses the humidity and temperature on the ground to calculate the actual absorption rates. Such an assumption leads to applying uniform absorption conditions over the classical straight ray path. The ray tracing uses the same standardized method but calculates the local, varying, atmospheric absorption conditions per layer of the atmosphere. As a result, a non-uniform atmospheric absorption is accumulated over a curved path and taken into account. To demonstrate typical differences between the default and the augmented ray trace solution, a single-event result is included in figure 4.3. In this particular case, the aircraft is flying in the middle of the grid on a small segment heading towards the East (North direction refers to the top of the figure, thus East to the right side of the figure).

As shown in figure 4.3, the default solution differs significantly from the Doc.29 solution based on ray tracing. A striking asymmetry between the South-West and North-East of the grid is present. To the North-East of the aircraft, the sound level increases at a specific distance due to the fact that sound rays are curved downwards.

4.3 Multi-event calculation setup

A fictitious airport is modeled to analyze the multi-event case. The airport is assumed to be equipped with one runway in North-South direction and one in East-West direction. A standardized approach and departure route is defined on each runway. A route is selected depending on the wind direction on the ground since aircraft are bound to take-off and approach with headwind. There is only one runway, for a considered wind direction, that accommodates all approaching and departing traffic. For example runway 36 (heading 360 / heading North) is selected for departures and approaches if the wind is coming from the North. The actual wind direction stems from the atmospheric data and is categorized to come from either the North, East, South or West. A runway is then selected for the actual wind condition.

To model dispersion around a main route, as is common practice in noise modeling, sub tracks are defined to the left and right of the main route. The majority of aircraft (60%) is flown over the nominal route whereas the two sub-tracks each accommodate a traffic load of 20%. Figure 4.4 shows the departure, approach and sub-trajectories.

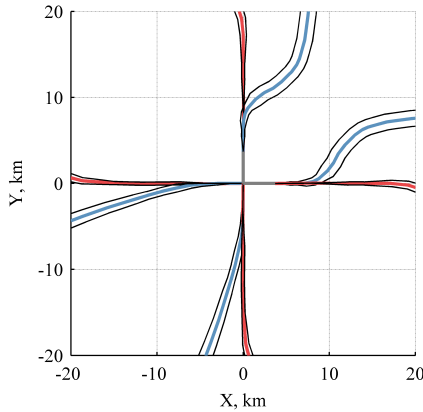


Figure 4.4: *Ground tracks from the two runways in all cardinal directions. The nominal departure track (blue) and nominal arrival track (red) are supported by the sub-tracks (black).*

For ease of comparison, a short to medium range (single-aisle) aircraft is used exclusively in this study together with an associated NPD table for the noise levels. The corresponding normalized A-weighted reference spectrum is shown in figure 4.5.

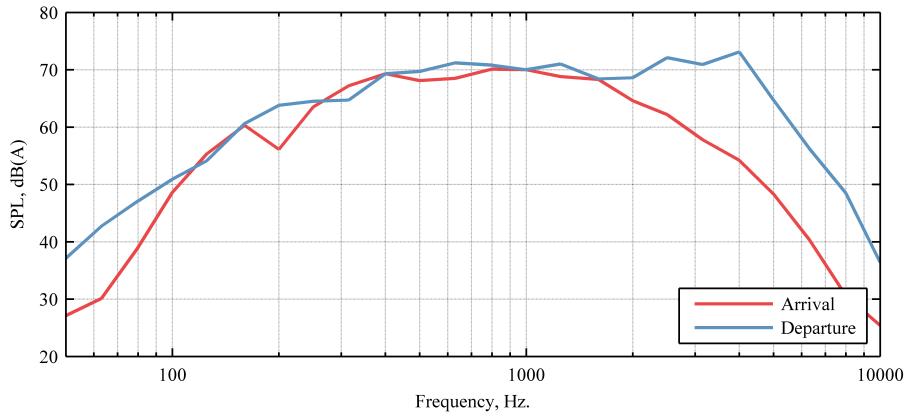


Figure 4.5: The normalized reference spectra of an aircraft equipped with CFM56-7B engines as used by Doc.29.

Due to the difference in thrust level between approach and departure procedures, the spectra in figure 4.5 are different. Please note that at 2500 Hz and 4000 Hz there are small peaks in the departure spectrum, these are believed to be modeled tones (see figure 2.9). Since atmospheric absorption is frequency dependent, the atmospheric absorption will differently affect both spectra.

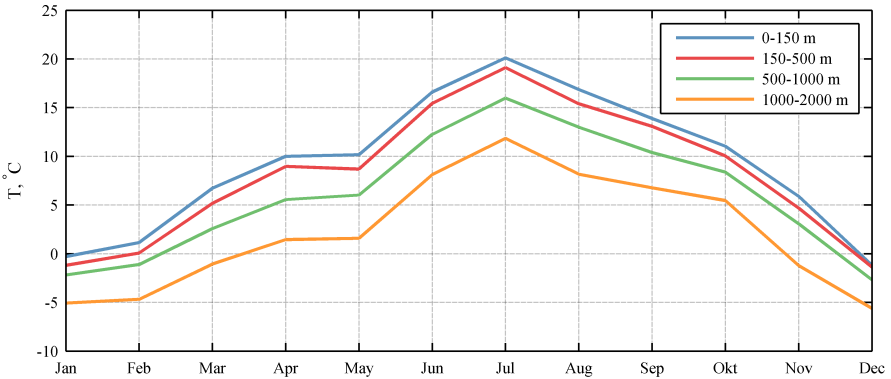
A common limitation for this type of research is the availability of weather data at different altitudes for an entire year. Data is taken from a balloon sounding station in the Netherlands where twice a day, at noon and midnight, a measurement of the atmosphere is executed. The results of a balloon sounding include temperature, humidity, wind direction and wind speed for a variety of altitudes and can be accessed through the internet.* The current simulation uses data for 2010 which amounts to a total of 730 balloon sounding files. Further analysis showed that 6 out of the 730 files contained invalid atmospheric data, i.e. empty wind, temperature, or humidity entries, and were therefore excluded. Figure 4.6 and 4.7, show the mean results of the used atmospheric conditions.

Due to the availability of two sounding files per day it is possible to simulate the atmospheric impact on two time instances. However, it is not possible to calculate individual aircraft departing or approaching during the day. To circumvent this, each sounding file is used for 200 effective flights evenly distributed over the approaches and departures. The number of effective flights (N_e) is defined according to,

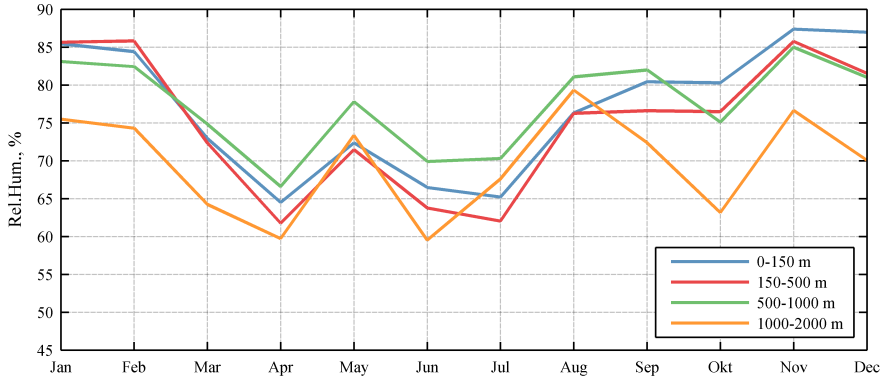
$$N_e = \Gamma \cdot N \sum_{i=1}^3 T_i, \quad (4.1)$$

where, Γ is the day ($\Gamma = 1$), evening ($\Gamma = 5$) or night ($\Gamma = 10$) time multiplier

*<http://weather.uwyo.edu/upperair/sounding.html>, visited 24-07-2012



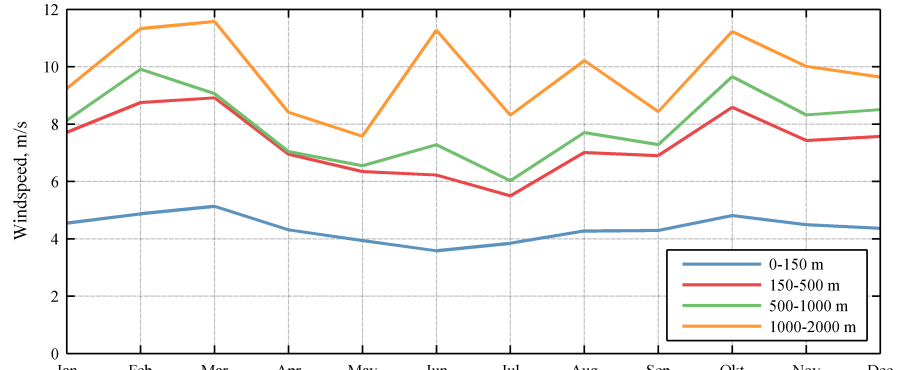
(a) Temperature



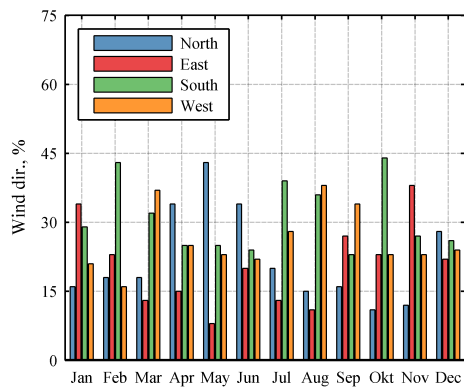
(b) Relative Humidity

Figure 4.6: Atmospheric conditions related to temperature and relative humidity grouped by altitude.

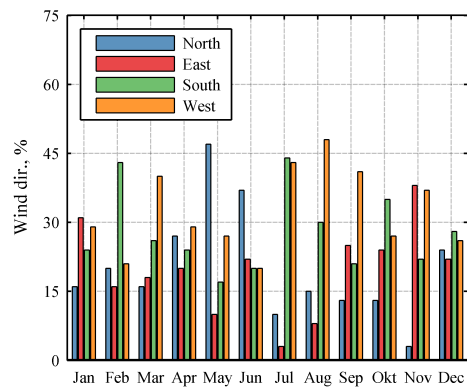
associated with the L_{DEN}, N is the amount of operations during that period and T_i is the traffic load ratio of the main and dispersed ground trajectories. For example, considering a traffic load of 0.6 for the main route and 0.2 for each sub route during a day event (Γ is 1), 200 operations are needed to model 200 effective flights. If the time period is changed to night, Γ becomes 10, which equates to 20 operations. By using 400 effective flights per day, the amount of traffic and L_{DEN} will resemble values typical for mid-size airports. While in reality the atmosphere will change from flight to flight, we are interested in the large variations in the atmosphere and the effects on the yearly contour. This effect is still captured by combining the sounding files with the effective flights.



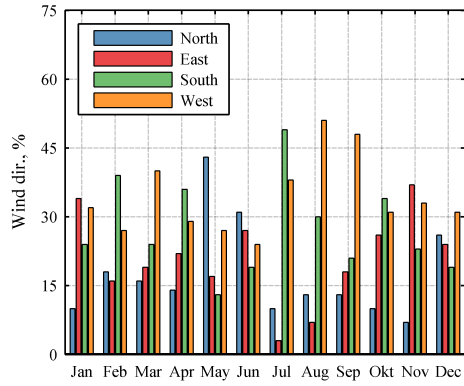
(a) Windspeed



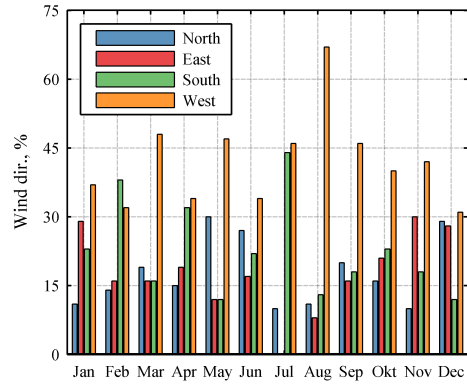
(b) Wind direction 0-150 m.



(c) Wind direction 150-500 m.



(d) Wind direction 500-1000 m.



(e) Wind direction 1000-2000 m.

Figure 4.7: Atmospheric conditions related to wind grouped by altitude.

4.4 Results

Results of the study are presented as noise contours for the 58 L_{DEN} and 48 L_{DEN} values, which are used (at least in the Netherlands) for noise policy purposes. These values are equivalent to L_{DN} values (relevant in the USA) because no specific evening flights are modeled. Since noise values are higher when the aircraft is near the ground, close to the airport, inner contours always represent the 58 L_{DEN} value whereas the outer contours are the 48 L_{DEN}. This holds for all the contour plots shown in this section. Three different options to calculate the EA for Doc.29 are used:

1. Default (standard LA correction)
2. Default + AA (standard LA correction, corrected for Atmospheric Absorption)
3. Ray tracing solution based EA

Option 1 is the basic setting of the noise model and includes the default, empirical LA. Option 2 is the same as option 1 but corrects for a non-standard atmosphere by correcting the difference in atmospheric absorption for uniform conditions (ground based values for humidity and temperature) through the atmosphere. Option 3 is the ray tracing based calculation of the EA. Figure 4.8 shows the resulting 58 and 48 L_{DEN} contour plots for 2010 using the three modeling options.

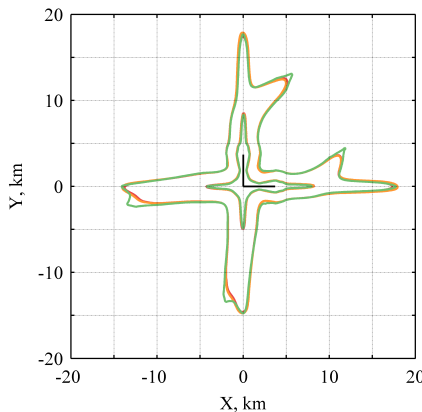
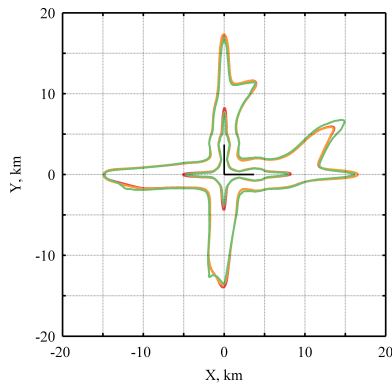


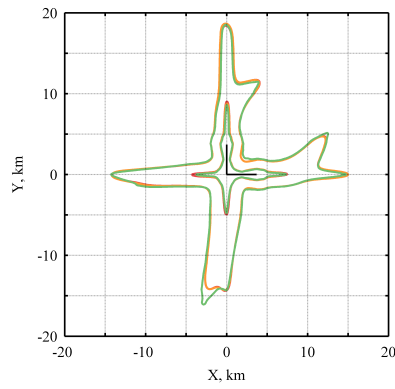
Figure 4.8: The L_{DEN} contours for 2010 using the standard (red), corrected for absorption (amber) and ray tracing (green) method.

From figure 4.8 it becomes clear that the contours are only slightly different. At first sight, it seems that only the 48 L_{DEN} (outer) contour shows noticeable differences between the modeling options. To compare the contours to each other more precisely, a comparison can be made based on the area enclosed by such a contour. This area is calculated and the results are listed in table 4.1.

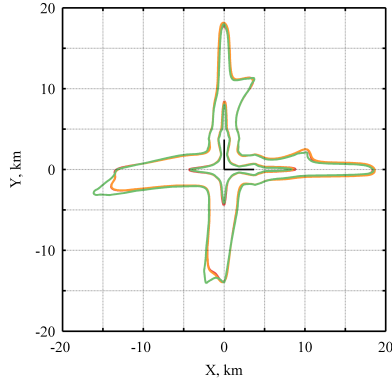
Monthly contour results for the year 2010 are shown in figures 4.9 and 4.10. These contours change from month to month due to the different wind directions on the



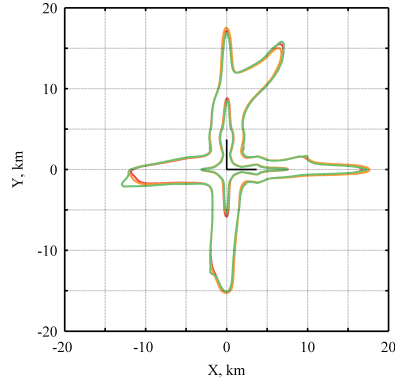
(a) January



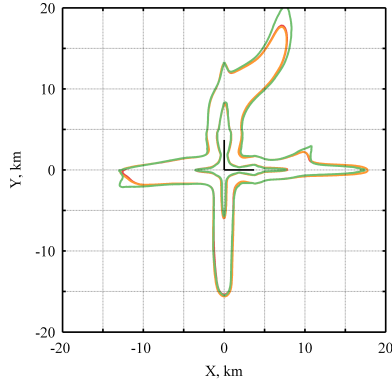
(b) February



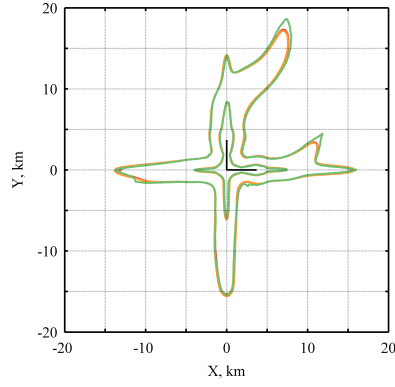
(c) March



(d) April



(e) May



(f) June

Figure 4.9: Contours for 58 & 48 L_{DEN} using standard Doc.29 (red), corrected for absorption (amber) and ray tracing (green).

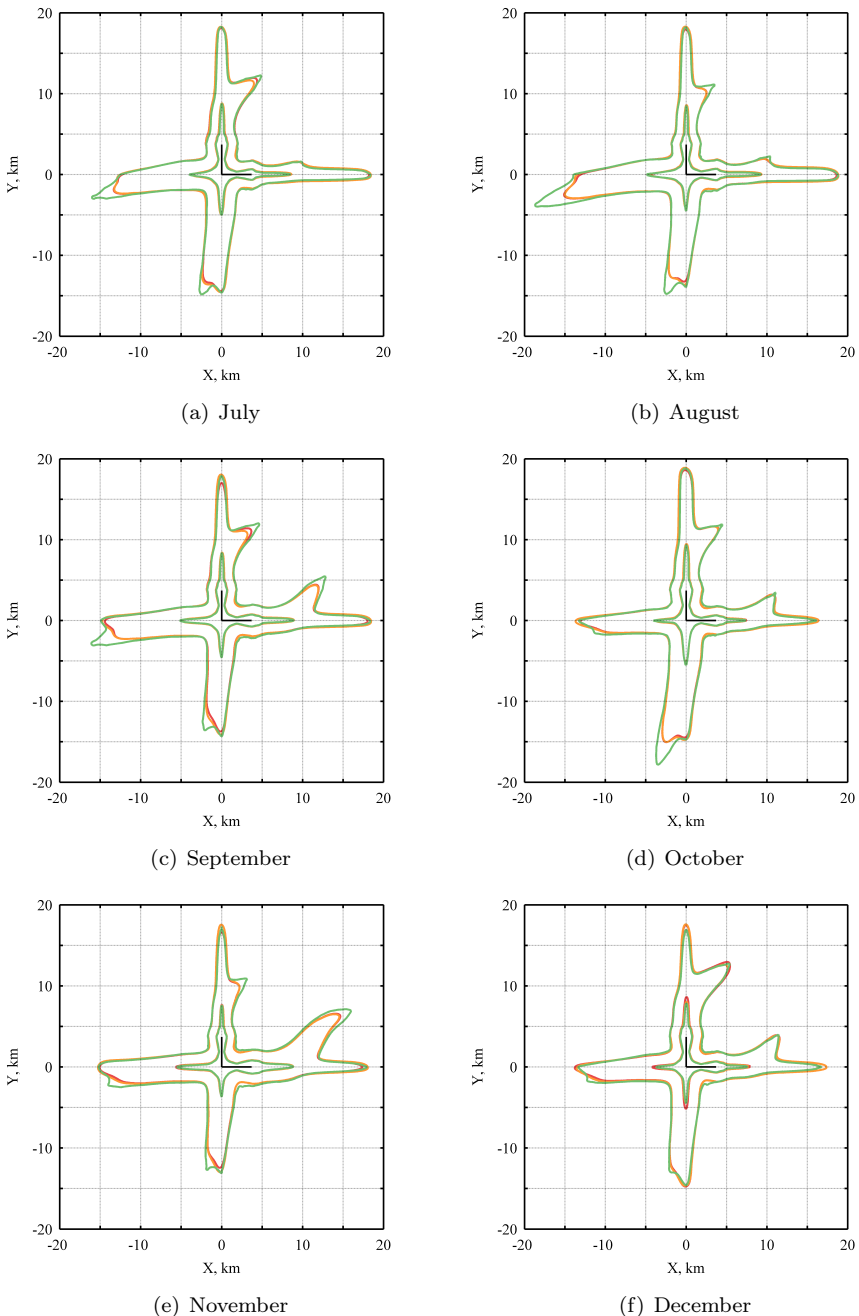


Figure 4.10: Contours for 58 & 48 L_{DEN} using standard Doc.29 (red), corrected for absorption (amber) and ray tracing (green).

Table 4.1: *The area of the 58 and 48 L_{DEN} contours for 2010.*

Doc.29 Method	58 L _{DEN} area, km ²	48 L _{DEN} area, km ²
Default	21.1	166.9
Default + AA	20.6	171.7
Ray tracing	18.1	175.0

ground. Depending on the wind direction, a specific arrival or departure tracks and runways is selected. For instance, from January until March there are not many occasions that the wind is coming from the North (see figure 4.7). However, from April until June a North wind is often present. As a result, the departures to the North are flown more often and the contour grows in that particular area. This causes the contours to change shape from month to month due to the different wind directions on the ground.

By calculating the enclosed area of the contours it is possible to get an impression of how the overall contours change. Figure 4.11 shows the contour area for both the 58 and 48 L_{DEN} on a monthly basis.

Based on these results, four observations are made that are further elaborated:

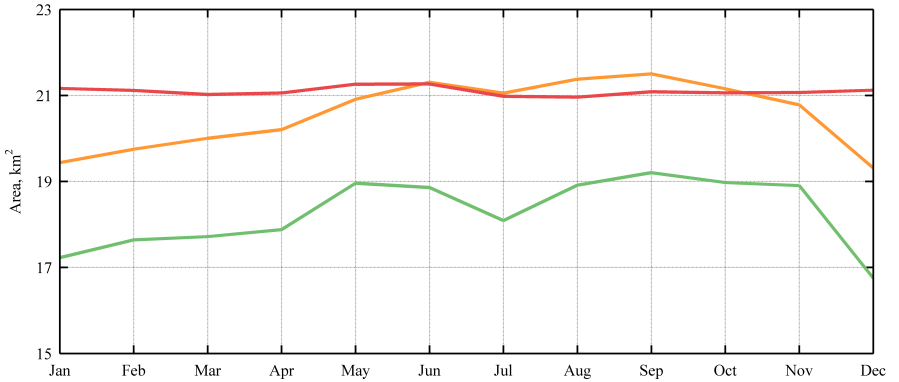
1. The large asymmetric differences found for single-event (figure 4.3) results are not present in the yearly contours.
2. The contour area of the 58 L_{DEN} predicted by ray tracing is always smaller than the area calculated using the default and the corrected default method.
3. A similar variation in contour area is visible in the ray tracing result and the corrected default method, see figure 4.11, especially for the 58 L_{DEN} contour.
4. Peaks occur in the 48 L_{DEN} contour area line, predicted by ray tracing, in the months May, September and November.

4.5 Discussion

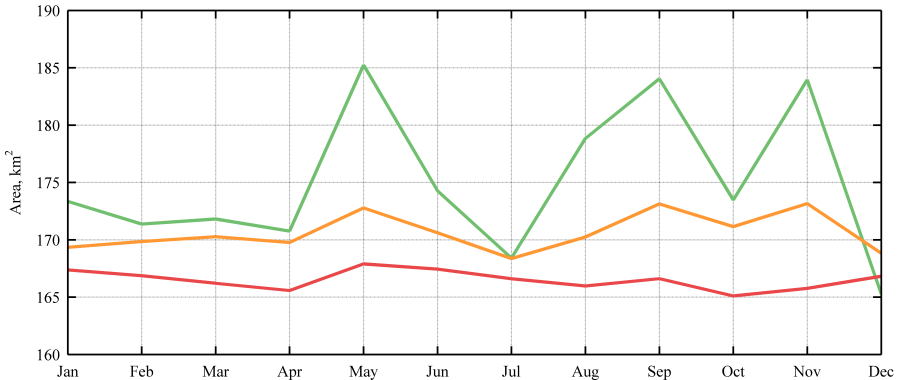
The observations made in the results section are treated next. Please note that observation 1 is related, for a large part, to refraction of sound. Observation 2 is judged to be caused by the ground reflection model whereas observations 3 and 4 are hypothesized to be related to atmospheric absorption.

4.5.1 Wind effects on contour

The difference between figures 4.3 and 4.8 is clearly noticeable. The single-event results are influenced significantly compared to the multi-event calculation. For the considered atmospheric input of the multi-event calculation, there is no clear prevailing wind although the South-West direction seems to be the most likely candidate.



(a) 58 L_{DEN} contour area



(b) 48 L_{DEN} contour area

Figure 4.11: The enclosed area of the contours from figure 4.9 and 4.10 using the standard Doc.29 method (red), corrected for absorption (amber) and ray tracing (green).

Since the multi-event results are based on multiple single-events, the associated effects visible in figure 4.3 are inherently included in the calculation. The yearly contours do not show striking differences between the modeling options. This confirms that refractive propagation effects average out when considering multi-event calculations for the used atmospheric data.

Only when zoomed in on a monthly contour small differences, which can be linked to refraction, become noticeable. Figure 4.12 shows an enlarged result for June, the original size picture is figure 4.9(f). If the 48 L_{DEN} contour in figure 4.12 is examined in the North direction, at a Y-distance of 4 kilometers, it is seen that the green ray tracing result shifts slightly to the East. A similar observation is made, although the

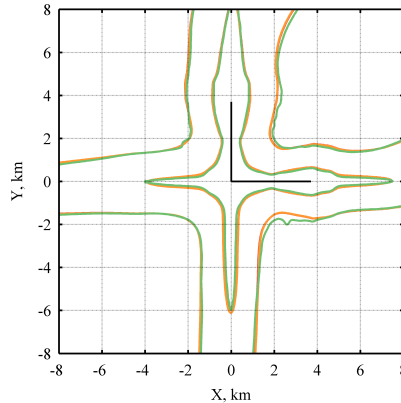


Figure 4.12: Enlarged contour for the month June using standard Doc.29 (red), corrected for absorption (amber) and ray tracing (green).

effect is less prominent, on the East part of the entire contour. At distances further away from the runways the absorption effects, which are omni-directional unlike wind, start to dominate. Consequently, these observations are only made relatively close to the runway. As long as a contour translates, the contour area does not change and therefore cannot explain the differences encountered in figure 4.11. The translation effect on the 48 L_{DEN} contour does not (prominently) occur in an enlarged example of the yearly contour which is, for that reason, not included here.

Another wind effect is the irregular North-East and South-East corner of the green 48 L_{DEN} contour lines near the airport predicted by ray tracing. Differences on the 48 L_{DEN} contour due to the wind thus only occur near the runway and the most noticeable increase in contour area is in between the two runways. It is also noted that these deviations occur around an angle of 45 degree from a particular runway. This corresponds to maximum cross-wind direction. If the cross-wind angle would be more than 45 degree, the arrival or departure is executed on a different runway. The wind effect is thus emphasized at the maximum cross-wind direction. These positions are close by the runway and thus influenced when the aircraft is flying relatively low. This is a favorable condition for refractive propagation effects to occur. On the overall yearly 48 L_{DEN} contour this effect is still noticeable, albeit small, as the contour area is increased by approximately 1 km².

4.5.2 Smaller 58 L_{DEN} contour due to ground reflection

Considering figure 4.12, it is observed that the green 58 L_{DEN} contour, calculated with ray tracing, shows a small constant offset everywhere relative to the amber contour. This constant offset, when integrated into an enclosed contour area, becomes the constant difference between the amber and green line in figure 4.11.

Due to the fact that the considered propagation distance for the 58 L_{DEN} contour is small, refractive effects are ruled out to cause the difference. The difference between the contours must therefore be caused by the varying atmospheric absorption or the ground model. Whereas the atmospheric absorption will vary for each sounding file, the ground attenuation (as currently modeled) is not influenced by the atmospheric variation. The additional ground attenuation is zero directly underneath the flight path to represent the measurement conditions for NPD tables, as mentioned in section 4.2. This does not exclude different ground attenuation results at positions not directly underneath the aircraft. As such, it is hypothesized that the difference in contour area between ray tracing and the (absorption corrected) default, for the 58 L_{DEN} contour, comprises a constant and variable component. The constant component is attributed to the ground model whereas the (smaller) variable component is due to the varying absorption.

For the 58 L_{DEN} contour, the relative distance between a route and the contour line is relatively small. As a result, the effect of variable atmospheric absorption is small as well. This is reflected in a contour area variation of the absorption corrected default option of roughly 2 km², visible in figure 4.11(a) as the amber line. This variation is similar to the variation in contour area as calculated with ray tracing, i.e. green line of figure 4.11(a). The remaining constant difference of roughly 2 km² is attributed to the additional ground attenuation at sideline angles.

The yearly contour shows the accumulated results of the individual months. As a result, the yearly 58 L_{DEN} contour becomes smaller when including atmospheric absorption to the default method and even smaller when selecting the ray tracing option due to the difference in ground attenuation.

4.5.3 Seasonal trends in 58 L_{DEN} contour

The 58 L_{DEN} contour areas based on the corrected default and ray tracing methods feature similar trends. This is noticed in figure 4.11 where the resulting curves are nearly parallel. Since both options take varying atmospheric absorption into account, this implies that absorption is the main cause of this behavior.

The small yearly contour area as predicted by ray tracing, relative to the default 58 L_{DEN} contour (shown in figure 4.11), is also noticeable in the monthly contour results (figure 4.9 and 4.10) except in the summer period ranging from May until September. The differences between the three modeling options is the smallest for this period as the absorption rates are close to the standard conditions used by the default EA method. To that end, the difference due to the atmospheric mean conditions on the ground and at 1000 meters altitude was calculated. This difference in absorption is shown for two different months in figure 4.13.

Figure 4.13 shows a few remarkable results. The bumps, visible in the departure results (circles) near the origin, are caused by the spectral shape of the departure which contains a modeled tone at 2500 Hz and 4000 Hz. More important is that the variation of humidity and temperature over altitude shows different trends for

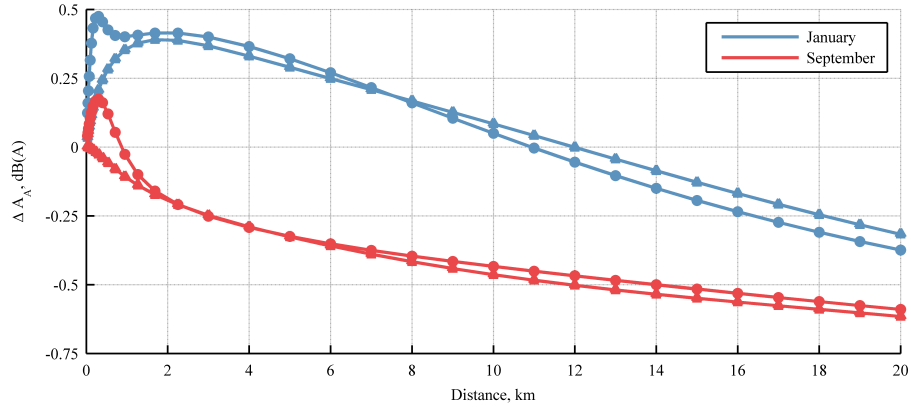


Figure 4.13: Difference in absorption (standard-actual). The circles depict departure conditions whereas triangles reflect arrival.

different months. Up to a distance of 12 kilometers, the results of January show additional attenuation whereas at larger distances the attenuation is decreased. In September, especially in the first kilometer, differences are smaller and, more or less, cancel out as the departure and arrival show opposite signs in absorption.

Based on the sensitivities shown in figure 4.13, it becomes evident that atmospheric absorption plays a role in the observed contour area variation throughout the year. The differences become larger with increasing distance from the source and may exhibit opposite behavior in different months.

4.5.4 Peaks in the 48 L_{DEN} contour area

A noteworthy effect, embedded in figure 4.11 is the occurrence of peaks in the 48 L_{DEN} contour area, as predicted using ray tracing, in the months May, September and November relative to the other months. Upon close inspection of the atmospheric data, specifically the relative humidity in figure 4.6(b), a more or less similar pattern is found. Considering the mean relative humidity encountered in the atmosphere from 500-1000 meter, peaks occur at exactly the same months. The uppermost layer of atmosphere considered here, 1000-2000 meter, shows a similar pattern except for the month September where a peak occurs in August. On the other hand, August shows the largest contour area right behind the mentioned three months.

Although the contour area's for the 48 L_{DEN} contour are rather similar considering the yearly contour, the location of a contour plays a role as well. Especially when population densities are coupled to the contour values to calculate the amount of disturbed people. In figure 4.8 it is noted that the ray tracing contour lines sometimes predict a local increment in contour size compared to the default lines whereas the corrected default show a slight decrease. Using the default correction thus sometimes

gives an erroneous indication where a contour can grow or shrink due to different atmospheric absorption.

In general, the deviations between the default and the ray tracing method are, for the 48 L_{DEN} contour, largest directly underneath the departure routes. There are two reasons why these deviations are more prominent for departures than for arrivals: the altitude and the source spectrum. During take-off, the aircraft flies a trajectory that quickly gains altitude whereas in arrival the aircraft descends gradually from an already relatively low altitude. A difference in altitude causes a longer acoustic ray path through layers of atmosphere described by varying humidity and temperature properties. In the case of ray tracing, these effects are aggregated along the path and therefore taken into account. Given the longer propagation path in a departure, the associated differences in absorption from figure 4.13 are accentuated compared to an arrival. This is further magnified by the difference in the source spectrum associated with the difference in thrust level used throughout the departure or arrival. This is due to the fact that absorption differences tend to increase with higher frequencies, as commonly present in the departure spectrum. The combination of higher altitude and source spectrum leads to the fact that the contours, calculated by the different models, vary most underneath the departure route.

4.6 Conclusions

The impact of wind on results predicted for a single aircraft operation can be large. These effects cannot be predicted by empirical models. The empirical model, based on measurements, is averaged out over long time span and thus reflects a solution for a similar period. The strong asymmetric results, as found by a prevailing wind condition in a single event case, are not found in multi event calculations.

The 58 L_{DEN} and 48 L_{DEN} contours are affected differently, compared to the default EA method, when ray tracing is applied to the varying atmospheric conditions. The 58 L_{DEN} contour area decreases (-3 km²) whereas the 48 L_{DEN} contour area increases (18 km²). This observation is made while comparing the default to both the corrected default and ray tracing options. Wind effects translate the contour location slightly and cause small irregular contour lines in the corners of the 48 L_{DEN} contour. The added area to the yearly contour due to this effect is in the order of 1 km². This effect only occurs for the 48 L_{DEN} contour as refraction effects are more prominent at larger distances. No refraction effects were distinguished for the 58 L_{DEN} contour. As such, the decrease in 58 L_{DEN} contour area is believed to be caused by the ground attenuation and the varying atmospheric absorption. The difference due to the ground attenuation is constant throughout the year whereas the atmospheric absorption may vary. Both components are, in this case, of approximately equal size (2 km²).

The yearly contour indicates that the major differences can be expected underneath the departure route for the 48 L_{DEN} contour. It is argued that this is caused by the combination of the departure source spectrum and the difference in absorption encountered on the ray path traveling through the varying atmosphere.

The default empirical model is, compared to the ray tracing solution, certainly applicable to calculate a yearly average since the difference in contour area is small. The absolute difference in contour area can be improved by including the default correction for atmospheric absorption as calculated on the ground. Although this must be treated carefully as contours may sometimes grow at a specific location whereas the corrected default predicts a shrinking contour. Differences due to absorption logically increase when the aircraft is flying at relative high altitudes when sound waves travel through, possibly, varying absorption layers due to atmospheric differences. Wind effects can be distinguished from a yearly contour but are or of minor importance compared to the varying absorption.

The stated conclusions only hold for the employed atmosphere, representative for the Netherlands. Other locations around the globe can have (other) prevailing winds, humidity and/or temperature conditions which may influence a contour calculation.

Chapter 5

Signal processing for aircraft noise synthesis

In this chapter, digital signal processing steps are employed to construct the waveform at a receiver from aircraft noise predictions. It is common, within the aircraft noise synthesis community, to separate the source noise and propagation processing.^(98;99) Such a separation allows a modular setup of the software and necessitates only updates at the source synthesis algorithms if a new flyover or design is considered.

The same methodology is adopted for the developed software and/or algorithms in this dissertation. The first paragraph of this chapter, section 5.1, describes the generation, or synthesis, of noise of an aircraft as predicted by the empirical source noise models. Noise synthesis, sometimes referred to as auralization, is not limited to aircraft but can also be used for other sources, e.g. cars and windturbines.^(100;101)

Since the interest is in an audible impression at the receiver location, atmospheric propagation needs to be applied to the source noise signal. To that end, the source noise signal is modified by signal processing steps. These steps apply the propagation effects (chapter 3) and the Doppler shift (paragraph 2.4). Hence, the second section, i.e. 5.2, describes the necessary signal processing steps for propagation.

The final section (section 5.3) concludes this chapter by combining a source noise synthesis result with the propagation signal processing. The interested reader is referred to signal processing literature⁽¹⁰²⁻¹⁰⁵⁾, on which this chapter is based, for a more concise background of the signal processing involved in this chapter.

5.1 Source noise synthesis

Aircraft noise is comprised of both broadband and tonal noise sources and is commonly predicted in the frequency domain. A prediction results in a finite amount

of tones, which can be synthesized using 'additive synthesis' (as will be explained in paragraph 5.1.1). Given the large bandwidth of sounds that the human ear can perceive, broadband noise synthesis based on additive synthesis is not a realistic option. Different synthesis procedures are therefore used for broadband or tonal sound.

5.1.1 Synthesis of tonal noise

The aircraft source noise prediction results in multiple discrete tones, see section 2.6.2. The fan rotor-stator tones are predicted to occur at an integer multiple of the Blade Passage Frequency (BPF). The tonal Buzz-Saw noise is predicted, by the Heidmann model, on a 1/3rd octave band spectrum whereas it is known to occur at discrete frequencies. Therefore, a translation is necessary from the 1/3rd octave band spectrum to the discrete frequencies at which the tones occur. These tones are harmonics of a fundamental frequency equal to RPM/60 (RPM refers to Revolutions Per Minute of the engine). By examining the number of discrete tones in the specific 1/3rd octave bands, the amplitude of the individual tones can be calculated if a distribution is assumed. For example, an even distribution of energy is assumed for the individual tones that fall in a 1/3rd octave band. Each tone is synthesized by its instantaneous phase, which is integrated to obtain the entire tone history.⁽¹⁰⁶⁾ Accordingly, a single synthesized tone p_i is generated by,

$$p_i(\tau) = A \cos(\Theta(\tau) + \Theta_0) \quad (5.1)$$

$$\Theta(\tau) = 2\pi \int_{-\infty}^{\tau} f(\tau') d\tau', \quad (5.2)$$

where A is the tone amplitude, Θ_0 is an initial (sometimes random) phase offset for each tone whereas $\Theta(\tau)$ is the phase constructed from instantaneous frequency $f(\tau)$. Note that the used frequency is at emission time τ , i.e. without Doppler shift see section 2.4. The instantaneous frequency of engine tones depends on the engine RPM (equation 2.64) and may vary in time. The total tonal acoustic pressure (p_T), combining all the predicted frequency components, is then obtained after summation. Such a technique is therefore known as additive synthesis,

$$p_T(\tau) = \sum_{i=1}^N p_i(\tau), \quad (5.3)$$

where index i is used to denote the different tones and p_T is the overall tonal acoustic signal. Research showed that temporal variations in frequency and amplitude are present in the tones at the source.⁽¹⁰⁶⁾ The perceived importance of these variations is, in general, diminished due to masking by broadband sound.

5.1.2 Synthesis of broadband noise

It is possible to reconstruct broadband noise by additive synthesis. However, such an approach is impractical since the audible bandwidth of the human ear, i.e. from 20 Hz to 10 kHz*, implies that thousands of individual frequencies should be synthesized and added. Therefore, two different techniques, both based on white noise, were explored.

The first technique applies a time varying 1/3rd octave band equalizer to a white noise signal. This method filters the white noise signal in 1/3rd octave bands and then sets the filtered output level to match the predicted source noise level. By summing the contributions of the individual filters, the total broadband source noise is obtained. Hence, by continuously adapting the results of the individual filter bands to match the predicted spectral shape at the source at a specific directivity angle, the aircraft source noise is created. There are limitations to this method. For instance, the signal will contain discrete transitions between frequency bands or time intervals. Furthermore, there is quite a bit of redundant computation involved since the time domain signal is first created, filtered, modified and then finally added together whereas these steps could be combined.

The second, more elegant, approach for broadband noise synthesis is to apply the source noise prediction directly in the frequency domain to white noise.^(98;102) This process is illustrated in figure 5.1 and is, from hereon, the method that is employed to create broadband noise in the time domain from a frequency domain prediction.

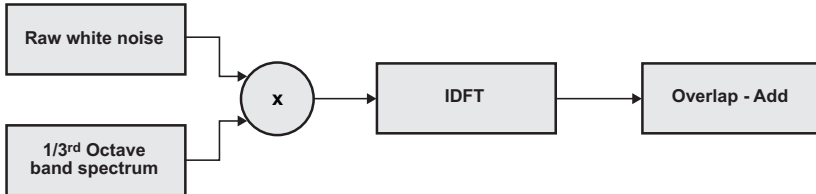


Figure 5.1: The applied procedure to synthesize a broadband signal.

The broadband noise generation starts by creating white noise, in the frequency domain, as a vector of random (normally distributed) real and imaginary parts. Depending on the size of the Inverse Discrete Fourier Transform (IDFT, see appendix B), the amplitude results from the 1/3rd octave band spectrum are subdivided into the narrow band bins of the IDFT. Consequently, the predicted 1/3rd octave band spectrum is included as a narrow band spectrum. For auralization purposes in this research, the used IDFT size is 8192. Such a relatively large IDFT size is necessary to ensure sufficient resolution at the low frequency bins. If shorter IDFT lengths would be used, aircraft jet mixing noise, containing low frequency sound, is inadequately

* Other human hearing definitions range from 20 Hz to 20 kHz, but this doesn't change the current argument.

represented in the synthesized sound. A multiplication is used (convolution in the frequency domain) to apply the narrow band spectrum to white noise. The results are transformed to the time domain using the IDFT resulting in a block of processed samples. If each block would be integrated in the broadband audiostream* after each other, a similar signal compared to the first approach would be obtained. As such, the discrete spectral transitions, i.e. possibly audible artifacts, are still present if the spectrum changes.

During a flyover, the source noise spectrum changes due to the directivity of the source, varying aircraft orientation and/or a varying engine state. To circumvent audible artifacts, especially prominent if the source spectrum changes rapidly (aircraft in overhead position), the blocks are combined using an Overlap-Add (OLA) technique. An OLA technique allows to shape filtered a white noise signal with varying spectral content using smooth transitions in time. The OLA technique is illustrated in figure 5.2.

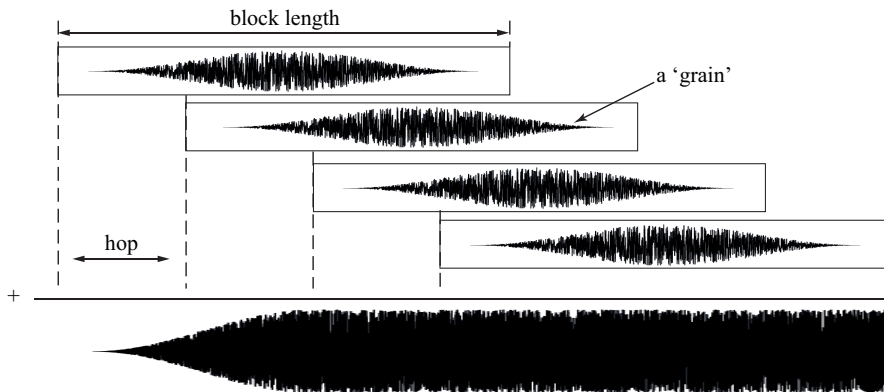


Figure 5.2: The OLA procedure as used to create a the broadband signal.

In this figure, the source noise signal is obtained as processed blocks after the IDFT of figure 5.1 and multiplied by a (Hann) window. The resulting element is called a 'grain' and each grain may contain a different spectral content. Note that the required blocks are offset by a small length ('hop') instead of the entire block length. The hop size is typically much smaller than the block size, i.e. in this dissertation we often use a hop size that is roughly 10 times smaller than the block size. The grains are overlapping in time, controlled by the hop size, and added together. This happens multiple times during the length of a block. Due to the consistent fading in and out of the individual grains, containing their own spectral content, the output of the entire signal reflects the appropriate spectral change. The sound level is now a function of the amount of added grains per block since for every doubling of the amount of grains per block, 3 dB is added to the output signal. The increased sound level is corrected by multiplying the output signal with the inverse square root of the number of grains per block.

*An audiostream refers to the signal after processing that is ready to be either played by the computer audio device, mixed with other audiostreams or to be written in an audio file such as .wav.

The predicted broadband source noise spectra, from the models described in section 2.6, contain no temporal variations. These models are used to provide the SPL on a ‘virtual’ 1 meter radius sphere and are fixed per directivity angle, engine setting and airframe configuration. Temporal information, such as amplitude fluctuations, is lost by constructing the 1/3rd octave band spectra as predicted by the empirical models. However, temporal variations make a perceivable impact in auralized jet noise.^(107;108) These temporal variations can be added in the broadband synthesis methods, this was not exercised in the current work.

5.2 Signal processing steps for propagation

The overall acoustic transmission loss through the atmosphere is accumulated from propagation calculations, as described in chapter 3. Three elementary Digital Signal Processing (DSP) steps (a gain, a delay line and a filter) are necessary to apply propagation characteristics to the source noise. The gain accommodates spherical spreading, the delay line allows inclusion of the absolute delay, the change of which over time simulates Doppler shift and the filter can include atmospheric absorption, a soft ground reflection and/or listener effects.

As indicated in figure 3.4, the reflection of sound of the ground results in an additional ray path that reaches the receiver. For a homogeneous atmosphere, with a single pair of ground reflected and direct ray, this results in two audio signals that need to be processed before they are summed. There is a preferred order in the processing steps since the Doppler shift (time delay) should be applied before absorption (filter) to ensure correct modeling. The correct order, in auralization lingo, is thus either TGF, TFG or GTF processing, where GTF stands for Gain-Time-Filter processing steps. An example of this procedure is illustrated in figure 5.3.

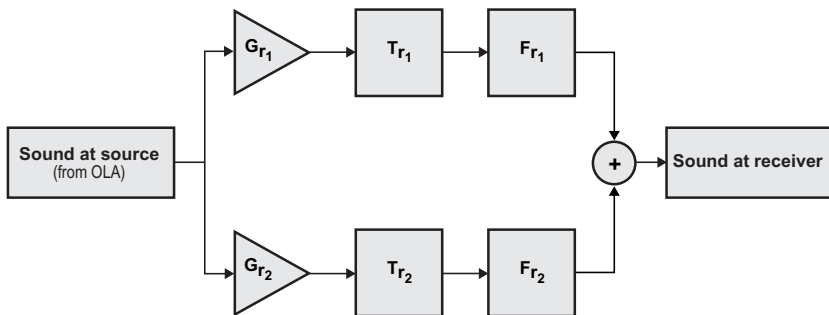


Figure 5.3: The signal processing applies a gain G , time delay T and filter F to the source noise signal for a direct path r_1 and ground reflected path r_2 .

Figure 5.3 starts with the entire source signal, i.e. for broadband this is after the processing steps illustrated by figures 5.1 and 5.2, that represents the total aircraft noise waveform. The signal is propagated in the time domain by signal processing elements for both paths, i.e. a direct path r_1 and ground reflected path r_2 . By applying a gain (G in figure 5.3) to include spreading loss, a time delay (T in figure 5.3) to model Doppler shift and an (FIR) filter (F in figure 5.3) to model frequency dependent losses, the sound is propagated to the receiver. After processing of the direct and ground reflected signal, a summation results in the signal at the receiver. As the travel time of the direct and ground reflected ray are different, ground interference is included upon addition. Further modifications of the interference, due to a phase change of the ground ray, can be accommodated in a ground reflection filter.

The spherical spreading loss, used in this section for demonstrative purposes, is independent of frequency and therefore implemented by a gain. It is equally possible to use equation 3.43 to include refractive effects, as is done in chapter 6. If diffraction into an acoustic shadow zone occurs, the diffractive loss becomes frequency dependent (equation 3.48). In that case, any additional spreading losses are implemented using a filter. Upon adding the ground reflected ray to the direct ray, the relative travel time delay emanates (partially) as the ground interference described by equation 3.21. There is also a contribution due to the (soft) ground constitution, i.e. phase shift angle ϕ in equation 3.21. This phase shift, together with the absorption, is implemented based on equation 3.16 by application of an FIR filter (F_{r_2} of figure 5.3).

To make the individual processing steps more tangible, the effects of the processing steps are demonstrated by application to a test signal. The test signal is comprised of tones, each of 110 dB at 1000 Hz and 2000 Hz, combined with a white noise signal with an OSPL of 120 dB. It is assumed that this source noise emanates from an aircraft flying over at 100 meters altitude at 100 m/s. Figure 5.4 shows the test signal; the lines at 1000 Hz and 2000Hz in figure 5.4(b) are the aforementioned tones.

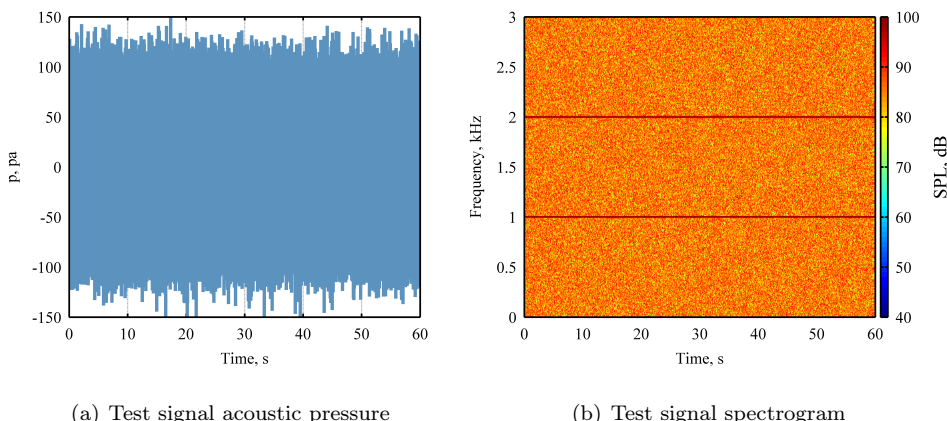


Figure 5.4: The test signal waveform and spectrogram at the source.

5.2.1 Gain

A gain is an element that multiplies the input signal by an amplification factor and effectively amplifies or attenuates the signal. This operation is independent of frequency, but the gain factor may vary in time. The notation in parenthesis $x(t)$ denotes a continuous time signal whereas the discrete time variant is denoted using brackets $x[n]$. If we consider an input signal $x[n]$, where $x[n]$ is the discrete equivalent of the continuous time signal $x(t)$, a gain $g[n]$ is applied to yield output signal $y[n]$,

$$y[n] = x[n]g[n]. \quad (5.4)$$

For demonstration purposes, the spherical spreading law (equation 2.22) is used to model spreading losses. Hence, the gain is solely a function of distance and is realized by,

$$G_{r_1}[n] = \frac{1}{r_1[n]}, \quad (5.5)$$

where $r_1[n]$ is the distance to the acoustic source for the direct ray. Figure 5.5 shows the result of applying equation 5.5 to the test signal.

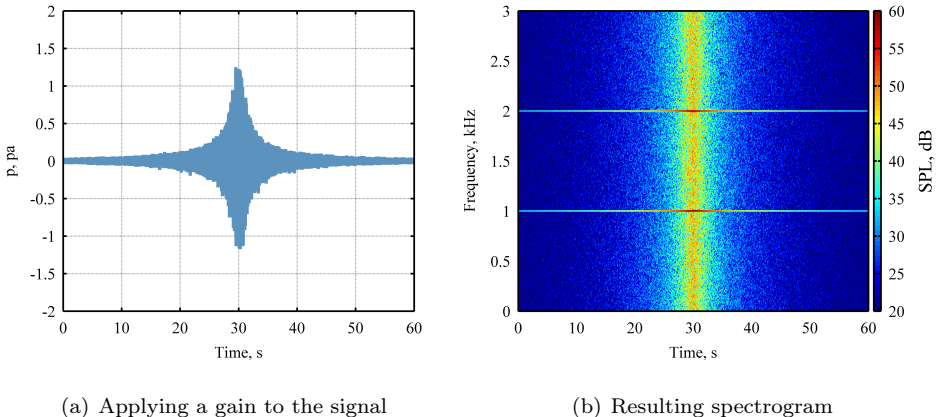


Figure 5.5: The resulting waveform and spectrogram after applying the gain from equation 5.5 to the test signal.

Figure 5.5 shows that the sound level is maximum if the aircraft is at the nearest position, in accordance with the spherical spreading law. The frequency content and temporal base of the source signal remain unaffected. The gain of both paths, i.e. $G_{r_1} = 1/r_1$ or $G_{r_2} = 1/r_2$, differ only slightly and can be safely set to equal values for the most common flyover situations when the listener is close to the ground.

5.2.2 Delay line

Per ray path there is a separate source signal and receiver signal, although the two source signals are usually assumed to be equal.* The difference between the source and receiver signal, besides amplitude modifications by spreading and absorption, is the travel time of the acoustic wave to reach the receiver. A practical example where this is important is in the case of an aircraft at cruise altitude. A listener can get the feeling that aircraft sound comes from a different direction than the actual aircraft position due to the long travel time. A Variable Delay Line (VDL) can be used to delay a signal, thereby incorporating the travel time from source to receiver. For moving sources, or listeners, this effectively incorporates the Doppler shift as demonstrated in section 2.4. The VDL operation is described as,

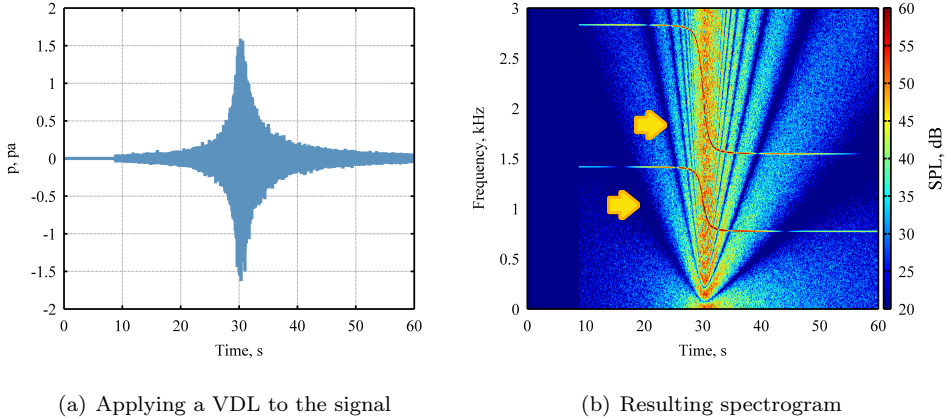
$$y[n] = x[n - m[n]], \quad (5.6)$$

where $m[n]$ is the time varying delay that is composed of an integer and fractional number of samples. An integer delay is realized by holding the audio signal for an integer amount of samples in a buffer before integration in the audiostream. Fractional delays occur due to the fact that the travel time between the source and receiver is not an integer amount of samples. For instance, consider an aircraft source audiostream and receiver audiostream both sampled at 44.1 kHz, i.e. an audio sample is stored at every $1/44.1 = 0.0227$ ms. If the propagation distance between source and receiver is 1 meter, the travel time, at a sound speed of 340 meters per second, equals $1/340 = 0.00294$ second or 2.94 ms. Consequently, the delay consists of $2.94/0.0227 = 129.7$ samples and thus contains an integer part (129) and a fractional part (0.7). Both parts are constantly varying during a flyover. Ignoring the fractional delay by using the nearest (integer) sample, leads to audible aliasing effects since parts of the signal are neglected.

Implementing a fractional delay is, in essence, an interpolation task. Linear interpolation is a first improvement with respect to using the nearest sample. However, if relatively high frequency content is present in the signal, with respect to the sampling frequency, aliasing may occur after linear interpolation. Aliasing effects manifest themselves as audible artifacts. This is especially a concern for relative high pitched tones originating from an aircraft fan. More sophisticated interpolation schemes, e.g. cubic or spline interpolation, result in reduced aliasing due to waveform gradients taken into account. The downside is an increased computational effort since more computational evaluations are required. Literature provides different options on how to implement and apply fractional delays in signal processing.⁽¹⁰⁹⁾ On the VCNS, the AuSim real-time signal processor⁽¹⁰⁾ has several options to choose from, including linear and spline interpolation. Throughout this research a spline interpolation is utilized in the VDL to implement the fractional part of the waveform.

For the ground reflected path the time delay is calculated as the path length divided

*Note that this is not strictly true. Although for sources that are far away (as is the case in a flyover) this assumption is valid since the source directivity angle is the same for both paths.



(a) Applying a VDL to the signal

(b) Resulting spectrogram

Figure 5.6: The resulting waveform and spectrogram after applying the VDL to the test signal modified by the gain. The arrows in the spectrogram indicate the cancellation dip of the ground interference pattern.

by sound speed, i.e. $T_{r_2} = r_2/c$, whereas for the direct ray this is $T_{r_1} = r_1/c$. Since $r_2 > r_1$ (see figure 3.4, paragraph 3.2) there is a time delay between the two rays that is taken into account. Due to the difference in travel time of the direct path and the ground reflected path, after VDL processing and summation of both signals, the ground reflection interference pattern is retained. Both the interference pattern and Doppler shift are illustrated in figure 5.6 for the test signal (after processing by the gain in the previous section).

The first 8.8 seconds of figure 5.6 show no sound due to the finite amount of time necessary for the waves to propagate from the initial position to the receiver. The abrupt transition from silence to audible sound at 8.8 seconds is thus an artifact due to the current setup of the simulation. If a longer part of the aircraft trajectory is simulated, the transition would be less abrupt. Note that the spectrogram clearly shows the Doppler shift in both tones, which coincide very closely (± 1 Hz) with the calculated theoretical results of equation 2.60.

The ground interference pattern is identified by the arrows in figure 5.6(b). Not only the broadband noise exhibits this effect, the tonal components are equally affected. The position of the cancellation and reinforcement is clearly changing during the flyover and characterizes, to a large extent, the perceived noise. Please also note that the interference pattern is not symmetrical around the direct overhead location, i.e. at around 30 s. This is caused by the change from the emission time frame to the receiver time frame, effectively by taking the travel time into account.

5.2.3 Filter

A (digital) system is defined by its impulse response that describes the relation between the output $y[n]$ and input $x[n]$ of that system,

$$y[n] = h[n] \otimes x[n], \quad (5.7)$$

where, $h[n]$ is the impulse response (in the time domain) that is convolved with the input signal. In the frequency domain, the transfer function shows the ability of a system to attenuate or amplify an incoming signal of a specific frequency.

A digital filter, that is applied in aircraft noise synthesis, should fulfill causality and stability conditions. A filter is causal if the output signal is zero, $y[n] = 0$, when the time variable is smaller than zero $n < 0$. The filter is stable if the output signal does not diverge $|y[n]| < \infty$ after application of a finite input signal $|x[n]| < \infty$. The stability criterion is (without proof),

$$\sum_{n=-\infty}^{\infty} |h[n]| < \infty. \quad (5.8)$$

In case of a truncated impulse response, the filter is called a Finite Impulse Response (FIR) filter. In that case the output depends exclusively on a finite amount of past input samples. The resulting signal, after filtering, is described by a difference equation⁽¹⁰²⁾ and follows as,

$$y[n] = \sum_{d=0}^{M-1} b_d x[n-d]. \quad (5.9)$$

The output signal $y[n]$ at time instant n is thus a combination of past input samples $x[n-d]$ multiplied by coefficients b_d . These coefficients are known as filter coefficients and are constant during the processing of a block of samples. The subscript d refers to the 1^{st} , 2^{nd} , ..., M^{th} filter coefficient. An FIR filter thus depends on filter coefficients and past input samples, i.e. it does not depend on past output samples as is the case of Infinite Impulse Response (IIR) filters. Hence, the FIR filter is inherently stable, which is a desirable feature for real-time signal processing applications since the filter coefficients can be interpolated without running into stability issues. The impulse response of an FIR-filter in the time domain ($h[n]$) subjected to a unit impulse response δ input signal* yields,

$$h[n] = \sum_{d=0}^{M-1} b_d \delta[n-d], \quad (5.10)$$

* δ Is the Kronecker delta, i.e. $\delta_n = 1$ if $n = 0$ and $\delta_n = 0$ if $n \neq 0$.

and can be applied by convolution (see also equation 5.7,

$$y[n] = \sum_{d=-\infty}^{\infty} x[d] h[n-d] = x[n] \otimes h[n], \quad (5.11)$$

thereby effectively applying the impulse response to the input signal x . The frequency response of the filter is obtained with help of the IDFT (see appendix B),

$$H[k] = \sum_{n=0}^{M-1} h[n] e^{-j2\pi nk/(M-1)}, \quad k = 0, 1, \dots, M-1. \quad (5.12)$$

Hence, if a transfer function is known in the frequency domain (such as absorption given by equation 3.12), an Inverse Discrete Fourier Transform (IDFT, see appendix B) is all that is required to calculate the FIR filter coefficients b_d . Furthermore, no phase distortion occurs as long as the impulse response of the FIR-filter is symmetric.⁽¹⁰⁴⁾

Including the absorption of a soft ground reflection is possible by transforming Q (see equation 3.16) into a filter, i.e. using the approach of Rizzi.⁽¹¹⁰⁾ Here, the FIR filter realization is demonstrated for an atmospheric absorption transfer function. The methodology described in section 3.1 is used to calculate the attenuation at 3 km distance for $RH = 80\%$, $T = 20^\circ C$ and $p = 101.325 \text{ kPa}$, see figure 3.2. Thus, $F_{r_1} = \text{IDFT}\{-\alpha r_1\}$ and $F_{r_2} = \text{IDFT}\{-\alpha r_2\}$, see figure 5.3. Note that no additional losses, such as implied by diffraction or a soft ground, are included. Figure 5.7 shows different FIR filter responses created by using FIR filters of different size for the atmospheric absorption.

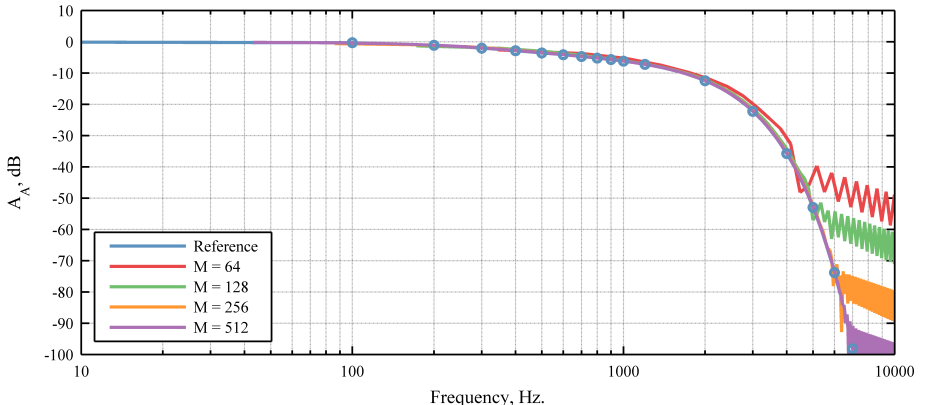
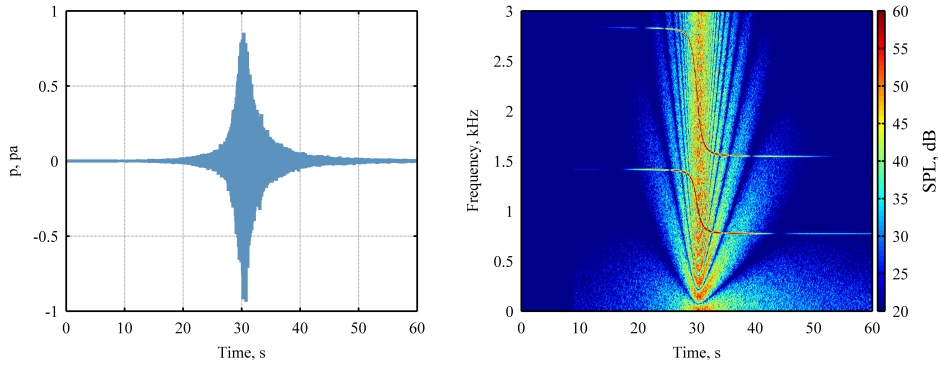


Figure 5.7: The FIR filter (F_{r_1}) realizations for different filter lengths. The reference shows $-\alpha r_1$ and M denotes the used amount of filter coefficients.

Since FIR filters are applied by convolution (in the time domain), shorter filters are preferred given the computational time. Longer filters can be implemented more efficiently in the frequency domain. Relative short filter implementations suffice for realizing atmospheric absorption as a transfer function.⁽⁹⁸⁾ By applying the varying absorption transfer function (FIR filter with 512 coefficients) to the test signal, which is already modified by the gain and time delay, the results of figure 5.8 are obtained.



(a) Applying a FIR filter to the signal

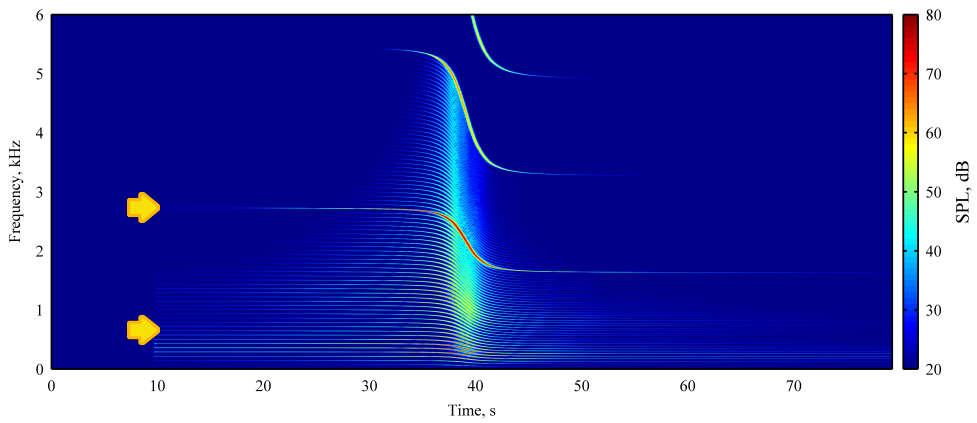
(b) FIR spectrogram

Figure 5.8: The resulting waveform and spectrogram after applying gain, delay line and filter to the test signal.

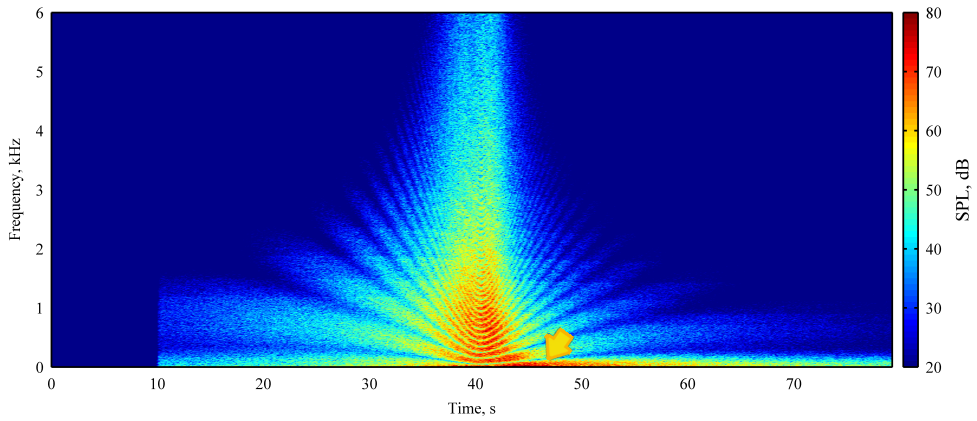
The spectrogram of figure 5.8 shows that the higher frequencies are more affected by absorption compared to the lower frequencies. This is, for instance, demonstrated by the fact that the lowest frequency tone is visible near 20 s whereas the highest frequency tone is first visible near 25 s.

5.3 Combining source synthesis and propagation

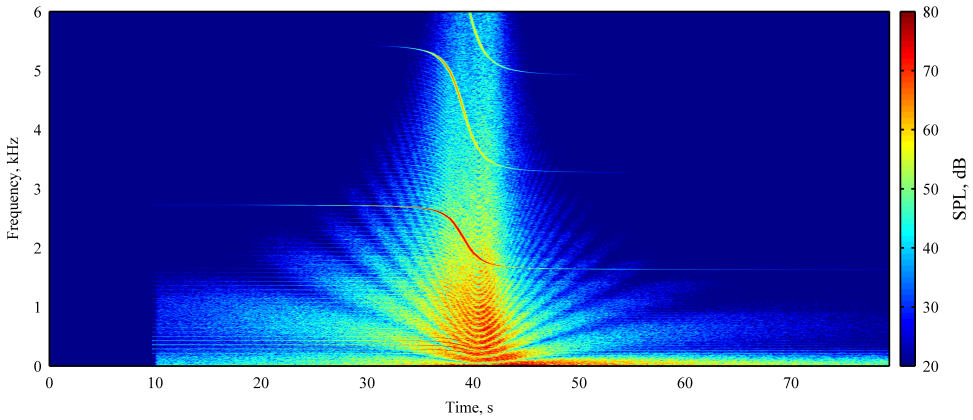
The previous sections covered source synthesis and propagation of aircraft noise whereas this paragraph combines the two to demonstrate an artificial flyover. In paragraph 2.7 the source noise of a Boeing 747-400 was predicted for take-off and approach. The same prediction is used here as input for aircraft noise synthesis. For both conditions, the aircraft is assumed to fly straight and level at an altitude of 150 m. The considered atmosphere is uniform as prescribed by the following parameters, $RH = 80\%$, $T = 20^\circ C$ and $p = 101.325 \text{ kPa}$. The ground surface is defined as a grass surface, i.e. $\sigma_e = 250 \text{ kPa/m}^2 \cdot \text{s}$ in equation 3.20. Figure 5.9 shows the take-off (see figure 2.14 for the source components) and figure 5.10 shows the flyover in approach conditions (see figure 2.15 for the source components). These audible end results are available as download from the internet, see appendix E or table E.1.



(a) Tonal components; the lower arrow shows Buzz-Saw tones, the top arrow the 1st BPF tone



(b) Broadband component; the arrow indicates jet noise



(c) Complete aircraft

Figure 5.9: Synthesized departure with source noise based on figure 2.14.

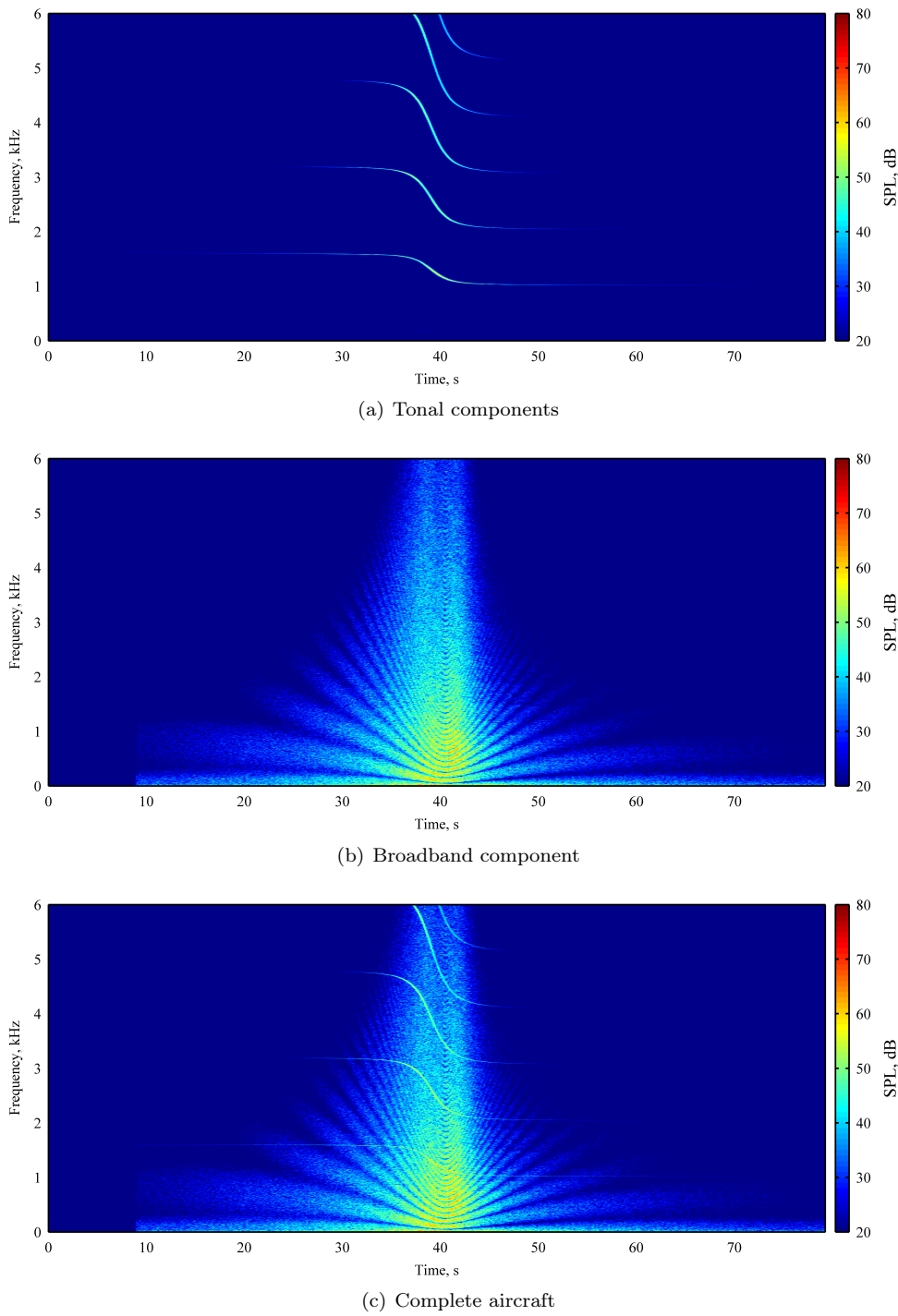


Figure 5.10: Synthesized approach with source noise based on figure 2.15.

In figure 5.9(a) the lower arrow indicates a typical Buzz-Saw tone whereas the top arrow indicates the 1st BPF tone. Due to the relative high power setting (100%N1), resulting in sonic Mach numbers on the fan-tips, Buzz-Saw noise is present. Furthermore, the BPF tone is relatively high pitched at 2000 Hz, i.e. before being Doppler shifted. The broadband result (figure 5.9(b)) shows that, when the aircraft has passed after 40 s, a clear shift in frequency content is experienced as low frequency jet noise starts to dominate. The arrow in figure 5.9(b) represents the jet noise contribution. Examination of the ground interference pattern in the broadband content shows that the interference is not as pronounced as is the case in figure 5.8(b). This is attributed to the fact that figure 5.8(b) is created using a perfect 'hard' acoustic reflection, whereas the current flyover is for a grass surface. Effectively, the current difference in ground reflection is the same difference as presented in figure 3.7 between an asphalt and grass surface.

The approach condition requires not as much thrust as the take-off and the source noise (spectrum) is severely different, i.e. see figure 2.15. For instance, due to the lower power setting the BPF tones are at a lower frequency and Buzz-Saw tones do not occur. The 1st BPF tone, before being Doppler shifted, is now near 1200 Hz, i.e. at 60% RPM instead of 2000 Hz in the departure. Due to the lower BPF, five BPF tones are present in the spectrograms frequency range whereas three tones were included for the departure. Furthermore, the jet noise contribution, that was clearly visible in the departure, is more or less absent in the approach.

Hence, by using signal processing techniques it is possible to generate an audible impression of an aircraft noise source prediction. As such, the current spectrograms reflect an acoustic signal that could be used in the VCNS to be presented to a listener.

One of the aspects not explicitly mentioned in this chapter are listener effects. Due to the propagation of acoustic waves around the body and head of a listener, the travel time and sound level as perceived by each ear is different. Such differences allow humans to locate where a noise signal is coming from. A Head Related Transfer Function (HRTF) models this 'binaural' sound effect, i.e. time, sound level and spectral differences between the left and right ear. An HRTF depends on the relative angle between the sound and ear and can be applied using the same convolution methodology as applied for FIR filters. An open-source database containing measured impulse responses for a symmetric acoustic test dummy can be found online.*

In a virtual reality environment, as created by the VCNS, the immersion of a test subject is based on both visual and audible cues. By tracking the listener head orientation with respect to the virtual sound source position, an HRTF is applied in real-time on the AuSim goldserver⁽¹⁰⁾. Consequently, the listener is able to locate the source not only by looking in the right direction, but can also listen to the direction from which the aircraft is coming and is thus immersed in the scenario.

*<http://sound.media.mit.edu/resources/KEMAR.html>, visited on 04-03-2014.

Chapter 6

Atmospheric propagation effects in aircraft noise synthesis

Because annoyance to both current and future aircraft may not be well captured by integrated noise metrics, there is a need for subjective assessments of individual flyovers. Therefore, prediction-based noise synthesis is required to evaluate new designs (inclusive of changes to both source and operations) based on subjective measures. This chapter describes a general framework, based on chapters 2, 3 and 5, for aircraft flyover noise synthesis in a non-standard atmosphere.

6.1 Review of the prior approaches

A virtual reality environment for the simulation of aircraft flyover noise was first created at NASA using ground-based, monaural recordings of actual aircraft flyover events.⁽¹¹¹⁾ To assess future designs and to pre-evaluate future operational changes or varying atmospheric conditions, aircraft source noise must be synthesized. To that end, subsequent developments were geared toward noise synthesis of various source components (jet, fan, rotary wing) using frequency and time domain predictions, and to the flyover simulation thereof.^(98;110;112;113) This resulted in the Community Noise Test Environment (CNoTE).

CNoTE was developed at NASA using a distinctive source-path-receiver paradigm. By treating the aircraft noise source as a compact acoustic source, the noise received at a listener in the far-field can be described as coming from a single emission angle. The emission angle, and its receiver angle complement, are determined by the straight-line path between the source and listener. Source noise synthesis amounts to generating an emission angle specific pressure time history at the moving source, based on source directivities from predictive programs like ANOPP⁽²⁸⁾ and ANOPP2⁽³¹⁾. The atmospheric propagation along the straight-line path takes into account time-

varying spherical spreading loss, atmospheric and ground-plane absorption and time delay. Finally, the receiver processing takes the listener orientation into account and applies binaural simulation using HRTF's for playback over headphones, or vector base amplitude panning (VBAP)⁽¹¹⁴⁾ for playback over a loudspeaker array. The propagation and receiver processing stages are performed in real-time on the AuSIM Goldserver, a dedicated audio DSP computer.⁽¹⁰⁾ When coupled with the remaining elements of CNoTE, the listener is exposed to synthesized aircraft flyover noise within a 3-D virtual reality environment, inclusive of computer graphics visualization. The NLR software (VCNS) is a derivative of NASA CNoTE. The NLR uses the VCNS to demonstrate potential changes around airports to policy makers and to study aircraft noise impact in urban environments. Results from both the prior NASA and NLR frameworks are uniquely capable of presenting predicted flyover noise in an early design stage of an aircraft or new procedure.

The strength of the synthesis and simulation codes developed at both organizations is that measurements of flyover noise are not needed, unlike other recording-based methods.^(111;115) As such, the laboratory environment allows the controlled testing of a variety of parameters without the need for costly flight test measurements. The limitations to the approach are the necessity to have good source noise prediction tools for synthesis and the challenge to accurately capture the propagation effects in the simulation. In particular, curved propagation paths associated with any non-uniform atmosphere affect not only the integrated atmospheric and ground plane absorption, time delay, and spreading loss along the curved path, but also the emission angle and the receiver angle, which govern the source noise and where it appears to come from, respectively. To overcome these limitations, NASA and the NLR adopted a new framework to allow evaluation of novel source prediction tools, new aircraft designs, aircraft procedures and atmospheric propagation codes for aircraft operating in non-standard atmospheres.

6.2 New simulation framework

6.2.1 Requirements

The goal of the framework is, in the end, to allow real-time simulation of flyover noise created by an arbitrary aircraft flying an arbitrary trajectory, through an arbitrary atmosphere. Including an arbitrary atmosphere adds the requirement to determine the curved path(s) as a function of time along the flight trajectory, and to compute and apply the integrated absorption, time delay and spreading loss along those paths.

The curved path influences the emission and receiver angles in a more complicated fashion than in the straight-line propagation. As in the existing approach, the simulation framework should allow immersion of a test subject in a virtual reality environment to reproduce outdoor listening conditions as closely as possible. It should additionally allow the subject to affect the propagation path through his own move-

ment. These effects could potentially become important in large virtual reality simulators (cave environments) where listener movement is not confined. In such a case, a listener in an urban environment could move behind a virtual house thereby modifying the propagation characteristics. This particular shielding effect is not included in the current simulations although the listener movement is retained to keep it as a possible future extension. The calculation of the curved path is computationally intensive and is presently not performed in real-time. However, an architecture was desired which allows off-line processing for present use, but is amenable to future real-time implementation with minor modifications. Further details regarding real-time implementations are postponed until chapter 8.

6.2.2 Non-standard atmosphere implications

The ray tracing method model, see chapter 3, is used to calculate the propagation characteristics. Other wave equation based methods, such as the Parabolic Equation (PE) approach and/or FFP, do not provide the necessary path information for noise synthesis. Since no path is available, the directions of the sound waves at the receiver and source are unavailable. It is thus unknown at which angle to synthesize the sound at the source, or under which incidence angle the sound at the receiver is perceived. Furthermore, wave equation based methods usually calculate a transmission loss spectrum at the receiver position including (implicit) time delay information. This is undesirable given the current setup of virtual acoustic simulation, where time delay takes care of Doppler shift and ground interference. For these reasons, besides the computational efficiency, ray tracing is a logical choice to integrate atmospheric effects in auralization.

In downwind conditions there are multiple rays that can reach a listener, see figure 3.12. Each ray reaching a listener is called an eigenray. By tracing and summing the contribution of each eigenray, the sound field from the source can be propagated towards the listener. To actually simulate the curved paths in the new framework, the following critical points emerged:

- The rays each originate from a different angle compared to the straight-line path case. This is important since most aircraft noise sources have directional radiation patterns. As a result, the noise that must be synthesized depends on the atmospheric characteristics of the medium and the distance between the source and the listener.
- The number of paths is increased. In the case of the straight-line path assumption, there is only one ray pair containing a direct and ground reflected path. In case of downwind propagation, there are (possibly) multiple ray pairs if eigenrays reach the receiver. Consequently, the number of paths increases. This requires additional bookkeeping and increases the simulation workload which is directly proportional to the number eigenrays.
- Along each path, the travel time of the sound is integrated to obtain the total travel time to reach the listener. The time rate of change of the time delay at

the listener simulates the Doppler shift (see chapter 5) and can lead to audible aliasing effects if not properly treated.

- Along each path, the atmospheric absorption is accumulated as the sum of piecewise frequency dependent absorption per length. For the straight-line path with a stationary listener, this could be computed solely as a function of slant range (distance from source to listener).
- Along each path, the interaction of the ray with the ground must be accounted for by integrating the frequency dependent attenuation associated with each reflection. In realistic wind fields, the sound might reach a listener only through reflection off the ground, i.e. no direct eigenray from the source reaches the listener.
- The angle at which the rays reach the listener vary per path. This has an impact on the propagated sound since the ground attenuation is a function of the incidence angle. Further, direction of the sound received by the listener is simulated using the receiver angle to determine the set of HRTFs used for binaural simulation, or the VBAP weights used for loudspeaker playback.

The propagation through a non-uniform atmosphere thus has an effect on every part of the simulation, i.e. on source, path and receiver effects. As such, the simulation has to start with calculation of the curved eigenray(s).

6.2.3 Compact source considerations

Aircraft sound is composed out of many individual sources that propagate towards the listener. Sources can be spatially distributed over the aircraft geometry, e.g., the jet noise comes from a different location than the landing gear noise. In case of the new framework, this would necessitate the ray tracing to be performed for every source location on the aircraft. This brute force approach requires an undesirable computational expense and therefore a slightly different approach is used. The alternative approach assumes the entire aircraft to be a compact sound source. As such, all sources follow the same propagation path, as found by ray tracing, and the source position is assumed to be some reference location, e.g., the center of gravity. The underlying assumption is that the difference in source locations on the aircraft does not affect the propagation path in such a way that different propagation characteristics are required. This assumption seems especially valid in flyover noise simulations since a relative long propagation distance (w.r.t. the source distribution on the aircraft) is covered. Consequently, differences in the effective sound speed and ray path length are negligible. This was confirmed by a ray tracing analysis showing similar transmission losses thereby rendering the compact source approach valid in flyover noise simulations. As a result, the total sound is composed by adding all individual sources that are propagated with a common ray tracing result. The only difference that is taken into account is the difference in travel time between individual sources. This difference is calculated based on straight-line path calculations. First the straight-line path travel time for each spatially distributed source is calculated and subtracted

from the straight-line path travel time for the reference location. The resulting differences are then added to the common travel time of the curved ray path to obtain a unique travel time for each spatially distributed source. Using this approach, modeling of phase differences between (correlated) noise sources on the aircraft is still possible.

6.2.4 Framework architecture

It is convenient to describe the framework as consisting of three processing chains. The first chain is devoted to path definition and source noise synthesis. The second chain is responsible for applying the integrated time delay, atmospheric absorption, ground plane attenuation and spreading loss to propagate the sound to the ground. The third chain is responsible for rendering the propagated sound to the listener over headphones or a loudspeaker array. Figure 6.1 shows the newly developed framework and individual chains.

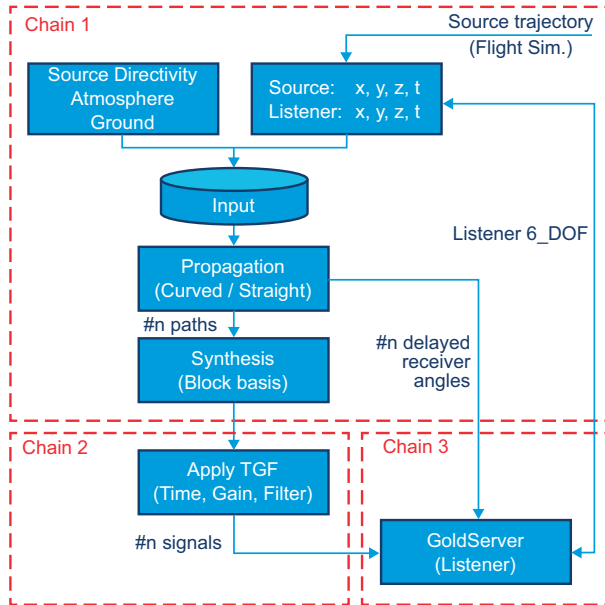


Figure 6.1: Flowchart of the new framework showing three processing chains.

In the first chain, information about the source and propagation medium as well as the source and listener positions are required as input. Source noise synthesis may be based either on a priori computed source noise directivity patterns, as a function of discrete polar and azimuth angles (spheres or hemispheres), or on real-time computed directivity patterns using empirically based models. In either case, the directivity is a function of the operating condition and can be expressed in either the frequency or

time domain. Calculation of realistic atmospheric input is not trivial⁽¹¹⁶⁾ and therefore measurements are preferred as input. Note that scattering due to atmospheric turbulence is a time dependent characteristic not presently included in the simulation. Ground impedance model parameters, e.g., flow resistivity, are also required as input.

In the initial, non-real-time, version of the framework, the source and listener trajectories are specified as part of the input. In a future real-time implementation, the aircraft position could come from a flight simulator and the listener position from a tracking sensor. Under either scenario, once the input data is specified, a loop over simulation time is started in which the curved path analysis and synthesis are performed. For every time increment, the aircraft and listener positions are interpolated. It should be noted that the source and listener trajectories are also required for visual scene generation in the virtual reality environment (not explicitly shown in figure 6.1). Within the virtual reality environment, the real-time listener orientation is required to position the virtual source according to the receiver angle obtained from the path analysis. The operation is performed within the third processing chain.

Note that some limitations on the listener movement are presently required. The path calculation is performed at each time increment based on the instantaneous source and listener positions, i.e., at the emission time. Since the travel time may be many seconds, it must be assumed that the listener does not translate sufficiently far during that time so as to necessitate a new path calculation. Further, although the ground impedance can vary according to location, the terrain in which the listener moves must be flat to preclude the possibility of the listener moving behind an obstacle, e.g., mountain or building, and partially shield the incoming sound. Diffraction around obstacles is presently not incorporated.

From the ray tracing analysis, the number of possible paths and their corresponding emission and receiver angles are computed. As indicated above, the receiver angles are used in the third rendering chain to position the source in the virtual reality environment. The emission angles are used to synthesize the instantaneous pressure time histories (one per path) at the moving source, using the source directivity as described above.

Concurrent with the synthesis operation, the integration of time delay, atmospheric and ground plane absorption, and spreading loss is performed per path. The absorption and spreading loss are expressed as linear phase FIR filters, as described in chapter 5. This information, together with the synthesized pressure time histories, is passed to the second chain for propagation processing. In the present implementation, the time loop is incremented through the course of the full trajectory until the entire pressure time histories of the moving sources are synthesized along with the time histories of integrated time delays and filters.

In the second chain, the synthesized sounds at the moving sources are propagated to produce pseudo-recordings at the listener position. The framework was built in Matlab and a dedicated off-line digital signal processing engine was programmed to apply the integrated time delay and filter to the synthesized sound source. In the

future real-time framework, this operation will be executed on the GoldServer or on the to be developed NASA Auralization Framework.⁽¹¹⁷⁾

In the final processing chain, the sounds are rendered to a tracked listener using the Goldserver, which works together with a graphics server to produce the virtual reality environment. Together, the audio and graphics servers complete the simulation of the flyover event including realistic positioned audio and visual cues. The positional audio is achieved using binaural simulation with HRTF filtering for playback over headphones. In the present implementation, the time delayed receiver angles are used to position the virtual sources. In this fashion, the rendering chain is performed in the same manner as if the propagated source at the listener position were an actual microphone recording at the simulated listener height.

6.3 Results

A full flyover simulation using the newly developed framework is demonstrated. The aircraft source was comprised of jet noise combined with tonal components of fan noise. The jet noise prediction was based upon a CF6-80C2 engine from a Boeing 747-400, whereas the fan noise prediction was based upon the Honeywell Tech977 engine.⁽¹¹⁸⁾ Because the simulation is prediction-based, alternative configurations are possible. Each noise component is synthesized independently and combined prior to propagation. The aircraft itself is flying a straight and level trajectory from $x = 6000$ to $x = -6000$ m, at an altitude of 152 m (500 ft.), with a speed of 100 m/s. Both the engine fan and jet noise components are simulated at 87% N1.

The listener is moving perpendicularly away from the ground track of the aircraft at a walking pace (5 km/h). As a consequence the aircraft does not fly directly over the listener. The ground surface impedance has a variable effective flow resistivity and is calculated with the Delaney & Bazley model (equation 3.20). As the listener was allowed to walk through the virtual environment, the impedance changed slowly. The varying impedance is categorized, for the entire simulation, as 'roadside dirt' in table 3.1.

Researchers often apply a boundary layer model that is valid close to the ground, which yields logarithmic wind and linear temperature profiles for acoustic propagation problems. A well-known boundary layer model is represented by the Businger-Dyer equations.⁽¹¹⁶⁾ These equations exclude the possibilities of wind speed inversions and changing wind directions. These limitations are circumvented by using measurements. The atmosphere specified was measured at Wallops field (VA) on the 5th of October 2011 at noon. The measurement is accessible through a University of Wyoming internet site*, as depicted in figure 6.2.

The depicted atmosphere has a temperature inversion around 200 m. An inversion is defined here as an altitude where the gradient of the quantity changes sign. In this particular atmosphere, the temperature increases from the ground level up until

*<http://weather.uwyo.edu/upperair/sounding.html>, accessed on 05-12-2011

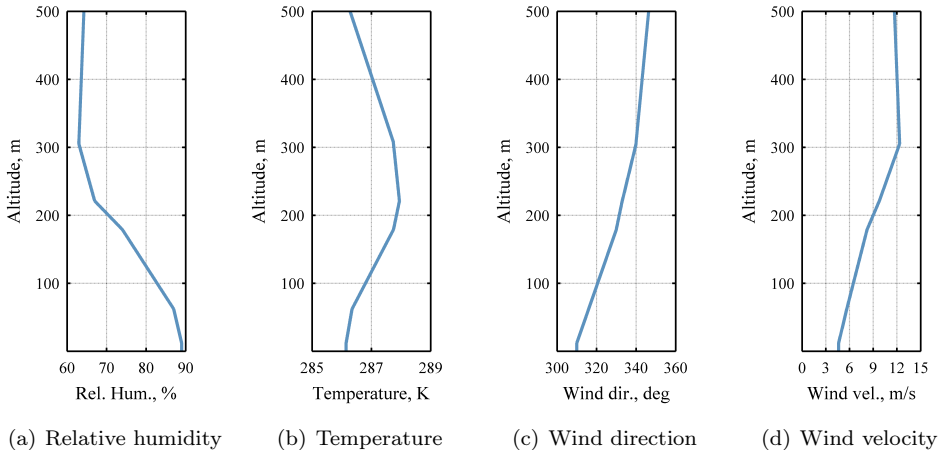


Figure 6.2: The atmospheric conditions as used in this simulation.

200 m where it starts to decrease. Since the simulated aircraft flyover occurs at 152 m, it is below the temperature inversion. The relative humidity and temperature are important in the calculation of the atmospheric absorption.⁽⁹⁷⁾ The wind direction changed slightly from a North-East wind at the ground to a Northern wind at higher altitudes. The corresponding wind speed increased to a maximum of roughly 12 m/s at 300 m. The aircraft is flying on a North bound track, i.e., going towards the North thus moving from an upwind to a downwind position relative to the listener.

6.3.1 Ray tracing results

The ray tracing algorithm launches sound rays from the source position at many initial launching angles. Only the ray that reaches the listener, i.e. the eigenray, is of interest for further processing as it is the path that the synthesized sound needs to follow. Finding the eigenray is exercised in an iterative manner by zooming in on the closest ray, and re-launching a new cluster of rays in the direction of the closest ray. After a few iterations an eigenray is found with the desired accuracy. The angular and temporal resolution are refined during consecutive iterative steps. As a result, the first iterations are done computationally fast to establish a direction of where to find the eigenray. Further temporal and angular refinement gives the desired accuracy, albeit with increasing computational expense.

As the aircraft flies along the trajectory, the speed of sound profile changes according to equation 3.32 to comprise the downwind and upwind conditions. The ray tracing is recalculated to obtain the eigenray(s) for each new aircraft position relative to the listener. Figure 6.3 and 6.4 shows snapshots of the eigenray(s) as the aircraft is flying through the atmosphere along its trajectory. The distance indicated on the x-axis is the relative distance between the projected source and listener.

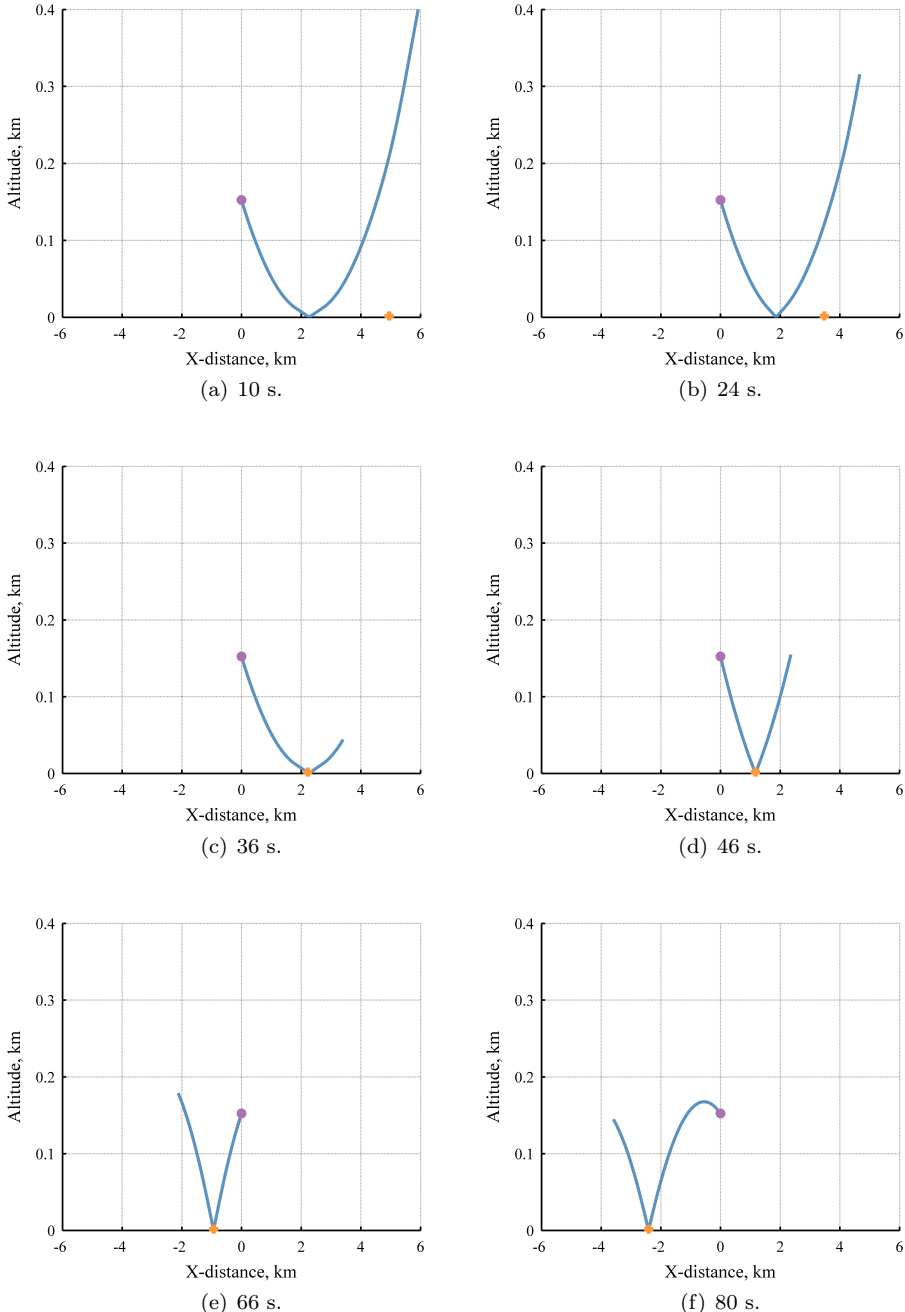
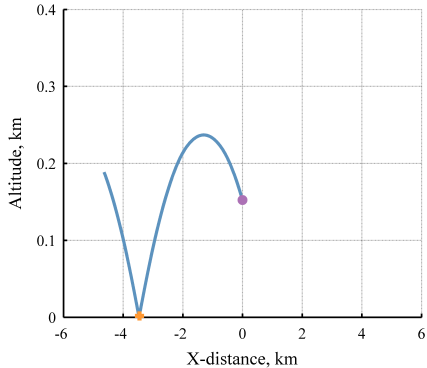
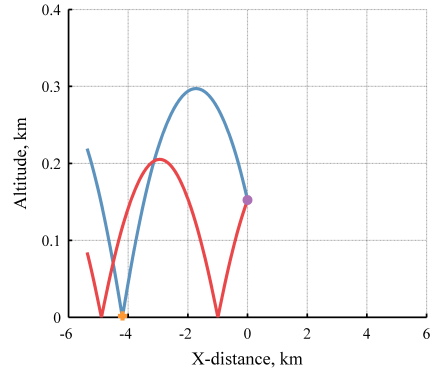


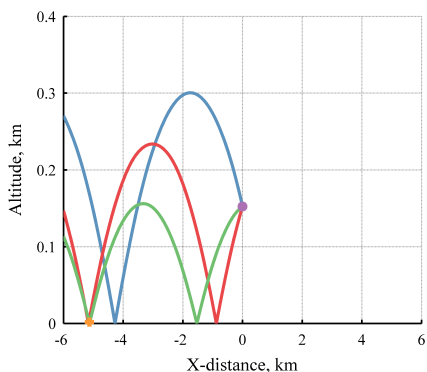
Figure 6.3: Eigenray snapshots from the aircraft at emission time. The 1st eigenray is blue. The purple dot is the aircraft source position and the amber + sign is the listener position.



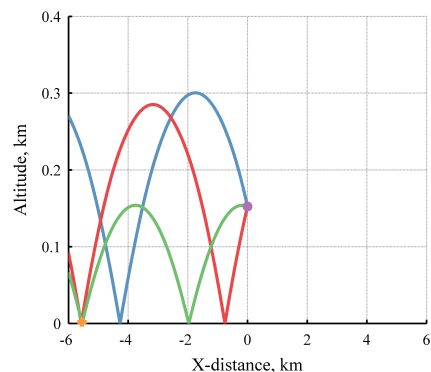
(a) 90 s.



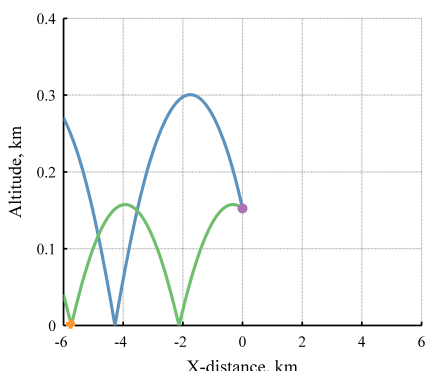
(b) 97 s.



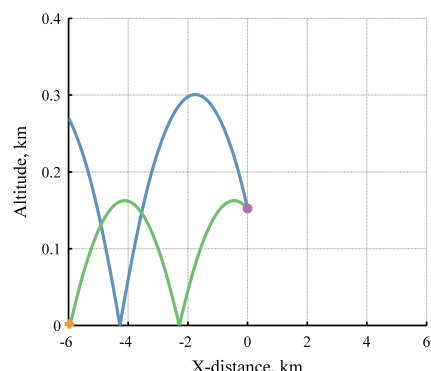
(c) 106 s.



(d) 110 s.



(e) 112 s.



(f) 114 s.

Figure 6.4: Eigenray snapshots at emission time. The 1st eigenray is blue, the 2nd is red and the 3rd is green; the purple dot is the aircraft source position and the amber + sign is the listener position.

The emission angle of the sound can be calculated for use in noise synthesis from the launch angle of the eigenray(s). The emission angle is the angle used in the calculation of the source directivity pattern. In case of the Stone jet noise model or the Heidmann fan model the source is assumed to be axisymmetric, i.e., no azimuthal dependency. First, the engine can be tilted upward or even change its orientation during flight, e.g., like a Bell Boeing Osprey tilt-rotor. Second, the source directivity models may be limited to a range of emission angles, as discussed below. Taking these considerations into account, the emission angle is calculated and is shown in figure 6.5 for a fixed upward tilt angle of 1 degree.

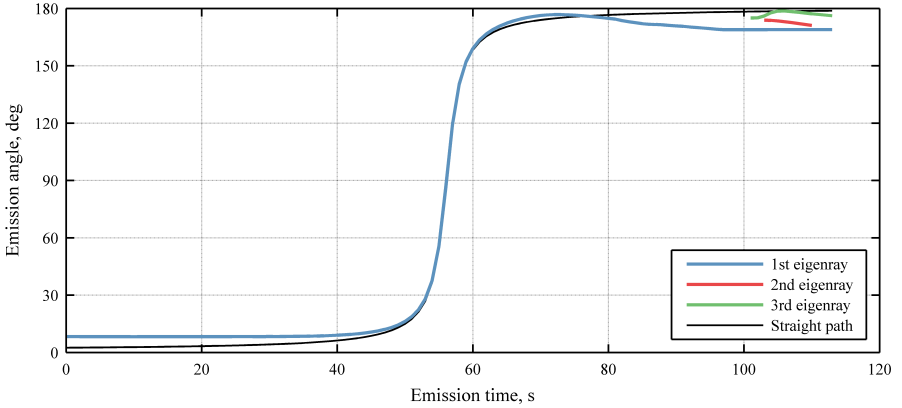


Figure 6.5: As a result of the curved eigenrays, the emission angle has changed from the straight path assumption. The effect is the largest at the start and end of the simulation.

From 0-36 seconds there is a difference visible between the straight and curved path emission angles in figure 6.5. This is because the aircraft is in a shadow zone. The first eigenray has a constant emission angle from the limiting ray, i.e., the ray that forms the boundary between the 'illuminated' zone and the shadow zone. This effect is also noted in the snapshots of figure 6.5, during the first 36 seconds where the eigenray remains the same. Due to bending of the rays, no ray reaches the listener and therefore the limiting ray and its characteristics are used.

When the aircraft emerges from the shadow zone, the difference between the emission angle of the first eigenray and the straight path quickly diminishes and the straight path result is essentially recovered. In other words, the rays nearly follow the straight line ray paths. This is also noticeable in the snapshots of figure 6.3 where the curvature becomes larger for larger distances between the source and listener.

The snapshots illustrate the change in launch angle when going from upwind to downwind positions. Consider for instance the snapshots at 36 and 80 seconds, where the receiver is at a similar distance from the source albeit in upwind and downwind conditions. In the first case the rays are launched downward and curved upwards, whereas in the latter case the rays are launched upwards and bent downwards.

Around 75 seconds, the first eigenray is launched horizontally. The emission angle shows a maximum at that position, but is less than 180 degrees because the source is tilted and the listener is down and to the side. After about 75 seconds, eigenrays are launched upward. However, note that the directivity pattern is axisymmetric, it is mirrored about 180 degrees, in compliance with the empirical models from chapter 2. As a matter of bookkeeping, directivity angles in excess of 180 degrees are indicated at their mirrored value. Consequently, emission angles shown in figure 6.5 decrease after 75 seconds as the launch angle becomes more upward, see figure 6.3.

After 102 seconds, there are multiple eigenrays that reach the observer, each with a unique emission angle and ray path. This is in contrast with the straight-line path result for which there can only be one ray. In the case of multiple eigenrays due to atmospheric conditions, the straight path assumption is not valid. As such, comparing the emission angle of the straight path to the second and third eigenray is not valid.

The receiver angle is also affected by the curved rays. A change in receiver angle affects the ground plane reflection in two ways; the wave reflection coefficient is dependent on the incidence angle and differences in path length between the direct and ground reflected rays (relative to the straight line path case) cause a different ground interference pattern. A change in receiver angle from the straight-path also affects the perception of the source location by the listener. Figure 6.6 shows the receiver angle for the curved paths and the straight path.

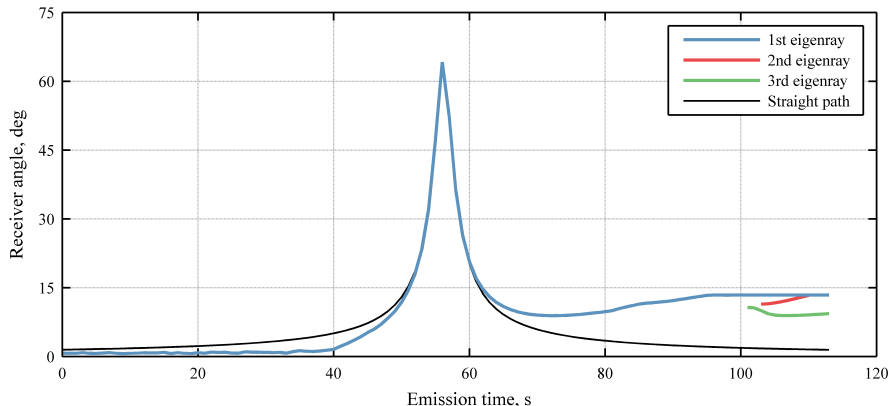


Figure 6.6: The receiver angle as used for the ground reflection coefficient calculation and the path length difference between the direct (eigen)ray and the ground reflected ray.

From figure 6.6 it is clear that the receiver angle is symmetric for the straight path assumption whereas the receiver angle is asymmetric for the curved ray paths. The receiver angle does not reach 90 degrees as the listener is moving, at a walking pace, to the side of the aircraft ground track. The first eigenray receiver angle is, as for the emission angle, constant during the first 36 seconds due to the fact that the limiting

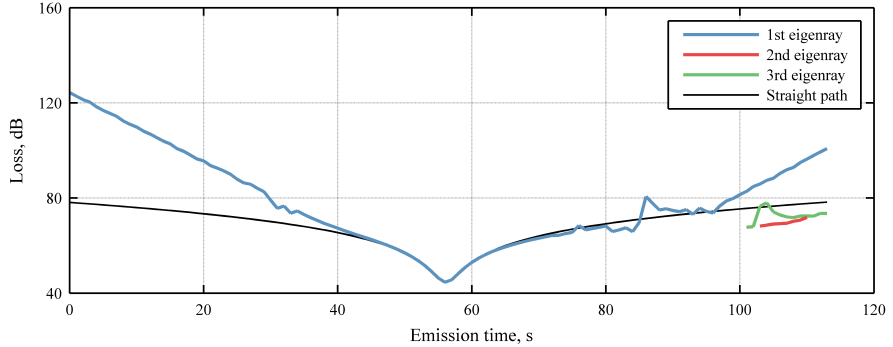
ray is used. After emerging from the shadow zone around 36 seconds, the difference between the straight path and the first eigenray quickly diminishes. As the aircraft flies over (approximately 57 seconds) the receiver angles are similar as the rays do not exhibit much curvature. Around 65 seconds, the receiver angle of the first eigenray does not decrease further and is relatively constant up until 80 seconds, after which it starts to increase again. This means that the sound at the listener is coming in from a steeper angle than expected from a straight path assumption. After roughly 97 seconds the receiver angle becomes constant for the first eigenray. This can be explained, by the snapshots, where it is seen that the first eigenray can no longer reach the listener. If a ray goes over an altitude of 300 meter along its trajectory, the ray is refracted upwards. This is due to the decreasing effective sound speed above this altitude in downwind condition. As such, the eigenray cannot reach the listener and a constant angle of the limiting case is used together with the (shadow zone) diffraction correction to simulate the sound emanating from the nearest ray position. The eigenray solution is retained as the aircraft retreats because the same eigenray might again reach the listener at some greater distance.

Like the emission angle, the receiver angle of the second eigenray grows towards the angle of the first eigenray. Looking back to the snapshots it is seen that the corresponding ray paths reach the same maximum altitude of 300 m. Any ray going over this altitude is refracted upwards and thus outside the range of interest for this simulation. Since both eigenrays follow similarly curved trajectories, albeit offset, similar receiver angles are found since the rays follow identical arcs.

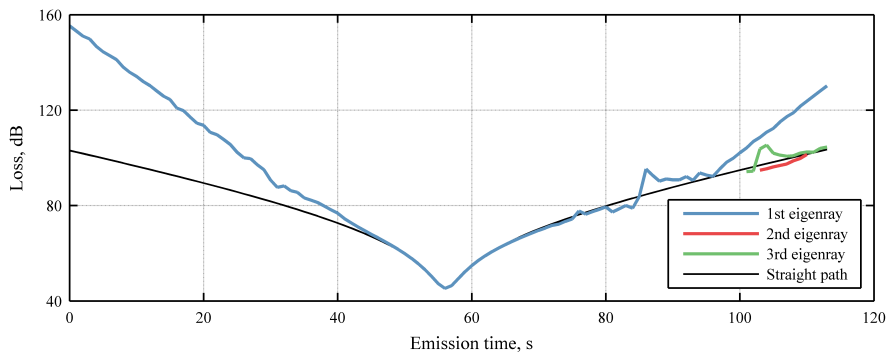
The associated losses per ray, as used in the filters by accumulation of spreading, atmospheric absorption and ground absorption, are depicted in figure 6.7 for three different frequencies. Note that the shown losses are generally compiled from the spreading loss and the atmospheric absorption. In case the eigenray has reflected off the ground before reaching the listener, e.g., eigenray 2 and 3, the cumulative ground attenuation is included as well.

As with the emission- and receiver-angle, the straight path is symmetric whereas the curved path results are not. The shadow zone associated with the upwind propagation is present from 0-36 seconds. Clearly the losses are much larger compared to the straight path result due to the shadow zone and these losses increase with increasing frequency. Around 36 seconds the shadow zone ceases to exist as the aircraft comes closer. This is noticeable by small wrinkles in the loss lines for the first eigenray. Note that the wrinkles become more pronounced for the 2500 Hz result even before the 30 seconds mark. This is due to the fact that the limiting ray is very sensitive to launch angle. A small deviation in launching angle due to a moving aircraft or listener, changes the effective sound speed profile and results in a small difference in the shadow zone position and corresponding spreading loss. Since the losses are well over 80 dB, or even closer to 100 dB for the 2500 Hz solution, small wrinkles have no audible effect on an already highly attenuated signal.

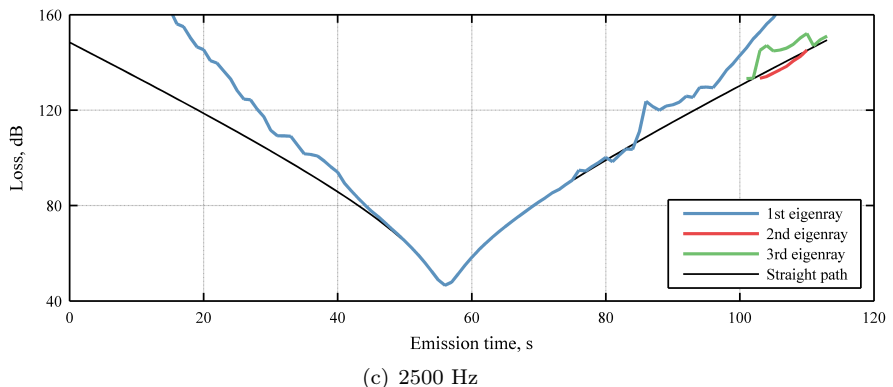
As the aircraft emerges from the shadow zone and comes closer to the listener, the rays become less curved. As a result the differences in total loss between the straight path and the first eigenray becomes smaller and diminishes when the aircraft is flying



(a) 100 Hz



(b) 1000 Hz



(c) 2500 Hz

Figure 6.7: The loss as used to obtain the filter characteristics for three typical frequencies.

near the listener. From 75 seconds onwards, the first eigenray loss line starts to show some wrinkles again. Looking back to the snapshots in figure 6.3, it is noticed that the launching angle has crossed the horizontal axis. At that point the ray is launched at a

very shallow angle from the source. At shallow launching angles, rays are susceptible to small changes in the sound speed profile. As the aircraft is moving, and the sound speed profile changes, eigenrays reaching the listener launched at a shallow angle show the small changes in sound speed profile in their overall loss as small wrinkles. At around 85 seconds, this effect becomes more prominent as the rays reach an altitude of 220 m. At that point, the wind direction changes slightly causing, yet again, a tiny irregularity in the sound speed profile. Rays traveling through this irregularity at a shallow angle are affected, i.e. curved more towards the ground. Rays reaching this altitude at a steeper angle are relatively unaffected and curve at a more gradual rate towards the ground. Figure 6.8 shows this effect with a snapshot of some rays launched from the source at an emission time of 85 seconds.

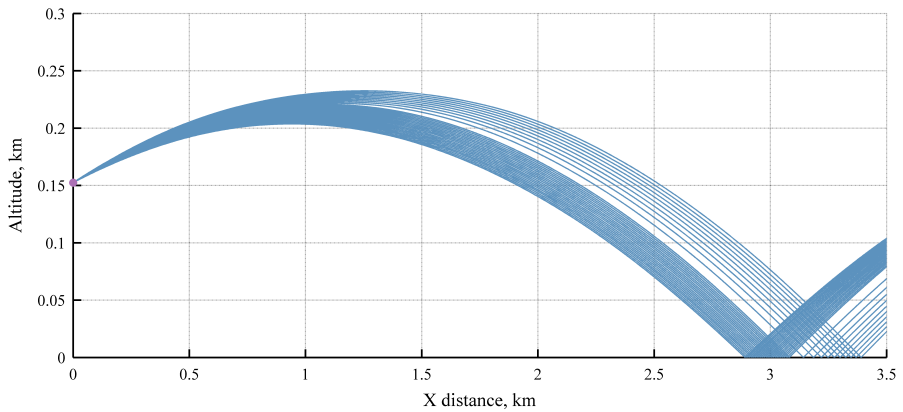


Figure 6.8: At an emission time of 85 seconds, rays launched from the source experience a shallow propagation angle at a downwind range of around 1250 meter. At this altitude a small irregularity in the sound speed gradient is present, note the difference in ray density before and after 3050 meter due to this effect.

Further downwind, at distances larger than 3050 meter, the rays reach the ground but are spread farther apart and are defocused. Close observation of figure 6.7 shows that before 85 seconds, the loss is lower compared to the straight path result. After a few seconds the loss becomes higher again. This is due to the focusing and defocusing of the rays originating as a combination of a small irregularity in the sound speed profile and the shallow angle at which the ray reaches the irregularity. The consequence of this is audible as a modulation of the overall sound level.

At around 97 seconds, the first eigenray reaches the limiting altitude of 300 meter, above which upward refraction negates the possibility of that ray reaching the listener. From that time on, the diffraction correction is applied as the listener is in the shadow zone. This condition remains in effect up until 102 seconds, at which point the second eigenray becomes feasible and propagates sound from the source towards the listener. From 104 s onwards, the third eigenray is feasible as well. Both the second and the third eigenray are focused and lead to a smaller spreading loss compared to the straight

path result. However, due to the curvature, the ray path is slightly extended and therefore experiences a bit more absorption. Furthermore, sound energy is attenuated by the ground reflection along the ray paths. These two effects balance the effect of focusing. The low frequency results are not influenced as much by the attenuation and therefore show the distinct effect of focusing, a (slightly) lower total loss than the straight path. In this case, focusing has a noticeable effect on the low frequency sound emanating from the aircraft at a relative long propagation range.

6.3.2 Synthesis results

Having all the propagation characteristics at hand, it is possible to apply them to the synthesized source sound and render the sound at the listener. These audible results are available as download from the internet, see appendix E or table E.2. The resulting pseudo-recordings are presented as spectrograms showing the distribution of sound energy for the aircraft flyover. Figure 6.9 shows the spectrograms for both straight and curved path propagation. In figure 6.9, the indicated time is the receiver time and the maximum frequency is limited to 10 kHz for clarity.

The forward and aft radiated fan tones are clearly visible and were synthesized at the BPF and three harmonics thereof. Also visible are 'Buzz-Saw' tones which are present at multiples of the shaft speed at high power settings. The effect of Doppler shift is clearly seen in the tones. At the flyover position, the Doppler shift factor is closest to unity and the tones are therefore close to the source frequency.

The indentations in the spectrogram indicate the comb filtering effect caused by the ground interference. The ground interference pattern associated with the curved path is markedly changed from the straight path. The indentations are curved as a result of the different receiver angles demonstrated in figure 6.6. The asymmetry of the receiver angles manifests itself in the spectrogram and results in an upward turned interference pattern for upwind conditions and downward turned pattern for downwind conditions.

Because the synthesis was started at an upwind distance of 6000 meter, this resulted in roughly 17 seconds period of dead time before the sound is audible. This is an artifact of the manner in which the simulation began. For the curved path, the upwind conditions indicate the presence of the shadow zone which attenuates the sound until it emerges at a receiver time of roughly 45 seconds.

Besides the changes in the ground interference pattern, there is an increasing transmission loss near a receiver time of 98 seconds as in the curved ray spectrogram less sound is present. From that point up until 117 seconds the sound level is actually decreased due to the aforementioned sound speed irregularity, see figure 6.8 at an emission time of 85 seconds. At a receiver time of 117 seconds, the second and third eigenray paths propagate sound to the listener and increase the noise level. During the period from 98-117 seconds, only low frequency noise is present. After 117 seconds, the ground interference pattern is delicate and, upon close inspection, is seen to follow a comparable trend to the receiver angle of the third eigenray (see figure 6.6).

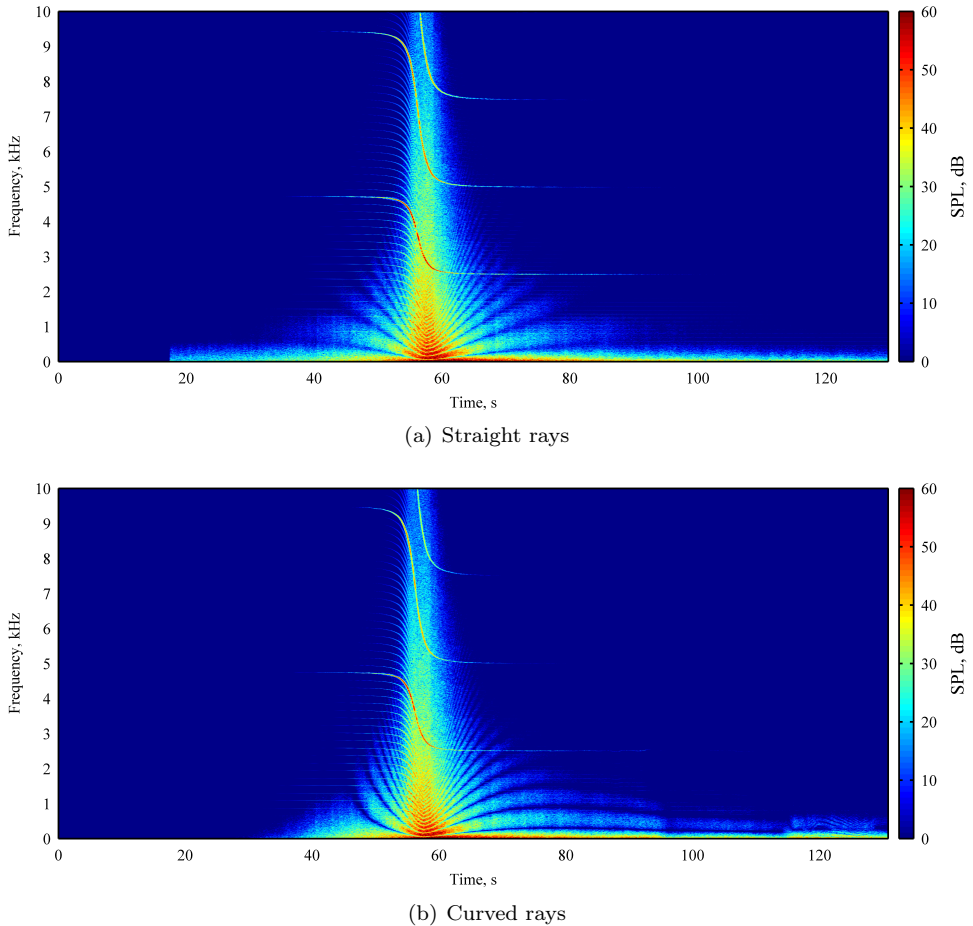


Figure 6.9: The spectrograms for the straight path assumption and the curved path assumption at receiver time.

The resulting $L_{A,\max}$ and SEL values, integrated over the entire flyover, can be calculated for both the straight path and curved path approach. These values should be evaluated with care since they integrate the results into a single number and therefore cannot do justice to the audible differences in the entire simulation. The metrics are reported in table 6.1.

Table 6.1: Noise metrics for the straight path and curved path.

Metric	Straight path, dB(A)	Curved path, dB(A)
$L_{A,\max}$	78.9	78.4
SEL	84.2	84.1

From table 6.1 it becomes clear that the difference between the straight and curved path approach is small. This is due to the fact that the $L_{A,\max}$ value is typically measured when the distance between the aircraft and listener is the smallest. At that point the eigenrays are relatively straight and, as a result, return the same results as using the straight path assumption. The difference in SEL is, as a result, minute since it is dominated by the $L_{A,\max}$ value. This effectively shows that weather dependent effects are not reflected in typical metrics in case of an aircraft flyover for the used atmosphere and trajectory. If an aircraft is not flying directly over the observer, thereby being at a more shallow propagation angle, the effects due to refraction will grow larger. Additionally, for more prominent directional sources that also emit a lot of low frequency sound like helicopters, curved path results are likely to have more influence. Furthermore, audible differences can be perceived in the simulation results thereby showing the importance of the current methodology. Integrated sound metrics can only describe a part of the problem, listening to the results gives a clearer impression on the implications. As such, it is actually a good demonstration why auralization is an attractive way to perceive day-to-day atmospheric propagation differences that could not be ascertained from sound metrics or noise contours.

6.4 Conclusions

A framework that allows the synthesis of aircraft flyover noise through a non-standard atmosphere is generated. Although it is known that the curved paths will affect aircraft sound, inclusion of curved path atmospheric propagation in a synthesis environment is not trivial. The new framework emerged after consideration of several options. Ultimately it was settled on not only for its ability to perform the simulation now, but also because it is amenable to real-time implementation in the future. Through the use of new and existing codes, the new framework allows simulation of aircraft flyovers in non-homogeneous atmospheres.

It is shown that the propagation losses, emission and receiver angles are affected by the curved path. This is especially true at low elevation angles of the aircraft and relatively large distances. For the case considered, the differences in emission angle and total losses diminished at elevation angles greater than around 5 degrees and ranges less than 2000 meter. The receiver angle is more sensitive with deviations indicated up to roughly 10 degrees elevation angle and ranges up to 1000 meter. Based on this, it is concluded that if the aircraft elevation angle, with respect to the listener, is greater than 10 degrees, curved path effects due to refraction do not cause prominent audible differences compared to straight path results. This result is atmosphere dependent, so different atmospheric conditions might show more (or less) of an effect.

The real computational bottleneck, for real-time implementation in virtual acoustic simulation, is in the ray tracing calculation. Two ideas have emerged from this study which can help reduce the computational burden. The first is to speed up the algorithm by starting each new trajectory point with the previous solution. Currently

each new ray-tracing calculation is started without regard to the prior solution. The second idea is to take advantage of the parallelism offered by graphics processing units (GPU) over a standard CPU. Further details regarding the latter solution are postponed until chapter 8.

Chapter 7

Synthesis of aircraft departures

The previous chapter demonstrated aircraft flyover noise through a non-standard atmosphere. To quantify the overall auralization method, it is vital to see if it is possible to re-synthesize measured flyover noise and identify future improvements. To that end a study is executed where flyovers, from two different departure procedures, are auralized and compared to measurements from a noise monitoring station near Amsterdam Airport Schiphol (AAS).

7.1 Objective

The sound at two locations enclosed in an aircraft noise induced 48 L_{DEN} contour (or other regulatory metric for that matter) can be perceived differently by a person. As a result, implications from noise contours are not trivial for non-experts that live near an airport and are exposed to aircraft noise on a daily basis. Experiencing the audible results for different flyover conditions may aid as a translation tool between noise contours and everyday experience. Therefore noise synthesis of aircraft flyovers may benefit the communication between airlines, airports and communities that are affected.

Differences between the auralization methods that are used by other researchers exist. For instance, synthesis can be based on recordings to create new flyover noise for psychoacoustic evaluation.⁽¹¹⁵⁾ Such an approach was also adopted, as mentioned in the introduction, to create audible impressions near Lelystad airport in the Netherlands that were presented during town-hall meetings.* Furthermore, aircraft noise synthesis can be based on system noise predictions (like the current work) to evaluate new aircraft concepts or advanced psychoacoustic metrics.^(9;98;99;119) Using predictive models has the benefit of being able to experience aircraft flyovers that are still

*See for example the movies created with help of the VCNS on the Alders tafel website: <http://www.alderstafel.nl/routes-en-geluid.html>

in the conceptual or preliminary design stage. An intermediate approach is to use recordings from dedicated windtunnel tests of novel propulsion concepts and apply the propagation processing steps to create an audible impression.⁽¹²⁰⁾

It is possible to predict the noise for any flyover based on the empirical predictive models. However, it is worthwhile to compare predictive based auralization tools to actual measurements to obtain an estimation of the current capability, accuracy and limitations of the noise synthesis method. Researchers have compared to measurements before. For instance, the aircraft noise synthesis team at NASA looked at static cases including temporal variations.^(106;108;113;121) A comparison of a synthesized flyover and an actual measurement is rare. The only comparison reported in literature⁽¹²²⁾ involves a limited comparison. Furthermore, the employed source noise prediction is of a proprietary source. Therefore it remains unclear what the ability of a synthesis technique based on general empirical predictive methods (see section 2.7) is. As such, it is necessary to compare the synthesis predictions, on an objective spectral level*, to measurements. This is the objective of the current chapter.

7.2 Study setup

The flyover data of four departures at AAS[†] are used for auralization purposes. This data is recorded in a nearby noise monitoring terminal and includes the measured acoustic signature of the flyover as well as the trajectories of the aircraft. Consequently, all input data is available to use the toolchain to artificially create the noise of a flyover.

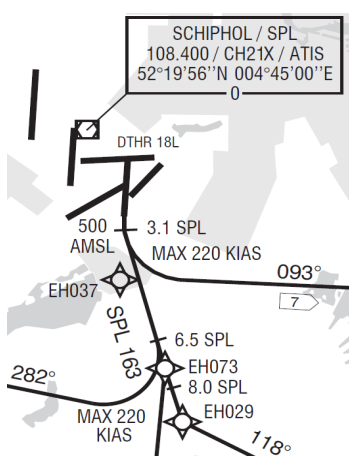
7.2.1 Flight mechanics

The four departing aircraft studied here are Boeing 747-400's equipped with GE CF6-80C2 engines. Figure 7.1(a) shows the air route as documented for the departure of runway 18L of Schiphol airport. The ground tracks of the flights used in this study are qualitatively shown by figure 7.1(b).

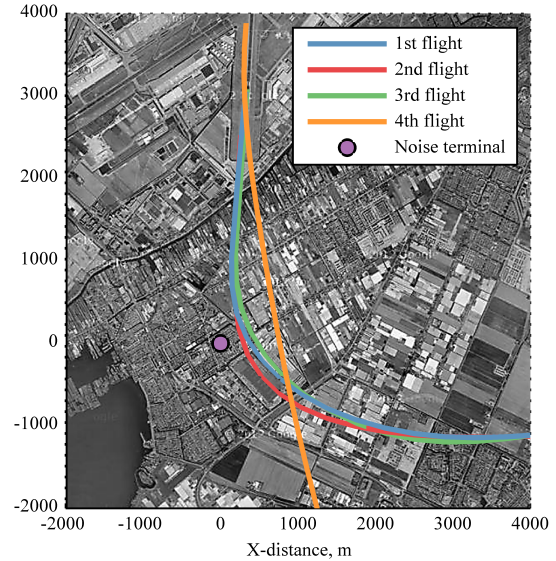
Figure 7.1 shows three departures, i.e. ground tracks turning towards the West, that fly more or less the same trajectory. The 4th flight continuous in a South-bound direction. The difference between the first three flights and the fourth just after take-off is small if figure 7.1(a) is observed. The actual observed difference can be substantially larger, as is implied in figure 7.1(b), and causes audible differences between the departure routes. The shortest distance between the noise control terminal and the fourth flight is larger than the others, which will be shown to have a clear effect on the observed sound levels at the noise control terminal.

*Subjective comparisons are not within the scope of the current work. The author believes that, at first, the spectral differences should be evaluated before subjective comparisons can take place

[†]AAS is greatly acknowledged for providing both the measurements and trajectory data.



(a) Air routes



(b) Radar based trajectory

Figure 7.1: The air routes and actual ground track of the departing aircraft. The location of the used noise control terminal is also indicated.

The radar data are supplied at a 4 s interval. At every data point the aircraft is assumed to be in equilibrium, see appendix D. Consequently, the effect of aircraft acceleration is excluded from the analysis at every data point. The airspeed is obtained by the (radar based) ground speed minus a 3 m/s headwind component, this headwind was the average wind velocity component at Schiphol during the measurement day. Solving for equilibrium conditions, using a B747-400 lift-drag polar and assuming maximum take-off weight, allows calculation of the required thrust, drag and lift.

The calculated required thrust culminated in a high (maximum) power setting for the trajectory under study here, which is in line with the take-off condition. The engine state was calculated, iteratively, for the calculated required thrust. The engine state provides the necessary engine flow conditions to the source noise prediction modules, see figure 2.4. The engine component data of the used GE CF6-80C2 engine was constructed from publicly available data and data available within the NLR GSP model.⁽⁵³⁾ Some more details regarding gasturbine modeling are found in appendix D. The resulting source noise prediction corresponds more or less, due to different ambient conditions, to figure 2.14.

7.2.2 Propagation

It is convenient to calculate the propagation characteristics for a single compact source, i.e. all sound emanates from the aircraft center of gravity, instead of the actual source positions on the aircraft. Such an assumption is valid for a flyover situation where relative large distances between observer and source are implied. If the actual source position on the aircraft is taken into account, acoustic 'beating' of tonal noise* may occur due to differences in Doppler shift between the engines.⁽⁹⁾ Acoustic beating of aircraft tones is, to the best of the authors knowledge, not reported to occur in real life. A possible explanation of the occurrence of beating in synthesis may be that 'perfect' propagation conditions are simulated in absence of turbulence. For a compact source, where all sound is subjected to the same Doppler shift, acoustic beating does not occur. Due to the absence of this phenomenon in daily experience, the compact source approximation is used. The source sound is thus calculated for one engine and enhanced, using incoherent addition, by the 3 other engines.

Three propagation effects are simulated in the current application, see chapter 5. The first effect is the application of spreading losses calculated by the spherical spreading law. Hence, this implies a homogeneous atmosphere where straight acoustic ray paths occur. The occurrence of curved-ray paths and its effect on noise synthesis was demonstrated in chapter 6. These curved paths occurred for two conditions, i.e. shallow propagation angles and particular atmospheric wind conditions. Since both conditions were not met during the measurements the curved-ray path capability was not utilized.

Atmospheric absorption is modeled using the standard model from section 3.1.⁽⁶⁰⁾ The average weather conditions of the measurement day ($T = 10 \text{ }^{\circ}\text{C}$, $p = 999.6 \text{ hPa}$, $RH = 96\%$) were used to calculate the atmospheric absorption. See figure 3.3 for an indication of the absorption coefficient at this condition for 1000 Hz.

The third propagation effect is due to ground reflection of sound waves. The reflection coefficient Q (equation 3.15) is calculated for a plane wave ($F = 0$ in equation 3.16) for the different incidence angles during the flyover. The ground impedance is calculated with the model described by Delaney & Bazley, as in equation 3.20. Since the noise monitoring microphone is located on a grass field an effective flow resistivity of $250 \text{ kPa/m}^2 \cdot \text{s}$ was used. The microphone is located at 10 m height to minimize the effect of coherent ground reflection. Equation 3.15 inherently assumes that the ground reflected ray and direct ray (or sound waves) are fully coherent. However, it is well known that turbulence decreases the coherence of a signal.⁽⁶⁵⁾ This is the reason why the microphone is at 10 m height. Since the synthesis uses equation 3.15 to calculate the effect of the ground reflection a fully coherent condition is simulated.

* Acoustic beating is a modulation of the amplitude of tonal noise that occurs if two tones differ slightly in frequency.

7.3 Results and Discussion

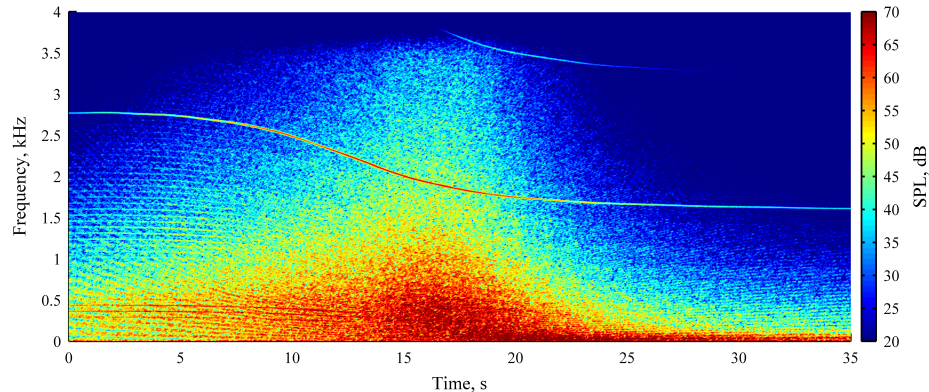
The objective of this chapter is a spectral comparison of synthesized and measured sound of four flyovers. The actual noise recordings is processed to minimize data storage since a lot of air traffic is monitored. Specifically, the recording low-pass filtered (cut-off at 3500 Hz) and resampled (at 8000 Hz). A similar procedure is applied to the synthesized sound to obtain comparable results, i.e. the synthesized sound is downsampled to 8000 Hz and a similar low-pass filter is applied. Sound metrics like $L_{A,max}$ and SEL are, however, calculated for the entire spectrum for both the recording and synthesized sound.

7.3.1 Results

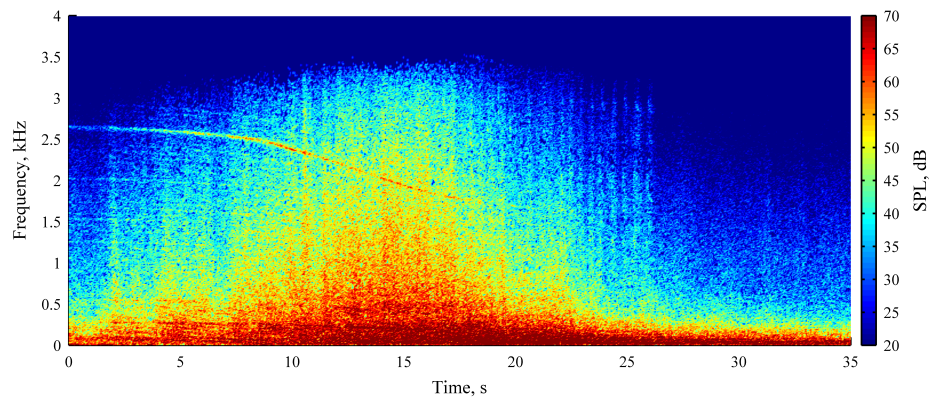
Figures 7.2 through 7.5 present the resulting spectrograms, for both the synthesized and measured signal, for all 4 flights. These audible results are available as download from the internet, see appendix E or table E.3.

A few differences are visible in all spectrograms. There is, for all cases, more low frequency content in the measurements than in the synthesis. Furthermore, the amplitude of the first BPF tone seems to be overpredicted compared to the measurement, especially if the aircraft has passed. The second BPF tone is lost in the low-pass (anti-aliasing) filter due to the cut-off frequency at 3500 Hz. This limitation can not be circumvented and is due to the used measurement settings in the noise terminal. In general, the frequency at which the Doppler shifted BPF tones are synthesized and measured coincide relatively well. The ground interference effect in the synthesized results are more pronounced compared to the measurements. The recorded data only show interference for low frequencies if the aircraft is nearby. A final observation is the presence of temporal variations in the measured sound levels, these variations can be identified as vertical stripes (thus more or less frequency independent) in the spectrogram. This effect is not found in the synthesis result. Temporal variations at the source are known to exist and can be implemented although they are usually frequency dependent.^(106;108) No temporal variations are currently employed since no explicit input data of possible variations at the source are known for this particular engine. No temporal variations due to the atmospheric propagation effects are captured by the current synthesis methodology.

The Overall A-weighted Sound Pressure Levels (OASPL), typical for noise monitoring purposes, are calculated and shown in figure 7.6. From these figures it can be observed that the sound levels of the first flight are well captured by the synthesis techniques. The agreement deteriorates for the second and the third flight. Especially when the maximum level has passed it seems that the lines are diverging slightly. The overall sound metrics are reported in table 7.1.



(a) Synthesis



(b) Measurement

Figure 7.2: Spectrograms of the synthesized and measured flyover for the 1st trajectory.

Table 7.1: Flyover sound metrics, synthesized and measured, in dB(A).

Flight	Synth. L _{A,max}	Meas. L _{A,max}	Synth. SEL	Meas. SEL
1	82.9	82.8	91.2	91.3
2	84.7	86.5	92.5	94.2
3	82.1	84.3	90.6	94.5
4	75.3	72.9	86.0	85.2

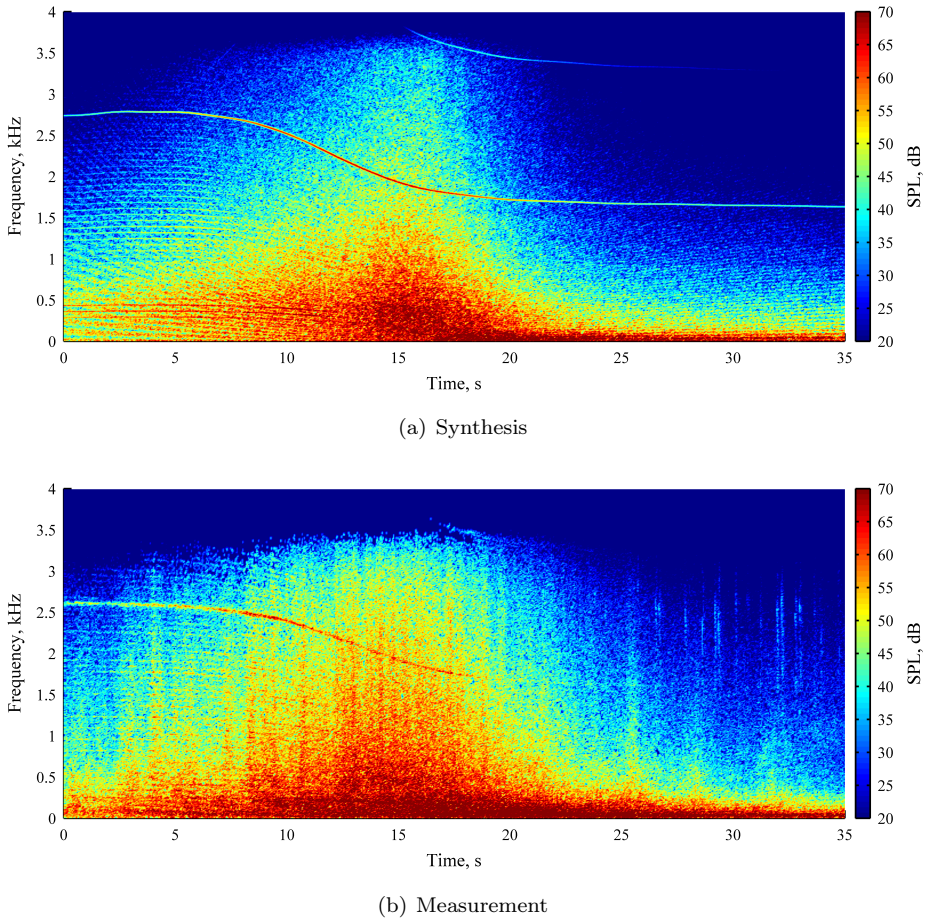
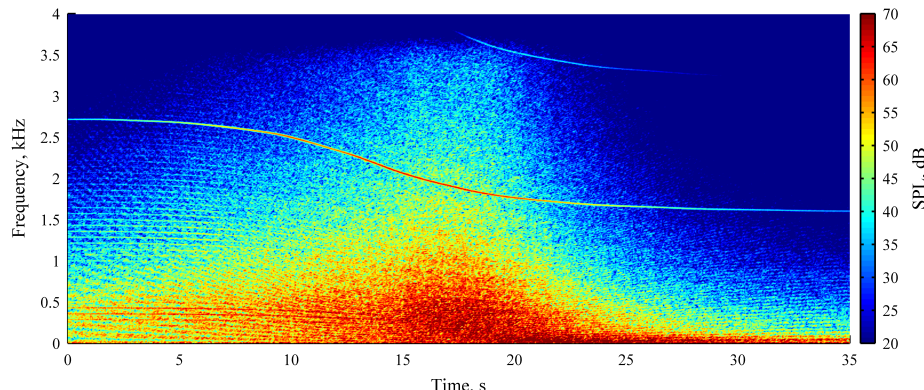


Figure 7.3: Spectrograms of the synthesized and measured flyover for the 2nd trajectory.

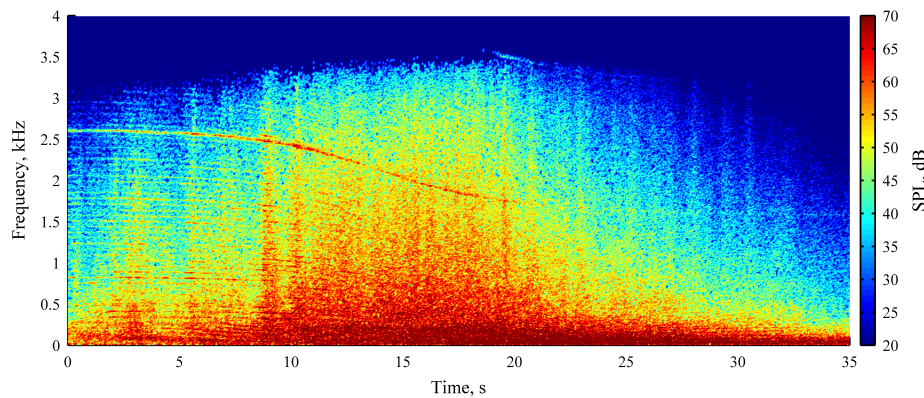
7.3.2 Discussion

Source noise prediction related differences

Differences between measurement and prediction sound metrics are known to exist. For instance, similar noise prediction methods were used and compared to measured certification values of aircraft in literature.⁽¹²³⁾ That analysis showed similar deviations for take-off and sideline angles. ANOPP differences with respect to dedicated measurements are published as well.⁽¹²⁴⁾ Furthermore, similar results are found for the PANAM empirical noise prediction model.⁽²⁹⁾ Consequently, the differences in sound metrics reported here are in line with the state-of-art in empirical source noise prediction.



(a) Synthesis



(b) Measurement

Figure 7.4: Spectrograms of the synthesized and measured flyover for the 3rd trajectory.

It can be noted that low frequency sound, i.e. frequencies up to 500 Hz, is underpredicted in all synthesized spectrograms. This can be attributed, to some extent, to low frequency background noise that is not included in the synthesis. Due to the use of A-weighting, see appendix B, low frequency differences will not manifest themselves severely in the accumulated noise metrics of table 7.1. Hence, empirical source noise prediction tools may calculate similar A-weighted noise metrics whilst different spectra are present.* Since noise metrics are used to validate and verify empirical noise models it may be very hard to assess those predictions at low frequency.

* A similar effect occurs in EPNL calculations were sound below 50 Hz is not included in the accumulated noise metric.

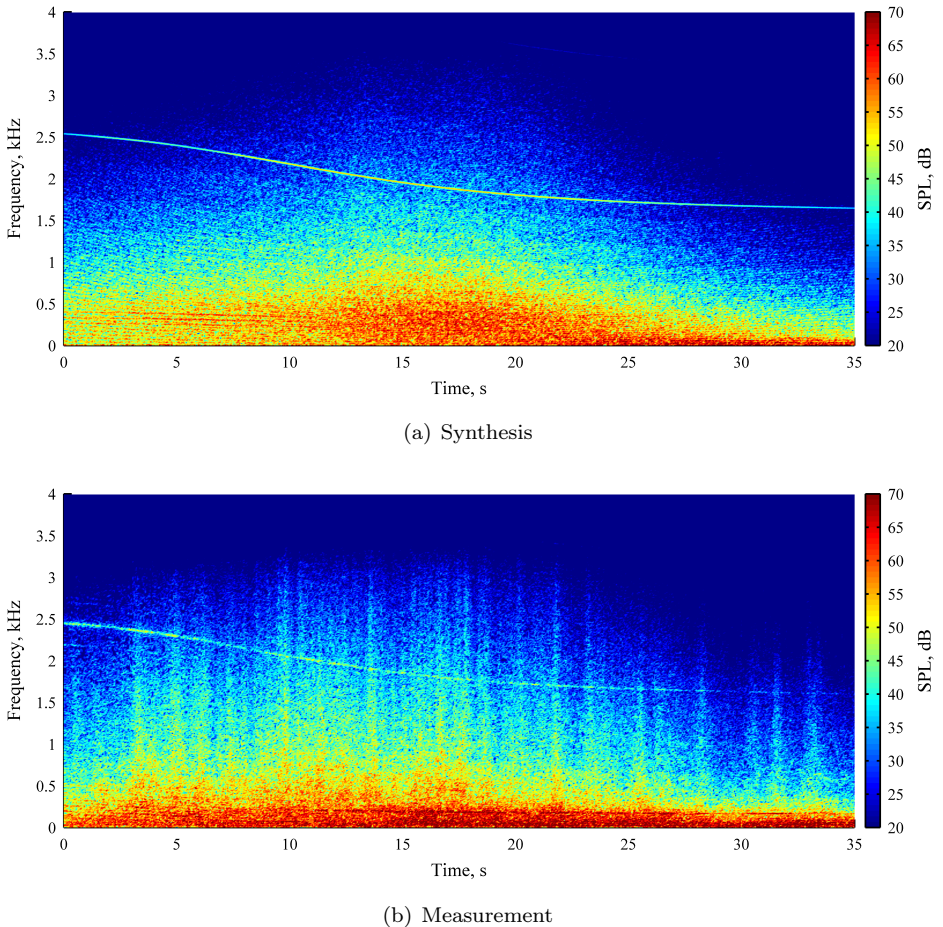


Figure 7.5: Spectrograms of the synthesized and measured flyover for the 4th trajectory.

Differences in the broadband component from 500 Hz up until the 1st BPF are larger, in general, for increasing frequency. On first sight the differences seem small, especially for the 1st flight. For the 3rd flight the differences are relatively large. Close observation of figure 7.4 reveals that at the moment when the aircraft is closest, i.e. around 15 s, the measurement contains more broadband sound around the 1st BPF. The spectrum above the 1st BPF tone contains even larger differences. In this range, the synthesis sound level is approximately 40 dB whilst the measurement is roughly 10 dB higher. Broadband noise in this spectral area, especially for the considered take-off conditions, the spectral domain of fan noise generated noise.

Tonal noise content forms another (audible) difference between the synthesis and measured result. The synthesized 1st BPF tone is, unlike the measurement, domin-

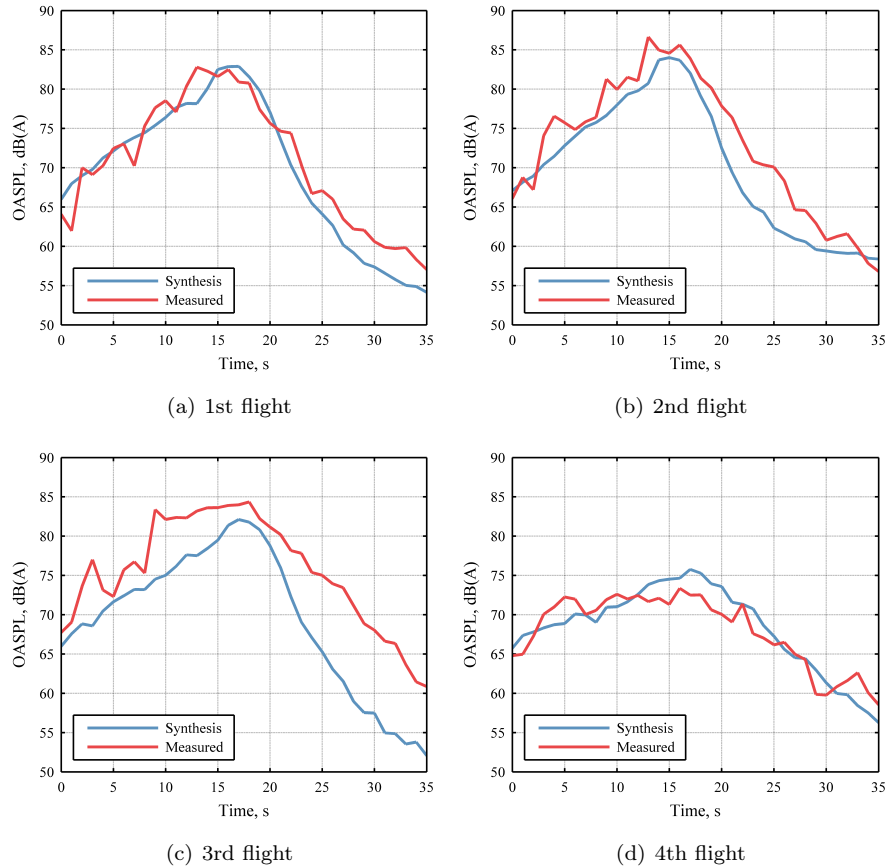


Figure 7.6: Differences in the sound levels between the synthesized and measured data.

antly audible as the amplitude is overpredicted. Buzz-Saw tones are overpredicted for all flights except for the 3rd. Two feasible explanations exist. The first is that a slightly different power setting between the flyovers is not captured (or not well enough) by the current methodology. Buzz-Saw is susceptible to small changes in power setting. A second explanation might be that the acoustic liner attenuation is underpredicted.

Propagation related differences

The 1st BPF tone is very clean, i.e. not diluted by disturbances in amplitude or phase. Tonal fluctuations at the source were added in literature⁽¹⁰⁶⁾ to predictions, but these fluctuations were largely masked by the broadband content. Therefore it is believed that disturbances along the propagation path, for instance turbulence, are

causing the difference between synthesis and measurement. Literature⁽¹²⁵⁾ indicates that turbulent spectral broadening can occur during propagation. The effect is to effectively distribute tonal sound energy to other nearby frequencies. A method to calculate these effects, together with some measured results, can be found in literature.⁽¹²⁶⁾

Variations in the sound level, i.e. the vertical lines visible in the spectrograms, are thought to be a propagation effect as well. It is not yet clear what the basis of this phenomena is, although wind-gusts and/or turbulence are suspected.⁽¹²⁵⁾ The spectrograms reveal that this effect seems frequency independent and acts as a time-varying gain. As such, it is suspected that this effect is most likely caused by gusts rather than turbulence since turbulence has a frequency dependent behavior.^(27;65;126)

A prominent difference is distinguished in the ground interference effect. The synthesized results reveal a ground interference at high frequencies, albeit for a grass surface, whereas this is not the case for the measured sound. This interference pattern causes a 'rasping' sound in the synthesized results. The absence of this effect in the measurement is contributed to turbulence as the coherence between the direct and ground reflected ray is affected. Theoretical predictions⁽⁶⁵⁾ of this effect were applied in synthesis before.⁽¹²²⁾ They showed that it is possible to remove the high-frequency part of the interference pattern. However, the employed technique was tedious since its effect was included by modifying the source noise prediction to compensate the interference effect. How to include turbulence-induced coherence loss effects using a VDL is postponed until chapter 8.

To examine the influence of the uncertainty related to some of the propagation input parameters used in the synthesis, small variations have been applied. As such, it is possible to see if such variations can explain the observed differences. The results are quantified here by the differences for both the $L_{A,max}$ and SEL sound metrics. The ground surface was varied by varying the effective flow resistivity and thereby the surface impedance. The effective flow resistivity was changed from $250 \text{ kPa/m}^2 \cdot s$ to both 125 and $300 \text{ kPa/m}^2 \cdot s$, a typical range for grass surfaces (see table 3.1), to assess the audible differences. Deviations were in the order of $\pm 0.4 \text{ dB(A)}$ for all flights, audible differences were not noticed. Relative drastic changes to different surfaces, i.e. a concrete or snow surface, do lead to audible differences. Given the fact that the noise monitoring station is on a grass field, such large changes are deemed unreasonable.

A similar procedure was executed for atmospheric absorption. Changes in absorption were simulated by changing temperature ($8\text{--}13^\circ C$) and relative humidity (85%–100%). These values are within reasonable (reported) bounds for the average atmospheric conditions of that day and period. These variations made no audible difference. This is quantified by deviations in the order of $\pm 0.1 \text{ dB(A)}$ for the first three flights and $\pm 0.35 \text{ dB(A)}$ for the 4th flight due to the larger distance to the noise terminal.

To assess the uncertainty of the measured ground track of the aircraft, deviations of ± 50 meter were applied to the ground track. This leads to a different spherical spreading and results in a deviation of $\pm 0.2 \text{ dB(A)}$ for all flights. Not audible dif-

ferences were reported. If the altitude of the aircraft is assumed to have a similar uncertainty, i.e. ± 50 meter, this would result in larger deviations for the first three flights ± 0.5 dB(A) than for the fourth flight ± 0.2 dB(A). This difference is attributed to the relative close distance at which the first three flights pass the noise terminal. A deviation of 50 meters ground track and altitude was arbitrarily chosen and may be considered as large, especially for the altitude.

Overall, this rough quantification of uncertainty lead to maximum deviations of about ± 1 dB(A) for all flights. A deviation of ± 1 dB(A) is extremely hard to notice as an audible difference. Therefore, it is believed that the reported audible and visible spectral deviations are caused by inadequate modeling of atmospheric absorption, ground impedance or trajectory deviations but due to source noise prediction.

7.4 Conclusion

Audible differences remain between synthesized and the measured results. With the current state-of-art empirical source noise prediction tools, it is possible to approximate the audible noise in a noise terminal for a departure. Consequently, the current combination of source noise prediction and synthesis gives an indication on what to expect rather than to exactly reproduce a measurement or real-life experience. If a close reproduction is required, it might be best to use a technique based on measurements.

The differences between the fourth flight and the first flight, i.e. the experienced difference between two departure routes, is adequately simulated by the current synthesis technique. Hence, with the help of an aircraft noise synthesis technique it is possible to evaluate (gross) differences between different departure routes. The effect of new departure routes could thus not only be studied by looking to changes in noise contours but be experienced in the VCNS.

Chapter 8

Turbulence-induced coherence loss and ray tracing parallelization

Two shortcomings emerged from the analysis of chapters 6 and 7. The first was that the ray tracing algorithm was too slow for real-time implementation, the second that the effect of turbulence on ground reflection was absent leading to a 'rasping' sound in auralizations. Both topics are treated in this chapter and solutions are proposed.

8.1 Turbulence-induced coherence loss in ground reflection

8.1.1 Current methodology

The current propagation doctrine in virtual acoustic simulation adds the ground reflected wave using the mirror source approach. For auralization this means that two waves need to be synthesized (transformed from frequency to time domain) and added at the listener position. Due to the difference in ray path length, the ground reflected waves reach the observer at a phase offset with respect to the direct wave. This causes an amplitude enhancement or cancellation depending on the phase difference. As the source (aircraft) is moving, the incidence angle and path length are constantly changing, leading to a continuously changing phase difference resulting in the characteristic interference pattern.

When including ground interference effects in the aforementioned way in auralization, in absence of turbulent atmospheric disturbances, the interference pattern is very pronounced. This is only experienced in ideal situations that hardly occur in real flyover situations (to the best of the author's knowledge). For hard ground surface

conditions the interference effect is even more present since both waves are assumed to be coherent and the amplitude of the ground reflected wave is hardly damped by the ground (see figure 3.5).

One of these side effects is the modulation of tonal noise sources of an aircraft. Due to the ground interference the tone is distinctively modulated in amplitude. Especially when the aircraft is flying directly overhead this becomes noticeable and might lead to an improbable representation compared to everyday experience. This effect is reduced in the case of an acoustically soft ground since the amplitude of the ground reflected wave is reduced. Furthermore, Acoustic 'beating' has also been reported⁽⁹⁾ to occur due to differences in Doppler shift between the engines. These effects are, in real life, diminished by coherence loss due to phase disturbances caused by turbulence.

Due to the absence of turbulence, a ground interference pattern was presented in chapter 7 that provided a 'rasping' sound effect. The auralization was compared to measurements that, upon inspection, did not demonstrate this effect. This measurement was executed at 10 meters altitude, a common practice for noise monitoring stations, to minimize interference by utilizing the effect of turbulence.

By including an acoustically soft ground reflection in auralization, these side effects are usually already diminished although not completely gone. To get a closer match to everyday experience, thus eradicating unexpected audible side effects, it is necessary to include the effect of turbulence on ground reflection. In literature⁽¹²²⁾, this effect was included by correcting the source spectrum to fill in the interference dips. The resulting very long filter kernel prohibits this approach for inclusion in real-time auralizations. Furthermore, such an approach does not comply with the current doctrine in aircraft noise auralizations where the source, propagation and listener effects are separately treated. Therefore a new method is proposed to treat these shortcomings.

8.1.2 Coherence function and implementation in auralization

The ground interference effect of equation 3.21 is implicitly included in auralization by the difference in path length (r_1 and r_2 of figure 3.4). A phase offset occurs when the two waves reach the microphone position since the travel time of the ground reflected ray is always larger than that of the direct ray. This effect is explicitly apparent when calculating the root-mean-square (rms) of equation 3.15(see appendix A, specifically equation A.18),

$$p_e^2 = \frac{1}{r_1^2} + \frac{|Q|^2}{r_2^2} + \frac{2|Q|}{r_1 r_2} \cos(k(r_2 - r_1) + \phi). \quad (8.1)$$

The third term includes the interference effect. The cancellation and reinforcement occurs due to the cosine term depending on the phase. If this factor is taken into account, the sound waves are added in a coherent fashion. If the phase of the rays is affected by turbulence, the coherence between the two signals is diminished. This results

in a modification of the interference. To include this effect, Clifford and Lataitis⁽¹²⁷⁾ introduced the coherence factor T_c in equation 8.1,

$$p_e^2 = \frac{1}{r_1^2} + \frac{|Q|^2}{r_2^2} + \frac{2|Q|T_c}{r_1 r_2} \cos(k(r_2 - r_1) + \phi), \quad (8.2)$$

where T_c ranges from zero to one and follows from an extensive analysis assuming that the phase and amplitude fluctuations are Gaussian distributed. As such, the coherence factor T_c can nullify the interference and is calculated by,

$$T_c = e^{-\sigma_t^2(1-\rho_c)} \quad (8.3)$$

$$\rho_c = \frac{\sqrt{\pi}L_0}{2h_d} \operatorname{erf}\left(\frac{h_d}{L_0}\right) \quad (8.4)$$

$$\sigma_t^2 = A\sqrt{\pi}\langle\mu^2\rangle k^2 r_1 L_0, \quad (8.5)$$

where k is the wave number, σ_t is the phase fluctuation variance and ρ_c is the phase covariance which is a function of the outer scale of turbulence L_0 . The phase covariance depends on the maximum path traverse distance h_d defined by,

$$\frac{1}{h_d} = \frac{1}{2} \left(\frac{1}{h_s} + \frac{1}{h_r} \right), \quad (8.6)$$

where the subscripts s, r denote the source and receiver height. Daigle found that half the value for h_d , as calculated by equation 8.6, provided better results⁽¹²⁸⁾, which is therefore applied. The phase fluctuation variance depends on the fluctuating index of refraction $\langle\mu^2\rangle$ and coefficient A follows as,

$$\begin{aligned} A &= \frac{1}{2} && \text{if, } d \gg kL_0^2 \\ A &= 1 && \text{if, } d \ll kL_0^2, \end{aligned}$$

where, d is the x-distance from the source to the observer, i.e. $d = x_m - x_s$ using the definition of figure 3.4. The fluctuating index of refraction can include both temperature and wind variations. It is defined as the variance of the index of refraction as used in ray tracing (η of chapter 3) and its value is much smaller than one, i.e. $\langle\mu^2\rangle \ll \eta^2$ thus $\langle\mu^2\rangle \ll 1$. Although the current model is strictly valid for temperature fluctuations only⁽⁶⁵⁾, wind fluctuations and/or different spectra (von Karman instead of Gaussian) could be used^(65;66). However, the objective of this study is not to reinvent the turbulence model, but to apply the behavior to auralization using a proper method. Therefore we stick to the relatively simple Gaussian method.

Since the interference term is included implicitly in auralization, a method was devised to include the effect of (de-)coherence due to turbulence on ground reflection. This is not trivial since transforming T_c into a filter, and applying it in equation 3.15 to the ground path, would result in an absence of the ground reflected sound in cases when T_c is zero. In other words, the ground reflected wave would be completely lost instead of an incoherent addition. The difficulty in auralization is that T_c should still be applied to the ground reflected term since this is the only way to reduce the ground interference effect.

To solve this issue we propose to counterbalance this effect by enhancing the direct wave. Consequently, we need to apply a filter following a reciprocal behavior of T_c to the direct wave. The form of this filter R_c must be established from an equation, similar to equation 3.15, of the following form,

$$p = R_c \frac{e^{ikr_1}}{r_1} + QT_c \frac{e^{ikr_2}}{r_2}, \quad (8.7)$$

where, R_c is the reciprocal filter that should counterbalance the loss of the ground reflected wave should T_c become zero (high-frequencies, strong turbulence). In that case the interference pattern is modified by T_c , which is consistent with the third (cross) term of equation 8.2. Calculating the rms of equation 8.7 yields the following behavior,

$$p_e^2 = \frac{R_c^2}{r_1^2} + \frac{|Q|^2 T_c^2}{r_2^2} + \frac{2R|Q|T_c}{r_1 r_2} \cos(k(r_2 - r_1) + \phi), \quad (8.8)$$

where the difference with equation 8.2 is the inclosion of T_c^2 in the second term and R_c in all terms. In our auralization approach the effect of turbulence on ground reflection is included by filter functions. Therefore the gain and time-delay remain unaffected. Consequently, the following equality can be established by comparing the numerators of equations 8.2 and 8.8,

$$1 + |Q|^2 + 2|Q|T_c = R_c^2 + (|Q|T_c)^2 + 2|Q|R_cT_c, \quad (8.9)$$

where, the left hand side of the equality is the desired behavior due to the filter terms in equation 8.2 and the right hand side due to the proposed reciprocal approach. R_c can be solved and yields (retaining the positive root),

$$R_c = -|Q|T_c + \sqrt{|Q|^2 + 2|Q|T_c + 1}. \quad (8.10)$$

By using R_c for the direct ray, it is possible to correct the loss of the incoherent addition when applying T_c to the ground reflected ray. Due to the fact that T_c is a relative smooth function, it is possible to use a relatively short filter. Consequently, this method is applicable for real-time implementation in the current virtual acoustic simulators.

8.1.3 Results

To verify the method, a test case is considered simulating a straight and level aircraft flyover (velocity of 100 m/s at 200 meters altitude). Spherical spreading losses and absorption are included ($T = 15^\circ C$, $p = 101.325 \text{ kPa}$, $RH = 80\%$). The source is a white-noise signal of 140 dB. The microphone height is 1.8 meter.

Usually, for horizontal propagation, the outer (inertial) scale of turbulence L_0 is assumed to equal the source height or receiver height⁽⁶⁵⁾. A commonly used value is 1.1 m, as deduced from measurements.⁽¹²⁹⁾ It is reported⁽⁷³⁾ that this value, in case of ground reflection, should be taken as the microphone height within a range of 1 to 7 meter. Therefore this parameter is assumed to equal the microphone height, i.e. $L_0 = 1.8 \text{ m}$. The filters are realized with 128 taps. The ground surface is comparable to roadside dirt ($\sigma_e = 550 \text{ kPa/m}^2 \cdot s$), which is not too soft and therefore leads to clear interference patterns, thereby providing an adequate test of the method. A typical fluctuating refractive index range is from $\langle \mu^2 \rangle = 1 \cdot 10^{-6}$ (weak turbulence) to $\langle \mu^2 \rangle = 1 \cdot 10^{-4}$ (strong turbulence).⁽⁶⁵⁾ To test the reciprocal filter technique, a medium level of $\langle \mu^2 \rangle = 1 \cdot 10^{-5}$ is used in this study.

For this case, an example of the transfer functions associated with the individual filters is plotted in figure 8.1 for a ray incidence angle of 15 degrees. Figure 8.1 illustrates the form of both the transfer function of the coherence function (T_c) and the reciprocal filter (R_c). For a non-turbulent atmosphere the coherence and reciprocal transfer functions are equal. The reciprocal filter transfer function is not allowed to become smaller than unity because it would otherwise eliminate the direct ray contribution. The transfer function of the atmospheric absorption filter has been included in these figures because it is applied to both the direct and ground reflected ray. This

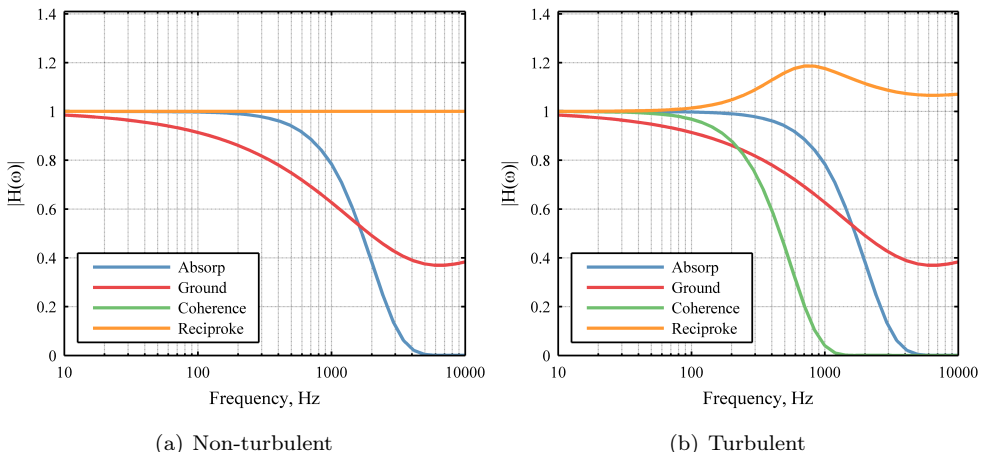


Figure 8.1: Transfer functions in non-turbulent and turbulent atmospheric conditions.

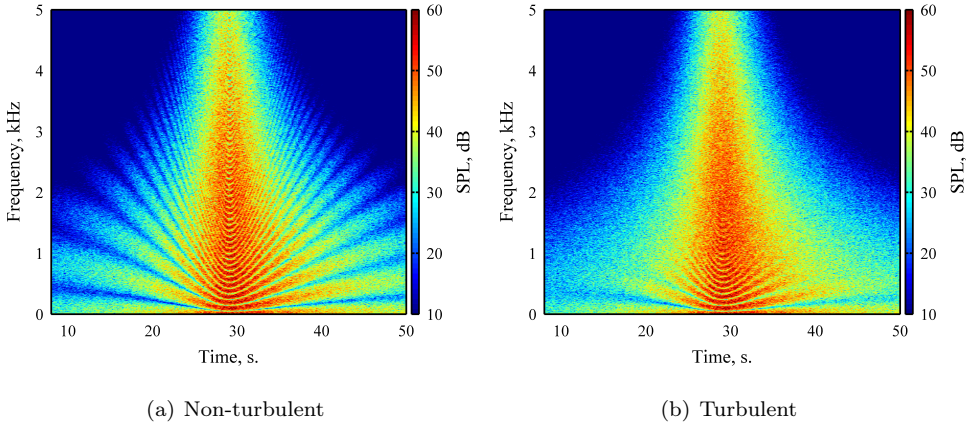


Figure 8.2: The spectrograms for a non-turbulent and turbulent atmospheric conditions.

does not impact the modeling of the turbulence effect. The resulting spectrograms of this (pseudo-) flyover, note that currently the aircraft source spectrum and directivity are ignored by assuming white noise, are shown in figure 8.2. The audible results are available as download from the internet, see appendix E or table E.4. The spectrograms in figure 8.2 both show the ground interference pattern, although the interference pattern for the non-turbulent case is more pronounced. This is due to the coherent assumption of the interfering rays. For the turbulent atmosphere the ground interference pattern has been removed above 2 kHz. The overall effect on flyover noise metrics like $L_{A,max}$ and SEL is small, in the order of 0.2 dB(A). However, there are audible differences. This illustrates the importance of modeling small effects (in the absolute dB sense) that add to the overall perception of an auralization.

Figure 8.3 compares the theoretical calculations from equation 8.2 to the synthesized results using the reciprocal method. Figure 8.3 shows the interference patterns at discrete ray incidence angles (θ). The synthesis results follow from the reciprocal approach, whereas the theoretical results are from the calculation. The two results match very well and the reciprocal method follows the theoretical behavior closely. Noteworthy is the incoherent addition present at higher frequencies at 45 and 90 degrees in case of the turbulent atmosphere. Longer filters, i.e. up to 1024 coefficients, did not further affect the difference between theory and synthesis in figure 8.3.

The proposed method is used to evaluate if the mentioned artifacts (tonal modulation and rasping sound) are positively affected. By simulating the same flyover, using a single source tone of 2000 Hz, results of the proposed methodology on tones are assessed. These audible tonal results are available as download from the internet, see appendix E or table E.4. The ground surface is changed to simulate an acoustically hard reflection to maximize the ground interference modulation.

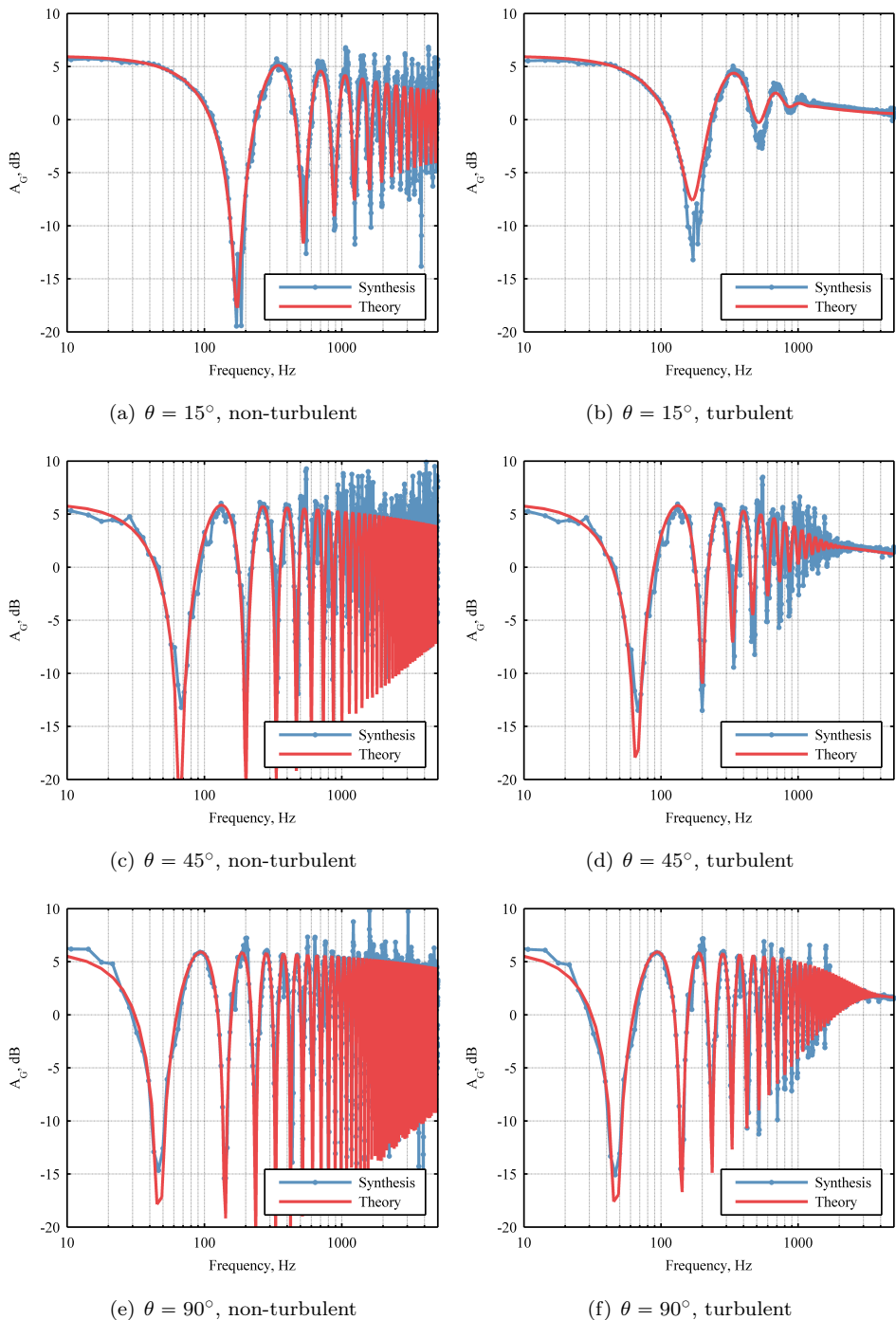


Figure 8.3: Ground interference at various incidence angles in non-turbulent and turbulent conditions.

By applying a Hilbert transform to the auralized waveform, constructing an 'analytic signal'^(106;130), the amplitude and frequency modulation are tracked. The amplitude shows, in figure 8.4, the combined effect of spreading, absorption and ground interference. From figure 8.4, it is deduced that the amplitude modulation of the tone at

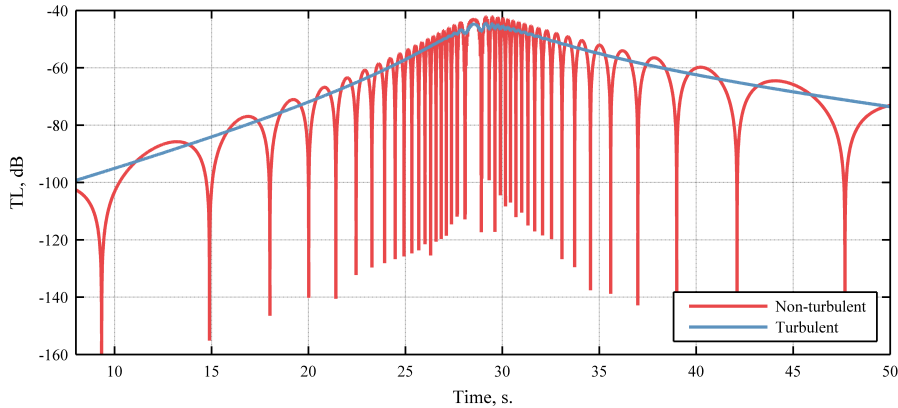


Figure 8.4: *Transmission loss of a 2000 Hz tone in the simulated turbulent and non-turbulent conditions.*

the listener is strong in the case without turbulence, especially near the time of the flyover (25-32 s). The amplitude can easily vary 60 dB within a few seconds, which is clearly audible. Notice that the amplitude is not symmetric around the time of the aircraft passage (28 s), because the Doppler shift has lowered the perceived frequency at the listener. Due to the effective lower frequency of the tone, the atmospheric absorption has decreased leading to higher amplitudes. In case of turbulent atmospheric conditions, the incoherent addition of roughly 3 dB due to the ground is noticeable throughout the entire flyover. Only during the passage of the aircraft directly overhead, i.e. short propagation distance, some of the coherent addition remains.

The audible result resulting from the simulation including the effect of turbulence-induced coherence loss in ground reflection is more in line with real-life experience of flyover noise. Tonal modulation is masked by the broadband content of the signal. However, in case of auralizations utilizing a hard ground reflection the tonal modulation can still be noticed, despite the broadband content, if the effect of turbulence on ground reflection is not included. Therefore the proposed method is attractive since it offers a way to limit this effect based on physical arguments.

Chapter 7 reported an audible rasping sound due to the ground interference effect. It was hypothesized that this was due to the absence of turbulence. We are now able to revisit that hypothesis and see if the proposed method improves the audible effect. To that end, the analysis of chapter 7 is repeated for flight number two of that study. That flight is a departing Boeing 747-400 from Schiphol, which was auralized and compared to measurements of a noise monitoring station to validate our auralization capabilities. Although the radar tracks were available, weather information

was limited. The variance in temperature or wind were not available during those measurements, therefore a turbulence level had to be assumed. Consequently, the same value ($\langle \mu^2 \rangle = 1 \cdot 10^{-5}$) is used. Regarding the outer scale of turbulence, the microphone height was used but limited to 7 meters, i.e. the maximum as indicated in literature.⁽⁷³⁾ Hence, the results are only suited for a qualitative comparison to validate the hypothesis that the rasping sound in the auralization was caused by the absence of this turbulence effect. The audible results is available as download from the internet, see appendix E or table E.4. Figure 8.5 shows the corresponding spectrogram of the simulation, inclusive of turbulence, and can be compared to the original synthesized and measured result of figure 7.3 at the noise monitoring station.

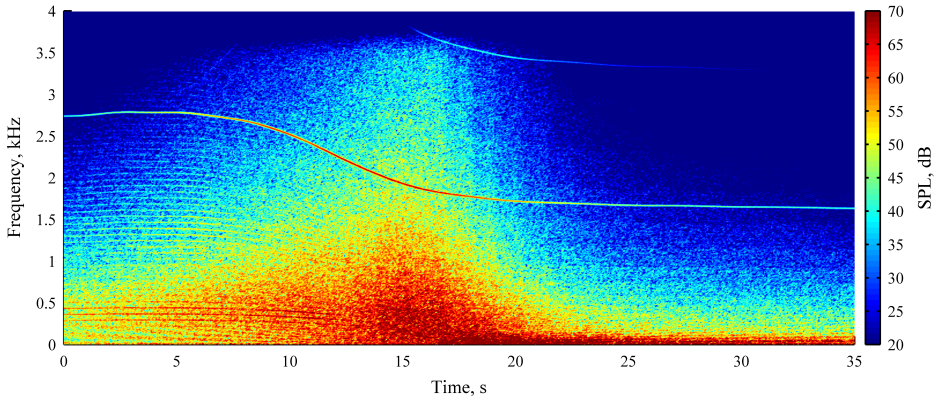


Figure 8.5: The modified ground reflection due to turbulence for flight 2, i.e. figure 7.3.

It is observed that the ground interference pattern is diminished when the turbulence is included and, consequently, matches the audible measured result a lot better. When listening to the results it is noted that the rasping sound has, to a large extent, disappeared. This confirms that including the effect of turbulence on ground reflection in auralizations is important.

8.1.4 Conclusions

A novel method is proposed to include the coherence loss effect with a relative short filter implementation. The method performs well and follows the theoretical predictions closely. Although a simple Gaussian turbulence model was used, the proposed solution is equally capable to include a more advanced turbulence model.

In case of auralizing strong tonal components of the aircraft, the ground interference pattern causes a modulation of the tonal amplitude that is not experienced in real-life. The current method simulates an incoherent addition thereby diminishing the modulation. When comparing results from a noise control monitoring station to auralizations, an audible difference was noted which was attributed to the absence of

turbulence in the simulation. By using the current method for inclusion of the effect of turbulence on ground reflection, this audible difference has been resolved. Consequently, the proposed method forms an essential addition to modeling the behavior of ground interference in auralizations.

8.2 Ray tracing parallelization

8.2.1 GPU acceleration

The use of a straight ray path allows the calculation of propagation effects in real-time, which makes it applicable for virtual acoustic simulators. Chapter 6 concluded that including curved rays proved to be impossible due to the computational expense, which was only feasible if faster algorithms exist.

Ongoing advances in Graphics Processing Unit (GPU) technology allow parallelizing algorithms to accelerate the computation. Therefore it was studied if acoustic ray tracing could benefit from this technology. One of the drawbacks, from a GPU stand point of view, is that ray tracing algorithms may be concerned with an imbalanced work load. Specifically, atmospheric effects may cause particular rays to have a long calculation time compared to other rays. This results in a workload imbalance that cannot be efficiently accommodated on the GPU. To that end, a solution was developed by utilizing both the multi-core CPU (Central Processing Unit) and the GPU. The resulting framework that was created is called Glinda and created in cooperation with the TU Delft faculty of Computer Science.

Glinda is used here to calculate the propagation input for a typical aircraft flyover noise synthesis. Consequently, it is evaluated if the performance provided by a GPU implementation is sufficient for the potential use in real-time auralization applications of the framework of figure 6.1.

8.2.2 Glinda framework

Under particular atmospheric conditions, the sound speed profile may contain an acoustic duct that bends rays upwards and downwards as illustrated in figure 8.6. These acoustic ducts can also occur near the ground if the sound speed profile includes an inversion. If a source is at an altitude where these ducted rays occur, the computation time is adversely effected. The formation of an acoustic duct forms a thorough test to see what gains in computational efficiency can be obtained by parallelization because the ray tracing workload is heavily imbalanced. A well balanced workload is formed if no acoustic duct is present, i.e. all rays have approximately the same amount of computational steps. The resulting workload is shown in figure 8.7(a). In this situation, Glinda parallelizes the computation on the GPU or on the multi-core CPU, because the whole computation can be evenly distributed on the processing cores of the underlying processor. If an acoustic duct occurs, as shown in

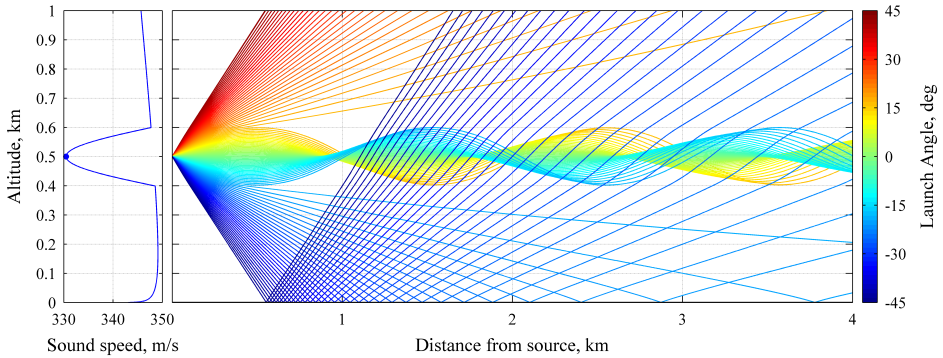


Figure 8.6: *Rays trapped in an acoustic duct. The acoustic duct region can be distinguished as the indentation in the sound speed profile.*

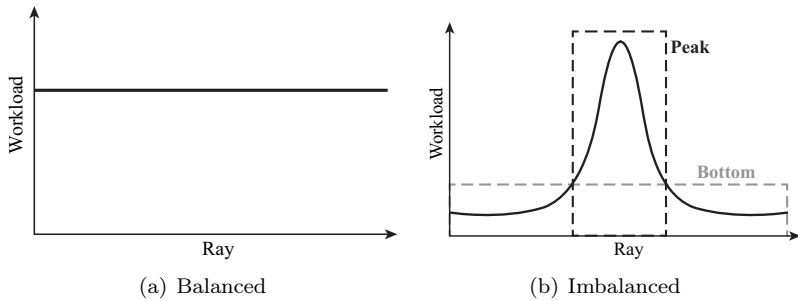


Figure 8.7: *The computational workload for balanced and imbalanced conditions.*

figure 8.6, the workloads of rays are imbalanced (see figure 8.7(b)). Most rays finish their simulation within a finite amount of steps whereas the rays trapped in the duct area need considerably more effort. These trapped rays pick finer time steps to ensure sufficient simulation accuracy, and finally form a narrow 'peak' out of the 'bottom' in the workload distribution. In order to efficiently parallelize the computation, Glinda adopts a heterogeneous approach by utilizing both the GPU and the multi-core CPU. As the 'bottom' part is wide and relatively flat, a GPU with hundreds or thousands of cores provides the massive parallelism suitable to accelerate this part. The CPU has fewer, yet larger and faster cores, but provides enough parallelism to efficiently process the narrow 'peak' part. Glinda cuts the whole computation into the 'bottom' task on the GPU and the 'peak' task on the CPU, and runs the two tasks again in parallel. The point where the bottom and peak box intersect is called the 'cut point'. By choosing and performing this task-mapping, Glinda provides a balanced execution of the workload. In turn, this leads to significant improvements in performance when compared against the CPU or the GPU used in isolation.

As the workload shape (flat or with 'peaks') depends on the atmospheric conditions,

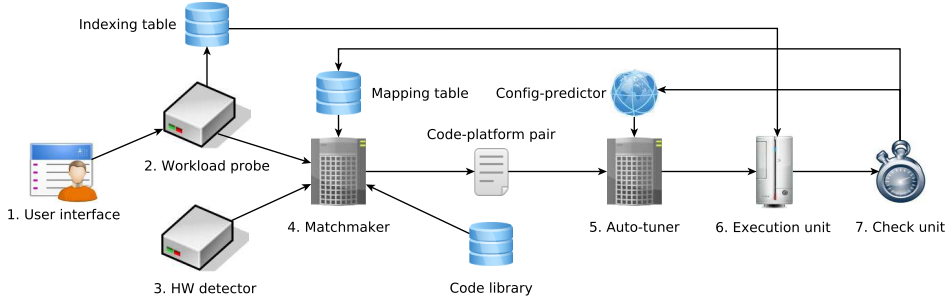


Figure 8.8: An overview of the individual components included in Glinda.

and the hardware platform can be altered or upgraded, Glinda is designed to be adaptive to all these changes. It automatically selects the right parallel solution and hardware configuration for the user. In addition, to ensure the best performance, the optimal execution configuration (e.g., the 'cut point' in the imbalanced workload distribution) is obtained.

Figure 8.8 shows an overview of Glinda. The 'User interface' receives the acoustic ray tracing parameters (e.g., the number of rays, atmospheric conditions, etc.), and interacts with the workload probe. The 'Workload probe' characterizes the workload distribution by sampling, and the 'HW detector' detects the available hardware resources. According to the outputs from the workload probe and the HW detector, the 'Matchmaker' proposes the optimal code-platform pair. The code candidates are stored in the 'Code library', which has three parallel solutions: all on the CPU, all on the GPU, and the use of both. The 'Auto-tuner' receives the selected code-platform pair and generates the optimal execution configuration. As this can be time-consuming, the 'Config-predictor' analytically detects a theoretical 'cut point', which can then be used to skip the time-consuming auto-tuner. The 'Execution unit' performs the real computation. If the results are correct and the computation time meets the user requirement, the 'Check unit' writes the code-platform mapping pair and the execution configuration into the 'Mapping table' and the 'Config-predictor', respectively, for future uses. When a workload distribution is irregular, we first sort the rays by their number of steps. The sorting result is stored in the 'Indexing table', and used by the execution unit to de-sort the output data.

8.2.3 Test application

Figure 8.9 shows the trajectories of the aircraft used to test Glinda. Here, the 1st flight resembles a slow climbing aircraft (1300 ft/min) and the 3rd flight resembles an aircraft that climbs twice as fast. The 2nd flight is at a constant altitude in the middle of the acoustic duct area. Consequently, if the 2nd flight is past the observer, the downwind conditions with a duct at the source altitude exist.

The aircraft is assumed to cover this trajectory in 60 seconds and is discretized every

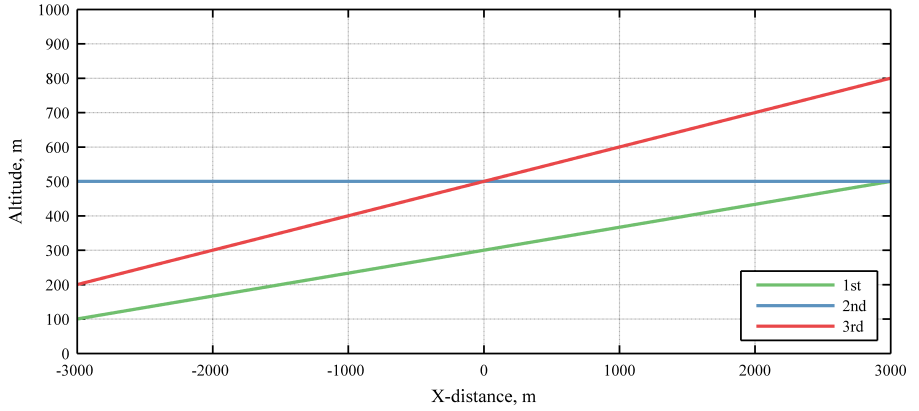


Figure 8.9: The 2D trajectories of the 3 flights flying from negative to positive x-distance. Negative x-distances imply upwind propagation conditions whereas positive implies downwind conditions.

100 milliseconds (ms.). Accordingly, there are 600 discrete source positions where ray tracing calculations have to be performed. Next, Glinda is used to calculate the propagation characteristics using a set of 1200 rays. For the current simulations, Glinda utilizes a dual-socket Intel Xeon E5645 six-core CPU (2.4 GHz, 24GB) and an NVIDIA Tesla C2050 GPU with 448 cores (1.15GHz, 3GB). For each case the sequential code and the parallel code (with Glinda) is evaluated. Both the sequential and parallel results coincide, thereby verifying the correct implementation of the parallel algorithm. Timing results of both implementations are plotted in figure 8.10.

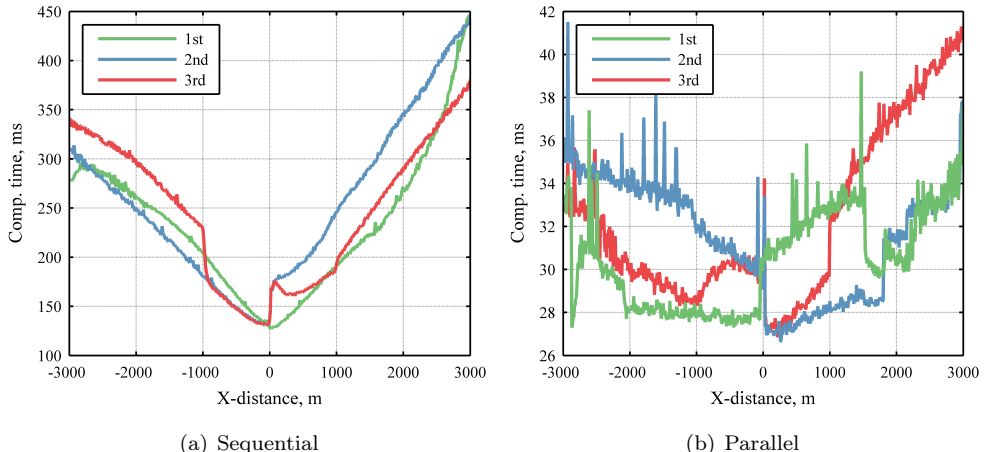


Figure 8.10: The computational times for the sequential and parallel implementation. Note the different scale on the y-axis.

From figure 8.10, the first observation is that for all trajectory points a significant speed-up is achieved. Since every 100 ms a new trajectory point is simulated, the sequential results are not ready when a new point has to be simulated. This is a show stopper for inclusion in real-time environments. For the parallel case the maximum computation time is approximately 42 ms. In comparison, the traditional straight ray path approach, as currently employed by virtual acoustic simulators, can be based on update intervals of 6 ms using multiple sources at the same time. However, a quasi real-time implementation could be achieved by interpolating between the propagation results for a single source when calculated in parallel using Glinda. Another difference is visible in the variation of the computation time for the trajectory points. Glinda balances the computation workload and, as such, the overall performance is more or less constant (the execution time difference is within 6 ms) compared to the sequential version. This makes it attractive for implementation in virtual acoustic simulation since, like for the straight path, the computation time demand remains predictable.

In figure 8.10(a), the 3rd trajectory shows a drop in computation time around -1000 m. At that position, i.e. 400 meters altitude and upwind conditions, the propagation characteristics change severely. If the aircraft is below that altitude, the inversion caused by the duct in upwind conditions, cause rays to have an imbalanced workload. In contrast, Glinda tuned the parallel implementation and balanced the workloads between GPU and the multi-core CPU at that trajectory point. If the aircraft is above this altitude, fewer rays are captured in the duct and the sequential computation time decreases. The reverse of this phenomenon occurs direct overhead where conditions change from upwind to downwind for the 1st and 2nd trajectory and more rays become trapped in the duct.

Figure 8.10(b) shows the performance of the parallel implementation. As a result of the balanced workload, the performance is largely improved. There is a sharp change in workload shape for all the trajectories when switching from upwind to downwind conditions. At these points Glinda adjusts the optimal allocation of rays to be calculated on the CPU or GPU through auto-tuning for the new input conditions. The resulting 'cut point' as found by auto-tuning is saved for future purposes. This saves the auto-tuning computation time although more optimal 'cut points' can be found at other trajectory points. This also causes the discrete changes in performance around point 400 (3rd flight), 450 (1st flight) and 480 (2nd flight). In the future we envisage that the 'auto-tuning' can be scheduled according to keeping track of the varying atmospheric conditions and/or the computation time.

The results as delivered by Glinda need to be interpreted before they can be applied in virtual acoustic simulation. This process, constructing gain and filter coefficients, will add some small overhead, but this is not any different than for the sequential implementation. In the effort described in chapter 6, eigenrays were iteratively searched to find the propagation characteristics since less rays could be used. The current parallelization allows the use of many rays and, depending on the GPU memory size, could house up to 6000 rays in our experiment. However, calculating more rays will increase the overall computation time again. Making use of 1200 rays already elim-

inated the use of eigenray finding since the ray density on the grid is sufficient. The results from Glinda can thus directly be interpolated upon using an 'Interpreter' for application in the simulator. By combining the ray tracing with the 'Interpreter' directly in the simulator, the grid of the ray tracing results does not need to be stored in temporary files for offline access. This saves another quarter of the parallel computation time. In addition, as the results on the GPU and the CPU have to be transferred and gathered on the host (the CPU) for the latter 'Interpreter', more computation time can be saved if only the results near the receiver is transferred. However, care is necessary to treat acoustic multiple paths and shadow zones since multiple rays or no rays can be present near a receiver.

8.2.4 Conclusions

The computational efficiency of the ray tracing was increased by a factor of (almost) 10 through parallelization. Noteworthy is that the variation in computational time is nearly flat, i.e. can be predicted within 6 ms. This is attractive for the use in real-time simulation where an update of relevant acoustic parameters is necessary at a finite interval. Due to these facts, it is expected that it is possible to include curved ray tracing in real-time outdoor acoustic simulations.

The use of Glinda is not limited to the current ray tracing implementation by Snell's law. The framework is equally able to accelerate other time-stepping (differential equation) based ray tracing algorithms, such as solving the Eikonal equation or application in a Gaussian beam method.

Chapter 9

Conclusions

The current dissertation had two objectives. The first was to examine the influence of atmospheric effects, such as wind, temperature and humidity, on noise contours. The second objective was to create an advanced tool chain for aircraft noise synthesis, make an analysis of the corresponding predictions and start improvements.

9.1 Conclusions

To analyze aircraft noise, an understanding of noise generating mechanisms and propagation must be obtained. A source noise prediction is comprised of more than the acoustic noise sources, but needs an understanding of the aircraft and engine operating conditions. If these are available, physics based or empirical models can be used to make a source noise prediction. Empirical models are especially suited for aircraft noise synthesis (or auralization) due to the short computational time. Despite the short computational time, such models are still able to simulate various aircraft operating conditions and configurations. The empirical source noise models used in this dissertation are, typically, inspired by the physical nature of the noise sources. For instance, Lighthill's analysis provided an understanding of jet mixing noise and his theoretical power law, relating jet velocity to acoustic pressure, is found (to some extent) in the empirical jet noise model.

During propagation of aircraft noise from the source to the ground, the sound is modified by three different effects. The first effect is the absorption of sound by viscous and molecular effects, i.e. atmospheric absorption. The second effect is the reflection of sound waves from the ground surface. The third effect is the geometric spreading of sound. Atmospheric absorption and geometric spreading both depend on the distance between the source and listener. Atmospheric absorption and geometrical spreading cause, in general, a transmission loss. The ground reflection modifies the sound perceived by the listener and depends on the ground constitution and incidence

angle. Ground reflection causes, depending on the frequency, an amplification or partial cancellation of the sound. By combining the aforementioned three effects, the total transmission loss during propagation is obtained. If the transmission loss is applied to the source noise levels, the sound level on the ground is predicted.

To inform and explain to a population where effects of aircraft noise are imminent, use is made of noise contours. Noise contours depict the resulting sound level on the ground using, typically, an exposure based noise metric such as the Sound Exposure Level (SEL) or the L_{DEN} . Calculations of noise contours are performed, for policy support purposes, using standardized noise contour models. Such noise contour models have to predict the accumulated effects of air traffic for a long period, for different routes, procedures, aircraft, atmospheres and periods during the day. Consequently, approximations are made to keep the model amenable.

Current noise contour methods include non-homogeneous atmospheric propagation effects in an empirical fashion. The empirical relation was found after measuring and averaging over the time span of a year. Therefore, daily differences due to varying atmospheric conditions can not be captured by this empirical relation. To evaluate the performance of the empirical model in the real-life situation, a standardized noise contour model was augmented with a ray tracing model.

The augmented Doc.29 model was used, by providing atmospheric effects on a single-event basis, to evaluate daily differences for an entire year. Comparing the standard Doc.29 solution to the ray tracing solution showed large changes in noise footprints for a single-event. However, for multi-event noise contours, such as the 58 L_{DEN} and 48 L_{DEN} as used for regulatory purposes, these effects proved to be minor.

The 58 L_{DEN} contour area, as predicted by ray tracing, was slightly smaller than the standard calculation, see figure 4.11. Furthermore, the difference could be attributed to a varying atmospheric absorption part and a relative constant ground reflection part. The 48 L_{DEN} contour is larger, if calculated by ray tracing, than the standard solution. This behavior is attributed to varying atmospheric conditions throughout the year leading to varying atmospheric absorption. The varying absorption caused monthly increments in contour area. These effects are most prominent underneath departure routes where, due to the flight procedure, the distance between the aircraft and ground is larger than for approaches.

For the prevailing atmospheric conditions in the Netherlands, at least for the simulated year of 2010 and multi-event considerations, the empirical model showed similar results as the ray tracing model. Furthermore, if the ambient atmospheric absorption conditions on the ground are taken into account, in the standardized model, the empirical results showed even more similarity to the ray tracing. For the latter condition the difference in the predictions, expressed in contour area per month, were smaller than 10%. For a yearly contour the difference was even smaller. Consequently, the use of the empirical modeling approach is thus valid for multi-event aircraft noise contour calculations for the considered atmospheric conditions. If single-event cases are considered, the augmented Doc.29 methodology allows the prediction of, with greater detail, the actual effects as perceived on the ground.

Besides noise contour plots, it is possible to convert an aircraft noise prediction into an audible impression of a flyover. The Virtual Community Noise Simulator (VCNS) allows to experience such an audible result. In the VCNS people are immersed in a virtual reality environment and subjected to a flyover. Hence, it is possible to experience both the visual and acoustic appearance of a passing aircraft. Such a scenario is based on either a measured recording, or on a synthesized aircraft flyover. The latter comprises a transformation of a prediction into an audible acoustic signal using signal processing elements such as a gain, filter and delay line. The results can be experienced on the VCNS system for psychoacoustic evaluation.

A transformation of predicted sound into an audible signal is known as aircraft noise synthesis or auralization. Software tools that synthesize aircraft noise often use the traditional straight ray path approach, which is only valid for a homogeneous atmosphere. To execute aircraft noise synthesis in a more precise way for a non-homogeneous atmosphere, a framework was constructed that includes the non-straight ray path effects. The framework, see figure 6.1, combines atmospheric propagation and source noise prediction to synthesize a flyover. By using the generic empirical noise models and ray tracing, it is now possible to simulate an arbitrary aircraft, flying an arbitrary trajectory through an arbitrary atmosphere.

Atmospheric propagation plays a more fundamental role in such a framework than intuitively envisaged since it alters both the source emission and receiver angle. By executing the propagation step before the synthesis stage, as is implied in the framework, the sound at the correct directivity angle is synthesized. The framework allows for multiple paths that may occur in downward refraction atmospheric conditions.

By simulating a flyover through a homogeneous and a non-homogeneous atmosphere, the functionalities of the framework were demonstrated. The source prediction was comprised of jet mixing noise of a CF6-80C2 engine and fan noise from an experimental Honeywell fan. Figure 6.9 show the resulting spectrograms. Propagation effects, such as shadow zones and multiple ray paths, are present in the audible signal and the corresponding spectrograms. The ground interference pattern is modified differently for upwind and downwind conditions with respect to the non-homogeneous case. For upwind conditions, the interference pattern is shifted upward. For downwind conditions the opposite behavior occurs as the interference pattern is shifted down. This is directly related to upward or downward bending of sound rays due to refraction.

Refractive effects are significant at shallow propagation grazing angles and a first indication on its relevance is based on the aircraft elevation angle. If the elevation angle is larger than 10 degrees, refractive effects are minute and negligible for the considered atmosphere. In other cases involving the auralization of low flying aircraft such as applying take-off power on the ground, braking using reverse thrust, unmanned aerial vehicles, military aircraft or other sources, it remains important to include refraction effects. The current application involved aircraft that flew directly over the listener. This resulted in equal noise metrics for the non-homogeneous and homogeneous atmosphere due to similar peak levels.

The current implementation of the framework is not fast enough for real-time implementation as the applied ray tracing algorithm formed a computational bottleneck. Using the abilities of the Graphics Processing Unit (GPU) of a computer, the computational load was decreased nearly 10 times. Besides being faster, the computation displayed a relative flat workload, which is favorable for real-time implementation. The resulting algorithm delivers approximately 20 ray tracing calculations per second, i.e. fast enough for a first integration attempt in real-time acoustic simulators.

The demonstration of atmospheric propagation effects in aircraft noise synthesis was for a fictitious aircraft source. To obtain an impression of the framework's capabilities, an assessment of four departure procedures near Schiphol has been conducted. It was shown that the measured difference in overall noise metric, that occur for large differences in ground tracks between different departure routes, is reproduced by aircraft noise synthesis. Although the differences in noise metrics between the measured and synthesized results were sometimes small, ranging from 0-4 dB(A), audible differences were always noted. The source noise prediction seems the most likely candidate to result in the reported differences.

Audible differences may not be surprising given the simplifying assumptions that underly the empirical noise models. Empirical noise predictions provide spectral content at a 1/3rd octave band level. This might not be enough to ascertain all the narrowband details that are typically found in a recording. An aircraft noise auralization can only be as good as the approximations used in the noise prediction, i.e. no rich audible details can be expected if they are not included in the source noise prediction.

Listening to the measured and synthesized tones revealed differences in amplitude prediction and the audible nature of the tones. The synthesized tones are predicted at a single frequency and therefore distinctively audible, which is not the case in a measured result. Another difference between the measured and synthesized signal is formed by the presence of the ground interference pattern of the synthesized signal. The interference pattern created a noticeable audible effect that is not noted in the measured results. Upon inspection, the measured result shows that the interference pattern is largely absent. The inability to model turbulence coherence loss was suspected to be the cause of this modeling shortcoming.

The aforementioned presence of the ground interference pattern is treated, in this dissertation by including turbulence-induced coherence loss. The coherence loss between the direct ray and ground reflected ray cause the interference pattern, at high frequencies, to be suppressed. A method was designed to include this effect using short filters. The results show that the theoretical behavior was closely resembled in the synthesized results. Furthermore, the amplitude modulation of tones by the interference pattern is diminished and the distinctive audible presence of the interference pattern was removed.

9.2 Future topics

Open challenges remain that should be addressed in the future. The listed topics in this section are merely a starting point for future research from the authors research perspective, experience and interests.

Current noise contour modeling algorithms rely on the Noise-Power-Distance (NPD) relations. Based on the description of noise sources included in this dissertation, it seems not that obvious to solely use Noise-Power-Distance (NPD) relations in noise contour algorithms. It is well known that airframe noise is proportional to airspeed (either a 5th or 6th power law) instead of power or thrust. Therefore the author suggests to investigate and include velocity dependencies, i.e. a Noise-Velocity-Distance (NVD) relation, concurrent with the NPD relations.

Aircraft noise synthesis is a small and emerging research area. As a result, aircraft noise synthesis capabilities have increased over the past years and are gaining in popularity. However, any prediction-based auralization starts with a trajectory and gasturbine prediction. Re-calculating the required thrust from a trajectory is not hard if an equilibrium of forces is assumed. This equilibrium might exclude some of the fine details that are required to further improve the audible results. Furthermore, estimating the actual flap setting from trajectory data is hard, although this is vital for the auralization of airframe noise on approach conditions. Smarter algorithms could be developed to this end.

Further improvements in airframe source noise modeling, such as including flap-side-edge noise and/or parasitic noise sources, would enhance the audible modeling of approaches. Besides implementing new sources, the resolution in source noise prediction can still be improved. In that light it might be good to study whether it is possible to include a higher frequency resolution than the *onethird* octave band in the (empirical) source noise predictions. Making an audible comparison between a narrow-band Computational Fluid Dynamics calculation result and a 1/3rd octave band empirical prediction, might indicate if frequency resolution is important.

Besides modeling options, a common benchmark of both predictions and synthesis results (possibly complemented by measurements), would aid future developers to assess their calculations and models.

In the current tool chain, the effect of shielding surfaces at the source are not included. Inclusion of shielding allows an integral evaluation of an aircraft design once the framework is included in an aircraft design tool chain. This would provide a new feedback loop to aircraft designers as they can actually evaluate the acoustic implications of their design.

Alternative models to include propagation effects, such as a PE model, could be utilized for auralization as well. This would circumvent some of the problems that ray tracing has with frequency dependent phenomena such as diffraction and turbulence. The effect of wind gusts on propagation is likely to explain some of the differences between measured and synthesized results. Other researchers have started an advanced simulation of propagation through turbulence using detailed calculations of

linearized Euler equations. The results of that study should provide more information regarding the effect of turbulence in propagation and will benefit future auralization studies.

An interesting propagation effect, that might enhance the audible perception of aircraft noise synthesis, is the spectral broadening of tones by the atmosphere. By means of turbulence along the propagation path, some of the tonal energy is redistributed to nearby frequencies. An evaluation of this effect was setup by narrow band filtering white noise to represent the tone using a very narrow band filter having a pass-band of a few Herz. The result indicated that this smearing out of the frequency content may have a perceptual impact. Although theoretical models are available that describe this phenomenon, from an auralization stand point (hence, a real-time calculation perspective) the implementation of this effect is not yet investigated.

Bibliography

- [1] G. G. Stokes. On the idea of refraction. *Report of the Britisch Association, Dublin*, pages 22–23, 1857, reprinted in Mathematical and Physical papers of G. G. Stokes volume 4, pages 110-111 in 1904.
- [2] J. Tyndall. On the atmosphere as a vehicle of sound. *Phil. Trans. R. Soc. London*, 164:183–247, January 1874.
- [3] O. Reynolds. On the refraction of sound by the atmosphere. *Roy.Soc. of London*, XXII:531–550, 1874.
- [4] M. J. Lighthill. On sound generated aerodynamically I: General theory. In *Series A, Mathematical and Physical Sciences*, pages 564–572. Royal Society of London, 1952.
- [5] M. J. Lighthill. On sound generated aerodynamically II: Turbulence as a source of sound. In *Series A, Mathematical and Physical Sciences*, pages 1–32. Royal Society of London, 1954.
- [6] M. Kroesen. *Human response to aircraft noise*. PhD thesis, Technical University Delft, 2011.
- [7] M. Huijs. *Building castles in the (Dutch) air*. PhD thesis, Technical University Delft, 2011.
- [8] C. Velarde. Outcomes of the aircraft noise non acoustic factors ANNA discussion group. In *ANERS 2011, Marseille, October 2011*, 2011.
- [9] S. A. Rizzi, A. R. Aumann, L. V. Lopes, and C. L. Burley. Auralization of hybrid wing body aircraft flyover noise from system noise predictions. In *AIAA Journal of Aircraft (ahead of print, pp. 1-13)*, doi: 10.2514/1.C032572, number AIAA-2013-0542, 2013.
- [10] W. Chapin. Goldserver, AuSIM3D Gold Series Audio Localizing Server System, User’s Guide and Reference, Rev. 1d,. Technical report, AuSIM Inc. Mountain View, CA, USA, October 2001.

-
- [11] A. D. Pierce. *Acoustics: An Introduction to its Physical Principles and Applications*. Acoustical Society of America, 1989.
 - [12] S. W. Rienstra and A. Hirschberg. *An Introduction to Acoustics*. Open source, via the homepage of Dr. Rienstra at Eindhoven University of Technology: <http://www.win.tue.nl/~sjoerdr/papers/boek.pdf>, accessed on 02-09-2013, version of 11 July 2013.
 - [13] G. J. J. Ruijgrok. *Elements of aviation acoustics*. VSSD, Delft University Press, 1999.
 - [14] J. Delfs. *Grundlagen der Aeroakustik: Basics of Aeroacoustics*. Open source, can be found through the DLR webpage of professor Delfs: http://www.dlr.de/as/Portaldata/5/Resources/dokumente/abteilungen/abt_ta/skript_GrundlagenAeroakustikWS1011.pdf, accessed 02-09-2013., version of 2010/2011.
 - [15] T. D. Rossing ed. *Springer Handbook of Acoustics*. Springer, 2007.
 - [16] S. Oerlemans. *Detection of aeroacoustic sound sources on aircraft and wind turbines*. PhD thesis, Technical University Twente, 2009.
 - [17] W. de Roeck. *Hybrid Methodologies for the computational aeroacoustic analysis of confined, subsonic flows*. PhD thesis, Katholieke Universiteit Leuven, 2007.
 - [18] D. I. Blokhintzev. *Acoustics of Non-Homogeneous Moving Media*. NACA TM-1399, 1956.
 - [19] J. E. Ffowcs-Williams and L. H. Hall. Aerodynamic sound generation by turbulent flow in the vicinity of a scattering half plane. *Journal of Fluid Mechanics*, 40(4):657–670, 1970.
 - [20] N. Curle. The influence of solid boundaries upon aerodynamic sound. *Proceedings of Royal Society of London A*, 231:505–514, 1955.
 - [21] J. E. Ffowcs-Williams and D. L. Hawkings. Sound generation by turbulence and surfaces in arbitrary motion. *Philosophical Transactions of the Royal Society of London*, 264(1151):321–342, 1969.
 - [22] C. K. W. Tam. Computational aeroacoustics: Issues and methods. *AIAA Journal*, 33(10):1788–1796, 1995.
 - [23] L. Morino. Is there a difference between aeroacoustics and aerodynamics? an aeroelastician’s viewpoint. *AIAA Journal*, 41(7):1209–1223, July 2003.
 - [24] D. T. Blackstock. *Fundamentals of Physical Acoustics*. Wiley, New York, 2000.
 - [25] A. Dowling. Convective amplification of real simple sources. *Journal of Fluid Mechanics*, 74(3):529–546, 1976.
-

-
- [26] D. G. Crighton, J. E. Ffowcs Williams, and I. C. Cheeseman. The outlook for simulation of forward flight effects on aircraft noise. In *3rd AIAA Aeroacoustics conference, 20-23 July, Palo Alto, California USA*, 1975.
 - [27] V. E. Ostashev. *Acoustics in Moving Inhomogeneous Media*. Taylor and Francis, 1st edition, December 1997.
 - [28] W. E. Zorumski. Aircraft noise prediction program theoretical manual parts 1 & 2. Technical Report TM 83199, NASA, 1982.
 - [29] L. Bertsch, S. Guerin, G. Looye, and M. Pott-Pollenske. The parametric aircraft noise analysis module - status overview and recent applications. In *17th AIAA/CEAS Aeroacoustics Conference 5-8 June, Portland, OR*, number AIAA-2011-2855, 2011.
 - [30] E. L. Bertsch. *Noise Prediction within Conceptual Aircraft Design*. PhD thesis, Technical University Braunschweig, 2013.
 - [31] L. V. Lopes and C. L. Burley. Design of the next generation aircraft noise prediction program: ANOPP2. In *17th AIAA/CEAS Aeroacoustics Conference 5-8 June, Portland, OR*, number AIAA-2011-2854, 2011.
 - [32] anon. Prediction of noise generated by fans and compressors in turbojet and turbofan engines. Technical Report 98008, ESDU, 2010.
 - [33] anon. Prediction of combustor noise from gas turbine engines. Technical Report 05001, ESDU, 2011.
 - [34] anon. Airframe noise prediction. Technical Report 90023, ESDU, 2008.
 - [35] M. J. T. Smith. *Aircraft Noise*. Cambridge Aerospace Series. Cambridge University Press, 2004.
 - [36] J. R. Stone. Interim prediction method for jet noise. Technical Report TM-X 71618, NASA, 1974.
 - [37] J. R. Stone. An improved method for predicting the effects of flight on jet mixing noise. Technical Report TM 79155, NASA, 1979.
 - [38] J. R. Stone. An improved prediction method for the noise generated in flight by circular jets. Technical Report TM 81470, NASA, 1980.
 - [39] J. R. Stone, E. A. Kresja, and B. J. Clark. Jet noise modeling for coannular nozzles including the effects of chevrons. Technical Report CR 212522, NASA, 2003.
 - [40] J. R. Stone, E. A. Kresja, B. J. Clark, and J. J. Berton. Jet noise modeling for suppressed and unsuppressed aircraft in simulated flight. Technical Report CR 215524, NASA, 2009.
 - [41] M. F. Heidmann. Interim prediction method for fan and compressor source noise. Technical Report NASA TMX-71763, NASA, 1979.
-

-
- [42] K. B. Kontos, B. A. Janardan, and P. R. Gliebe. Improved NASA ANOPP noise prediction computer code for advanced subsonic propulsion systems. Volume 1: ANOPP evaluation and fan noise model improvement. Technical Report NASA CR-195480, NASA, 1996.
 - [43] K. B. Kontos, R. E. Kraft, and P. R. Gliebe. Improved NASA ANOPP noise prediction computer code for advanced subsonic propulsion systems. Volume 2: Fan suppression model development. Technical Report NASA CR-202309, NASA, 1996.
 - [44] H. H. Hubbard (editor). Aeroacoustics of Flight Vehicles - Volume 1: Theory and Practice. Technical Report TR 90-3052, NASA, 1991.
 - [45] M. D. Dahl. Assessment of nasa's aircraft noise prediction capability. Technical Report TP 215653, NASA, 2012.
 - [46] SAE. Gas turbine jet exhaust noise prediction. Technical Report SAE-ARP-876 rev. E, Society of Automotive Engineers, 2006.
 - [47] J. J. Emmerling, S. B. Kazin, and R. K. Matta. Core engine noise control program. Vol 3: Prediction methods, suppl. 1: Extension of prediction methods; Final report. Technical Report FAA-RD-74-125, FAA, 1976.
 - [48] P. Y. Ho and V. L. Doyle. Combustion noise prediction update. In *5th AIAA Aeroacoustics conference, 12-14 March, Seattle, Washington USA*, number AIAA-1979-588, 1979.
 - [49] L. Hultgren. A comparison of combustor-noise models. In *18th AIAA/CEAS Aeroacoustics Conference 4-6 June, Colorado Springs, CO, USA*, number AIAA-2012-2087, 2012.
 - [50] W. Dobrzenski. Almost 40 years of airframe noise research: What did we achieve? *Journal of Aircraft*, 47(2):353–367, March-April 2010.
 - [51] M. R. Fink. Noise component method for airframe noise. In *AIAA 4th Aeroacoustics conference, October 3-5, Atlanta, Georgia, USA*, number AIAA-1977-1271, 1977.
 - [52] M. Pott-Pollenske, W. Dobrzenski, H. Buchholz, S. Guérin, G. Saueressig, and U. Finke. Airframe noise characteristics from flyover measurements and predictions. In *12th AIAA/CEAS Aeroacoustics conference, 8-10 May, Cambridge, Massachusetts, USA*, 2006.
 - [53] W. P. J. Visser and M. J. Broomhead. GSP - a generic object oriented gas turbine simulation environment. Technical Report TP-2000-267, NLR, 2000.
 - [54] H. W. Veerbeek, J. Nijmeijer, and D. H. T. Bergmans. Grondgeluid rondom schiphol (in Dutch). Technical Report TP-2008-569, NLR, 2008.
 - [55] H. W. Veerbeek and D. H. T. Bergmans. A long term low frequency noise outlook for aircraft during take-off. Technical Report TP-2009-266, NLR, 2009.
-

-
- [56] U. Ingard. *Notes on acoustics*. Infinity Science Press LLC, Massachusetts, 2008.
 - [57] A. D. Pierce. Aeroacoustic fluid dynamic equations and their acoustic energy conservation corollary with o_2 and n_2 vibrational relaxation effects included. *Journal of Sound and Vibration*, 58(2):189–200, 1978.
 - [58] L. C. Sutherland and H. E. Bass. Atmospheric absorption in the atmosphere up to 160 km. *Journal of Acoustical Society of America*, 115(3):1012–1032, 2004.
 - [59] L. C. Sutherland and H. E. Bass. Erratum: 'Atmospheric absorption in the atmosphere up to 160 km'. *Journal of Acoustical Society of America*, 120(5):2985, 2006.
 - [60] ANSI. Method for calculation of the absorption of sound by the atmosphere. Technical Report ANSI Standard S1.26-1995, American National Standards Institute, ed. 2009.
 - [61] L. B. Evans, H. E. Bass, and L. C. Sutherland. Atmospheric absorption of sound: Theoretical predictions. *Journal of Acoustical Society of America*, 51(5B):1565–1575, 1972.
 - [62] H. E. Bass, L. C. Sutherland, and A. J. Zuckerwar. Atmospheric absorption of sound: Update. *Journal of Acoustical Society of America*, 88(4):2019–2022, 1990.
 - [63] H. E. Bass, L. C. Sutherland, A. J. Zuckerwar, D. T. Blackstock, and D. M. Hester. Atmospheric absorption of sound: Further developments. *Journal of Acoustical Society of America*, 97(1):680–683, 1995.
 - [64] ISO. Acoustics - attenuation of sound during propagation outdoors. Technical Report ISO 9613-1:1993(E), International Organization of Standardizations, 1993.
 - [65] K. Attenborough, K. M. Li, and K. Horoshenkov. *Prediction of Outdoor Sound Propagation*. Taylor and Francis, 1st edition, 2007.
 - [66] E. M. Salomons. *Computational Atmospheric Acoustics*. Elsevier, 1st edition, 1999.
 - [67] H. H. Hubbard (editor). Aeroacoustics of Flight Vehicles - Volume 2: Noise Control. Technical Report TR 90-3052, NASA, 1991.
 - [68] C. I. Chessel. Propagation of noise along a finite impedance boundary. *Journal of Acoustical Society of America*, 62(4):825–834, 1977.
 - [69] U. Ingard. On the reflection of a spherical sound wave from an infinite plane. *Journal of Acoustical Society of America*, 23:329–336, 1951.
 - [70] G. A. Daigle, T. F. W. Embleton, and J. E. Piercy. Some comments on the literature of propagation near boundaries of finite acoustical impedance. *Journal of Acoustical Society of America*, 66(3):918–919, 1979.
-

-
- [71] M. Abramowitz and A. I. Stegun. *Handbook of Mathematical Functions with Formulas, Graphs and Mathematical tables*. Dover publications inc., New York, 1972.
 - [72] M. E. Delany and E. N. Bazley. Acoustical properties of fibrous absorbent materials. *Applied Acoustics*, 3(2):105–116, April 1970.
 - [73] L. C. Sutherland and G. A. Daigle. *Encyclopedia of Acoustics - chapter 32: Atmospheric Sound Propagation*. Wiley, 1997.
 - [74] A. J. Cramond and C. G. Don. Effects of moisture content on soil impedance. *Journal of Acoustical Society of America*, 82(1):293–301, 1987.
 - [75] D. Botteldooren and Timothy v. Renterghem. Modelling outdoor sound propagation: a careful balance between physical rigour and engineering practice. In *Euronoise, Edinburgh*, 2009.
 - [76] F. B. Jenssen, W. A. Kupermann, M. B. Porter, and H. Schmidt. *Computational Ocean Acoustics*. Springer-Verlag, 2000.
 - [77] R. Raspet, A. L'Esperance, and G.A. Daigle. The effect of realistic ground impedance on the accuracy of ray tracing. *Journal of Acoustical Society of America*, 97(1):154–158, 1995.
 - [78] N. Bleistein. *Mathematical methods for wave phenomena*. Academic Press, Inc., Orlando, Florida, USA, 1984.
 - [79] O. A. Godin. An effective quiescent medium for sound propagating through an inhomogeneous, moving fluid. *Journal of Acoustical Society of America*, 112(4):1269–1275, 2002.
 - [80] J. Huber, J-P. B. Clarke, and S. Maloney. Aircraft noise impact under diverse weather conditions. In *9th AIAA/CEAS AeroAcoustics Conference and Exhibit, 12-14 May 2003, Hilton Head, South Carolina*, number AIAA-2003-3276, 2003.
 - [81] J. M. Prospathopoulos and S. G. Voutsinas. Determination of equivalent sound speed profiles for ray tracing in near-ground sound propagation. *Journal of Acoustical Society of America*, 122(3):1391–1403, 2007.
 - [82] S. L. Heath and G. L. McAninch. Propagation effects of wind and temperature on acoustic ground contour levels. In *44th AIAA Aerospace Sciences Meeting and Exhibit, 9-14 January 2006, Reno, Nevada*, number AIAA-2006-0411, 2006.
 - [83] A. S. Glassner, editor. *An Introduction to Ray Tracing*. Academic press limited, 3rd edition, 1990.
 - [84] anon. Prediction of sound attenuation in a refracting turbulent atmosphere with a Fast Field Program. Technical Report 04011, ESDU, May 2004.
 - [85] Y. W. Lam. An analytical model for turbulence scattered rays in the shadow zone for outdoor sound propagation calculation. *Journal of Acoustical Society of America*, 125(3):1340–1350, 2009.
-

-
- [86] J. Rosenbaum. *Enhanced propagation of directional aviation noise: a hybrid parabolic equation - fast field program method*. PhD thesis, Penn State University, 2011.
 - [87] A. F. G. P. de Oliveira. *The effect of wind and turbulence on sound propagation in the atmosphere*. PhD thesis, Universidade Tecnica de Lisboa, 2012.
 - [88] D. Hohenwarter. Measured sound propagation influenced by meteorology. In *InterNoise*, June 2010.
 - [89] Y. Gabillet, H. Schroeder, G. A. Daigle, and A. L'Esperance. Application of the gaussian beam approach to sound propagation in the atmosphere: Theory and experiments. *Journal of Acoustical Society of America*, 93(6):3105–3116, 1993.
 - [90] A. Berry and G. A. Daigle. Controlled experiments of the diffraction of sound by a curved surface. *Journal of Acoustical Society of America*, 83(6):2047–2058, 1988.
 - [91] anon. Integrated noise model (INM) version 7.0 technical manual. Technical Report FAA-AEE-08-01, FAA, 2008.
 - [92] ECAC.CEAC. Report on standard method of computing noise contours around civil airports. Technical Report Document 29, ECAC.CEAC, 2005.
 - [93] H. Olsen I. L. N. Granoien, R. T. Randeberg. Next generation aircraft noise models - need and requirements. In *InterNoise*, number 184, June 2010.
 - [94] Y. Okada, K. Yoshihisa, and T. Iwase. Effects of atmospheric absorption on aircraft noise propagation during takeoff and landing around airports in the various world regions. In *InterNoise*, number 173, June 2010.
 - [95] SAE. Method for predicting lateral attenuation of airplane noise. Technical Report SAE-AIR-5662, Society of Automotive Engineers, 2006.
 - [96] SAE. Procedure for the computation of airplane noise in the vicinity of airports. Technical Report SAE AIR 1845, Society of Automotive Engineers, 1986.
 - [97] SAE. Standard values of atmospheric absorption as a function of temperature and humidity. Technical Report SAE AIR 866A, Society of Automotive Engineers, 1975.
 - [98] S. A. Rizzi and B. M. Sullivan. Synthesis of virtual environments for aircraft community noise impact studies. In *11th AIAA/CEAS Aeroacoustics Conference, Monterey, CA*, number AIAA-2005-2983, 2005.
 - [99] A. Sahai, E. Anton, E. Stumpf, F. Wefers, and M. Vorlaender. Interdisciplinary auralization of take-off and landing procedures for subjective assessment in virtual reality environments. In *18th AIAA/CEAS Aeroacoustics Conference 4-6 June, Colorado Springs, CO*, number AIAA-2012-2077, 2012.
-

-
- [100] M. Sarrazin, K. Janssens, H. v.d. Auweraer, W. Desmet, and P. Sas. Virtual car sound synthesis approach for hybrid and electric vehicles. In *Euronoise, Prague*, pages 1340–1345, 2012.
 - [101] R. Pieren, K. Heutschi, M. Müller, M. Manyokyo, and K. Eggenschwiler. Auralization of wind turbine noise: Emission synthesis. *Acta Acustica United with Acustica*, 100:25–33, 2014.
 - [102] U. Zölzer, editor. *DAFX - Digital Audio Effects*. John Wiley and Sons, Ltd., West Sussex, England, 2002.
 - [103] D. R. Begault. *3-D Sound for Virtual Reality and Multimedia*. Academic Press, Inc., Chestnut Hill, MA, USA, 1994 edition, 1984.
 - [104] D. Rocchesso. *Introduction to Sound Processing*. Open source: <http://profs.sci.univr.it/~rocchess/SP/sp.pdf>, accessed 13-05-2014, March 2003.
 - [105] S. J. Orfanidis. *Introduction to Signal Processing*. Open source: <http://www.ece.rutgers.edu/~orfanidi/intro2sp>, accessed 13-05-2014, 2010.
 - [106] M. P. Allen. Analysis and synthesis of aircraft engine fan noise for use in psychoacoustic studies. Master’s thesis, Virginia Polytechnic Institute and State University, 2012.
 - [107] F. Grosveld, B. M. Sullivan, and S. A. Rizzi. Temporal characterization of aircraft noise sources. In *42nd AIAA ASM meeting, 5-8 Januray, Reno, NE*, number AIAA-2004-1029, 2004.
 - [108] S. Okcu, J. Rathsam, and S. A. Rizzi. Psychoacoustic analysis of synthesized jet noise. In *NoiseCon 26-28 august 2013, Denver, CO*, 2013.
 - [109] T. I. Laakso, V. Valimaki, M. Karjalainen, and U. K. Laine. Splitting the unit delay; tools for fractional delay filter design. *IEEE Signal processing magazine*, pages 30–60, January 1996.
 - [110] S. A. Rizzi, A. R. Aumann, M. P. Allen, R. Burdisso, and K. J. Faller II. Simulation of rotary and fixed wing flyover noise for subjective assessments (invited). In *161st Meeting of the Acoustical Society of America, Seattle, WA, 2011*, 2011.
 - [111] S. A. Rizzi, B. M. Sullivan, and C.A. Sandridge. A three-dimensional virtual simulator for aircraft flyover presentation. In *Proceedings of the 9th International Conference on Auditory Display (ICAD), Boston, MA, USA*, pages 87–90, 2003.
 - [112] S. A. Rizzi, B. M. Sullivan, and A. R. Aumann. Recent developments in aircraft flyover noise simulation at nasa langley research center. In *NATO Research and Technology Agency AVT-158 Environmental Noise Issues Associated with Gas Turbine Powered Military Vehicles Specialists Meeting, Montreal, Canada*, number 17, 2008.

-
- [113] M. P. Allen, S. A. Rizzi, R. Burdisso, and S. Okcu. Analysis and synthesis of tonal aircraft noise sources. In *18th AIAA/CEAS Aeroacoustics Conference 4-6 June, Colorado Springs, CO*, number AIAA-2012-2078, 2012.
 - [114] V. Pulkki. Virtual sound source positioning using vector-base amplitude panning. *Journal of the Audio Engineering Society*, 45(6):456–466, 1997.
 - [115] D. Berckmans, K. Janssens, P. Sas, W. Desmet, and H. v.d. Auweraer. A new method for aircraft noise synthesis. In *International Conference on Noise and Vibration Engineering, 2006*, pages 4257–4270, 2006.
 - [116] R. B. Stull. *An Introduction to Boundary Layer Meteorology*. Kluwer Academic Publishers, Dordrecht, Netherlands, 1987.
 - [117] A. Aumann, W. Chapin, and S. A. Rizzi. An open architecture for auralization of dynamic soundscapes. In *168th Meeting of the Acoustical Society of America, JASA, Vol 136, No 4, pt 2. Oct 2013, pp 2286*, 2013.
 - [118] D. Weir. Engine validation of noise and emission reduction technology, phase I. Technical Report NASA CR-2008-215225, NASA, 2008.
 - [119] A. Sahai and E. Stumpf. Incorporating and minimizing aircraft noise annoyance during conceptual aircraft design. In *20th AIAA/CEAS Aeroacoustics Conference, 16-20 June 2014, Atlanta, GA*, number AIAA-2014-2078, 2014.
 - [120] S. A. Rizzi, D. B. Stephens, J. J. Berton, D. E. v. Zante, J. P. Wojno, and T. W. Goerig. Auralization of flyover noise from open rotor engines using model scale test data. In *20th AIAA/CEAS Aeroacoustics Conference, 16-20 June 2014, Atlanta, GA*, number AIAA-2014-2750, 2014.
 - [121] S. Okcu, M. P. Allen, and S. A. Rizzi. Psychoacoustic assessment of a new aircraft engine fan noise synthesis method. In *164th Meeting of the Acoustical Society of America, Kansas City, MO*, 2012.
 - [122] H. C. Shin, C. Hall, and D. Crichton. Auralisation of turbofan engine noise components. In *12th AIAA/CEAS Aeroacoustics Conference 8-10 May, Cambridge, Massachusetts*, number AIAA-2006-2620, 2006.
 - [123] N. E. Antoine. *Aircraft Optimization for Minimal Environmental Impact*. PhD thesis, Stanford University, 2004.
 - [124] M. D. Dahl. A process for assessing NASA’s capability in aircraft noise prediction technology. In *14th AIAA/CEAS Aeroacoustics Conference 5-7 May, Vancouver, British Columbia Canada*, number AIAA-2008-26813, 2008.
 - [125] A. M. Cargill. Sound propagation through fluctuating flows - its significance in aeroacoustics. In *8th AIAA Aeroacoustics Conference 11-13 April, Atlanta, GA*, number AIAA-1983-0697, 1983.
 - [126] G. H. Goedekce, R. C. Wood, H. J. Auvermann, V. E. Ostashev, D. I. Havelock, and C. Ting. Spectral broadening of sound scattered by advecting atmospheric turbulence. *JASA*, 5(109):1923–1934, 2001.
-

-
- [127] S. F. Clifford and R. J. Lataitis. Turbulence effects on acoustic wave propagation over a smooth surface. *Journal of Acoustical Society of America*, 73(5):1545–1550, 1983.
 - [128] G. A. Daigle. Effects of atmospheric turbulence on the interference of sound waves above a finite impedance boundary. *Journal of Acoustical Society of America*, 65(1):45–49, 1979.
 - [129] G. A. Daigle, J. E. Piercy, and T. F. W. Embleton. Effects of atmospheric turbulence on the interference of sound waves near a hard boundary. *Journal of Acoustical Society of America*, 64(2):622–630, 1978.
 - [130] B. Boashash. Estimating and interpreting the instantaneous frequency of a signal - part 1: Fundamentals. *IEEE proceedings*, 80(4), April 1992.
 - [131] P. Spittle. Gas turbine technology. *Physics Education*, 38(6), 2003.
 - [132] H. Cohen, G. F. C. Rogers, and H. I. H. Saravanamuttoo. *Gas turbine theory*. Longman Group, Tottenham, England, 4th edition edition, 1996.

Appendix A

Coherent addition of sound waves

The effective pressure, resulting from a root-mean-square (rms) calculation, is used to quantify the logarithmic decibel scale. This also allows an explanation of coherent and incoherent addition, i.e. including or not including phase information. Since this is of vital importance in ground reflection modeling, or any other phenomena where two or multiple waves are added, a brief introduction is provided.

A.1 Addition of multiple waves

Individual sound waves can be added based on superposition due to the linearity of the underlying wave equation (see equation 2.12). Suppose that a number N of sound sources/waves are present. Every wave is presented by a simple cosine,

$$p_i = \frac{A_i}{r_i} \cos(\omega_i \tau_i), \quad \text{and} \quad \tau_i = t - \frac{r_i}{c}, \quad (\text{A.1})$$

where A is the amplitude, τ is the retarded time, e.g. time of emission, of the sound source as defined by a straight line path r and sound speed c . The index i denotes the particular source, i.e. $i = 1\dots N$. The effective pressure is defined as the root mean square level over one period t_p of the sound wave.

$$p_e^2 = \frac{1}{t_p} \int_0^{t_p} p_m^2 dt, \quad (\text{A.2})$$

where p_m is defined as the sum of multiple sound waves, e.g. $p_m = p_1 + p_i + p_{i+1} + \dots + p_N$. This is a coherent summation of all the sound waves since the complete

waveform (not only the amplitude) is taken into account. The square of p_m , as needed for eventual substitution into equation A.2, is expanded in equation A.3,

$$p_m^2 = \sum_{i=1}^N \left(p_i^2 + 2p_i \sum_{j=i+1}^N p_j \right). \quad (\text{A.3})$$

Next, a substitution of equation A.1 is executed:

$$p_m^2 = \sum_{i=1}^N \left(\underbrace{\left(\frac{A_i}{r_i} \right)^2 \cos^2(\omega_i \tau_i)}_1 + \underbrace{2 \frac{A_i}{r_i} \sum_{j=i+1}^N \left(\frac{A_j}{r_j} \cos(\omega_i \tau_i) \cos(\omega_j \tau_j) \right)}_2 \right). \quad (\text{A.4})$$

Two factors (1 and 2) emerge and are integrated separately.

A.2 Integration to effective sound pressure

Use is made of two trigonometric identities to rewrite the cosines in equation A.4:

$$\begin{aligned} \cos^2(x) &= \frac{1}{2}(1 + \cos(2x)) \\ \cos(x)\cos(y) &= \frac{1}{2}(\cos(x+y) + \cos(x-y)) \end{aligned}$$

Part 1 of equation A.4 is integrated first, where the order of summation and integration is changed. Please keep in mind that the integral of a sine or cosine wave over one period equates to zero.

$$p_{e1}^2 = \sum_{i=1}^N \frac{1}{t_p} \int_0^{t_p} \left(\left(\frac{A_i}{r_i} \right)^2 \cos^2(\omega_i \tau_i) \right) dt \quad (\text{A.5})$$

$$= \sum_{i=1}^N \left(\frac{A_i}{r_i} \right)^2 \frac{1}{2t_p} \int_0^{t_p} (1 + \cos(2\omega_i \tau_i)) dt \quad (\text{A.6})$$

$$= \sum_{i=1}^N \left(\frac{A_i}{r_i \sqrt{2}} \right)^2. \quad (\text{A.7})$$

Equation A.7 shows a familiar equation as found in many text books. The effective pressure is related to the amplitude of the pressure wave divided by the path length and the square root of two. Next, part 2 of equation A.4 is integrated:

$$p_{e_2}^2 = \frac{2A_i}{t_p r_i} \sum_{j=i+1}^N \frac{A_j}{r_j} \int_0^{t_p} \cos(\omega_i \tau_i) \cos(\omega_j \tau_j) dt \quad (\text{A.8})$$

$$= \frac{A_i}{t_p r_i} \sum_{j=i+1}^N \frac{A_j}{r_j} \int_0^{t_p} (\cos(\omega_i \tau_i + \omega_j \tau_j) + \cos(\omega_i \tau_i - \omega_j \tau_j)) dt. \quad (\text{A.9})$$

If the waves are similar, having the same frequency content as is a valid assumption for the mirror-source approach (see figure 3.4), some assumptions can be made:

$$\omega_i = \omega_j = \omega \quad (\text{A.10})$$

$$\delta r = r_j - r_i \quad (\text{A.11})$$

$$\tau_j = \tau_i + \frac{\delta r}{c}. \quad (\text{A.12})$$

As a result, the cosine terms in equation A.9 can be simplified,

$$\cos(\omega_i \tau_i + \omega_j \tau_j) = \cos\left(2\omega\tau_i + \frac{\omega\delta r}{c}\right) \quad (\text{A.13})$$

$$\cos(\omega_i \tau_i - \omega_j \tau_j) = \cos\left(\frac{\omega\delta r}{c}\right). \quad (\text{A.14})$$

These simplifications are substituted back in equation A.9 to yield the second part of the effective pressure:

$$p_{e_2}^2 = \frac{A_i}{t_p r_i} \sum_{j=i+1}^N \frac{A_j}{r_j} \left(\cos\left(\frac{\omega\delta r}{c}\right) + \int_0^{t_p} \cos\left(2\omega\tau_i + \frac{\omega\delta r}{c}\right) dt \right) \quad (\text{A.15})$$

$$= \frac{A_i}{r_j} \sum_{j=i+1}^N \frac{A_j}{r_j} \cos\left(\frac{\omega\delta r}{c}\right). \quad (\text{A.16})$$

Combining equations A.7 and A.16 leads to the effective pressure equation for coherent addition of (acoustic) waves,

$$p_e^2 = \sum_{i=1}^N \left(\left(\frac{A_i}{r_i \sqrt{2}} \right)^2 + \sum_{j=i+1}^N \frac{A_i A_j}{r_i r_j} \cos\left(\frac{\omega\delta r}{c}\right) \right). \quad (\text{A.17})$$

A.3 Application to ground reflection

The analogy of equation A.17 to ground reflection is clear, see chapter 3 or consequently equation 3.21. In the case of ground reflection it can be assumed that the difference in incidence angle of the direct and ground reflected ray is small. This only holds if the listener is relatively far from the source. Hence, it is assumed that both waves have the same initial amplitude $A_1 = A_2 = A$. Furthermore, the ground reflected ray r_2 is modified by Q (see equation 3.16). This results in,

$$p_e^2 = \frac{A^2}{2r_1^2} + \frac{A^2}{2r_2^2} |Q|^2 + \frac{A^2 |Q|}{r_1 r_2} \cos(k(r_2 - r_1) + \phi) \quad (\text{A.18})$$

wherein the direct wave contribution is recognized as $p_d^2 = A^2/2r_1^2$, which can be substituted to yield,

$$p_e^2 = p_d^2 \left(1 + \left(\frac{r_1}{r_2} |Q| \right)^2 + 2 |Q| \frac{r_1}{r_2} \cos(k(r_2 - r_1) + \phi) \right) \quad (\text{A.19})$$

where $Q = |Q| e^{i\phi}$. The difference induced by the ground reflection A_G can be calculated, in dB, by subtracting the direct wave,

$$A_G = 10 \log_{10} \left(\frac{p_e^2}{p_{ref}^2} \right) - 10 \log_{10} \left(\frac{p_d^2}{p_{ref}^2} \right) = 10 \log_{10} \left(\frac{p_e^2}{p_d^2} \right). \quad (\text{A.20})$$

Hence, A_G results as,

$$A_G = 10 \log_{10} \left(1 + \left(\frac{r_1}{r_2} |Q| \right)^2 + 2 |Q| \frac{r_1}{r_2} \cos(k(r_2 - r_1) + \phi) \right) \quad (\text{A.21})$$

Neglecting the third part of equation A.18 will lead to an incoherent addition of the sound waves into an incoherent effective sound pressure level. This was used in chapter 8, see equations 8.1 and 8.2.

Appendix **B**

Spectral analysis and noise metrics

B.1 Fourier transforms

A Fourier Transform (FT) transforms a signal in the time domain, to the frequency domain. In the frequency domain, the signal is constructed based on individual harmonic signal components, i.e. sine and cosine waveforms. To assess the frequency content of a signal, is called spectral analysis. On a computer, the implementation of the FT is by a Discrete Fourier Transform (DFT). This is implemented as,

$$X(k) = \text{DFT}[x(n)] = \sum_{n=0}^{N-1} x(n) e^{-j2\pi nk/N}, \quad k = 0, 1, \dots, N-1, \quad (\text{B.1})$$

where, $x(n)$ is the n^{th} sample in the time domain and N is the total number of samples. A fast implementation of such a transform is referred to as a Fast Fourier Transform (FFT). The inverse operation, i.e. transforming the frequency content into a time signal, is done by the Inverse Fast Fourier Transform (IFFT and IDFT) and follows as,

$$x(n) = \text{IDFT}[X(k)] = \frac{1}{N} \sum_{k=0}^{N-1} X(k) e^{j2\pi nk/N}, \quad n = 0, 1, \dots, N-1. \quad (\text{B.2})$$

B.2 Octave-bands

Frequency bands are a subset, in frequency, of the total spectrum. A band encompasses a part of the spectrum, as limited by a lower and upper band frequency, and

is usually referred to by its center frequency. The center frequency is the mean frequency, on a logarithmic scale, of the lower and upper frequency. For an octave-band, the frequency bandwidth doubles per band, i.e. the upper frequency is twice that of the lower frequency. Consequently, the bandwidth of octave bands grow very quickly. For analysis purposes, the average pressure in a band is taken to be representative and used in calculations.

If a signal is comprised of finer frequency specifics, then captured by the octave-band, an analysis can also be performed by bands that do not span over the wide bandwidth. For instance, $1/3^{\text{rd}}$ octave-bands could be used. In one-third octave bands, the upper frequency is $2^{1/3}$ times the lower frequency. This results in three $1/3^{\text{rd}}$ octave-bands necessary for one octave band. In aircraft noise calculations, analysis and simulations, $1/3^{\text{rd}}$ octave-bands are very common, see literature⁽¹³⁾ for an example as also used in this research.

B.3 A-weighting

Using A-weighting, the human response to equal loudness is taken into account. Ears perceive a different loudness for sound of different frequencies. Therefore, to get a loudness correction of the signal, a signal is A-weighted to take this response into account. The A-weighting, transfer function plotted in figure B.1, is effectively reducing very low and very high frequency content.

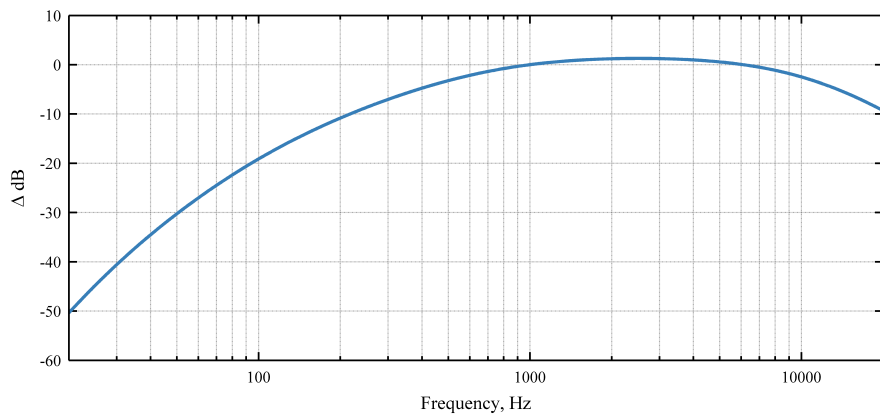


Figure B.1: The A-weighting correction.

Important to note is that the A-weighting adds to the sound level in between the range of 1000-6000 Hz. The low frequency content is reduced a bit.

B.4 Sound metrics

The OASPL of a signal is the Overall Sound Pressure Level. It is based on the individual (1/3rd) bands (b) and similar to the A-weighted Level LA,

$$\text{OASPL} = \sum_{b=1}^n 10 \log_{10} \left(10^{(SPL_b)/10} \right) \quad (\text{B.3})$$

$$\text{LA} = \sum_{b=1}^n 10 \log_{10} \left(10^{(SPL_b + \Delta A)/10} \right), \quad (\text{B.4})$$

where SPL_b is the SPL in a band and ΔA is the A-weighting for that particular band (see figure B.1). During the aircraft flyover, the LA will vary, the maximum LA value is referred to as the $L_{A,\max}$.

The Sound Exposure Level (SEL) integrates all the acoustic energy of the OASPL and normalizes it to a one-second interval,

$$\text{SEL} = 10 \log_{10} \left(\int_{t_1}^{t_2} 10^{\text{LA}/10} dt \right), \quad (\text{B.5})$$

where t_1 and t_2 specify the boundary, in time, where the signal is 10 dB below $L_{A,\max}$. The SEL is closely related to the L_{DEN} ,

$$L_{\text{DEN}} = 10 \log_{10} \left(\frac{1}{t_{\text{DEN}}} \int_0^{t_{\text{DEN}}} \Gamma \cdot 10^{\text{LA}/10} dt \right), \quad (\text{B.6})$$

where, Γ is the day ($\Gamma = 1$), evening ($\Gamma = 5$) or night ($\Gamma = 10$) time multiplier associated with the L_{DEN} for a duration t_{DEN} . If no evening events are considered, the L_{DEN} equals the L_{DN} . The L_{DEN} is frequently used in European regulations whereas the L_{DN} is used in the USA.

Appendix C

Propagation effects

C.1 Algebraic implementation of Snell's law

The derivation in this section follows⁽⁸³⁾ but contains a few more intermediate steps for the interested reader.

If the propagation medium is inhomogeneous, the wave front propagates with different velocities. Rather than keeping track of the entire wavefront, it is possible to track the rays that represent the wave front. Snell's law of refraction, found in any basics acoustics textbook, allows to calculate how the ray path direction changes as the medium properties change. Snell's law is shown by equation C.1,

$$\eta_{ti} = \frac{\sin(\theta_i)}{\sin(\theta_t)}, \quad (\text{C.1})$$

where η_{ti} is the index of refraction at the boundary being the ratio of the acoustic propagating velocities v_i/v_t . In our acoustics case, this is the change of effective sound speed gradient going from the incident medium to the transmitted medium. This is depicted in figure 3.11, repeated here for convenience as C.1.

As we enter the second medium, the incident ray \vec{I} is refracted and shown in the second medium as the transmitted ray \vec{T} . A reflected ray \vec{R} can appear when the medium boundary is a ground plane or if total internal reflection occurs. The vector \vec{N} is the unit normal in the upward direction. This method uses a representation of all rays having unit length $|\vec{I}, \vec{T}, \vec{R}| = 1$.

As the acoustic ray is propagating from the source to the listener, it experiences changes in the effective sound speed. This amounts to a change of the index of refraction. To that matter, a numerical discretization of the layered atmosphere is made in which the rays are traced. This paragraph continues to elaborate the equations accompanying figure C.1 to find the transmitted ray.

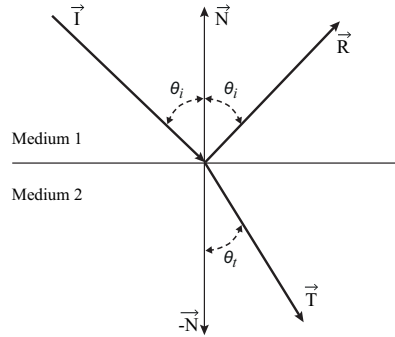


Figure C.1: The boundary at two different media.

Consider the transmitted ray that is refracted by means of the changing medium characteristics. To predict the direction of this vector, Snell's law is squared and rewritten using a trigonometric identity:

$$\sin^2(\theta) + \cos^2(\theta) = 1 \quad (\text{C.2})$$

$$(1 - \cos^2(\theta_i)) \eta_{it}^2 = (1 - \cos^2(\theta_t)), \quad (\text{C.3})$$

where, $\eta_{it} = 1/\eta_{ti}$. Next, the factor $\cos(\theta_i)$ from equation C.3 is written explicitly:

$$\cos(\theta_t)^2 = 1 + (\cos(\theta_i)^2 - 1) \eta_{it}^2. \quad (\text{C.4})$$

If we use this equation to calculate the transmitted angle we might end up with values at the right hand side that are larger than one. An area where the cosine function is not defined. To circumvent this problem we try to solve for the angle after rewriting the equations. A dot product is used to relate the angles to the relevant vectors,

$$\cos(\theta_i) = \vec{N} \cdot -\vec{I} \quad (\text{C.5})$$

$$\cos(\theta_t) = -\vec{N} \cdot \vec{T}. \quad (\text{C.6})$$

As a by product, the reflected ray can be quickly calculated from basic trigonometry. The parallel part of the incident ray is established, since the vectors are of unit length, as $-\cos(\theta_i) \vec{N}$. As a result, the reflected ray at the boundary is calculated using equation C.7:

$$\vec{R} = \vec{I} + 2 \cos(\theta_i) \vec{N}. \quad (\text{C.7})$$

Usually the interest is in the transmitted refracted ray. The results of equation C.6 are substituted in equation C.4 together with the notion of $T = \alpha\vec{I} + \beta\vec{N}$ to establish the vector parallel (α) and normal (β) parts. Further use is made of the identity $\vec{N} \cdot \vec{N} = |\vec{N}| = 1$, which holds for any vector having unit length,

$$\cos(\theta_t)^2 = (-\vec{N} \cdot \vec{T})^2 \quad (\text{C.8})$$

$$= \left(-\vec{N} \cdot (\alpha\vec{I} + \beta\vec{N}) \right)^2 \quad (\text{C.9})$$

$$= \left(-\alpha\vec{N} \cdot \vec{I} - \beta\vec{N} \cdot \vec{N} \right)^2 \quad (\text{C.10})$$

$$= (\alpha \cos(\theta_i) - \beta)^2. \quad (\text{C.11})$$

Combining equation C.4 and C.11 gives the first conditions to which $\cos(\theta_t)$ has to comply. A second condition can be stated by defining the transmitted ray \vec{T} as a unit vector:

$$1 = \vec{T} \cdot \vec{T} \quad (\text{C.12})$$

$$= (\alpha\vec{I} + \beta\vec{N}) \cdot (\alpha\vec{I} + \beta\vec{N}) \quad (\text{C.13})$$

$$= \alpha^2 + \beta^2 - 2\alpha\beta \cos(\theta_i), \quad (\text{C.14})$$

Equation C.14 forms the second condition to which T has to comply. The system of two equations, shown below, are solved for α and β to yield the correct transmitted ray direction in the second medium,

$$\eta_{it}^2 \left(\cos(\theta_i)^2 - 1 \right) + 1 = (\alpha \cos(\theta_i) - \beta)^2 \quad (\text{C.15})$$

$$1 = \alpha^2 + \beta^2 - 2\alpha\beta \cos(\theta_i). \quad (\text{C.16})$$

If the equations are subtracted, relation C.17 emerges:

$$\alpha^2 = \eta_{it}^2. \quad (\text{C.17})$$

The one solution that we are after is for a positive α , see figure C.1. This implies that we can deduce the only feasible solution from equation C.16 being $\alpha = \eta_{it}$. As a result, this can be substituted back in equation C.16 to yield a quadratic equation that is solved for its roots,

$$0 = \beta^2 - 2\eta_{it} \cos(\theta_i) \beta + \eta_{it}^2 - 1 \quad (\text{C.18})$$

$$\beta = \eta_{it} \cos(\theta_i) \pm \sqrt{1 + \eta_{it}^2 (\cos(\theta_i) - 1)}. \quad (\text{C.19})$$

And by evaluating figure C.1 again, it is clear that the negative version of β must be chosen. As result, the equation applicable for the calculation of the transmitted ray is found:

$$\vec{T} = \eta_{it} \vec{I} + \left(\eta_{it} \cos(\theta_i) - \sqrt{1 + \eta_{it}^2 (\cos(\theta_i)^2 - 1)} \right) \vec{N}. \quad (\text{C.20})$$

If the dot product of equation C.6 becomes negative, this corresponds to an upward traveling incident ray in figure C.1 rather than an downward ray, the positive solution of C.19 must be used as substitution.

A limiting condition is if the sum of the terms in the square root is negative. This indicates a condition that is referred to as total internal reflection. If this occurs, all sound is reflected at the boundary and no sound is penetrating into the second medium. Equation C.7 can be used for \vec{T} in this special case.

C.2 Spreading losses

Figures C.2-C.8 follow on figures 3.19-3.22 and show the same shadow zone transition for octave center band frequencies with a source height h_s of 100 m. Figures C.9-C.10 show a calculation at 500 Hz for different sound speed gradients.

C.3 Ground reflection

In case of a spherical wave reflection, the ground reflection coefficient is slightly different from a plane wave approximation. This is a function of source height, incidence angle and ground constitution. See equations 3.16 and 3.18, or the associated text with figures 3.5 and 3.6. In this appendix, a few figures illustrating this differences as a function of the aforementioned variables are shown. All figures demonstrate the difference as spherical - plane, i.e. $\Delta\text{dB} = 20 \log_{10} (Q_s/Q_p)$ and $\Delta\theta = \theta_s - \theta_p$. They confirm that the differences, under most circumstances, are small and apply primarily to low frequencies, acoustically 'soft' ground and small grazing angles.

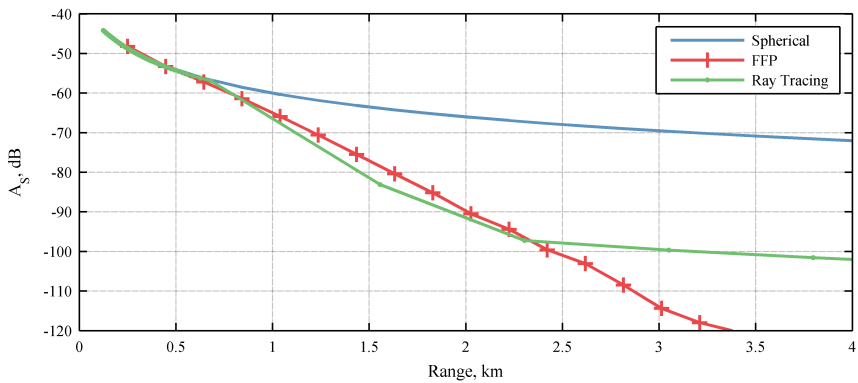


Figure C.2: Spreading loss at $f = 31.5 \text{ Hz}$, $(\frac{dc}{dz}) = -0.1 \text{ s}^{-1}$ and $h_s = 100m$.

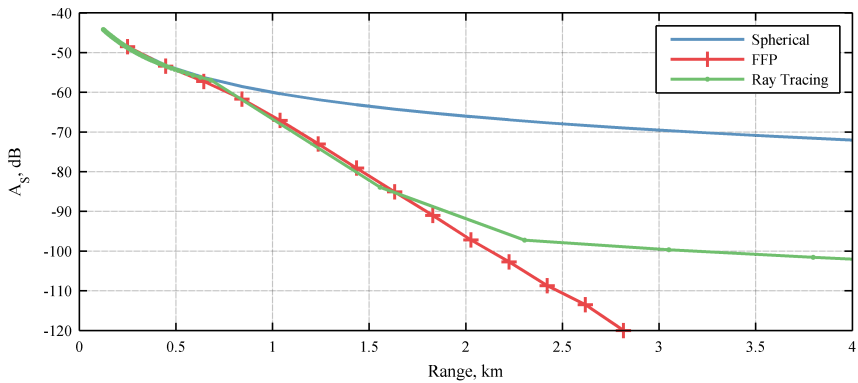


Figure C.3: Spreading loss at $f = 63 \text{ Hz}$, $(\frac{dc}{dz}) = -0.1 \text{ s}^{-1}$ and $h_s = 100m$.

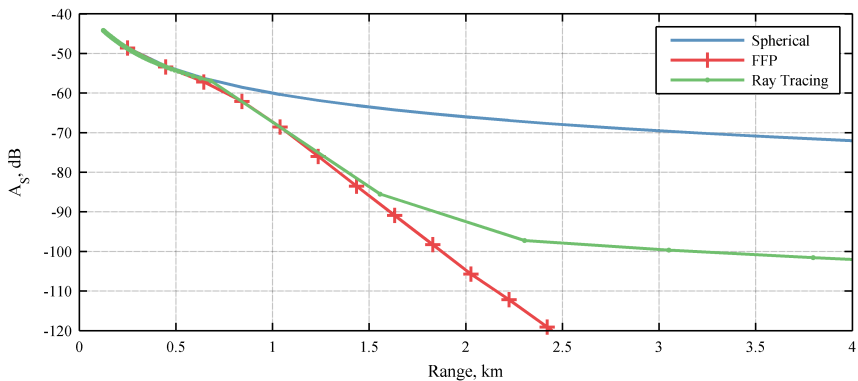


Figure C.4: Spreading loss at $f = 125 \text{ Hz}$, $(\frac{dc}{dz}) = -0.1 \text{ s}^{-1}$ and $h_s = 100m$.

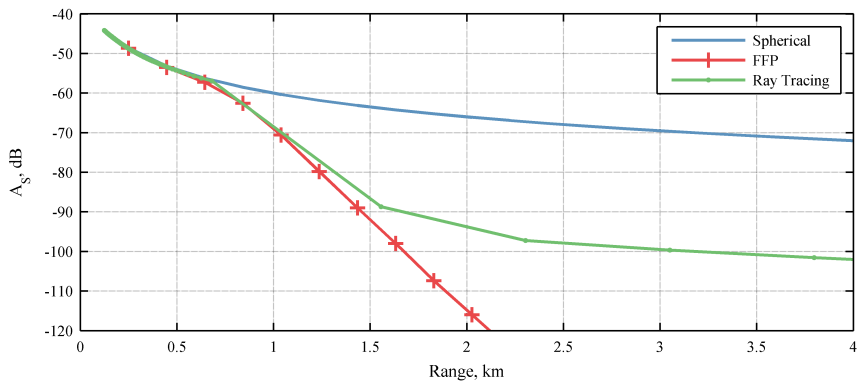


Figure C.5: Spreading loss at $f = 250$ Hz, $(\frac{dc}{dz}) = -0.1 \text{ s}^{-1}$ and $h_s = 100m$.

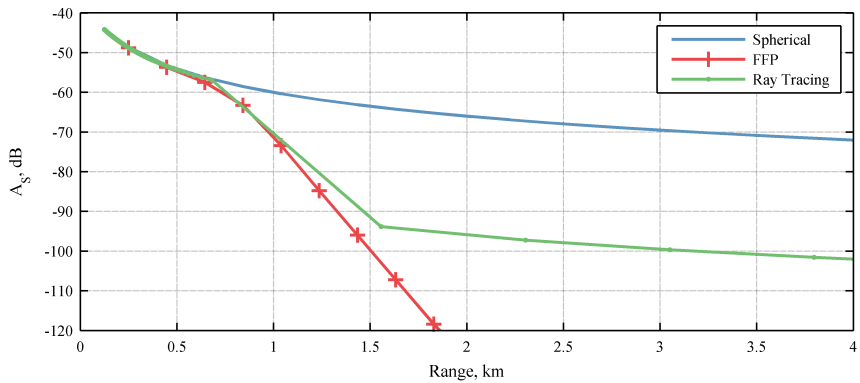


Figure C.6: Spreading loss at $f = 500$ Hz, $(\frac{dc}{dz}) = -0.1 \text{ s}^{-1}$ and $h_s = 100m$.

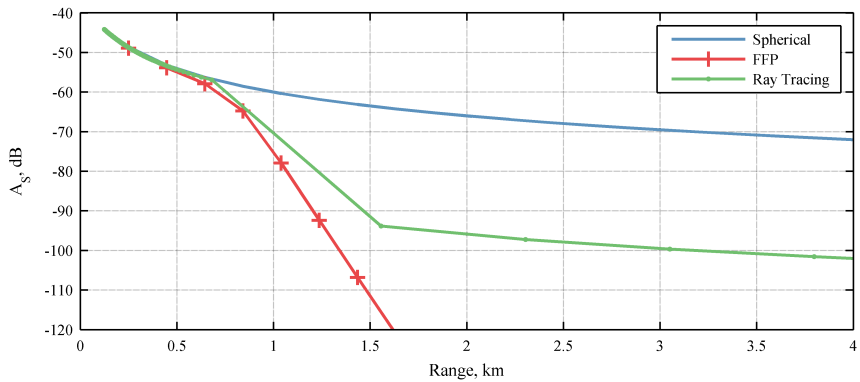


Figure C.7: Spreading loss at $f = 1000$ Hz, $(\frac{dc}{dz}) = -0.1 \text{ s}^{-1}$ and $h_s = 100m$.

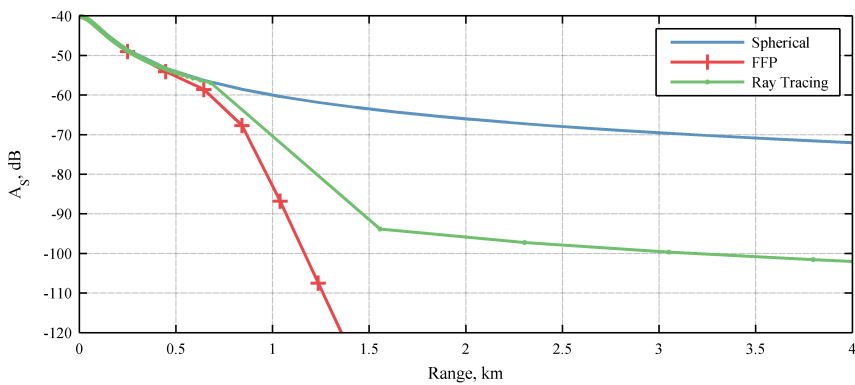


Figure C.8: Spreading loss at $f = 2000$ Hz, $(\frac{dc}{dz}) = -0.1$ s^{-1} and $h_s = 100m$.

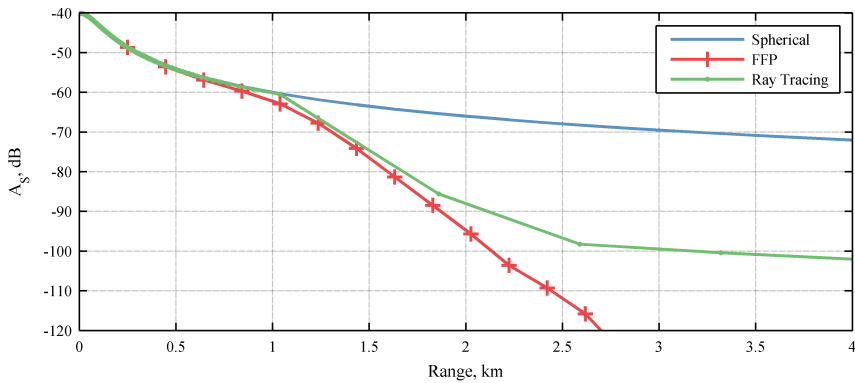


Figure C.9: Spreading loss at $f = 500$ Hz, $(\frac{dc}{dz}) = -0.05$ s^{-1} and $h_s = 100m$.

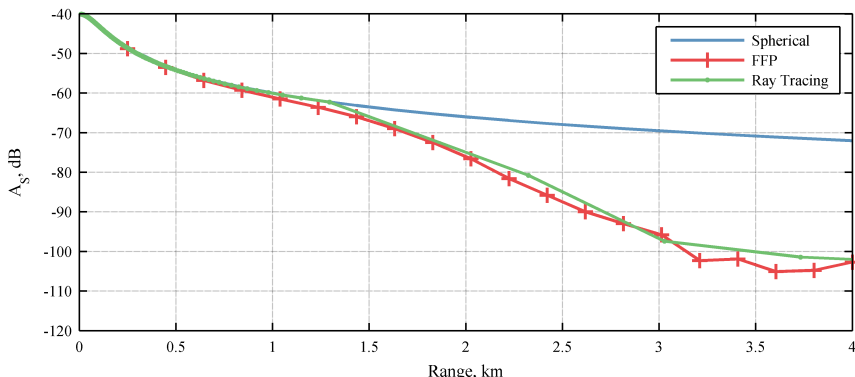


Figure C.10: Spreading loss at $f = 500$ Hz, $(\frac{dc}{dz}) = -0.025$ s^{-1} and $h_s = 100m$.

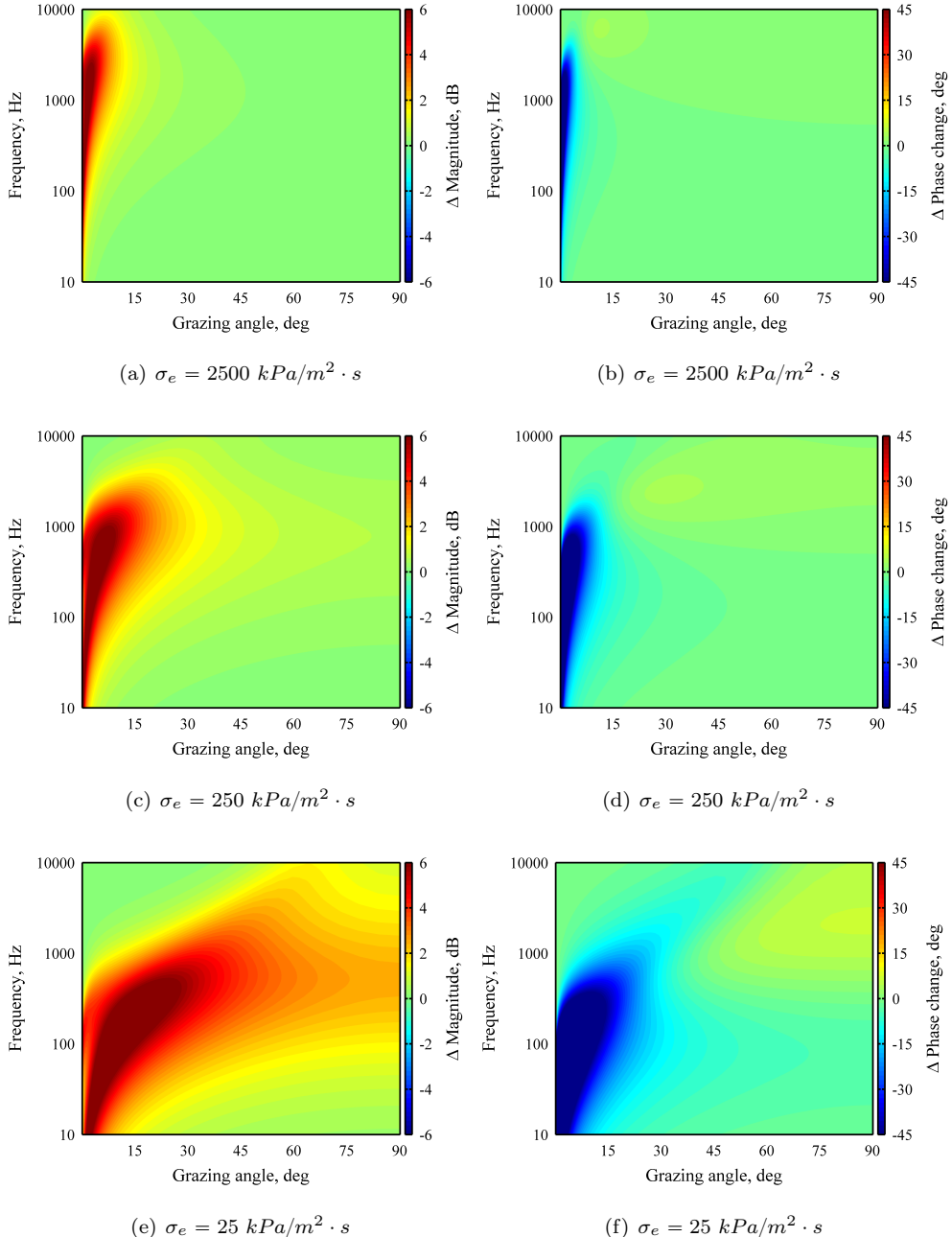


Figure C.11: Difference in magnitude (left column) and phase (right column) between spherical and plane wave approximations. The source is at a height of 1 meter.

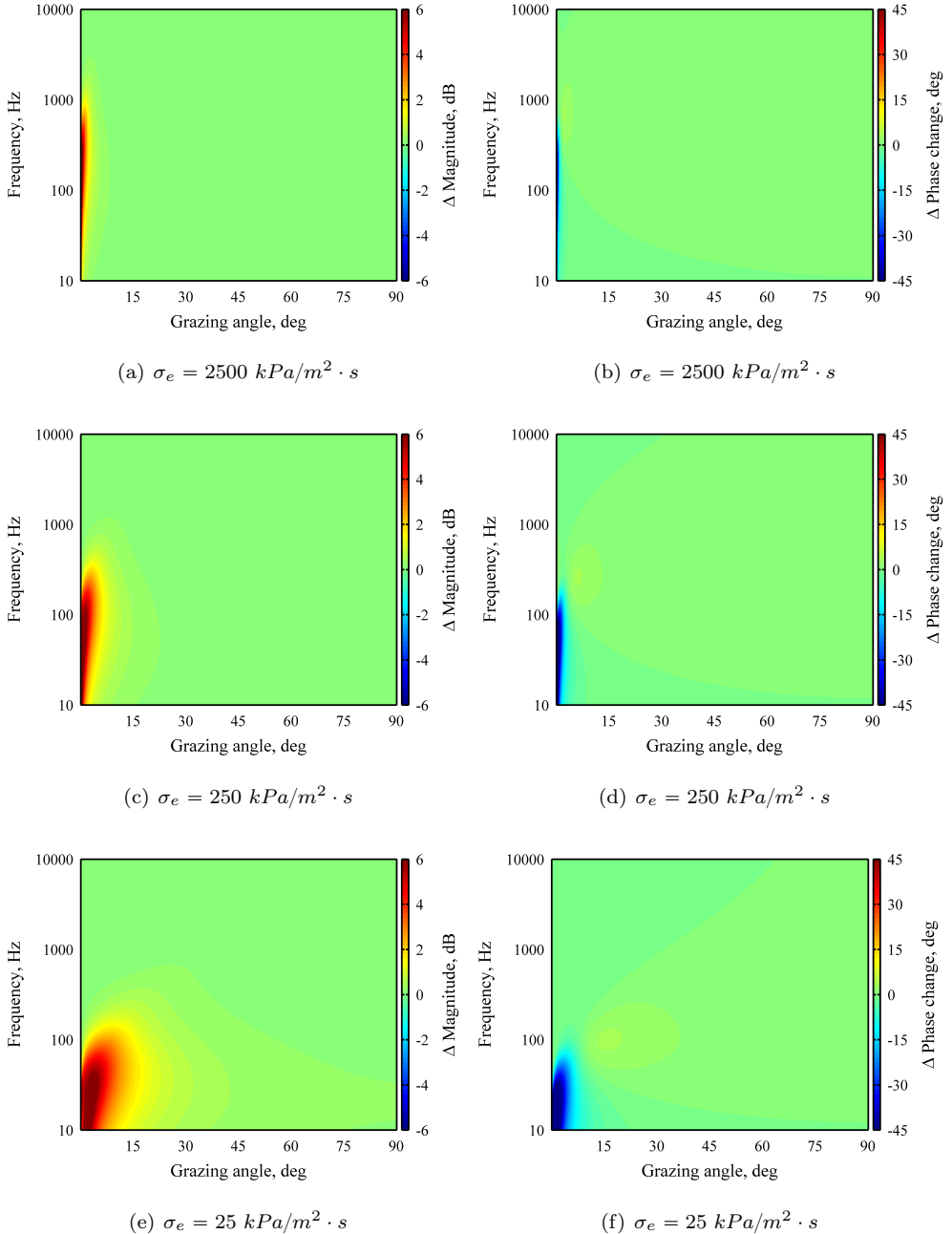


Figure C.12: Difference in magnitude (left column) and phase (right column) between spherical and plane wave approximations. The source is at a height of 10 meter.

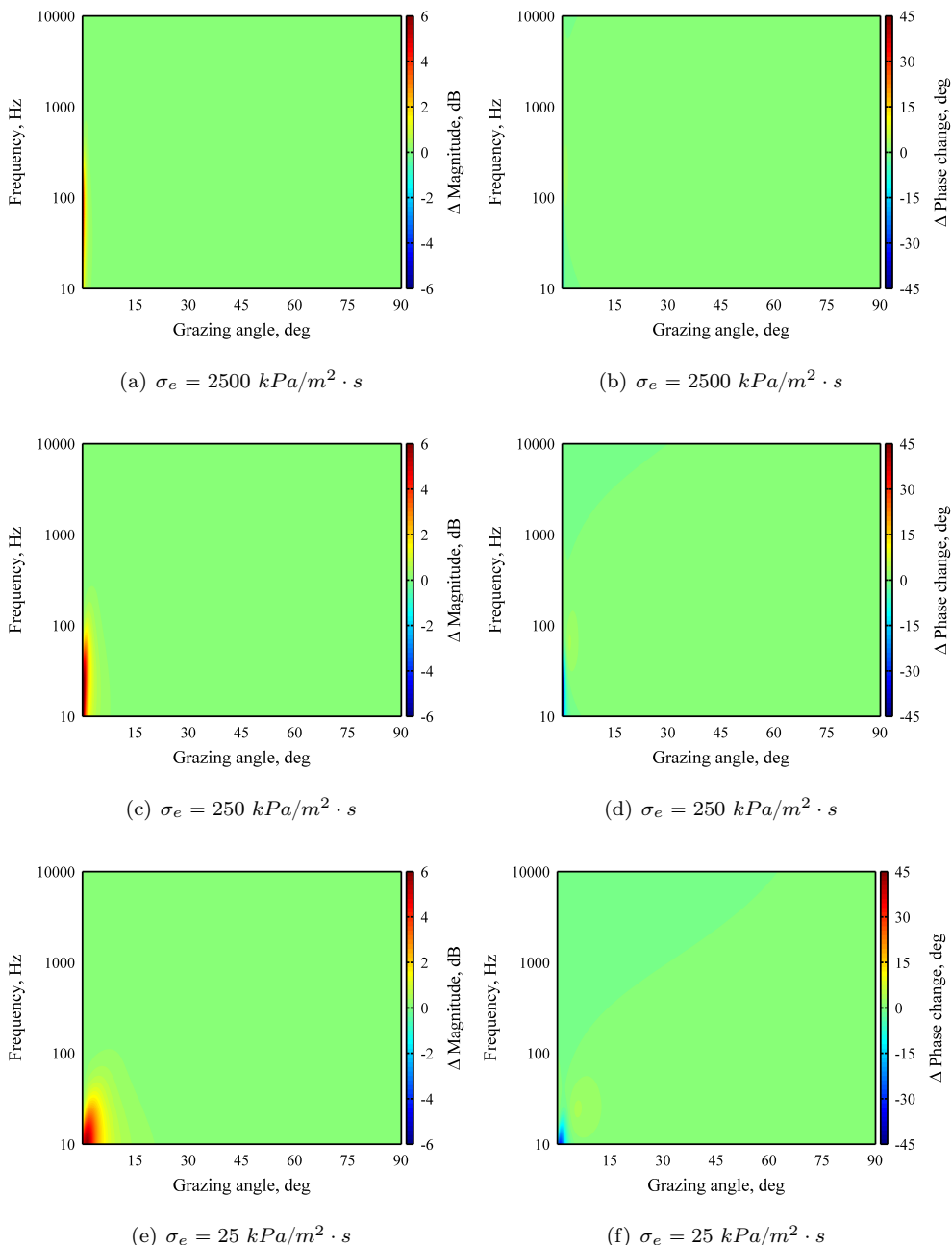


Figure C.13: Difference in magnitude (left column) and phase (right column) between spherical and plane wave approximations. The source is at a height of 100 meter.

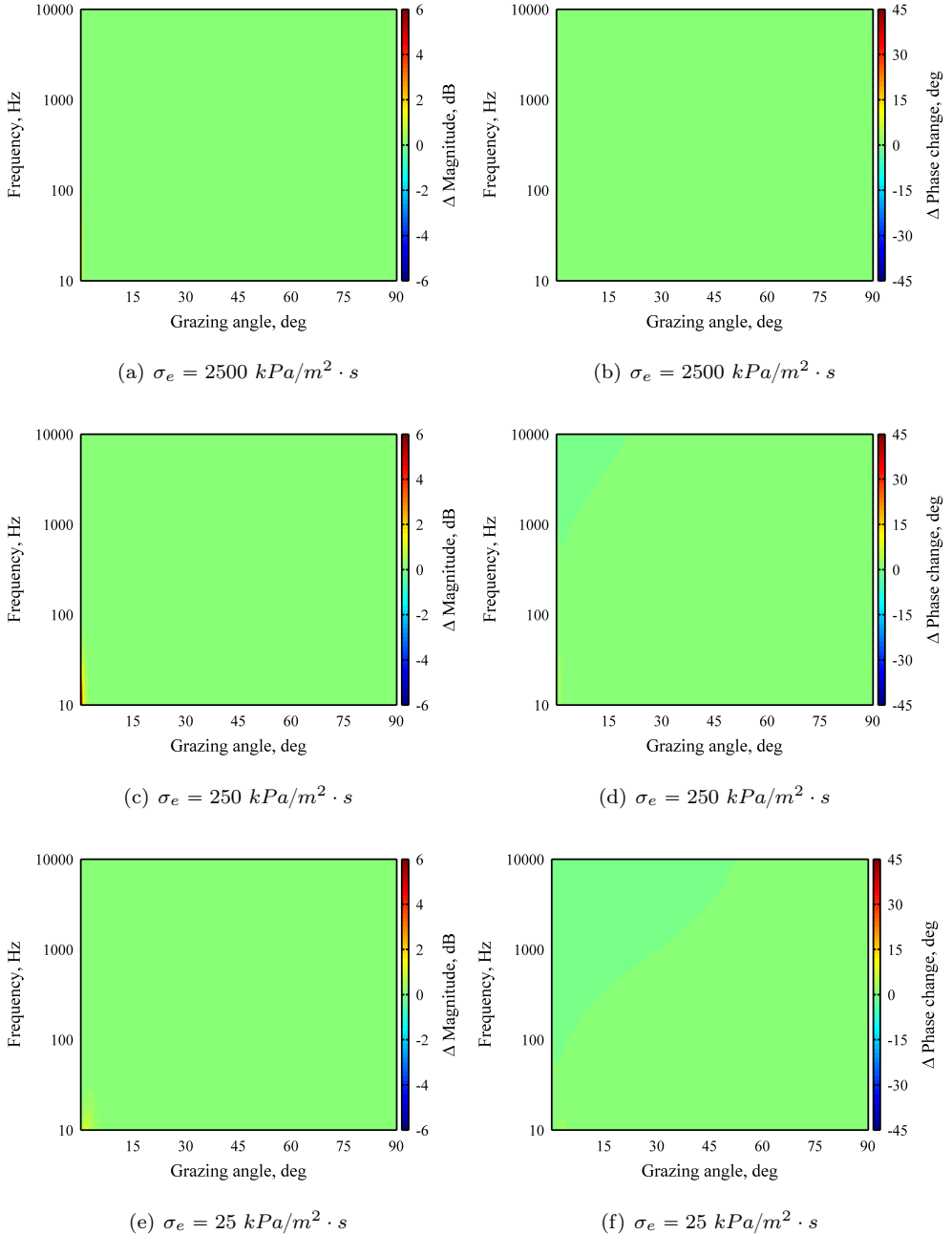


Figure C.14: Difference in magnitude (left column) and phase (right column) between spherical and plane wave approximations. The source is at a height of 1000 meter.

Appendix D

Toolchain variables, gasturbine and flight mechanics

D.1 Flight Mechanics

Flight mechanics are essential in providing input to the simulation of aircraft flyover noise. To evaluate the input for the acoustic source noise models, particularly those related to the engine, a good estimation of the thrust is required. The point mass equations, where it is assumed that the aircraft is condensed to its center of gravity, are:

$$T - D - W \sin(\gamma) = m\dot{V} \quad (\text{D.1})$$

$$L \cos(\mu) - W \cos(\gamma) = mV\dot{\gamma} \quad (\text{D.2})$$

$$V \cos(\gamma) = \dot{x} \quad (\text{D.3})$$

$$V \sin(\gamma) = \dot{h}, \quad (\text{D.4})$$

where, $T, L, D, W, m, V, \gamma, \mu, \dot{h}, \dot{x}$ are the aircraft thrust, lift, drag, weight, mass, air-speed, flight path angle, bank angle, rate of climb and ground speed. The lift and drag follow from,

$$L = \frac{1}{2}\rho V^2 C_L S \quad (\text{D.5})$$

$$D = \frac{1}{2}\rho V^2 C_D S, \quad (\text{D.6})$$

where ρ, S are the air density and wing surface reference area. The factors C_L, C_D are referred to as lift- and drag coefficient and are in general a function of angle of

attack (relative to the airspeed) and Mach number. Using a supplied drag polar, the required angle of attack of the aircraft for equilibrium conditions can be calculated. The pitch angle of the aircraft (in a non-banking situation) than follows by adding the flight path angle and angle of attack, i.e. $\theta = \gamma + \alpha$.

The required thrust, ignoring accelerations, is deduced as:

$$T = D + W \sin(\gamma), \quad (\text{D.7})$$

whereas the lift follows as:

$$L = W \frac{\cos(\gamma)}{\cos(\mu)}. \quad (\text{D.8})$$

If a turn is considered, a centrifugal force is defined by:

$$F_c = L \sin(\mu) = \frac{WV^2}{gR}, \quad (\text{D.9})$$

where R is the turn radius. Next, the turn rate (or heading change $\dot{\chi}$) is defined as $\dot{\chi} = V/R$. Therefore the required bank angle can be calculated:

$$\tan(\mu) = \cos(\gamma) \frac{V}{g} \dot{\chi}, \quad (\text{D.10})$$

where χ can be deduced from a measured trajectory. If no measured trajectory is available, i.e. in case of a full simulation, the tool and equations can be used to generate a flight trajectory based on pre-defined way points. In that case the equations of motion are integrated using a fourth order Runge-Kutta algorithm controlled by Proportional-Integrator-Differentiator (PID) controllers. These controllers take over the roll of a pilot to control the aircraft and let it fly through the way points. In both cases the required thrust is a variable that can be distilled and should be provided by the engine.

D.2 Gasturbine

In most cases, the propulsive energy of commercial aircraft is generated by a gasturbine whereas its transformation into propulsive power is either by a ducted fan or by propeller. In this dissertation the layout of a gasturbine combined with a fan in a ducted configuration is considered, see for example figure 2.8. The basic operation is well captured in figure D.1.

A gasturbine engine comprises many rotating discs of blades (stages) that either apply work or extract work from the air. The first stage is called the fan which

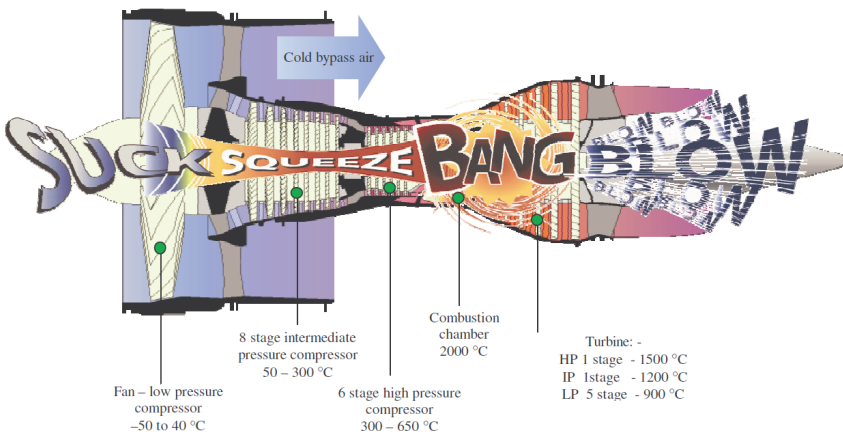


Figure D.1: A cutaway of a typical civil aviation bypass gasturbine. (131)

slightly accelerates the air. A lot of air moves through this fan and the larger portion of this air bypasses the core engine. Therefore this air is referred to as bypass air. By accelerating airflow the momentum of the flow is enlarged which leads to forward thrust. The bypass air is thus a large portion of air that is accelerated slightly. For the airflow through the core the opposite holds, i.e. a low mass but a high acceleration.

The core air is compressed, mixed with fuel and ignited through which energy is added to the flow. In the turbine the gas expands thereby accelerating and rotating the turbine blades. There are in general multiple rotating turbine disc sections (2 or 3) that extract some of the flow energy to drive the compressor and fan stages upstream. This power is transferred through multiple shafts, the same number as turbine sections, thereby generating a self-sustained engine operation as long as sufficient fuel is supplied.

Thrust, although being the main objective of such an engine, is a byproduct of the thermodynamic and aerodynamic processes in the gasturbine. To calculate the gasturbine performance these individual processes should be assessed. Basic calculations are efficiently executed by assuming that the engine is a connection of individual blocks/stages that each modify the airflow's pressure, temperature and/or velocity. Such a calculation is based on the Poisson relation:

$$\frac{T_2}{T_1} = \left(\frac{p_2}{p_1} \right)^{R/\gamma}, \quad (\text{D.11})$$

stating that for an adiabatic process the temperature rise and pressure rise are related by the gas constants R and γ (see chapter 2). By evaluating this equation for individual engine blocks such as the fan, compressor, combustion chamber and turbine,

the thermodynamic quantities can be calculated throughout the engine. Details can be found in the comprehensive book by Rogers & Cohen.⁽¹³²⁾

Several tools are available for the design and calculation of aircraft gasturbines. At the NLR, use is made of the Gas turbine Simulation Program (GSP).⁽⁵³⁾ This tool has been used to generate input for the acoustic noise prediction as a function of the required thrust.

D.3 Source model input

Table D.1: General flight parameters for all engine modules

Parameter	Description	Units
δ	Angle between engine inlet and aircraft axis	rad
M	Aircraft Mach number	-
c_∞	Speed of sound	m/s
ρ_∞	Ambient density	kg/m ³
T_∞	Ambient temperature	K
p_∞	Ambient pressure	Pa
θ	Polar angle, i.e. angle between receiver and engine inlet	rad
f	Frequency	Hz

Table D.2: Stone jet noise model input parameters

Parameter	Description	Units
$\dot{m}_{I,O}$	Inner/Outer jet mass flow	kg/s
$T_{I,O}$	Inner/Outer jet temperature	K
$\rho_{I,O}$	Inner/Outer jet density	kg/m ³
$V_{I,O}$	Inner/Outer jet velocity	m/s
$A_{I,O}$	Inner/Outer jet area	m ²
L	Length between inner/outer jet exhaust plane	m

Table D.3: Heidmann fan noise model input parameters

Parameter	Description	Units
\dot{m}	Mass flow through fan	kg/s
nr	Number of rotor blades	-
ns	Number of stator blades	-
d	Fan diameter	m
N_1	Fan rotational speed	RPM
RSS	Fan rotor-stator spacing; rel. to blade chord	%
ΔT	Temperature rise over fan stage	K
$MTRD$	Fan design tip Mach number	-

Table D.4: Liner model input parameters

Parameter	Description	Units
$L_{I,E}$	Effective liner length of fan (inlet/exhaust)	ft
d	Fan diameter	ft
h	Equivalent fan exhaust diameter	ft

Table D.5: Combustion noise model input parameters

Parameter	Description	Units
T_3	Temperature at combustor inlet	K
T_4	Temperature at combustor exit	K
T_5	Temperature at turbine exit	K
p_3	Pressure at combustor inlet	pa

Table D.6: *Fink airframe noise model input parameters*

Parameter	Description	Units
A_f	Flap area	m^2
A_h	Horizontal tail plane area	m^2
A_v	Vertical tail plane area	m^2
A_w	Wing reference area	m^2
B_h	Flap span	m
B_f	Horizontal tail plane span	m
B_v	Vertical tail plane span	m
B_w	Wing span	m
d_{mg}	Tire diameter main gear	m
d_{ng}	Tire diameter nose gear	m
l_{mg}	Strut length main gear	m
l_{ng}	Strut length main gear	m
n_{mg}	Number of wheels main gear	-
n_{ng}	Number of wheels nose gear	-
N_{mg}	Number of main gear (bogie)	-
N_{ng}	Number of nose gear (bogie)	-
s	Number trailing edge flap slots	-
δ_f	Trailing edge flap deflection angle	rad
N_g	Gear deploy flag	boolean
μ_∞	Ambient dynamic viscosity	$\text{kg}/(\text{sm})$
ψ	Observation azimuthal angle	rad

Appendix E

Supplementary audio files

This dissertation described the transformation of theoretical aircraft noise predictions into audible results. The resulting audio files can be downloaded, together with the electronic copy of this dissertation, through the TU Delft library. This online repository can be found at <http://repository.tudelft.nl/>. By searching for the electronic version of this dissertation, a compressed (zip) file with associated audio files will appear. Upon extracting the compressed file, the audio files become available and are sorted per chapter of this dissertation.

All the audio files are preferably listened too by using headphones to exclude background noise, or a high-end speaker system to correctly represent low-frequency noise.

Table E.1: *Audio files associated with chapter 5*

Full file name	Description
Chap5_File1.wav	Synthesized flyover of B747-400 in departure conditions, i.e. figure 5.9(c).
Chap5_File2.wav	Synthesized flyover of B747-400 in approach conditions, i.e. figure 5.10(c).

By listening to the two audio files of chapter 5, the synthesized difference in thrust setting and aircraft geometry (flaps and gears extended) is audible.

Table E.2: *Audio files associated with chapter 6*

Full file name	Description
Chap6_File1.wav	Straight ray path synthesis result, i.e. figure 6.9(a).
Chap6_File2.wav	Curved ray path synthesis result, i.e. figure 6.9(b).

By listening to the two audio files of chapter 6, the synthesized differences between the straight path and curved path results are audible. These differences are formed by atmospheric propagation effects. The shadow zone and multipath effects are especially noticeable, in these audio files, if the volume knob is turned to the max setting.

Table E.3: *Audio files associated with chapter 7*

Full file name	Description
Chap7_File1.wav	Flight 1 synthesis result, i.e. figure 7.2(a).
Chap7_File2.wav	Flight 1 measured result, i.e. figure 7.2(b).
Chap7_File3.wav	Flight 2 synthesis result, i.e. figure 7.3(a).
Chap7_File4.wav	Flight 2 measured result, i.e. figure 7.3(b).
Chap7_File5.wav	Flight 3 synthesis result, i.e. figure 7.4(a).
Chap7_File6.wav	Flight 3 measured result, i.e. figure 7.4(b).
Chap7_File7.wav	Flight 4 synthesis result, i.e. figure 7.5(a).
Chap7_File8.wav	Flight 4 measured result, i.e. figure 7.5(b).

By listening to the audio files of chapter 7, the differences between synthesized and measured results become clear. Note that a 'rasping' sound is present.

Table E.4: *Audio files associated with chapter 8*

Full file name	Description
Chap8_File1.wav	Non-turbulent broadband synthesis result, i.e. figure 8.2(a).
Chap8_File2.wav	Turbulent broadband synthesis result, i.e. figure 8.2(b).
Chap8_File3.wav	Non-turbulent tonal synthesis result, i.e. figure 8.4.
Chap8_File4.wav	Turbulent tonal synthesis result, i.e. figure 8.4.
Chap8_File5.wav	Turbulent flight 2 synthesis result, i.e. figure 8.5.

By listening to the audio files of chapter 8, the impact of turbulence induced coherence loss in ground interference is demonstrated. Both the broadband and tonal audio files can be played back. Furthermore, the inclusion of this technique in one of the flights of chapter 7, demonstrates the beneficial effect by reducing the 'rasping' sound.

Acknowledgements

At the start of PhD research position, 4 years seems to be a long period. It isn't. Only at the end of a PhD study, at the start of a job, one starts to realize what a privilege it has been to do research for 4 consecutive years on a single subject. I enjoyed it very much. A lot of people made that happen and I'd like to thank them all.

Professor Simons, beste Dick, thank you for taking me under your wings. I've learned a lot on acoustics and aircraft noise. You've stimulated me to go to conferences and to keep improving my methods. If I handed in a concept article or paper, you found details that I had not thought about. Furthermore, your notion that a dissertation should be aimed to be read by insiders, but also written such that a new (PhD) student can comprehend the matter, was spot on. It allowed me to compile the final dissertation into a neat booklet that I hope can find a good use.

Dries, thank you for your support all over the last four years. I enjoyed our discussions, ranging from soccer, students, the NLR or the University and of course my auralization work. Your door was always open for coffee or a quick chat. I enjoyed that quite a lot and hope that we can keep that up in the future.

As important as my TU Delft supervisors, was my manager at the NLR. Roland, thank you for giving me the possibility to come to the NLR. Working in the ATEP department on the VCNS was very motivating. The combination of the 'pragmatic' use cases allowed me to combine the academics and the real-world problems.

That being said, I have to thank my whole ATEP department at the NLR. According to Lync you are all offline right now, otherwise I could have called you and thank you in person. You now have to deal with this version. Without these wonderfull people I would not have been able to finish this dissertation.

Steve. Thank you for the thorough introduction to the subject. It is amazing what a 3-month period at NASA did to my knowledge, way of working and our friendship. I am glad that you are here during the defense and hope that we can bring our aircraft noise auralization efforts to even greater heights in the future.

Without a bunch of friends I couldn't have finished. Some of you I've just met, others

I know for quite a while already. Thank you for being at the defense and the party. Thank you all for: celebrations, soccer, dinner, going out, weddings, paragliding, movie marathons and so on.

There are those in my daily vicinity that contributed as much to this result as I did. I could not have finished this without my home base. Thank you Arjan and Stefan, my two brothers. I am glad that you are my family, paranimf and fallback option. Climbing the Kilimanjaro with you and my parents was an experience that I won't forget. Our family bond is strong, not in the least bit thanks to my parents. Birgit and Hans. You've always urged me to investigate my own potential and to develop it. That lesson, in the end, materialized in this work. I cannot express my gratitude in words. Thank you doesn't even come close.

And that leaves Kim. When we met you said I was more or less crazy that I wanted to do a PhD. I am glad that I didn't listen. Our relation has been, and is, the greatest thing that has happened so far in my life. Our house is just an empty place constructed out of bricks, it is only with you in there that I can call it my home. On to our next little challenge.

Publications

In this appendix a list of publications is printed, generated in the process of this PhD research, to which the author contributed.

Journal

1. Ground Reflection with Turbulence Induced Coherence Loss in Flyover Auralization, **M. Arntzen** and D.G. Simons, International Journal of Aeroacoustics, volume 13, number 5-6, 2014, pp. 447-460.
2. Modeling and Synthesis of Aircraft Flyover Noise, **M. Arntzen** and D.G. Simons, Applied Acoustics, volume 84, October 2014, pages 99-106.
Online: <http://dx.doi.org/10.1016/j.apacoust.2013.09.002>
3. Weather-Dependent Airport Noise Contour Prediction Concept Based on Ray Tracing, **M. Arntzen**, S.J. Heblrij and D.G. Simons, AIAA Journal of Aircraft, volume 51 (5), 2014, pp. 1351-1359.
Online: <http://arc.aiaa.org/doi/abs/10.2514/1.C032149>
4. Framework for Simulating Aircraft Flyover Noise through Nonstandard Atmospheres, **M. Arntzen**, S.A. Rizzi, H.G. Visser and D.G. Simons, AIAA Journal of Aircraft, volume 51 (3), 2014, pp. 956-966.
Online: <http://arc.aiaa.org/doi/abs/10.2514/1.C032049>

Conference

1. Ground Reflection with Turbulence Induced Coherence Loss in Flyover Auralization, **M. Arntzen**, *17th Workshop of the Aeroacoustics Specialists Committee of CEAS, 24-25 September, Sevilla, Spain*, presentation and abstract only.

-
2. Noise Attenuation Directly Under the Flight Path in Varying Atmospheric Conditions, S.J. Heblj, V. Sindhamani, **M. Arntzen**, D.H.T. Bergmans and D.G. Simons, *Internoise 2013, 15-18 September, Innsbruck, Austria*.
 3. Acoustic Ray Tracing Parallelization, **M. Arntzen**, D.G. Simons, J. Shen, A.L. Varbanescu, H. Sips, *Noisecon 2013, 26-28 August, Denver, CO, USA*, NC-13-31.
 4. Modeling of Ground Reflection Effects in Aircraft Flyover Noise Synthesis, **M. Arntzen**, J. Sijl and D.G. Simons, *Noisecon 2013, 26-28 August, Denver, CO, USA*, NC-13-30.
 5. A Framework for Accelerating Imbalanced Applications on Heterogeneous Platforms, J. Shen, A.L. Varbanescu, H. Sips, **M. Arntzen** and D.G. Simons, *Computing Frontiers 2013, 14-16 May, Ischia, Italy*, Number 14.
 6. A Weather Dependent Noise Contour Prediction Concept: Calculating Multi-Event Noise Contours with Ray-Tracing, **M. Arntzen**, S.J. Heblj and D.G. Simons, *12th AIAA Aviation Technology, Integration, and Operations (ATIO) Conference and 14th AIAA/ISSM 17 - 19 September 2012, Indianapolis, IN, USA*, AIAA-2012-5412.
 7. Optimization of Rotorcraft Noise Abatement Trajectories, S. Hartjes, Y. Buys, H.G. Visser, M.D. Pavel, M. Gennaretti, G. Bernardini and **M. Arntzen**, *Internoise 2012, 19-22 August, New York, NY, USA*.
 8. Flyover Noise Synthesis for the Virtual Community Noise Simulator, **M. Arntzen**, *3rd International Air Transport and Operations Symposium conference 2012, Delft, the Netherlands*.
 9. A Framework for Simulation of Aircraft Flyover Noise Through a Non-Standard Atmosphere, **M. Arntzen**, S.A. Rizzi, H.G. Visser and D.G. Simons, *18th AIAA/CEAS Aeroacoustics Conference 4-6 June 2012, Colorado Springs, CO, USA*, AIAA 2012-2079.
 10. A Weather Dependent Noise Contour Prediction Concept: Combining a Standard Method with Ray Tracing, S.J. Heblj, **M. Arntzen** and D.G. Simons, *Euronoise 2012, 10-13 June, Prague, Czech republic*, also NLR-TP-2012-251.
 11. Noise Attenuation in Varying Atmospheric Conditions, D.H.T. Bergmans, **M. Arntzen** and W.F. Lammen, *Internoise 2011, 4-7 September 2011, Osaka, Japan*, also NLR-TP-2011-262.
 12. Aircraft Noise Simulation for a Virtual Reality Environment, **M. Arntzen**, T.A. v. Veen, H.G. Visser and D.G. Simons, *17th AIAA/CEAS Aeroacoustics Conference, 5-8 June 2011, Portland, OR, USA*, AIAA 2011-2853.

About the author

Michael Arntzen was born on the 26th of June 1985 in Amersfoort where he attended secondary school and obtained his HAVO diploma in 2002. Hereafter he studied Aeronautical Engineering at Inholland (HTS) in Haarlem, did internships at KLM, Airbus (Germany) and the DNW, and obtained his Bachelor of Engineering in 2006 (cum laude). He decided to continue in engineering by enrolling at the Delft University of Technology and obtained his Master of Science in 2010. After his graduation he continued at the NLR with his PhD studies, in cooperation with the TU Delft, which culminated in the current dissertation in 2014.

During his PhD period he was a visiting researcher at NASA Langley (Virginia, USA) for 3 months. Next to the period in the USA, he also spent a brief period of 2 weeks at the University of Rome III.

He started, together with colleagues at NASA and the RWTH Aachen, the Virtual Acoustic Simulation Technology for Community Noise Technical Working Group (VASTCON TWG). The VASTCON mission is to 1) share applied research supporting simulation applications, including sound synthesis and propagation, sound reproduction, and creation of virtual environments, to 2) share the results of subjective testing utilizing these applications, and to 3) seek new application areas.

After this PhD study, he started as an R&D Engineer at the NLR, in the Environment & Policy Support department for four days per week. During the other day he is a researcher, and per 2015 also a lecturer, at the Aircraft Noise and Climate Effects group at the TU Delft faculty of Aerospace Engineering.

WHAT IS NLR?

The NLR is a Dutch organisation that identifies, develops and applies high-tech knowledge in the aerospace sector. The NLR's activities are socially relevant, market-orientated, and conducted not-for-profit. In this, the NLR serves to bolster the government's innovative capabilities, while also promoting the innovative and competitive capacities of its partner companies.

The NLR, renowned for its leading expertise, professional approach and independent consultancy, is staffed by client-orientated personnel who are not only highly skilled and educated, but also continuously strive to develop and improve their competencies. The NLR moreover possesses an impressive array of high quality research facilities.



NLR – Dedicated to innovation in aerospace

www.nlr.nl